



Guide to AERO2S and WINGDES Computer Codes for Prediction and Minimization of Drag Due to Lift

Harry W. Carlson
Lockheed Martin Engineering & Sciences • Hampton, Virginia

Julio Chu and Lori P. Ozoroski
Langley Research Center • Hampton, Virginia

L. Arnold McCullers
ViGYAN, Inc. • Hampton, Virginia

Available electronically at the following URL address: <http://techreports.larc.nasa.gov/ltrs/ltrs.html>

Printed copies available from the following:

NASA Center for AeroSpace Information
800 Elkridge Landing Road
Linthicum Heights, MD 21090-2934
(301) 621-0390

National Technical Information Service (NTIS)
5285 Port Royal Road
Springfield, VA 22161-2171
(703) 487-4650

Contents

Symbols	vii
Abstract.....	1
1. Introduction	1
2. Basic Lifting Surface Solution	2
2.1. Grid System and Lifting Surface Definition	2
2.2. Subsonic Linearized Theory Solution	3
2.3. Supersonic Linearized Theory Solution.....	6
3. Theoretical Leading-Edge Thrust.....	8
4. Attainable Leading-Edge Thrust and Vortex Forces	9
5. Aerodynamic Forces and Moments	13
6. Wing Analysis Method for AERO2S Code	16
6.1. Wing With Flaps	16
6.2. Wing in Combination With Second Surface	20
6.3. Two-Dimensional Airfoil.....	20
7. Wing Design Method for WINGDES Code.....	20
7.1. Candidate Surfaces.....	21
7.2. Influence of Leading-Edge Conditions on Wing Design.....	23
7.3. Selection of Leading-Edge Surfaces	23
7.4. Selection of General Camber Surfaces.....	24
7.5. Summary of Design Process	25
7.6. Evaluation of Design	26
7.7. User Control of the Design.....	26
7.8. Flap Design Feature	27
7.9. Design in Presence of Interference Flow Fields.....	29
7.10. Supersonic Empirical Corrections	29
8. AERO2S Computer Code and Its Use	32
8.1. Wing Surface Numerical Representation.....	33
8.2. Vortex Force Options	34
8.3. Optimization Capabilities.....	34
9. WINGDES Computer Code and Its Use	35
9.1. Wing Surface Numerical Representation.....	36
9.2. Design Surface Options	36
9.3. Mission Adaptive Design.....	37
9.4. Flap System Design	38
9.5. Design by Iteration.....	39
9.6. Leading-Edge Surface Control.....	39
9.7. Design With Moment Restraints	39
9.8. Interference Flow-Field Design	40

9.9. Empirical Correction	40
10. Drag Synthesis	40
11. Examples of Prediction of Aerodynamic Performance	42
11.1 Aspect Ratio 2 Wing–Body.	43
11.2. Cranked-Wing Supersonic Fighter.	43
11.3. Subsonic Transport.	46
11.4. Supersonic Transport Wing	46
11.5. Supersonic Transport Wing–Body–Horizontal Tail	46
11.6. Two-Dimensional Airfoil.	46
12. Examples of Design for Aerodynamic Performance Optimization	47
12.1. Supersonic Transport Cruise Surface Design.	47
12.2. Supersonic Transport Low-Speed Flap Design	49
12.3. Nonsymmetrical Wing Cruise Surface Design	51
13. Concluding Remarks	51
Appendix A—AERO2S Code Input and Output	52
A1. Wing Planform—Required Input	52
A2. Wing Planform—Optional Input	52
A3. Wing Camber Surface—Required Input	52
A4. Section Parameters for Attainable Thrust Calculation—Required Input.	53
A5. Flight Conditions—Required Input	53
A6. Leading- and Trailing-Edge Flaps—Optional Input	53
A7. Solution Convergence Criteria—Optional Input	54
A8. Canard or Horizontal Tail—Optional Input.	55
A9. Optional Two-Dimensional Airfoil Solution	55
A10. Code Output Data.	56
Appendix B—WINGDES Code Input and Output	57
B1. Wing Planform—Required Input	57
B2. Wing Planform—Optional Input	58
B3. Wing Camber Surface—Optional Input.	58
B4. Section Parameters for Attainable Thrust Calculation—Required Input.	58
B5. Flight Conditions—Required Input	59
B6. Solution Convergence Criteria—Optional Input	59
B7. Design Specifications—Required Input for Design Mode.	59
B8. Design Specifications—Optional Input for Design Mode	60
B9. Additional Optional Input.	61
B10. Reflex Surface Design—Optional Input for Design Mode	61
B11. Flap Design—Optional Input for Design Mode	61
B12. Design Surface Smoothness Control—Optional Input.	61
B13. Interference Flow Field—Optional Input.	62

B14. Empirical Corrections—Optional Input 62
B15. Code Output Data 62
Appendix C—Estimation of Idealized Minimum Drag and Maximum Suction Parameter 64
References 73
Tables 74
Figures 88

Symbols

The computer symbols used in the text, tables, and figures are defined in appendixes A and B.

A	candidate surface weighting factor
A_e	equivalent area due to lift
AR	aspect ratio, $\frac{b^2}{S}$
b	span
C_A	axial- or chord-force coefficient, $\frac{\text{Axial force}}{qS}$
C_D	drag coefficient, $\frac{\text{Drag}}{qS}$
ΔC_D	drag coefficient due to lift, $C_D - C_{D,0}$
$C_{D,0}$	drag coefficient at $\alpha = 0^\circ$ for configuration with symmetry about wing reference plane
C_L	lift coefficient, $\frac{\text{Lift}}{qS}$
$C_{L,\text{des}}$	design lift coefficient
$C_{L,\text{opt}}$	optimum lift coefficient, lift coefficient corresponding to maximum value of suction parameter
C_{L_α}	theoretical lift-curve slope at $\alpha = 0^\circ$, per deg
C_l	rolling-moment coefficient about lateral center of gravity for nonsymmetrical wings, $\frac{\text{Rolling moment}}{qSb/2}$
C_m	pitching-moment coefficient, $\frac{\text{Pitching moment}}{qS\bar{c}}$
$C_{m,\text{des}}$	design pitching-moment coefficient
C_N	normal-force coefficient, $\frac{\text{Normal force}}{qS}$
C_p	pressure coefficient, $\frac{p_l - p}{q}$
ΔC_p	lifting pressure coefficient
$C_{p,c}$	pressure coefficient on cambered wing at $\alpha = 0^\circ$
$(C_{p,c})_c$	component of $C_{p,c}$ due to pure camber loading (contribution with no leading-edge singularity)
$(C_{p,c})_f$	component of $C_{p,c}$ due to flat wing loading (contribution with leading-edge singularity)
$C_{p,f}$	pressure coefficient on flat wing at $\alpha = 1^\circ$
$C_{p,\text{lim}}$	limiting pressure coefficient used in definition of attainable thrust
$C_{p,o}$	pressure coefficient at specified initial point
$C_{p,\text{vac}}$	vacuum pressure coefficient, $-\frac{2}{\gamma M^2}$
c	local chord
\bar{c}	mean aerodynamic chord
c_A	section axial-force coefficient
$c_{A,c}$	component of c_A due to basic pressure loading of camber surface at $\alpha = 0^\circ$ acting on camber surface

$c_{A,flc}$	components of c_A due to basic pressure loading of flat wing at $\alpha = 1^\circ$ acting on camber surface
c_e	element chord at element midspan
c_{le}	streamwise chord for leading-edge design area
c_m	section pitching-moment coefficient
c_N	section normal-force coefficient
$c_{N,c}$	component of c_N due to basic pressure loading of camber surface at $\alpha = 0^\circ$ acting on camber surface
$(c_{N,c})_c$	component of $c_{N,c}$ due to pure camber loading (contribution with no leading-edge singularity)
$(c_{N,c})_f$	component of $c_{N,c}$ due to flat wing loading (contribution with leading-edge singularity)
c_{Nf}	component of c_N due to basic pressure loading of flat wing at $\alpha = 1^\circ$ acting on camber surface
c_R	section resultant force coefficient, $\sqrt{c_A^2 + c_N^2}$
c_r	wing root chord, chord at $y = 0$
c_t	theoretical section thrust coefficient
c_t^*	attainable section thrust coefficient
$c_{t,f}$	theoretical section leading-edge thrust coefficient for flat wing at $\alpha = 1^\circ$
c_{te}	streamwise chord for trailing-edge design area
e_x	exponent of x used in definition of candidate camber surfaces
e_y	exponent of y used in definition of candidate camber surfaces
e_1, e_2, e_3, e_4	exponents used in calculating attainable thrust
$F_c(x')$	normal-force integration factor for pure camber contribution to basic cambered wing loading at $\alpha = 0^\circ$ acting on camber surface
$F_f(x')$	normal-force integration factor for basic pressure loading of flat wing at $\alpha = 1^\circ$ acting on flat surface; normal-force integration factor for flat wing contribution to basic cambered wing loading at $\alpha = 0^\circ$ acting on camber surface; axial-force integration factor for basic pressure loading of flat wing at $\alpha = 1^\circ$ acting on camber surface
F'_L	rate of growth of lifting force per unit distance along equivalent body axis
f	location correction factor for code perturbation velocity
h	altitude
i	index of wing element longitudinal position within code grid system and index used in identification of candidate surfaces
j	index of wing element lateral position within code grid system and index used in identification of candidate surfaces
K	constant used in curve-fit equation
K_{des}	design lift-coefficient factor, $\frac{(C_{L,des})_{opt,exp}}{(C_{L,des})_{opt,th}}$
K_S	suction parameter factor, $\frac{(S_{S,max})_{exp}}{(S_{S,max})_{th}}$
K_t	attainable thrust factor, fraction of theoretical thrust actually attainable, $\frac{c_t^*}{c_t}$
k	arbitrary constant used in definition of pressure distribution

k_a	constant used in attainable thrust curve-fit equation
k_c, k_f	constants used in curve fitting of code perturbation velocities and pressure coefficients for integration purposes
$k_{h,1}, k_{h,2}$	constants used in hinge-line singularity correction
k_n	arrow wing notch ratio, see figure 40
k_s	constant used in candidate design surface definition
k_{vor}	constant used in definition of vortex force distribution
k_1, k_2	constants used in definition of camber surface slope
LE	leading edge
l	overall wing length
l_e	effective length of body of revolution representing distribution of equivalent area due to lift as defined by area rule cutting planes
$l_{e,v}$	effective length of body of revolution representing distribution of volume as defined by area rule cutting planes
M	Mach number
M_e	equivalent Mach number used in place of M_n to account for values of $C_{p,lim}$ differing from $C_{p,vac}$
M_n	normal Mach number, see figure 12
m_{le}	multiplying factor for tangent of leading-edge flap deflection angle
m_{te}	multiplying factor for tangent of trailing-edge flap deflection angle
p	free-stream static pressure
p_l	local static pressure
q	free-stream dynamic pressure
R	Reynolds number based on mean aerodynamic chord
\bar{R}	linearized theory perturbation velocity influence function
r	leading-edge radius
r_i	leading-edge radius index, $\frac{(r/c)\eta}{(\tau/c)^2}$
S	wing reference area
S_S	suction parameter, $\frac{C_L \tan(C_L/C_{L_\alpha}) - \Delta C_D}{C_L \tan(C_L/C_{L_\alpha}) - C_L^2/(\pi AR)}$
SST	supersonic transport
s	distance along section camber line
TE	trailing edge
t	theoretical section leading-edge thrust
U	free-stream velocity
u, v, w	perturbation velocity in $x, y,$ and z direction, respectively
Δu	longitudinal perturbation velocity difference across wing lifting surface as fraction of free-stream velocity
$(\Delta u \sqrt{x'})_o$	limiting value of leading-edge thrust parameter $\Delta u \sqrt{x'}$ at wing leading edge
$(\Delta u \sqrt{x'})_{o,c}$	limiting value of leading-edge thrust parameter $\Delta u \sqrt{x'}$ at wing leading edge for cambered wing at $\alpha = 0^\circ$

$(\Delta u \sqrt{x'})_{o,f}$	limiting value of leading-edge thrust parameter $\Delta u \sqrt{x'}$ at wing leading edge for flat wing at $\alpha = 1^\circ$
Δu_c	value of Δu for cambered wing at $\alpha = 0^\circ$
Δu_f	value of Δu for flat wing at $\alpha = 1^\circ$
V	configuration total volume
x, y, z	Cartesian coordinates, positive aft, right, and up, respectively
Δx	longitudinal spacing of grid lines used in establishment of code wing grid system
$\Delta x_C, \Delta x_R, \Delta x_L$	longitudinal distances employed in influence function \bar{R}
x_{cg}	longitudinal center of gravity
x_h	distance from wing leading edge to flap hinge line
x_{mc}	longitudinal moment center
x'	distance in x direction measured from wing leading edge
x'_e	distance in x direction measured from wing element leading edge
x'_0, x'_1, x'_2	values of x' at which camber surface z ordinates are specified
y_{cg}	lateral center of gravity
Y_0	limiting value of singularity parameter $\Delta C_p \sqrt{x'}$ at $x' = 0$
z_0, z_1, z_2	camber surface ordinate at $x'_0, x'_1,$ and $x'_2,$ respectively
α	angle of attack, deg
α_{des}	angle of attack corresponding to design lift coefficient, deg
$\Delta\alpha_{ft}$	range of angle of attack for full leading-edge thrust, deg
α_{zt}	angle of attack for zero thrust, deg
α_0	angle of attack corresponding to zero lift, deg
β	$\begin{cases} = \sqrt{M^2 - 1} & (M > 1) \\ = \sqrt{1 - M^2} & (M < 1) \end{cases}$
γ	ratio of specific heats, 1.4
δ_c	incidence of canard reference plane with respect to wing reference plane, positive with leading edge up, deg
δ_H	incidence of horizontal-tail reference plane with respect to wing reference plane, positive with leading edge up, deg
$\delta_{le,n}$	leading-edge flap deflection angle measured normal to hinge line, positive with leading edge down (segmented flap deflection specified as inboard/outboard), deg
$\delta_{le,s}$	leading-edge flap streamwise deflection angle, positive with leading edge down (segmented flap deflection specified as inboard/outboard), deg
$\delta_{te,n}$	trailing-edge flap deflection angle measured normal to hinge line, positive with leading edge down (segmented flap deflection specified as inboard/outboard), deg
$\delta_{te,s}$	trailing-edge flap streamwise deflection angle, positive with leading edge down (segmented flap deflection specified as inboard/outboard), deg
ϵ	angle between line tangent to wing section camber surface and camber surface reference plane, deg
ϵ_o	value of ϵ at wing leading edge
η	location of section maximum thickness, fraction of chord

Λ	sweep angle of wing constant percent chord line, deg
$\Lambda_{h,le}$	leading-edge flap hinge-line sweep angle, deg
$\Lambda_{h,te}$	trailing-edge flap hinge-line sweep angle, deg
Λ_{le}	wing leading-edge sweep angle, deg
λ	angle between intersection of distant fore Mach cone with wing plane and wing longitudinal axis, deg (see fig. 39)
$\lambda_N, \lambda_M, \lambda_R$	Lagrange multipliers
μ	Mach angle, $\sin^{-1}(1/M)$, deg
τ	section maximum thickness
ϕ	azimuth angle in frontal projection between line connecting field point with wing longitudinal axis and wing plane, deg (see fig. 39)
Subscripts:	
adj	adjusted
av	average
<i>b</i>	aerodynamic characteristics due to basic pressure distributions alone (no thrust or vortex forces)
<i>c</i>	cambered wing
cor	corrected
emp	empirical
eval	evaluated
exp	experiment
<i>f</i>	flat wing
le	leading edge
max	maximum
min	minimum
<i>n</i>	wing section normal to leading edge
opt	optimum
pre	previous
rep	replacement
te	trailing edge
th	theoretical
tot	total
vis	viscous
vor	vortex
<i>w</i>	wave

Abstract

The computer codes, AERO2S and WINGDES, are now widely used for the analysis and design of airplane lifting surfaces under conditions that tend to induce flow separation. These codes have undergone continued development to provide additional capabilities since the introduction of the original versions over a decade ago. This code development has been reported in a variety of publications (NASA technical papers, NASA contractor reports, and society journals). Some modifications have not been publicized at all. Users of these codes have suggested the desirability of combining in a single document the descriptions of the code development, an outline of the features of each code, and suggestions for effective code usage. This report is intended to supply that need.

1. Introduction

The computer codes, AERO2S and WINGDES, are now widely used for the analysis and design of airplane lifting surfaces under conditions that tend to induce flow separation and degrade performance. These codes have undergone continued development to provide additional capabilities since the introduction of the original versions over a decade ago. This code development has been reported in a variety of publications (NASA technical papers, NASA contractor reports, and society journals). Some modifications have not been publicized at all. Users of these codes have suggested the desirability of combining in a single document the descriptions of the code development, an outline of the features of each code, and suggestions for effective code usage. This report is intended to supply that need.

A method for estimation of attainable leading-edge thrust introduced in reference 1 provides the fundamental basis of a system applicable to partially attached-partially separated flow. The original computing code employing the attainable thrust numerical method which was applicable to analysis of a single lifting surface with twist and camber at subsonic speeds is described in reference 2. A modification of the analysis method to provide for the handling of simple hinged leading- and trailing-edge flaps is described in reference 3. A further modification to permit the analysis of a wing surface in combination with a second lifting surface such as a canard or a horizontal tail is described in reference 4. The present version of this code is designated "AERO2S."

The wing-design computer code described in reference 5 provides for the design of a wing mean camber surface (twist and camber in combination) to minimize drag for given design lift and moment conditions. The design method defines an optimum combination of candidate surfaces rather than the more usual optimum combination of loadings. In the design process, attainable leading-edge thrust is taken into account to provide the mildest possible camber surface which meets the design requirements. The use of candidate surfaces provides an

additional capability to design mission adaptive camber surfaces which restrict changes to designated areas of the planform. The design code was later modified to provide for the design of leading- and trailing-edge flap deflection schedules as described in appendix A of reference 3. The present code also has provision for the design of reflexed wing surfaces in the vicinity of engine nacelles and for the handling of asymmetrical planforms. These two modifications, as well as several others, were not previously documented. The design code is applicable to both subsonic and supersonic speeds and provides analysis as well as design capabilities. The present version of this code is designated "WINGDES."

A survey of research on wing design for reduction of drag due to lift at supersonic speeds reported in reference 6 led to the development of an empirical correction to account for real flow effects not covered by linearized theory methods. This correction provides an adjustment to the design process so that the wing design may be optimized with nonlinear penalties associated with excessive camber surface severity taken into account. The empirical correction, now incorporated into the WINGDES code, results in a milder camber surface than would otherwise be found. A second empirical correction provides a more realistic estimate of the achievable performance of the design. A further modification to the application of the correction, introduced in the present paper in section 7.10, now permits the additional benefit of reduced camber surface severity associated with an attainable thrust design to be included in the performance estimate.

Reference 7 describes a recent revision of the attainable thrust prediction method used in both codes. The newer method that provides for a greater range of airfoil shapes from very sharp to very blunt leading edges is based on experimental data for a wider range of Reynolds numbers than the previous method. References 8 and 9, in addition to references 2 to 7, give examples of correlation of code results (both AERO2S and WINGDES) with experimental measurements and offer

advice on application of the codes to problems of interest.

This report is intended to provide an understanding of code capabilities and guidance in effective application to problems of practical interest but not a demonstration of code validity. The many previously reported correlations of code data with experimental results used to validate the methods are reexamined only if they provide information pertinent to future code usage. Readers interested primarily in application of the codes will find information describing code input and output data in appendix A for AERO2S and in appendix B for WINGDES. Examples of code use given in sections 11 and 12 offer guidance in use of the codes for problems of interest. Data used in these examples are given in table I for AERO2S and in table II for WINGDES and serve as models for the preparation of code input.

The use of area rule concepts to provide a further understanding of design for drag minimization at supersonic speeds is the final topic of this report. Mathematical relationships presented in appendix C describe the dependence of vortex drag, wave drag due to lift, and wave drag due to volume on configuration geometric characteristics and establish minimum values for each of these drag components. The strategies for the estimation of drag minima outlined in appendix C have been incorporated into a computer code, CDMIN.

2. Basic Lifting Surface Solution

The primary component of both the WINGDES and the AERO2S codes is a modified linearized solution for the forces and moments acting on twisted and cambered lifting surfaces of arbitrary planform. Forces obtained by integration of pressure distributions on the zero thickness lifting surfaces used in these codes do not include a leading-edge thrust contribution arising from the high velocities and low pressures generated by a flow around the leading edge from a stagnation point on the wing lower surface.¹ However, methods are available that provide estimates of not only the theoretical leading-edge thrust but also the amount of this force that can actually be realized. A means of estimating attainable leading-edge thrust and also the vortex force generated as a result of leading-edge flow separation is included in the modified linearized theory solution used in these codes. Among the unique features of the linearized theory methods used herein are (1) solutions obtained by pure iteration and (2) the use of leading-edge singularity

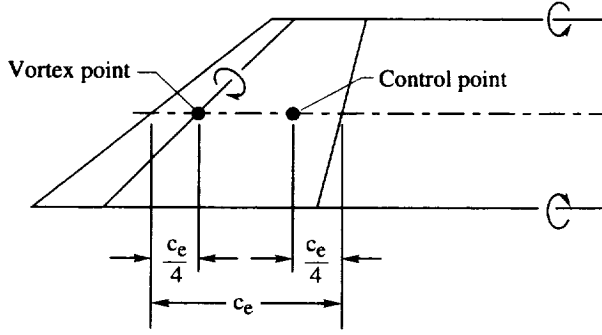
¹Under some circumstances (wings with symmetrical sections at negative angles of attack, for example), the stagnation point may occur on the upper surface. In either case, leading-edge thrust may be developed.

parameters to identify and separate velocity distribution components with and without singularities. The first feature permits an easy code expansion to accommodate more wing elements for greater accuracy as computer capabilities improve. The second feature permits more accurate determination of leading-edge thrust distribution for wings with twist and camber and provides improved pressure distribution integration techniques.

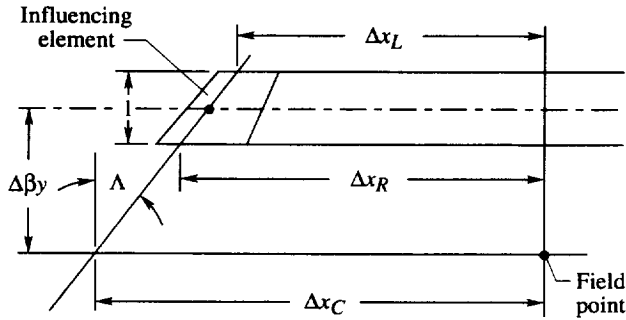
2.1. Grid System and Lifting Surface Definition

The linearized theory solutions are obtained by an iterative solution of influence equations for an array of wing elements representing the wing planform as depicted in figure 1. Only a right-hand wing panel is necessary because of the lateral symmetry of the wing and all the flow properties. Only recently has the WINGDES code been modified to permit solutions for asymmetric planforms. When that option is selected, the entire planform is represented as a right-hand panel and the imposition of symmetry is revoked. In figure 1 only a small number of elements are shown for the purpose of illustration; in practice several hundred to as many as 2000 elements would be employed. The elements are superimposed on a rectangular grid so that the inboard and outboard element boundaries lie along unit values of the spanwise parameter βy and the midspan leading and trailing edges lie on unit values of the chordwise parameter $x/\Delta x$. The scaling of the wing from model or airplane dimensions to code dimensions is chosen to provide the desired number of elements in the spanwise direction. The distance Δx controls the chordwise spacing of the elements; it is selected by specification of an element aspect ratio ELAR, which is constant for all but the leading- and trailing-edge elements. Each element is assigned a number and a record is kept of the number assigned to the leading- and trailing-edge elements in each chordwise row. The i and j indices ($i(x/\Delta x)$ and $j(\beta y)$) are used in determining the order of solution; elements are selected first according to advancing values of the index i then according to advancing values of the index j . The order of solution thus marches inboard to outboard and front to rear.

As shown in figure 1(b), the wing representation for supersonic speeds employs elements with unswept leading and trailing edges, a limitation made necessary by the peculiar nature of supersonic flow. For subsonic speeds, swept leading and trailing edges are acceptable and provide a more accurate solution. For subsonic solutions, element corner points at the wing leading and trailing edges are found by interpolation of the scaled input planform definition. These points determine the leading-edge sweep of the first element and the trailing-edge sweep of the last element in each chordwise row identified by the index $j(\beta y)$. Sweep angles for element leading and trailing edges at a specified span location are found from



Sketch 2-3



Sketch 2-4

sketch 2-4 is the reverse of that given in reference 2 so that distances behind an influencing element may be represented as positive quantities. In addition, the sign of the influence function \bar{R} has been changed so that the function has the same sign as the induced velocities.

A graphical representation of the subsonic influence function \bar{R} for an unswept element is given in figure 2. The vertical velocities generated by a given element are directly related to this function. Behind the bound leg and between the two trailing legs, only downwash is generated. Ahead of the bound leg and outside the trailing legs, only upwash is generated. The singularities which arise at the bound and trailing legs are shown only in part because values of \bar{R} are truncated for locations closer to the lines than one tenth the element span. These singularities dictate the need for a precisely defined grid and element system to represent a lifting surface. Clearly an unstructured random array of elements could lead to coincidence of singularities with control points and result in an unacceptable infinite local velocity. Even a near coincidence could result in unstable solutions. The grid system chosen places element inboard and outboard boundaries on streamwise lines with equal lateral spacing. The element control point location at the midspan of the element and at three quarters of the element chord provides a structured array of the vortex system so that

the influence of each element is dependent on the strength of its vortex and is not subject to distortions caused by geometric coincidences. The depiction of the influence factor in figure 2 shows clearly the relative advantage of high wing aspect ratios. A second element just to the left or right of the influencing element can, because of its upwash field, generate a given amount of lift at a smaller angle of attack than would an isolated element. The smaller angle of attack of course results in a smaller drag for a given lift. On the other hand, a second element directly behind the first would, because of the downwash field, require a large angle of attack to generate the same lift, and a higher drag would result. The relatively small effect of the lifting element at locations ahead of the element explains the applicability of the iterative solution.

The downwash at any point in the plane of the wing induced by the complete wing may be found by a summation of the contributions of all the individual elements. At the control point of a field element at which the boundary condition of no flow through the element is to be met, the downwash velocity is given as

$$\left(\frac{w}{U}\right)^* = \frac{\beta}{4\pi} \bar{R}^* \Delta u^* c_e^* + \frac{\beta}{4\pi} \sum \bar{R} \Delta u c_e$$

where the quantities with stars (\star) refer to the field element and the summation includes all elements but the field element itself.

The boundary condition is met when

$$\left(\frac{w}{U}\right)^* = \left(\frac{dz}{dx}\right)^*$$

or

$$\Delta u^* = \frac{4\pi}{\beta} \frac{1}{\bar{R}^* c_e^*} \left(\frac{dz}{dx}\right)^* - \frac{1}{\bar{R}^* c_e^*} \sum \bar{R} \Delta u c_e \quad (2)$$

The perturbation velocities are converted into pressure coefficients in accordance with the linearized theory assumption

$$\Delta C_p^* = 2 \Delta u^*$$

Before the solution by iteration is begun, perturbation velocities for all elements are set to zero. Then, each element in turn is considered as a field element, and a perturbation velocity for that element satisfying the boundary condition is found. This new velocity replaces the old one in the velocity table, and the calculation proceeds to the next element. As described in section 2.1, the order of solution proceeds from inboard to outboard at the front of the wing and repeats this inboard to outboard sweep at successive rearward positions. As a

means of verifying the solution convergence, the absolute value of the velocity differences between successive iterations is calculated for each element, and an average value of this difference for the whole wing is found. The iteration process is discontinued when the average difference for two successive iterations is less than one half of 1 percent (0.005) of the average pressure loading of the flat surface at $\alpha = 1^\circ$.

As a means of reducing computational time, only elements relatively close to the field point are considered in the first iteration. As the iteration process proceeds and the convergence criteria are approached, the region of influence considered is expanded. The influence region is related to the convergence criteria in such a way to ensure that, at least for the last two iterations, the whole wing is included. An element is excluded from the summation if $\Delta\beta y$ is greater than

$$4 + 2\sqrt{0.005/(\text{CNVGP})} [(JBYMAX) - 2]$$

or Δx_L or Δx_R (whichever is less) is greater than

$$2\Delta x + \sqrt{0.005/(\text{CNVGP})} [(XMAX)(SCALE) - 2\Delta x]$$

where CNVGP is the value of the average difference ratio for the previous iteration.

Because of the element system used to represent the wing, it was known at the outset that there would be errors in the numerical solution in the region of the wing leading edge. These errors were anticipated to be systematic in nature and thus predictable so that corrections could be made. To study the numerical solution errors, the coded solution was modified slightly to permit a solution for a two-dimensional wing. Typical code results for a flat (uncambered) two-dimensional wing at $\alpha = 1^\circ$ are shown in figure 3. Velocity distributions are shown for uniform chord elements at the left of the figure and for a smaller chord first element at the right. The code results are compared with the exact linearized theory solution which is

$$\Delta u = 2\alpha \sqrt{\frac{c}{x'} - 1}$$

or

$$\Delta u \sqrt{\frac{x'}{c}} = 2\alpha \sqrt{1 - \frac{x'}{c}}$$

with α in radians. The plot of the singularity parameter $\Delta u \sqrt{x'/\Delta x}$ allows a more critical comparison of numerical results with the exact linearized theory. The numerical result velocities are assumed to act at the element quarter-chord because the center of pressure for the critical leading-edge elements tends to occur at this point. As shown at the left of the figure, with uniform chord

spacing only the first element result is in error. For a smaller first chord as shown at the right, code results for the first two elements (but only the first two elements) behind the leading edge were found to be in error.

When other first element chords were employed, results such as those shown in the upper plot of figure 4 were obtained. The well-behaved nature of the errors suggested that a correction could easily be made. The correction is made to location, rather than to the velocity itself, because a shift in location will correct flat wing data but will not introduce appreciable errors in data for surfaces with pure camber loadings. As shown in sketch 2-5, if the location $x'/\Delta x$ is multiplied by a correction factor f , the singularity parameter now expressed as $\Delta u \sqrt{f(x'/\Delta x)}$ will follow the dashed-line curve. Thus, it is a simple matter to find a new x' location, defined by the factor f , which will produce agreement with the exact linearized theory. The required factor for each of the code data points is shown in the middle plot of figure 4. Also shown is a curve fit to the correction factor data defined by

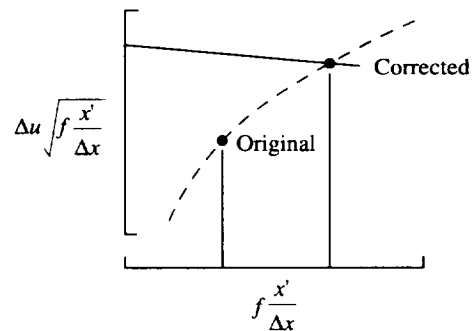
$$f = 1 + 0.36 \frac{1.25 - x'/\Delta x}{x'/\Delta x} + 0.18 \sin \frac{x'}{\Delta x} \pi \quad \left(\frac{x'}{\Delta x} < 0.5 \right)$$

and

$$f = 1 + 0.36 \frac{1.25 - x'/\Delta x}{x'/\Delta x} + 0.18 \sin \frac{1.25 - x'/\Delta x}{1.5} \pi \quad \left(\frac{x'}{\Delta x} > 0.5 \right)$$

The singularity parameter obtained when the location of the velocity is defined by the factor f is shown in the bottom plot of figure 4.

The simple correction derived from the two-dimensional results was found to be equally valid in three



Sketch 2-5

dimensions. Typical code results for constant-chord wings (right-hand panel only) of various sweep angles at $M = 0.01$ are shown in figure 5. The singularity parameter is shown as a function of chordwise position for a midspan section. No erratic behavior of the first two elements is seen. Results for other sweep angles between 0° and 80° at other Mach numbers up to 0.8 were similar.

The iterative solution converged quite rapidly to a reasonable approximation of fully converged results as estimated by extrapolation and as given by vortex lattice methods using matrix inversion. However, when stringent convergence criteria are applied, as required to obtain accurate leading-edge singularity information, many iterations may be necessary. An example for a constant-chord wing with $\Lambda_{le} = 40^\circ$ (right-hand panel only) is given in figure 6. The first and second iterations give the general character of the solution. More than four iterations are required before sufficiently accurate leading-edge perturbation velocities are provided. The code convergence criteria previously discussed are met after the tenth iteration in this example. For more complex planforms and for severely cambered wings, more iterations are required. For some of the examples shown later, up to 70 iterations were required.

2.3. Supersonic Linearized Theory Solution

Each rectangular element used to represent the wing for the supersonic solution is assumed to have an associated horseshoe vortex system with the same geometry as the subsonic solution except that the bound leg is unswept. The vortex strength, however, is different. At any point in the plane of the wing, the downwash velocity created by the vortex is given by

$$\frac{w}{U} = \frac{\beta}{2\pi} \bar{R} \Delta u c_e$$

where

Δu	longitudinal perturbation velocity difference across wing surface
c_e	element average chord
\bar{R}	supersonic influence factor

In terms of the geometry system used, \bar{R} is given as

$$\bar{R} = \frac{\sqrt{\Delta x_C^2 - (\Delta\beta y - 0.5)^2}}{\Delta x_C(\Delta\beta y - 0.5)} - \frac{\sqrt{\Delta x_C^2 + (\Delta\beta y + 0.5)^2}}{\Delta x_C(\Delta\beta y + 0.5)} \quad (3)$$

The quantity Δx_C is again defined as shown in sketch 2-4. For an unswept bound leg, $\Delta x_C = \Delta x_R = \Delta x_L$.

A graphical representation of the supersonic influence factor \bar{R} is given in figure 7. As with the subsonic distribution, only downwash is generated behind the

bound leg and between the two trailing legs. The upwash generated outside the trailing legs, however, is confined to a region behind Mach lines from the bound leg corner points. The aerodynamic advantage of high aspect ratio, clearly shown for subsonic speeds, applies to supersonic speeds only if additional outboard elements are arranged to lie behind the Mach line.

The downwash at any point in the plane of the wing induced by the complete wing may be found by a summation of the contributions of all the individual elements. At the control point of a field element where the boundary condition of no flow through the element is to be met, the downwash velocity is given as

$$\left(\frac{w}{U}\right)^* = \left(\frac{dz}{dx}\right)^* \quad (4)$$

or

$$\Delta u^* = \frac{2}{\beta} \left(\frac{dz}{dx}\right)^* - \frac{1}{\bar{R}^* c_e^*} \sum \bar{R} \Delta u c_e \quad (5)$$

and in accordance with linearized theory assumptions $\Delta C_p^* = 2 \Delta u^*$.

The strong influence along Mach lines dictates a more rigid element geometry than does the subsonic solution. Trapezoidal elements used in the subsonic solution could result in coincidence of the Mach line with an element control point; this coincidence gives erratic results. Even a near coincidence could result in large local velocities and unstable solutions. The rectangular elements employed in the supersonic solution ensure that such a coincidence cannot happen. The Mach line follows a path that places it no closer to the control point of any element than a longitudinal distance equal to one half the nominal element chord Δx ; this is true even for leading- and trailing-edge elements. The longitudinal separation distances are based on the grid space occupied by the element and are unaffected by changes in the element chord c_e .

For a supersonic solution, the iteration procedure employed for subsonic flow is not required. Because of the limited regions of influence, a single pass is sufficient. The solution proceeds from inboard to outboard of successive rearward positions as does the subsonic solution but is terminated when the last element on the wing is reached.

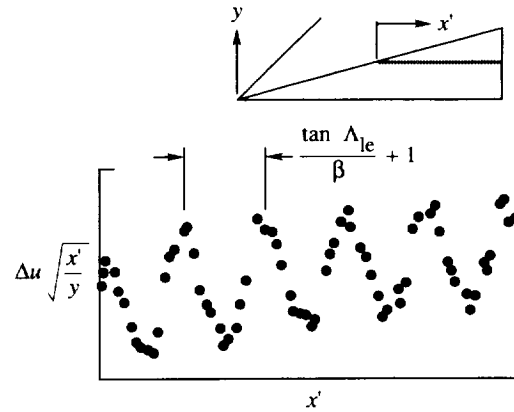
The enforced simplicity of the supersonic solution, however, brings with it a disadvantage not encountered in the subsonic solution. There is a strong tendency toward longitudinal oscillations in perturbation velocities. The oscillations are subdued in part by an aft-element sensing technique described in reference 10. The

aft-element sensing technique involves the determination of preliminary Δu^* results for a given field element and for the element immediately following combined with a subsequent fairing or smoothing of these preliminary results. The fairing is applied to the velocity potential (i.e., the integral of the velocity) rather than to the velocity itself because of the noticeable better behavior of the velocity potential in regard to the absence of discontinuities. The procedure which is described in detail in reference 10 is not repeated here.

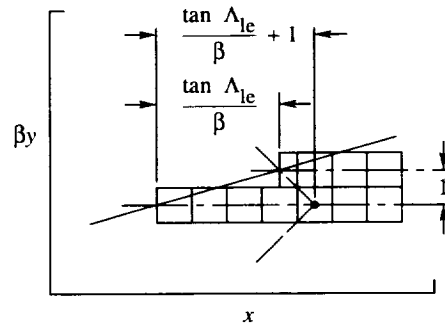
Generally, the numerical method employing aft-element sensing gives rather smooth distributions of the lifting pressure coefficient as evidenced by the numerous comparisons of numerical method results with exact linearized theory given in reference 10. But for very highly swept leading edges, a tendency is found for the formation of oscillations in flat wing pressure distributions. These oscillations center on the correct solution and thus create no large problems in the determination of overall wing forces and moments. Nevertheless, to find a means of suppressing or smoothing these oscillations which for very highly swept wings can become large is desirable. An exploration of the causes of the oscillations and the development of supplementary smoothing strategy is described in the following paragraphs.

An example of extreme oscillations in lifting pressure coefficient given by the basic supersonic analysis system is shown in sketch 2-6. The data shown are for a delta wing with $\Lambda_{le} = 75^\circ$ at a Mach number of 1.41 ($\beta \cot \Lambda = 0.27$). The parameter $\Delta u \sqrt{x'/y}$, derived from theoretical distributions of pressure loadings on flat delta wings, permits inclusion of data for several adjacent spanwise stations near the mid-semispan, and compensates for the $1/\sqrt{x'}$ decline in pressure aft of the leading-edge singularity. This and similar plots for other sweep angles and Mach numbers show a wavelength of the oscillations which correlates well with the parameter $\tan \Lambda_{le}/\beta + 1$. As shown in sketch 2-7, the code array of the rectangular elements for two adjacent spanwise stations dictates such a pattern. Because of the rectangular element structure and the nature of supersonic flow, any influence of the outboard span station on the inboard station is delayed to the chordwise position shown.

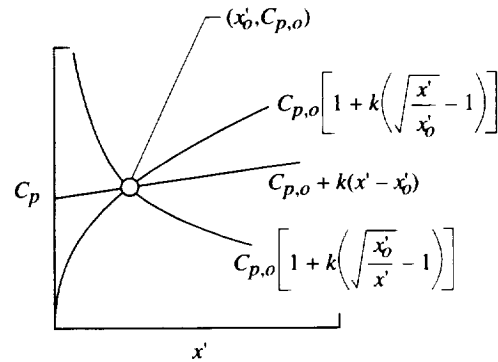
These considerations suggest a fairing which covers a number of elements equal to the absolute value of the local parameter $\tan \Lambda_{le}/\beta + 1$ and takes into account the nature of supersonic pressure distributions. This fairing can be accomplished by a least-squares curve fit of one of the pressure variation forms illustrated in sketch 2-8. Each curve passes through an initial $(x'_0, C_{p,o})$, and the least-squares solution is used to determine the factor k giving the best fit. In the code, a solution is found for each form, and the form giving the smallest value for the



Sketch 2-6



Sketch 2-7



Sketch 2-8

sum of the squares of the errors is selected. The process begins with Δu of the first element behind the leading edge. After application of the curve fit, the point immediately behind the initial point is given a new value defined by the factor k of the selected form. Then the process is repeated as often as necessary by advancing one element rearward and by using the just replaced value as a new initial point. In the region of the trailing edge, when the remaining points are less than the defined number, new values are found for all points.

Sketch 2-9 shows the Δu distribution with and without smoothing at the mid-semispan of the example 75° delta wing at $M = 1.41$. Some irregularities remain, but they are minor compared with the original large oscillations.

The two-step smoothing process for the supersonic solution just described was not required for the subsonic solution. However, errors in the subsonic solution in the region of the wing leading edge were corrected as previously described by relocation of calculated velocities. A comparable correction is also required in the region of the wing leading edge for the supersonic solution. The correction function covers only the first element behind the leading edge instead of the first two. This correction provides the original initial point for the previously described supplementary smoothing process which is applied to all elements. For aft elements, the perturbation velocity rather than its location is adjusted.

Figure 8 shows the ratio of Δu_{code} to Δu_{th} for leading-edge elements of a series of flat delta wings with different values of the leading-edge sweep parameter $\beta \cot \Lambda$. The data cover all code span positions up to the maximum permissible for a given value of $\beta \cot \Lambda$. The code velocities are assumed to act at the element quarter-chord and the ratios are plotted as a function of the element chord. Most observed scatter in the data is due to inclusion of inboard span stations where a stable numerical solution has not yet developed. For these leading-edge elements, a curve expressed by the equation

$$F(x') = \frac{\Delta u_{\text{code}}}{\Delta u_{\text{th}}} = \frac{1 - (1 - \sqrt{c_e})^{1.4}}{\sqrt{2\beta \cot \Lambda_{\text{le}}}}$$

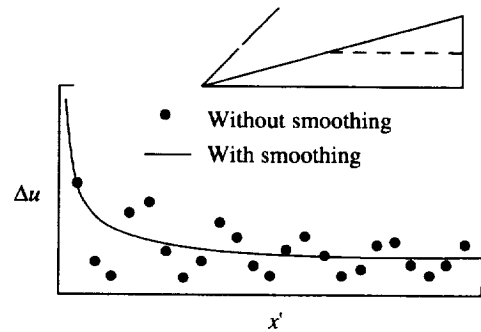
was found to adequately represent the data of figure 8. The corrected perturbation velocity location for leading-edge elements is

$$x'_{\text{cor}} = \frac{c_e}{4[F(x')]^2}$$

As in the subsonic solution, the location rather than the velocity itself is changed because a shift in location corrects flat wing data but does not introduce appreciable errors in data for surfaces with pure camber loadings.

3. Theoretical Leading-Edge Thrust

Both the subsonic and the supersonic linearized theory solutions apply to lifting surfaces of arbitrary planform with arbitrary distributions of twist and camber. The character of the calculated perturbation velocity and pressure coefficient distributions is strongly influenced by leading-edge flow conditions. For flat lifting surfaces



Sketch 2-9

(except for wings with supersonic leading edges), leading-edge singularities are present at all angles of attack other than zero. At positive angles of attack, the upwash just ahead of the leading edge and the perturbation velocity just behind the leading edge become infinite. The presence of twist and camber alters the flow conditions so that the singularities usually disappear not at zero angle of attack but at some other angle of attack. Because the theoretical leading-edge thrust is directly related to the strength of the leading-edge singularity, the angle of attack corresponding to the disappearance of the singularity has been designated as the angle of attack for zero thrust α_{z_t} . At other angles of attack, singularities form at the leading edge just as they do for the flat wing at angles other than zero.

A means of identifying the angle of attack for zero thrust offers considerable advantages in calculation of theoretical leading-edge thrust and in integration of perturbation velocity and pressure distributions to obtain forces and moments for wings with arbitrary twist and camber. The following discussion describes the calculation of α_{z_t} and its use in the calculation of theoretical leading-edge thrust. The use of α_{z_t} in the separation of perturbation velocities and pressure distributions into components with and without singularities for employment in integration techniques is discussed later in section 5.

In the WINGDES and AERO2S codes, results covering a range of angle of attack are obtained by combining the solution for the input cambered wing (considered to be at $\alpha = 0^\circ$) with a solution for a flat wing of the same planform at $\alpha = 1^\circ$. An example of these basic solutions for a 40° swept leading-edge, constant-chord wing (one panel only) is shown in figure 9. The mean camber surface is an arc of a circle with a radius selected to give a leading-edge slope of $dz/dx = 0.0875$ ($\epsilon_o = 5^\circ$). Results for the cambered wing are given at the top of the figure, and results for the flat wing are given at the bottom. Note that the cambered wing as well as the flat wing displays a leading-edge singularity.

Figure 10 shows results for other angles of attack obtained by combining solutions for the cambered and the flat wings by the following expression:

$$\Delta u = \Delta u_c + \Delta u_f \frac{\sin \alpha}{\sin 1^\circ}$$

The angle of attack of 1.8° was chosen for this illustration because at or near that angle the leading-edge singularity vanishes. The velocity distribution for this case may be considered to be a pure camber loading. For this constant-curvature surface, the velocity distribution closely follows a curve defined by

$$\Delta u = k_c \sqrt{\frac{x'}{c} \left(1 - \frac{x'}{c}\right)}$$

or

$$\Delta u \sqrt{\frac{x'}{c}} = k_c \frac{x'}{c} \sqrt{1 - \frac{x'}{c}}$$

A distribution of this form is used in the subsequent analysis of leading-edge thrust characteristics.

Figure 11 illustrates how the angle of attack for a vanishing singularity at a given spanwise station may be found directly. Singularity parameters in the form $\Delta u \sqrt{x'}$ are shown for the first three elements of both a cambered wing at $\alpha = 0^\circ$ and a flat wing at $\alpha = 1^\circ$. From previous observations of the nature of cambered and flat wing velocity distributions, assuming a leading-edge singularity parameter of the following form is reasonable:

$$\Delta u \sqrt{x'} = k_f \sqrt{c - x'} + k_c \frac{x'}{c} \sqrt{c - x'}$$

where the first term on the right-hand side represents a flat wing contribution and the second term, a pure camber contribution. Curve fits of the data for the first two elements using this equation are shown as the dashed lines. The singularity parameter values at the wing leading edge are designated as “ $(\Delta u \sqrt{x'})_{o,f}$ ” for the flat wing and “ $(\Delta u \sqrt{x'})_{o,c}$ ” for the cambered wing. It now becomes clear that the angle for a vanishing singularity or, in other terms, the angle for zero leading-edge thrust is simply

$$\alpha_{zt} = \frac{-(\Delta u \sqrt{x'})_{o,c}}{(\Delta u \sqrt{x'})_{o,f}}$$

Using relationships developed in reference 2 shows that the section leading-edge thrust coefficient is

related to the singularity parameter by the following expression:

$$c_t = \frac{\pi}{2} \frac{b}{S} \sqrt{\tan^2 \Lambda_{lc} \pm \beta^2} [(\Delta u \sqrt{x'})_o]^2 \quad (6)$$

where the positive sign of β^2 applies to subsonic flow and the negative to supersonic flow.

For the flat wing,

$$(\Delta u \sqrt{x'})_o = (\Delta u \sqrt{x'})_{o,f} \frac{\sin \alpha}{\sin 1^\circ}$$

and

$$c_{t,f} = \left(\frac{\sin \alpha}{\sin 1^\circ}\right)^2 \frac{\pi}{2} \frac{b}{S} \sqrt{\tan^2 \Lambda_{lc} + \beta^2} [(\Delta u \sqrt{x'})_{o,f}]^2$$

For the cambered wing, the theoretical leading-edge thrust is assumed to act in the same fashion as it does for the flat wing except that the center point, at which c_t is zero, occurs at α_{zt} not $\alpha = 0^\circ$. With the definition of α_{zt} and $c_{t,f}$ the section theoretical leading-edge thrust coefficient at any angle of attack that may employ camber may be found by use of the expression

$$c_t = c_{t,f} \left(\frac{\sin \alpha - \sin \alpha_{zt}}{\sin 1^\circ} \right)^2$$

This method provides a more accurate result than a direct application of equation (5), which does not recognize the existence of an angle of attack for zero thrust.

4. Attainable Leading-Edge Thrust and Vortex Forces

The original method for the estimation of attainable leading-edge thrust was introduced in reference 1. An improved method described in reference 7 has recently been developed that provides for a greater range of airfoil shapes from very sharp to very blunt leading edges. This new method is based on a wider range of Reynolds numbers than available for the previous method. An additional aesthetic appeal of the new approach is a relationship between flow over the wing surface and the corresponding two-dimensional airfoil analysis more consistent with actual flow patterns. Because development and use of the new method are covered in great detail in reference 7, only an outline of the method with emphasis on the calculation steps is given herein.

The attainable thrust method is based on (1) the use of simple sweep theory to permit a two-dimensional analysis, (2) employment of theoretical airfoil codes to define thrust dependence on section geometric characteristics with pressures limited to a vacuum, (3) generalization of the thrust dependence on limiting pressures to

include more realistically achievable pressures, and (4) the examination of experimental two-dimensional airfoil data to define the more realistic limiting pressure dependence on local Mach and Reynolds numbers. The applicability of the method was demonstrated by comparisons of theoretical and experimental aerodynamic characteristics for a series of wing-body configurations.

The relationship between streamwise airfoil sections and the normal sections used in method development is illustrated in figure 12. Steps in the solution process may be outlined as follows.

For each of a large number of wingspan stations, the following terms define the normal section geometric characteristics:

$$c_n = c \cos \Lambda_{le}$$

$$\left(\frac{\tau}{c}\right)_n = \frac{\tau}{c} \frac{1}{\cos \Lambda_{le}}$$

$$\eta_n = \eta$$

$$\left(\frac{r}{c}\right)_n = \frac{r}{c} \frac{1}{\cos^2 \Lambda_{le}}$$

$$r_{i,n} = \frac{(r/c)_n \eta}{(\tau/c)_n^2}$$

In addition, for each span station the normal Mach number, Reynolds number, and normal section thrust coefficient are defined as

$$M_n = M \cos \Lambda_{le}$$

$$R_n = R \frac{c_n}{c} \cos \Lambda_{le}$$

$$c_{t,n} = c_t \frac{c}{c_n} \frac{1}{\cos^2 \Lambda_{le}}$$

or

$$c_{t,n} = c_t \frac{c_{av}}{c_n} \frac{1}{\cos^2 \Lambda_{le}}$$

with c_t nondimensionalized as in AERO2S and WINGDES. The theoretical thrust coefficient c_t is supplied by the linearized theory lifting surface analysis. This coefficient accounts for variations of the theoretical leading-edge thrust coefficient with such factors as free-stream Mach number, wing planform, and wing twist and

camber. Then for each span station, the limiting pressure coefficient is calculated by use of the following equation:

$$C_{p,lim} = \frac{-2}{\gamma M_n^2} \left(\frac{R_n \times 10^{-6}}{R_n \times 10^{-6} + K} \right)^{e_4} \quad (7)$$

where

$$K = 10^{8(1-M_n)}$$

$$e_4 = 0.028 M_n^{-0.75}$$

The equivalent Mach number

$$M_e = \frac{\sqrt{2}}{\gamma C_{p,lim} \sqrt{1-M_n^2}} \sqrt{\sqrt{1 + (\gamma C_{p,lim} \sqrt{1-M_n^2})^2} - 1} \quad (8)$$

which accounts for differences between the limiting pressure coefficient and the vacuum pressure coefficient, is then used in the calculation of the attainable thrust factor.

The attainable thrust factor K_t is found by use of the following equation:

$$\frac{K_t}{1 + (\tau/c)_n^{1.2}} = k_a \left\{ c_{t,n} \beta_n \left[\frac{(\tau/c)_n (\eta/0.5)^{e_1}}{0.9} \right]^{e_2} \right\}^{e_3} \quad (9)$$

with K_t limited to values no greater than 1.0 where

$$k_a = \left\{ 0.14 \left[1.0 - (1.0 - \sqrt{r_{i,n}}) M_e^5 \right] + 0.11 \sqrt{r_{i,n}} \right\} \left(\frac{1 - M_e}{M_e} \right)^{0.48(1+r_{i,n}^{0.3})}$$

$$e_1 = \frac{\eta}{0.5} (0.4 r_{i,n}^{0.16} - 0.7)$$

$$e_2 = 1.6 r_{i,n}^{0.10} - 3.0$$

$$e_3 = 0.32 r_{i,n}^{0.10} - 0.3$$

The expression defining the exponent e_1 differs slightly from that given in reference 7. The change was made to remove irregularities in the variation of K_t with leading-edge radius that sometimes occur for airfoils with a very forward location of the maximum thickness and very small leading-edge radii. For standard and near-standard airfoils ($n = 0.3$ to 0.5 and $r_i = 0.25$ to 0.35), this change has a negligible effect.

The ratio of attainable theoretical thrust K_t for each normal airfoil section is then applied to the theoretical thrust for the wing at the wing spanwise station from which the normal section was derived to arrive at a spanwise distribution of attainable thrust. The attainable thrust section coefficient then is

$$c_t^* = K_t c_t$$

where c_t is the full theoretical leading-edge thrust coefficient defined by the attached flow linearized theory lifting surface solution.

For a given wing and a given set of test or flight conditions, the theoretical leading-edge thrust coefficient c_t , given by a linearized theory code, varies with span position and wing angle of attack. The attainable thrust factor K_t determined by the attainable thrust method varies with those quantities and with other factors including local leading-edge sweep angle and wing section characteristics. The effect of wing twist and camber (or flap deflection) is accounted for in the calculated value of c_t . Because the attainable thrust factor is dependent on the theoretical thrust, it too is influenced by twist or camber and flap deflection. The same spanwise integration techniques used in the lifting surface code can be employed to calculate wing attainable thrust coefficients.

As discussed in section 7, it may be desirable for design purposes to know how much a local leading-edge deflection angle may be changed from the local flow alignment condition (presumed to be defined by α_{zt}) and still retain attached flow and full theoretical thrust. As described in reference 7, this angle-of-attack range $\Delta\alpha_{ft}$ may be found by a two-step process. First, K_t is set to a value of 1.0 (attainable thrust equals full theoretical thrust) and the corresponding value of the theoretical thrust coefficient is found. Then the equation relating the full theoretical thrust coefficient to angle of attack is applied to a flat wing ($\alpha_{zt} = 0$) to define the limiting angle to give

$$\Delta\alpha_{ft} = \sin^{-1} \left(\sin 1^\circ \sqrt{\frac{c_t}{c_{t,f}}} \right)$$

For a flat wing, full theoretical thrust at a particular wing spanwise location is developed over a range from $-\Delta\alpha_{ft}$ to $\Delta\alpha_{ft}$. For a wing with twist and camber, full theoretical leading-edge thrust is presumed to develop over a range from $\alpha_{zt} - \Delta\alpha_{ft}$ to $\alpha_{zt} + \Delta\alpha_{ft}$.

For very thin flat wings with sharp leading edges, little or none of the theoretical leading-edge thrust can actually be realized. The real flow about these wings cannot remain attached to the surface as it negotiates the turn around the leading edge from a stagnation point on

the wing lower surface. A detached vortex flow pattern, with embedded circulation, forms and induces an additional lifting force. If the flow reattaches to the wing upper surface ahead of the trailing edge, the attached flow potential lift associated with the change in vertical momentum from just ahead of the leading edge to just behind the trailing edge is not lost. Thus the wing lift is increased by the amount of the vortex induced lift. As discussed in section 7, for conditions which tend to create a vortex flow which does not reattach ahead of the trailing edge, wing camber or leading-edge flaps can usually be employed to reduce vortex strength and bring about an earlier reattachment. Polhamus (ref. 11) established a relationship between the normal force induced by the separated vortex flow and the theoretical leading-edge thrust. According to the Polhamus suction analogy, the suction vector $c_t/\cos \Lambda_{le}$ is assumed to rotate to a position normal to the wing surface, where it affects the normal force rather than the axial force. Because the present method treats a partially developed leading-edge thrust, considering a partial development of the vortex force seems logical. The simplest approach is to equate the vortex force with the undeveloped thrust as follows:

$$c_{vor} = \frac{c_t - c_{t,a}}{\cos \Lambda_{le}}$$

This flow separation always causes an increase in drag. The increase in lift cannot compensate for the loss of leading-edge thrust. An ability to predict these changes, however, is very useful in airplane design trade-off studies. Also, an understanding of the mechanism of flow separation can be helpful in the search for strategies to reduce separation and improve performance.

The suction analogy provides no information on the point of application of the vortex force vector. An implied assumption is that it acts just behind the leading edge. Because the vortex flow field can act at locations which under some conditions may be far removed from the leading edge, accurate estimates of the vortex-induced normal force, axial force, and pitching moment can be made only with some knowledge of the location of the vortex flow field. Both the WINGDES and the AERO2S codes offer the following options for the location and distribution of vortex forces.

Option 0: The vortex force is assumed to act perpendicular to the wing reference plane at the wing leading edge. This option, which provides no contribution of vortex force to the wing axial force, was at one time the only choice available in the AERO2S predecessor code SUBAER.

Option 1: For delta wings and delta wing derivatives, the vortex force center may be located through use of

an empirical relationship derived with the aid of figure 13. In this figure, data for uncambered delta wings with sharp leading edges are used to define, in an approximate fashion, the lateral location of the center of the vortex flow pressure field as a function of the wing local semispan ($x \cot \Lambda_{le}$) and the angle of attack. The fairing of the data represented by the equation

$$\frac{y_{vor}}{x \cot \Lambda_{le}} = \frac{1}{1 + \sqrt{\tan \alpha}}$$

has been found to be applicable to a range of sweep angles from about 30° to about 80° . An approximate location of the center of the vortex pressure field may be provided for wings that depart from the delta planform and for wings which may employ twist and camber or deflected flaps. The vortex center x'_{vor} shown in sketch 4-1 may be calculated by use of the following equations:

$$x'_{vor} = 0.0 \quad (\alpha_{zt} - \Delta\alpha_{ft} \leq \alpha < \alpha_{zt} + \Delta\alpha_{ft})$$

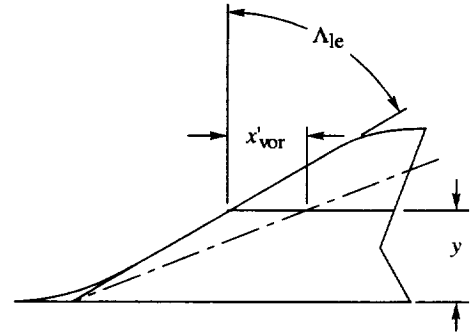
$$x'_{vor} = \frac{y}{\cot \Lambda_{le}} \left[1 + \sqrt{\tan(\alpha - \alpha_{zt} - \Delta\alpha_{ft})} \right] \quad (\alpha > \alpha_{zt} + \Delta\alpha_{ft})$$

$$x'_{vor} = \frac{y}{\cot \Lambda_{le}} \left[1 + \sqrt{\tan(\alpha_{zt} - \Delta\alpha_{ft} - \alpha)} \right] \quad (\alpha < \alpha_{zt} - \Delta\alpha_{ft})$$

in which Λ_{le} is the local leading-edge sweep angle, α_{zt} is the wing angle of attack for a local leading-edge thrust of zero, and $\Delta\alpha_{ft}$ is the range of angle of attack for full thrust. This formulation locates the vortex center aft of the leading edge when full thrust is not realized. However, it does not account for the initiation of leading-edge separation at points along the leading edge other than the apex of the superimposed delta wing. This option, which is the default for both the WINGDES and the AERO2S codes, has been used for the vast majority of the correlations with experimental data reported in the references.

Option 2: An alternate and very simple means of locating the vortex force center is given by Lan and Chang in reference 12. When applied to the present numerical method, the location of the vortex force center is

$$x'_{vor} = c_t c_{av}$$



Sketch 4-1

For options 1 and 2, the distribution of the force is assumed to take the form shown in sketch 4-2. Mathematically this form can be expressed as

$$\Delta C_{p,vor} = k_{vor} \left(1 - \cos \pi \frac{x'}{x'_{vor}} \right)$$

Over an element chord $x'_2 - x'_1$, the incremental normal force due to the vortex is given by

$$\begin{aligned} \Delta c_{N,vor} &= \frac{1}{c_{av}} \int_{x'_1}^{x'_2} \Delta C_{p,vor} dx \\ &= \frac{k_{vor}}{c_{av}} \left[(x'_2 - x'_1) - \frac{x'_{vor}}{\pi} \left(\sin \pi \frac{x'_2}{x'_{vor}} - \sin \pi \frac{x'_1}{x'_{vor}} \right) \right] \end{aligned}$$

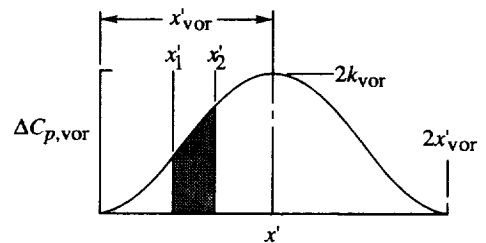
and over the entire interval from 0 to $2x'_{vor}$ by

$$\Delta c_{N,vor} = \frac{1}{c_{av}} 2k_{vor} x'_{vor}$$

so that

$$k_{vor} = \frac{\Delta c_{N,vor} c_{av}}{2x'_{vor}}$$

The factor k_{vor} establishes the magnitude of the $\Delta C_{p,vor}$ distribution action on the wing surface. Because the surface may be cambered and may include deflected



Sketch 4-2

flaps, contributions to axial force as well as normal force are present. If the vortex center lies aft of the local chord midpoint, part of the vortex force does not affect the wing and is lost.

5. Aerodynamic Forces and Moments

Section aerodynamic coefficients are found by integration of the section pressure distributions, for which the pressure coefficient is assumed to be given by $C_p = 2 \Delta u$. Because perturbation velocities are obtained by superposition of cambered and flat wing solutions, the pressure coefficient may be expressed as

$$C_p = C_{p,c} + C_{p,f} \frac{\sin \alpha}{\sin I^\circ}$$

or

$$C_p = 2 \Delta u_c + 2 \Delta u_f \frac{\sin \alpha}{\sin I^\circ}$$

As shown in sketch 5-1 the pressure acting on the airfoil camber surface produces an incremental section normal force given by

$$dc_N = C_p ds \cos \epsilon = C_p dx'$$

where

$$\cos \epsilon = \frac{dx'}{ds}$$

and an incremental section axial force given by

$$dc_A = C_p ds \sin \epsilon = -C_p \frac{dz}{dx'} dx'$$

The section coefficients may be expressed as

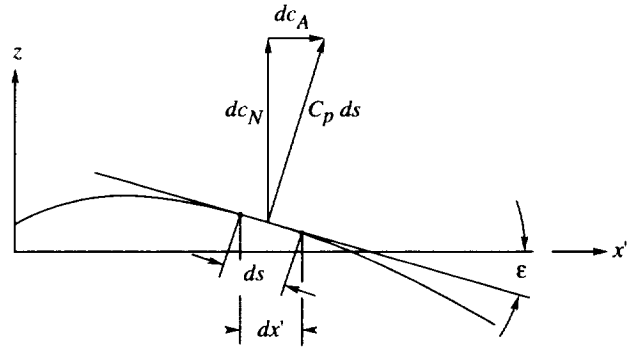
$$c_N = \frac{1}{c_{av}} \int_0^c C_p dx'$$

$$c_A = \frac{1}{c_{av}} \int_0^c C_p \frac{dz}{dx'} dx'$$

$$c_m = \frac{1}{c_{av}} \frac{1}{\bar{c}} \int_0^c C_p (x' + x_{le} - x_{mc}) dx'$$

In order to account for leading-edge singularities where appropriate and to avoid them where not appropriate, the integrations are performed by parts. The total section normal-force coefficient (exclusive of thrust or vortex forces) is given by

$$c_N = c_{N,c} + c_{N,f} \frac{\sin \alpha}{\sin I^\circ}$$



Sketch 5-1

The section normal-force coefficient generated by the flat wing pressure distribution for $\alpha = I^\circ$, $c_{N,f}$, is obtained by the integration depicted in sketch 5-2. Within the limits of a given element (x'_1 to x'_2), the pressure distribution is assumed to have the form

$$C_{p,f} = 2 \Delta u = 2k_f \sqrt{\frac{c}{x'} - 1}$$

with the constant k_f defined so that the curve passes through the C_p value at the element quarter-chord (or the corrected location for the first two elements). The incremental section normal-force coefficient for this element is given by the integral

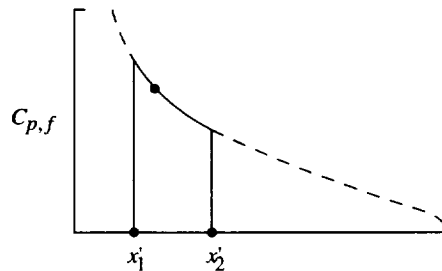
$$dc_{N,f} = \int_{x'_1}^{x'_2} C_{p,f} dx' = 2k_f \int_{x'_1}^{x'_2} \sqrt{\frac{c}{x'} - 1} dx'$$

The integration may be performed through use of the following substitutions:

$$\sqrt{\frac{c}{x'} - 1} = \cot \frac{\theta}{2}$$

and

$$dx' = \frac{c}{x'} \sin \theta d\theta$$



Sketch 5-2

with

$$\cos \theta = 1 - 2 \frac{x'}{c}$$

The result is

$$dc_{N,f} = F_f(x') C_{p,f}$$

where

$$F_f(x') = \frac{c}{2} \tan \frac{\theta}{2} (\theta_2 - \theta_1 + \sin \theta_2 - \sin \theta_1)$$

with

$$\theta = \cos^{-1} \left(1 - \frac{2x'}{c} \right)$$

$$\theta_2 = \cos^{-1} \left(1 - \frac{2x'_2}{c} \right)$$

$$\theta_1 = \cos^{-1} \left(1 - \frac{2x'_1}{c} \right)$$

The section normal-force coefficient generated by flat wing pressure distributions for $\alpha = 1^\circ$ is simply the integral of the incremental coefficients as follows:

$$c_{N,f} = \frac{1}{c_{av}} \int_0^c dc_{N,f} dx'$$

which, as carried out in the code, is merely a summation.

The section normal-force coefficient generated by the cambered wing pressure distribution $c_{N,c}$ is the result of two integrations. First, as indicated in sketch 5-3, the cambered wing pressure distribution is separated into two parts. This separation is accomplished through use of the angle of attack for a section thrust coefficient of zero α_{zt} as follows:

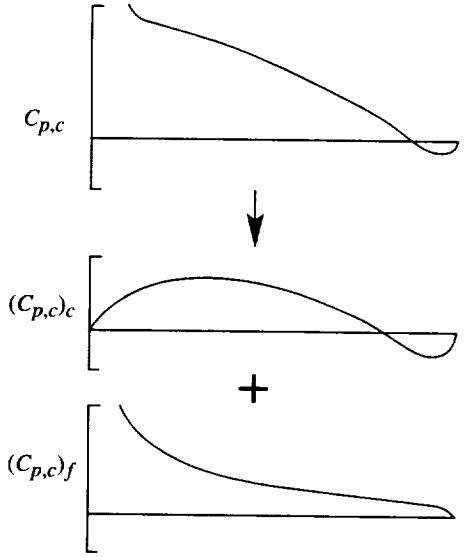
$$C_{p,c} = (C_{p,c})_f + (C_{p,c})_c$$

$$(C_{p,c})_f = -\alpha_{zt} C_{p,f}$$

$$(C_{p,c})_c = C_{p,c} - (C_{p,c})_f$$

The integration of the flat plate component $(C_{p,c})_f$ is handled in the same fashion as was the basic flat wing pressure distribution at $\alpha = 1^\circ$ previously discussed to obtain a cambered wing normal-force contribution $(c_{N,c})_f$. The integration of the pure camber loading $(C_{p,c})_c$ may be explained through the use of sketch 5-4. Within the limits of a given element, the pressure distribution is assumed to have the form

$$C_p = 2 \Delta u = 2k_c \sqrt{x'(c-x')}$$



Sketch 5-3

with the constant k_c defined so as to pass the curve through the C_p value at the element quarter-chord (or the corrected location for the first two elements). The incremental section normal-force coefficient for the element is given by the following integral:

$$(dc_{N,c})_c = \int_{x'_1}^{x'_2} C_p dx' = 2k_c \int_{x'_1}^{x'_2} \sqrt{x'(c-x')} dx'$$

When integrated,

$$(dc_{N,c})_c = F_c(x') (C_{p,c})_c$$

where

$$F_c(x') = \frac{c}{2 \sqrt{\left(1 - \frac{x'}{c}\right) \frac{x'}{c}}} \left[\left(\frac{x'}{c} - \frac{1}{2} \right) \sqrt{\left(1 - \frac{x'_2}{c}\right) \frac{x'_2}{c}} - \left(\frac{x'_1}{c} - \frac{1}{2} \right) \sqrt{\left(1 - \frac{x'_1}{c}\right) \frac{x'_1}{c}} + \frac{1}{4} \sin^{-1} \left(\frac{2x'_2}{c} - 1 \right) - \frac{1}{4} \sin^{-1} \left(\frac{2x'_1}{c} - 1 \right) \right]$$

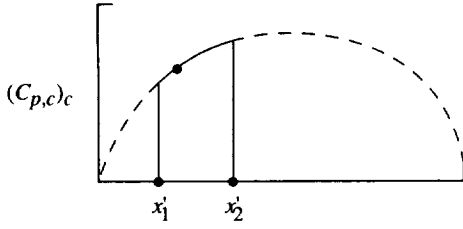
Then

$$dc_{N,c} = (dc_{N,c})_c + (dc_{N,c})_f$$

and

$$c_{N,c} = \frac{1}{c_{av}} \int_0^c dc_{N,c} dx'$$

which is obtained as a simple summation.



Sketch 5-4

The total section pitching-moment coefficient (exclusive of thrust or vortex forces) is found in a similar fashion as follows:

$$c_m = c_{m,c} + c_{m,f} \frac{\sin \alpha}{\sin 1^\circ}$$

$$c_{m,f} = \frac{1}{c_{av}} \frac{1}{c} \int_0^c dc_{N,f} (x' + x_{cg} - x_{mc}) dx'$$

$$c_{m,c} = \frac{1}{c_{av}} \frac{1}{c} \int_0^c dc_{N,c} (x' + x_{cg} - x_{mc}) dx'$$

The total section axial-force coefficient (exclusive of thrust and vortex forces) is given by

$$c_A = c_{A,c} + c_{A,f/c} \frac{\sin \alpha}{\sin 1^\circ}$$

The section axial-force coefficient generated by the flat wing pressure distribution for $\alpha = 1^\circ$ acting on the cambered wing surface $c_{A,f/c}$ is obtained by the integration depicted in sketch 5-5. As before within a given element, the pressure distribution is assumed to have the following form:

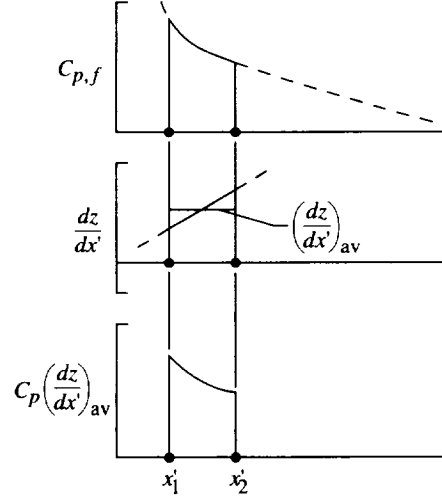
$$C_p = 2 \Delta u = 2k_f \sqrt{\frac{c}{x'} - 1}$$

The camber surface slope within the element is assumed to be

$$\frac{dz}{dx'} = k_1 + k_2(x' - x'_1)$$

with an average or midchord slope of

$$\frac{dz}{dx'} = k_1 + k_2 \frac{(x'_2 - x'_1)}{2}$$



Sketch 5-5

The incremental section interference coefficient for this element is given by the integral

$$\begin{aligned} dc_{A,f/c} &= - \int_{x'_1}^{x'_2} C_p \frac{dz}{dx'} dx' \\ &\approx -2k_f \left[k_1 + k_2 \frac{(x'_2 - x'_1)}{2} \right] \int_{x'_1}^{x'_2} \sqrt{\frac{c}{x'} - 1} dx' \end{aligned}$$

With the exception of the negative sign and the average slope term, the integral is identical to that for $dc_{N,f}$. Therefore

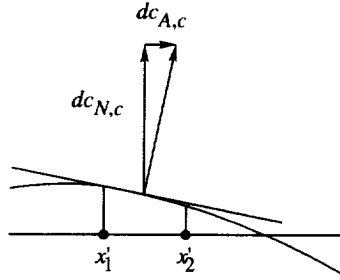
$$dc_{A,f/c} = - \left[k_1 + k_2 \frac{(x'_2 - x'_1)}{2} \right] F_f(x') C_{p,f}$$

with $F_f(x')$ as previously defined. Then

$$c_{A,f/c} = \frac{1}{c_{av}} \int_0^c dc_{A,f/c} dx'$$

is obtained as a summation. The approximation resulting from the use of the average slope is acceptable because element chords can be reduced to make the change in slope small compared with the average value. Studies discussed in sections 8 and 9 help to establish element chords (defined by element aspect ratio) necessary to provide acceptable accuracy of the numerical solution.

As indicated in sketch 5-6, the section axial force due to the cambered wing pressures acting on the camber



Sketch 5-6

surfaces $dc_{A,c}$ is calculated from the previously discussed cambered wing section normal-force coefficient $dc_{N,c}$ as

$$dc_{A,c} = dc_{N,c} \frac{dz}{dx}$$

with dz/dx evaluated at the element midchord to represent an average slope. Then

$$c_{A,c} = \frac{1}{c_{av}} \int_0^c dc_{A,c} dx'$$

is obtained as a summation.

An overall view of the way components of the section force coefficient are combined with thrust and vortex forces is given in figure 14. The cambered wing at its reference condition (assumed to be $\alpha = 0^\circ$) produces a normal-force coefficient $c_{N,c}$. At other angles, the normal force is increased by the flat wing loading increment given by $c_{N,f} \sin \alpha / \sin 1^\circ$. In addition, there may be a small change in normal force due to a component of the attainable thrust acting in the normal-force direction $c_t \sin \epsilon_o$. Another, often larger, increment can result from the vortex force c_{vor} that arises when the attainable thrust is less than the full theoretical thrust.

The cambered wing at zero angle of attack produces an axial-force coefficient $c_{A,c}$. An important interference term contributing to axial force at all other angles of attack is produced by the flat wing loading on the camber surface. That increment is given as $c_{A,f/c} \sin \alpha / \sin 1^\circ$. This term is primarily responsible for the performance benefits of twisted and cambered wings. Finally, at angles of attack other than that for zero section thrust, there is an attainable thrust contribution, $c_t^* \cos \epsilon_o$.

A sample of code-generated section force coefficients is shown in figure 15. The wing planform used in the code included the body. The most noticeable breaks in the general shape of the distributions are explained by the wing-body juncture at a semispan fraction of 0.127 and a cambered wing spanwise load distribution that was designed to be constant to the 0.625-semispan station and linear from there to the tip. The quantities $c_{t,f}$ and α_{zt}

are used as described to give theoretical section thrust coefficients as a function of angle of attack.

As has been discussed in section 5, with the exception of c_t^* and c_{vor} , the section force coefficients shown in figure 15 may be obtained by fairly simple operations involving the angle of attack and the basic section parameters illustrated in figure 14. The attainable thrust and the vortex force coefficients, although predictable, have no simply defined dependence on angle of attack. In employing the attainable thrust method to calculate these coefficients, separate calculations for each span station at each angle of attack are required; the results are stored for subsequent use in the section force coefficient buildup.

The code techniques for integration of section forces to obtain overall wing characteristics are very simple. The section force coefficients c_N and c_A are assumed to be constant over the span of a given section. Because the section force coefficients are nondimensionalized by the wing average chord, the wing coefficients C_N , C_A , and C_m for a given angle of attack are determined by a simple summation covering the wing semispan which is then divided by the semispan to produce coefficients based on the reference area. Wing lift and drag coefficients are defined as

$$C_L = C_N \cos \alpha - C_A \sin \alpha$$

$$C_D = C_N \sin \alpha + C_A \cos \alpha$$

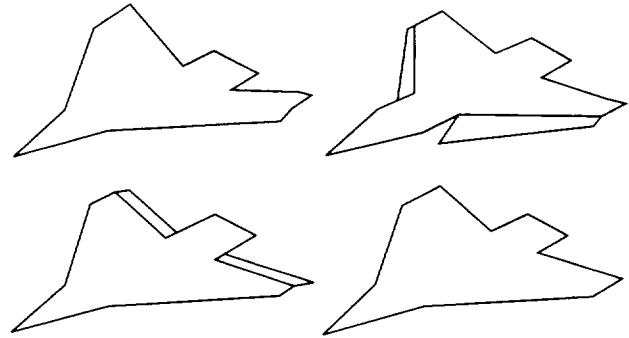
6. Wing Analysis Method for AERO2S Code

The AERO2S computer code uses lifting surface analysis methods developed in sections 2 through 5 for a wing which may employ leading- and trailing-edge flaps in combination with a canard or a horizontal tail surface.

6.1. Wing With Flaps

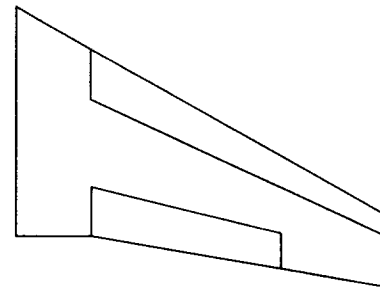
The analysis of a wing with flaps is constructed from contributions of four basic lifting surface solutions, a twisted and cambered surface, a leading-edge flap surface, a trailing-edge flap surface, and a flat surface at $\alpha = 1^\circ$. These components are illustrated in sketch 6-1. For the analysis of a wing with flaps in combination with a canard or horizontal tail, a second lifting surface solution with, in general, a different planform is combined with the first four component surfaces. This second lifting surface does not, however, include leading- or trailing-edge flaps. Lifting surface solutions for the wing in combination with a second surface are performed in an iterative fashion so that the mutual influence of one on the other is taken into account.

In representation of leading- and trailing-edge flaps as component surfaces in a solution by superposition, it is important to conform to the same rules as for the wing representation. The flap surfaces must be represented by the same grid system, and the flap surface elements must also be placed so that inboard and outboard element chords lie along unit values of the spanwise parameter βy . The code provides an automated adjustment to input flap planform definitions to meet this requirement. As shown in sketch 6-2, flap chords are defined by tabular inputs which extend from the wing centerline to the wingtip. New entries in the table are required only when the chord changes. A discontinuity in chord requires entries at the closely spaced but not identical span stations. The automated code adjustment alters the flap planform to provide trapezoidal elements with inboard and outboard boundaries coincident with unit values of the spanwise parameter βy as shown in sketch 6-3. The adjustment preserves the original flap area.



Sketch 6-1

For input flap surfaces, described as a spanwise distribution of flap chord and streamwise deflection angle, values of surface slope for each of the wing elements are determined within the code. Solutions for the longitudinal perturbation velocities corresponding to these new surfaces are performed simultaneously with the solutions for the flat and cambered wings. For the surfaces composed of flat panels, an assumption of lifting pressures proportional to the sine of the deflection angle rather than the tangent (the surface slope) gave better agreement with experimental data. For curved camber surfaces, however, the sine substitution resulted in a tendency to underestimate the camber drag and overestimate the wing performance. Thus, for the wing analysis method, the lifting pressures are defined as



y_{le}	c_{le}	y_{te}	c_{te}
0	0	0	0
8.0	0	8.0	0
8.1	5.0	8.1	5.2
38.5	2.2	28.0	4.0
		28.1	0
		38.5	0

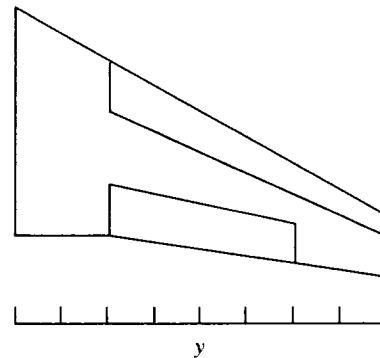
Sketch 6-2

$$C_p = 2 \Delta u_f \frac{\sin \alpha}{\tan 1^\circ} \quad (\text{Flat wing})$$

$$C_p = 2 \Delta u_{le} \frac{\sin \delta_{le}}{\tan \delta_{le}} = 2 \Delta u_{le} \cos \delta_{le} \quad (\text{LE flap})$$

$$C_p = 2 \Delta u_{te} \frac{\sin \delta_{te}}{\tan \delta_{te}} = 2 \Delta u_{te} \cos \delta_{te} \quad (\text{TE flap})$$

$$C_p = 2 \Delta u_c \quad (\text{Cambered surface})$$



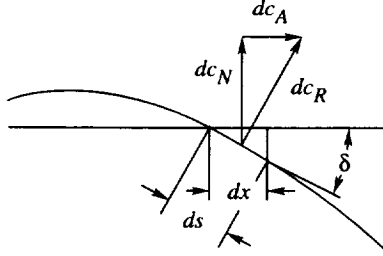
Sketch 6-3

Section force coefficients are found through the integration techniques described in section 5. Now, however, the cambered wing coefficients include deflected flaps as well as camber surface contributions. Both solutions are handled as described for the cambered surface except that, for the flap contribution, additional $\cos \delta_{le}$ and $\cos \delta_{te}$ terms are introduced. Sketches 6-4 and 6-5 illustrate the necessity for this correction. As shown in

sketch 6-4, an incremental force for the cambered wing section may be defined as

$$\begin{aligned} dc_N &= dc_R \cos \delta \\ &= \int C_p ds \cos \delta \\ &= \int C_p dx \end{aligned}$$

because $dx = ds \cos \delta$.



Sketch 6-4

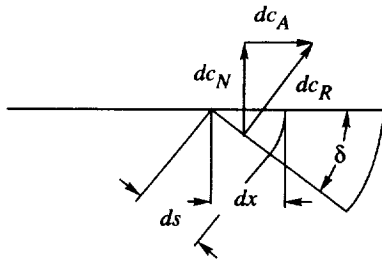
But for the flap surface shown in sketch 6-5,

$$\begin{aligned} dc_N &= dc_R \cos \delta \\ &= \int C_p ds \cos \delta \\ &= \int C_p dx \cos \delta \end{aligned}$$

because $dx = ds$.

These refinements, which introduce a $\cos \delta$ term in both the lifting pressure and the normal-force coefficients for deflected flap surfaces, increase the accuracy of the code application to flap systems.

Code results for additional flap deflections may be obtained by the use of input flap deflection multipliers. Solutions may be obtained for wing surfaces composed of all possible combinations at leading-edge and trailing-edge flap settings provided by the original deflections and by the flap deflection multipliers. Up to 25 pairs of leading-edge and trailing-edge flap deflection schedules may be treated simultaneously. Solutions obtained by using the multipliers are determined by a perturbation process and are not as accurate as solutions for the original or nominal input deflections. When increased accuracy is required or when the change in performance with the change in deflection must be evaluated—as in the construction of suction-parameter contour maps—individual solutions without recourse to multipliers may be required.



Sketch 6-5

For additional flap deflection angles, the user may specify factors m_{le} and m_{te} for the leading and trailing edges, respectively, to produce results for new deflection angles:

$$\delta_{le} = \tan^{-1} (m_{le} \tan \delta_{le,o})$$

$$\delta_{te} = \tan^{-1} (m_{te} \tan \delta_{te,o})$$

where the subscript o indicates the original input flap deflections. These factors act on the complete input spanwise schedule of flap deflections. Thus the magnitude but not the form of the deflection distribution is changed. When the variations of element chord and pressure coefficient with $\cos \delta$ (for both influencing and field element) are taken into account, the flap-induced pressure coefficients for the new deflection are

$$\begin{aligned} \Delta C_{p,le} &= 2 \left[\left(\Delta u_{le,o} + \frac{\pi}{\beta} \tan \delta_{le,o} \cos \delta_{le,o} \right) \right. \\ &\quad \left. \times m_{le} \frac{\cos^2 \delta_{le}}{\cos^2 \delta_{le,o}} - \frac{\pi}{\beta} \tan \delta_{le} \cos \delta_{le} \right] \end{aligned}$$

$$\begin{aligned} \Delta C_{p,te} &= 2 \left[\left(\Delta u_{te,o} + \frac{\pi}{\beta} \tan \delta_{te,o} \cos \delta_{te,o} \right) \right. \\ &\quad \left. \times m_{te} \frac{\cos^2 \delta_{te}}{\cos^2 \delta_{te,o}} - \frac{\pi}{\beta} \tan \delta_{te} \cos \delta_{te} \right] \end{aligned}$$

These relationships are found by consideration of equation (2) which shows the effect of the summation of the influence of all elements except the field element in producing the field element pressure coefficient for the input nominal deflection. For a different flap deflection, this influence is multiplied by the ratio of deflection angles m_{le} and by the ratio of the cosine of the deflection angles squared to form an estimate of the influence of all the other elements for the new deflection. The adjustment is based on the assumption that the new deflection is constant for a sufficiently large region in the vicinity of the field point so that the multiplication factor represents the change in influence of all the other elements to a sufficient degree of accuracy. Then with this new estimate of the influence of all other elements, equation (2) is applied again to find the field element pressure coefficient for the new deflection angle. These new pressure coefficient distributions are integrated in

the same way as those for the original deflections to obtain force and moment coefficients.

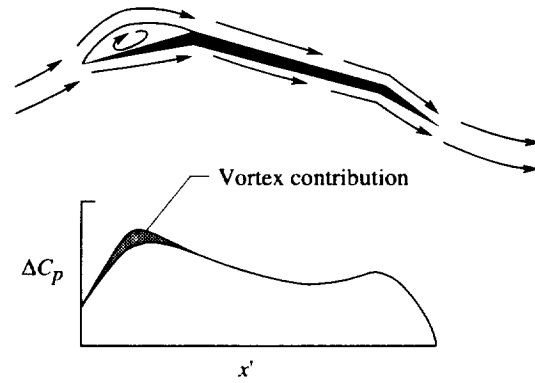
The present code provides an improved accounting of hinge-line singularities in determination of wing forces and moments. The technique used is illustrated in figure 16. In the original code, only wings with smooth camber surfaces were treated, and there was no provision for flaps. When the code was expanded to cover leading- and trailing-edge flaps, two new surfaces were added, but the fairing and integration techniques were not changed. The flap surface loadings were simply added to the existing camber surface component. Thus, the fairing for a case with leading- and trailing-edge flaps and a camber surface with $z = 0$ would appear as shown at the top of figure. As can be seen, the code fairing is not well suited to the character of the flap loadings. In spite of this handicap, acceptable results were obtained when a sufficient number of chordwise elements were used. However, there is a tendency for part of the singularity loading to be lost in the integration process. To provide a partial remedy, the adjustment procedure illustrated in the middle portion of figure 16 is now used. The adjustment to the camber surface pressure distribution is made only for contributions of the leading- and trailing-edge flap surfaces. A curve of the form

$$\Delta C_p = k_{h,1} \sqrt{\frac{c}{x'} - 1} + \frac{k_{h,2}}{\sqrt{|x_h - x'|}}$$

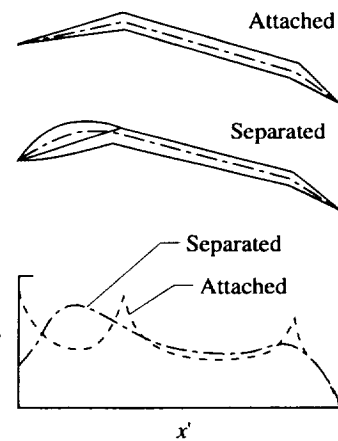
is fitted to the ΔC_p data for a given element and for the preceding and following elements. The integrated area under this curve is compared with the integrated area under a linear fairing, and the difference is represented as an adjustment to ΔC_p extending over the given element. When this adjustment is made for all the chordwise elements, a revised distribution, as shown at the bottom of figure 16, is obtained. The original code integration procedures, when applied to the revised distribution, account for the lost singularity areas and provide an improved integration in the calculation forces and moments.

The attention given to the proper handling of theoretical singularities may be questioned because it is well-known that singularities do not develop in the real flow. The following discussion, which enlists the aid of sketches 6-6 and 6-7, can be used to justify this special treatment.

The actual flow about an airfoil with a deflected leading-edge flap can be quite different from that depicted in figure 16. A flow field similar to that shown in sketch 6-6 would be expected to form. The boundary layer separates from the surface at the leading edge and encloses a region of circulation whose strength is related



Sketch 6-6



Sketch 6-7

to the theoretical leading-edge thrust. Because the theoretical thrust for the deflected leading-edge flap is relatively small (compared with the theoretical thrust for the flat wing), the vortex force associated with the circulation within the separated region is also relatively small.

The relationship between separated and theoretical attached flow for efficient flap systems may be further explored with the aid of sketch 6-7. The dashed line represents the mean camber surface of a flap system airfoil section and the corresponding theoretical attached flow lifting-pressure distribution. For the same section in separated flow, most of the force distribution (excluding the vortex force) is caused by the flow external to the separated region, a flow described by a streamline which emanates from the wing leading edge and reattaches on the wing upper surface. The short-dash-long-dash line represents an effective mean camber surface for the separated flow and the corresponding lifting-pressure distribution.

If, as shown at the bottom of sketch 6-7, the separated flow returns to the surface in the vicinity of the

leading-edge flap hinge line, the efficiency of the system is close to that of the fully attached flow depicted at the top of the sketch. This can happen because the change of downward momentum of the flow over the flap itself is approximately the same for separated and attached flow; therefore, the lifting force is approximately the same. The distribution of this force over the flap is different from the attached flow, perhaps as shown in the pressure distribution of the sketch; however, because of the uniform slope of the flap surface, the integrated force in separated and attached flow is approximately the same. Thus, for reasonably efficient flap systems, the attached flow solution can model the forces generated in the actual separated flow, even though the attached and separated flow fields have entirely different structures. This equivalency, however, is complete only if all the theoretical force (singularities included) is taken into account. The additional contribution of the vortex force may be accounted for by employment of the Polhamus analogy.

Severe flow separation in which the separated flow does not reattach to any portion of the wing can bring about extreme performance penalties. Then the AERO2S code is no longer applicable. When flow separation occurs on the trailing-edge flap after remaining essentially attached over the rest of the wing, code results are also questionable. However, as shown later, trailing-edge flap flow separation is not nearly as disastrous as leading-edge flap flow separation that does not reattach at or ahead of the leading-edge flap hinge line.

6.2. Wing in Combination With Second Surface

Figure 17 depicts the way the present modified code represents a typical wing-canard configuration. The inboard and outboard boundaries of the second surface are made to lie along unit values of the spanwise parameter βy . The code routine that provides for this adjustment also changes the second-surface chords to preserve the surface area (but not the aspect ratio). There may be some overlap of the canard and the wing in the region of the wing-body juncture. This overlap and the change in aspect ratio introduce a small error in the numerical solution. This error and other errors associated with discretization are reduced as the number of spanwise subdivisions is increased. Second surface elements are numbered in the same manner as those of the wing, and a code index distinguishes between the two surfaces. The order of solution still marches from front to rear and inboard to outboard, and either a wing or a second surface element is taken as its turn comes up.

The computer code has no provision for vertical displacement of the two lifting surfaces, but comparison of theory and experiment for two canard-wing

configurations with considerable vertical displacement of the canard above and below the wing (ref. 4) indicated that this vertical displacement might not impose a significant problem. Further work is required to establish the applicability and limitations of the AERO2S code to this type of problem.

6.3. Two-Dimensional Airfoil

As explained in section 4, the effects of Reynolds number and Mach number on attainable thrust are derived empirically by use of available two-dimensional airfoil experimental data. The accuracy of the system thus depends on the availability and accuracy of these experimental data. A new set of two-dimensional airfoil experiments tailored specifically for this problem would make a significant contribution to the technology. In particular, a better definition of limiting pressure coefficients at high Reynolds numbers for low Mach numbers is needed.

The problem in calibrating the attainable thrust method is to find by iteration values of $C_{p,lim}$ that give axial-force coefficients fitting the experimental data as they break away from the full theoretical thrust curve. To facilitate any future recalibration of the system, the AERO2S code has been modified as described in appendix A to provide a two-dimensional airfoil solution. In obtaining this solution, the values of $C_{p,lim}$ used in the current calibration may be replaced by arbitrary selected values. When a chosen XMCPLT value, acting as a multiplier of current values, gives a curve for ΔC_A matching the experimental data for a range of angle of attack near the breakaway point, the corresponding limiting pressure coefficient included in the output data is taken to be the value for the input Mach number and Reynolds number. A collection of such data for a large number of airfoils and test conditions then can be used to generate a revised curve-fit equation in a manner similar to that used in the original development.

7. Wing Design Method for WINGDES Code

The design method employed in the WINGDES computer code is directly dependent on the lifting surface analysis methods, discussed in sections 2 through 5, which are applied to a series of candidate wing surfaces. Considerations of leading-edge flow condition in combination with drag minimization techniques are used to find an optimum combination of these surfaces. Inclusion of the influence of attainable thrust on the design dictates that the solution be found by an iterative process.

The process begins with the evaluation of the aerodynamic characteristics of a code input surface. Except

for special design purposes discussed later, that surface is flat. The important design information supplied by this evaluation includes the angle of attack at which the design lift is achieved, the spanwise distribution of the angle of attack for zero thrust, and the range of angle of attack for full thrust. This information is used to tailor the wing surface in the leading-edge region to provide distributed leading-edge thrust forces which compensate for failure to achieve the full theoretical leading-edge thrust. Because this change in the wing surface changes the overall wing lift coefficient at the design condition, introducing additional incremental wing surfaces is then necessary to restore the design lift coefficient. The Lagrange method of undetermined multipliers is used to find a

combination of additional surfaces which produces the necessary lift increment with a minimum axial-force coefficient. The tailoring of the leading edge plus the combination of additional surfaces defines a new wing surface whose aerodynamic characteristics may be determined by reapplication of evaluation methods. The new surface generally has a different angle of attack for the design lift coefficient and a different distribution of the angle of attack for zero thrust; these differences necessitate a revised tailoring of the leading-edge surface and a revised definition of the additional surfaces. Thus a solution by iteration is required; the discussions in sections 7.1 through 7.4 elaborate on the steps taken in this process.

7.1. Candidate Surfaces

To provide data for use in the optimization process, the evaluation methods are applied to a series of candidate surfaces to evaluate normal-force, axial-force, and pitching-moment coefficients and interference axial-force coefficients as well. The candidate surfaces are given in the following table:

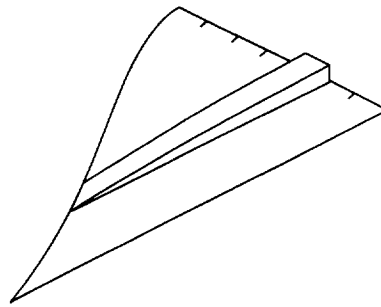
Type	Surface	Defining equation
Input	1	z (defined by table of coordinates)
Flat	2	$z = -(\tan 1^\circ) x'$
General camber surfaces	3	$z = k_{s,y} e^{y,3} (x')^{e_{x,1}}$
	4	$z = k_{s,y} e^{y,3} (x')^{e_{x,1}}$
	5	$z = k_{s,y} e^{y,3} (x')^{e_{x,1}}$
	6	$z = k_{s,y} e^{y,4} (x')^{e_{x,1}}$
	7	$z = k_{s,y} e^{y,1} (x')^{e_{x,2}}$
	8	$z = k_{s,y} e^{y,2} (x')^{e_{x,2}}$
	9	$z = k_{s,y} e^{y,3} (x')^{e_{x,2}}$
	10	$z = k_{s,y} e^{y,4} (x')^{e_{x,2}}$
Trailing-edge camber surfaces	11	$z = k_{s,y} e^{y,1} (x' - c + c_{te})^{e_{x,te}}$
	12	$z = k_{s,y} e^{y,2} (x' - c + c_{te})^{e_{x,te}}$
	13	$z = k_{s,y} e^{y,3} (x' - c + c_{te})^{e_{x,te}}$
	14	$z = k_{s,y} e^{y,4} (x' - c + c_{te})^{e_{x,te}}$
Leading-edge camber surfaces	15 ↓ 64	$\begin{cases} z = (\tan 1^\circ) x' \left(1 - \frac{2}{3} \sqrt{\frac{x'}{c_{lc}}}\right) & (0 < x' < c_{lc}) \\ z = \frac{1}{3} (\tan 1^\circ) c_{lc} & (c_{lc} < x') \end{cases}$

The first surface is defined by an input TZORD table described in appendix A. For special design problems, the user may choose to use such a surface. However, for conventional design purposes, a surface with $z = 0$ everywhere is preferable and this surface is provided by a code default. The second surface is a flat surface at an angle of attack of 1° .

Surfaces 3 to 10 affect the entire wing and are called general camber surfaces. The code user may select a desired number of these surfaces from 0 to 8 to be taken in the order listed (for instance, if four surfaces are called for, surfaces 3 to 6 are used). The order cannot be changed, but other exponents can be substituted for $e_{y,1}$, $e_{y,2}$, $e_{y,3}$, and $e_{y,4}$ and for $e_{x,1}$ and $e_{x,2}$. The code uses all eight surfaces unless the user chooses otherwise; the code default for the number of general camber surfaces is 8. Typical general camber surfaces for a delta wing with default exponents are illustrated in figure 18.

Surfaces 11 to 14 are intended to cover a wing trailing-edge region for special purposes such as design of mission adaptive surfaces or selection of trailing-edge flap geometry. If desired, these surfaces can be used as additional general camber surfaces by setting the trailing-edge surface chords equal to the wing chords and selecting a value of $e_{x,te}$ different from $e_{x,1}$ and $e_{x,2}$ but greater than 1.0. The user may select a desired number of these surfaces up to 4 to be taken in the order listed. The code default for the number of trailing-edge modifying surfaces is 0. Typical trailing-edge surfaces are also illustrated in figure 18.

The remaining surfaces serve the purpose of modifying the wing leading-edge region. They are designed to have a much larger effect on leading-edge surface slope dz/dx than any other surfaces (except the flat surface at $\alpha = 1^\circ$) and, thus, to exert a strong influence on the important design factor, the wing angle of attack for a local leading-edge thrust of zero. One leading-edge modifying surface is used for each wing spanwise station from root to tip. Each surface has the specified surface ordinates only for a strip one unit wide centered on that particular station. Everywhere else, the surface has an ordinate of zero. A typical leading-edge modification surface for the third of seven semispan stations for a subsonic design Mach number is shown in sketch 7-1. For supersonic speeds, the shape would be similar but the leading edge would be unswept.



Sketch 7-1

Since the optimization process is critically dependent on these leading-edge surfaces, the user has no option for reducing the number. The user may, however, select the area to be affected by the leading-edge modification by entering a tabular schedule of c_{le} versus span station to replace the code default table which sets c_{le} at all span stations equal to the wing root chord. Reduced areas for the leading-edge modification could very well give an optimized wing design with better performance than that given by the conservative code default. However, very small leading-edge modification areas could lead to erroneous results. Section aerodynamic and geometric data at span stations where fewer than 2 or 3 elements cover the chord of a leading-edge modification surface could be suspect. The number of elements N in a given chord may be approximated as

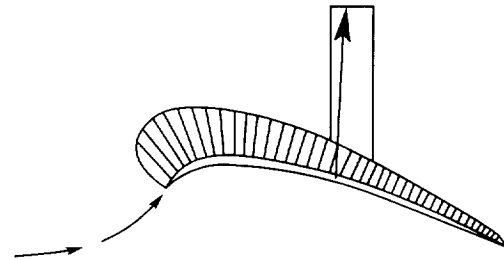
$$N = \frac{c_{le}}{b/2} (\text{JBYMAX})(\text{ELAR}) \quad (\text{Subsonic speeds})$$

$$N = \frac{c_{le}}{b/2} \frac{\text{JBYMAX}}{\beta} \quad (\text{Supersonic speeds})$$

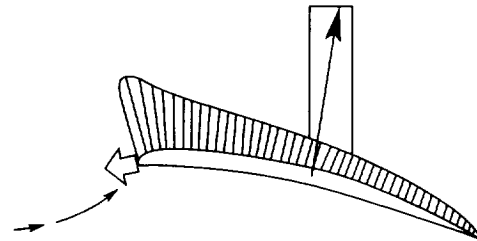
Because computational costs tend to increase as the fourth power of JBYMAX and the second power of ELAR, an increase in the element aspect ratio is the more efficient means of providing for increased definition. At supersonic speeds the only recourse is to increase JBYMAX.

7.2. Influence of Leading-Edge Conditions on Wing Design

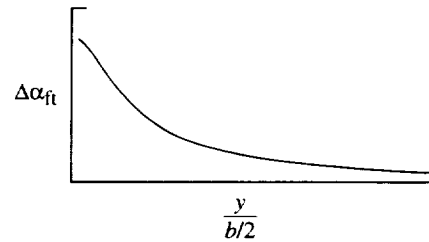
Wing aerodynamic performance is critically dependent on leading-edge flow conditions. If, as depicted in sketch 7-2, the wing section thickness and leading-edge radius are large enough to retain attached flow and full leading-edge thrust for a given set of flight conditions, there is little need to depart from a flat lifting surface. If, on the other hand, the wing section is very thin with little or no possibility for the development of leading-edge thrust, comparable aerodynamic performance can be obtained only by shaping the wing camber surface as shown in sketch 7-3 to distribute the pressures so that as much of the section lifting force as possible is generated on the forward portion of the section where a thrust force can be generated. For wing sections with thickness and radius which are appreciable but not large enough to generate full thrust at the design condition, a compromise may be made by introducing just enough camber to reduce the angle between the upwash vector and the mean camber surface to a value which permits attached flow. Such an intermediate solution is depicted in sketch 7-4. As discussed subsequently, the attainable thrust prediction method provides the basic information required in a design process which takes advantage of the possibilities for thrust generation to reduce the severity of the design camber surface.



Sketch 7-3



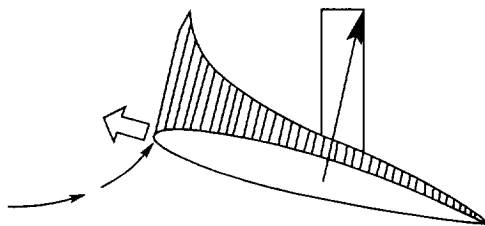
Sketch 7-4



Sketch 7-5

7.3. Selection of Leading-Edge Surfaces

The design process begins with the evaluation of the aerodynamic characteristics of the code input surface. Except for special purpose designs, that surface is flat (the code default surface), and such a surface is used for illustrative purposes. The input surface is not allowed to change in the design process, and thus the greatest potential for drag minimization is permitted with an input surface which places no restraints on the design. Among the information provided by the code evaluation of the input surface is a spanwise distribution of the range of angle of attack for full thrust, which might appear as shown in sketch 7-5. For angles outside this range, the attainable thrust levels are less than the full theoretical values. The evaluation of the input surface also provides an estimate

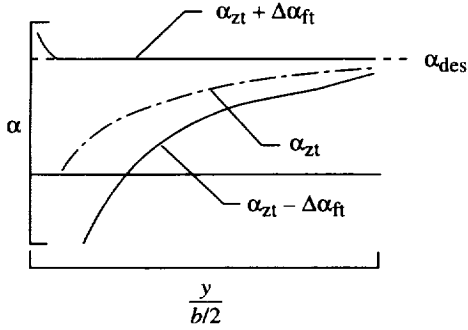


Sketch 7-2

of the angle of attack required to generate the design lift coefficient which is designated the "design angle of attack."

The object of the design process is to alter the wing angle of attack for zero thrust distribution to create a relationship similar to that shown in sketch 7-6 wherein the upper limits of the range of full thrust for the cambered wing are coincident with the design angle of attack. This process gives a design with the mildest camber surface capable of a theoretical aerodynamic efficiency comparable with the full theoretical leading-edge thrust efficiency. A milder camber surface offers an obvious advantage in wing structural simplicity. An additional advantage for supersonic speeds is the reduced real flow drag penalties associated with camber surface severity discussed in reference 6. The supersonic empirical correction first devised in reference 6 has now been modified to provide a means of incorporating an estimate of these penalties in performance predictions.

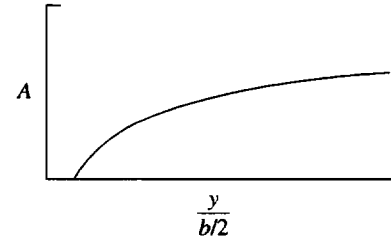
The code design is carried out by iteration. For any design iteration, the leading-edge surface weighting factors are set equal to $\alpha_{des} - (\alpha_{zt} + \Delta\alpha_{ft})$. For a flat



Sketch 7-6

input surface with $\alpha_{zl} = 0^\circ$, leading-edge surface weighting factors for the first iteration might be as shown in sketch 7-7.

The resultant surface defined by the addition of the spanwise distribution of leading-edge surface weighting factors alters the wing lift and pitching-moment coefficients. The optimization procedure, described in section 7.4, is then used to find additional surfaces



Sketch 7-7

(general camber surfaces) which restore the wing lift coefficient to the design value and introduce a moment increment to approach the design pitching-moment coefficient with the least possible chord force. Because these general camber surfaces have an influence on the spanwise distribution of the angle of attack for zero thrust and the design angle of attack, it is necessary to evaluate these quantities and then find a distribution of incremental leading-edge surface factors to rematch the upper limit of the range of full thrust with the design angle of attack.

7.4. Selection of General Camber Surfaces

The Lagrange method of undetermined multipliers is used to define general camber surface weighting factors which minimize the wing axial-force coefficient while producing a specified increment in normal-force coefficient and, if desired, a specified increment in pitching-moment coefficient. For the design of an asymmetrical wing, an additional restraint which eliminates a rolling moment about a specified center of gravity may also be applied. Application of this method to the problem of selecting an optimum combination of loadings was covered in some detail in reference 10. For the present application, the following set of equations is used to establish the strength of each of the candidate surface factors:

$$\begin{aligned}
 \sum_{i=2}^{i=n} C_{A,2i} A_i + \lambda_N C_{N,2} + \lambda_M C_{m,2} + \lambda_R \Delta y_2 C_{N,2} &= 0 \\
 \cdot & \quad \cdot \quad \cdot \quad \cdot \quad \cdot \\
 \cdot & \quad \cdot \quad \cdot \quad \cdot \quad \cdot \\
 \cdot & \quad \cdot \quad \cdot \quad \cdot \quad \cdot \\
 \sum_{i=2}^{i=n} C_{A,ni} A_i + \lambda_N C_{N,n} + \lambda_M C_{m,n} + \lambda_R \Delta y_n C_{N,n} &= 0 \\
 \sum_{i=2}^{i=n} C_{N,i} A_i + 0 + 0 + 0 &= - \sum_{i=n+1}^{i=N} C_{N,i} A_i \\
 \sum_{i=2}^{i=n} C_{m,i} A_i + 0 + 0 + 0 &= C_{m,des} - C_{m,pre} + C_{m,cor} - \sum_{i=n+1}^{i=N} C_{m,i} A_i \\
 \sum_{i=2}^{i=n} \Delta y_i C_{l,i} A_i + 0 + 0 + 0 &= - C_{l,pre} + C_{l,cor} - \sum_{i=n+1}^{i=N} \Delta y_i C_{N,i} A_i
 \end{aligned}$$

where

- n number of general camber surfaces and trailing-edge camber surfaces
- N total number of camber surfaces, $n + \text{JBYMAX}$
- $C_{m,pre}$ pitching-moment coefficient evaluated in previous iteration
- $C_{m,cor}$ pitching-moment coefficient correction based on differences between design and realized pitching-moment coefficients in previous iterations
- Δy_i distance between center of pressure of candidate surface i and wing center of gravity
- $C_{l,pre}$ rolling-moment coefficient evaluated in previous iteration
- $C_{l,cor}$ rolling-moment coefficient correction based on differences between design and realized rolling-moment coefficients in previous iterations

If a rolling-moment restraint for an asymmetrical wing is not applied, the terms in the bottom row and the column just left of the equal sign are eliminated. If a pitching-moment restraint is not applied, the next to bottom row and the second column from the equal sign are eliminated. With the surface factors evaluated by standard numerical procedures for solutions of simultaneous equations (up to 15), surface slopes and pressure distributions of the optimized surface are found by linear combination as follows:

$$\left(\frac{dz}{dx}\right)_0 = \sum_{i=1}^{i=N} A_i \left(\frac{dz}{dx}\right)_i$$

$$\Delta C_{p,o} = \sum_{i=1}^{i=N} A_i C_{p,i}$$

7.5. Summary of Design Process

As described, the design process is carried out by cycling through the following steps:

1. Definition of aerodynamic characteristics of wing surface including spanwise distribution of angle of attack for zero thrust and design angle of attack
2. Definition of incremental leading-edge surface factors to match upper limit of range of full thrust with design angle of attack
3. Definition of general camber surface factors to minimize wing axial-force coefficient while maintaining design lift coefficient and approaching design pitching-moment coefficient

The iteration is stopped when, from one iteration to the next, the design angle of attack changes by less than 0.01° and the design pitching-moment coefficient changes by less than 0.001.

Although the code design procedures were developed specifically to take advantage of attainable thrust in an attempt to define mild camber surfaces which yield aerodynamic performance comparable with that attainable with full theoretical thrust, the code design features can be used in other ways. For example, a design which provides a margin of error in meeting leading-edge alignment conditions for thrust recovery can be achieved by designing for wing sections with zero thickness and

using a subsequent evaluation with actual wing section thickness and leading-edge radius to give performance estimates. Such a design, however, can be expected to suffer more severe real flow drag penalties at supersonic speeds than the milder surface design; these penalties may now be estimated through use of the revised empirical correction.

Two principal goals of the design approach of this paper, as applied to a sharp leading-edge wing, are the alignment of the wing leading edge with the local upwash and the generation of a significant amount of normal force in the vicinity of the leading edge to create a distributed thrust to replace the lost concentrated leading-edge thrust. At first glance, these two goals may appear to be contradictory. The alignment of the leading edge with the local flow gives a loading of zero at the leading edge which, of course, cannot produce the desired thrust. The saving feature of the design concept is the rapid curvature of the surface behind the leading edge due to the optimized combination of candidate surfaces. This permits the rapid development of thrust producing loadings immediately behind the leading edge. The handling of leading edges in linearized theory has always created problems such as theoretically infinite pressures for flat surfaces and theoretically infinite slopes for wing design surfaces. However, this is a very localized condition and, except in the immediate vicinity of the singularities, the solutions are reasonable. The failure of

numerical methods to produce these singularities poses no real handicap.

7.6. Evaluation of Design

Although evaluation methods are used to determine the aerodynamic characteristics of each of the candidate surfaces, the results for the optimized combination of surfaces may not provide a true representation of the aerodynamic efficiency of the wing design. Because the evaluation data provided in the code design mode are based on the direct addition of surface ordinates and aerodynamic coefficients for up to 64 different candidate surfaces, each of which may introduce numerical calculation errors, an accumulation of errors is a possibility.

To provide a better assessment of the aerodynamic characteristics of the just completed design which is consistent with evaluation of other wing surfaces, a special code feature has been provided. Unless the code user chooses not to use this feature, the many contributing surfaces are consolidated to provide a single camber surface which in combination with a flat surface at $\alpha = 1^\circ$ is used in a standard evaluation. When this code default option is exercised, the code creates, through interpolation and extrapolation, a table of camber surface ordinates to replace the original input (or code default) surface and then performs the normal evaluation procedures beginning with the determination of code geometry information for this new surface.

7.7. User Control of the Design

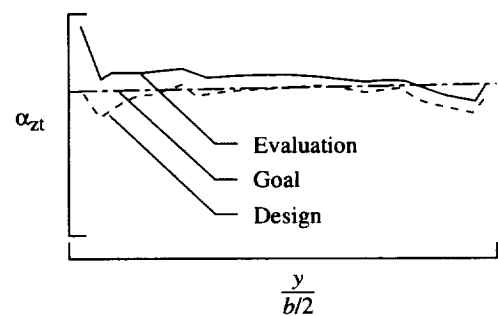
The code user can find a number of ways in which to exert an influence on the design beyond the normal selection of design Mach number, Reynolds number, lift coefficient, and if desired, pitching-moment coefficient. As mentioned previously, the user may exercise some control over the candidate surfaces to be used in the design. The use of this capability for special purpose designs is illustrated in one of the code application examples given in section 12.

The user may also affect the design by overriding the distribution of leading-edge surface factors provided by the code. Because these factors are determined by a numerical iteration process, the design may result in a wing surface with irregularities in the spanwise variation of camber surface ordinates. As described later, the user may substitute a smoothed set of leading-edge surface factors and redesign the wing to produce a camber surface without irregularities.

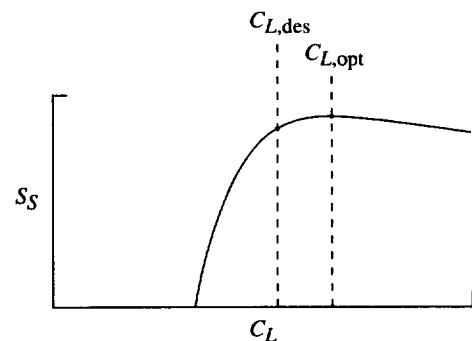
The provision for alteration of the distribution of leading-edge surface factors may also be used for another purpose. When aerodynamic data for a camber surface design from the code evaluation mode differ significantly

from the data developed in the design mode, there is a possibility that the wing performance may be improved by user control of the leading-edge surface factors. There are two primary ways in which the design as evaluated may differ from the design goals. First, as shown in sketch 7-8, differences may occur between the design goal and the evaluation in the spanwise distribution of the angle of attack for zero thrust. This difference is a measure of the failure to provide the proper relationship between leading-edge surface slope and the local upwash. For reasons discussed previously, the evaluation data must be considered as the more accurate. Any tendency for the design data to underestimate or to overestimate this angle can be compensated for by an adjustment to the leading-edge surface factors used in the design. Second, as shown in sketch 7-9, the evaluation data may give an optimum lift coefficient that does not correspond to the design lift coefficient. Again the evaluation data must be regarded as the more accurate and a correction may be made by an adjustment to the leading-edge surface factors. The following equation has been found to provide a revised leading-edge surface factor distribution that offers improved performance most of the time when either or both of the preceding discrepancies are significant:

$$A_{1e,adj} = \frac{C_{L,des}}{C_{L,opt}} (A_{1e} + \alpha_{zt,goal} - \alpha_{zt,eval})$$



Sketch 7-8



Sketch 7-9

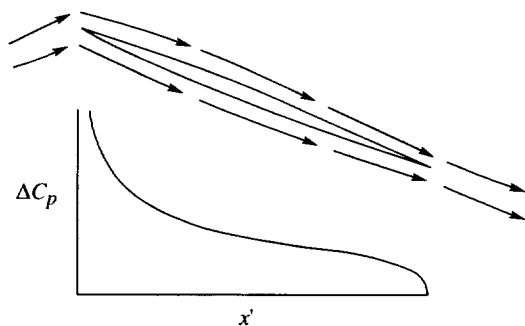
For the user's convenience, a listing of the leading-edge factors used in the design and a listing of suggested values which may lead to improved performance are provided.

7.8. Flap Design Feature

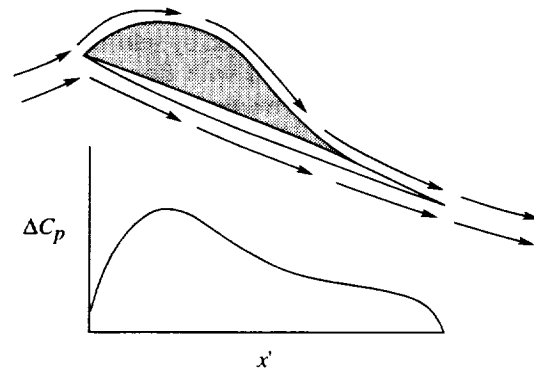
The design method employed in the WINGDES code provides for the definition of a wing lifting surface employing twist and camber which is generally smooth without discontinuities in surface slope. The method can, however, be extended to the design of simple hinged leading- and trailing-edge flap systems. Use of an attached flow design method for optimization of specialized lifting systems which obviously lead to appreciable flow separation is justified by the following logic.

If it were possible for thin wings to achieve attached flow and develop the full theoretical leading-edge thrust, high levels of aerodynamic efficiency could be achieved without the use of twist and camber or of flaps of any type. As depicted in sketch 7-10, a thin flat wing could, if the flow remained attached to the surface, develop a lifting-pressure distribution with very high suction pressures in the vicinity of the leading edge (a singularity in the case of a flat section with no thickness). The high pressures acting on the nose of the wing section produce a leading-edge thrust which counteracts a large portion of the drag distributed over the remainder of the section. For two-dimensional flow, the counteraction is complete, and theoretically the drag disappears. Even for a flat section with no thickness, thrust is theoretically developed because in the limit, as the thickness approaches zero, the integral of the pressure acting on the projected frontal area tends to remain constant.

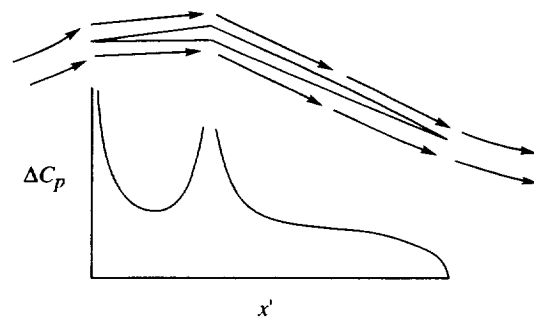
However, in the real flow there are severe limitations on the levels of suction pressures that can be achieved. When the high suction pressures associated with attached flow cannot be achieved, the flow tends to separate from the surface, and flow patterns and pressure distributions such as those shown in sketch 7-11 may result. The



Sketch 7-10



Sketch 7-11



Sketch 7-12

shading represents a separated flow region with an embedded circulation. Although the actual leading-edge thrust may disappear, the force associated with the singularity is not lost, but according to the Polhamus analogy (ref. 11) is redistributed to appear as a normal force instead of a thrust force. Because the gain in normal force cannot compensate for the loss in thrust, the aerodynamic efficiency becomes much poorer.

As shown in sketch 7-12, use of a leading-edge flap can make the problem less severe. The theoretical attached flow lifting pressures in the vicinity of the leading edge are much reduced. The one singularity at the leading edge is replaced by two singularities, one of lesser strength than the original at the leading edge and a second at the flap hinge line. Thus, a distributed thrust force replaces the concentrated leading-edge thrust of the flat wing. For the proper deflection angle, pressures in the vicinity of the two singularities can be made comparable. This distributed lifting pressure acting on the frontal projected area of the flap produces a theoretical thrust force approaching that of the concentrated leading-edge singularity of the flat wing. Because of the generally reduced pressures required to produce nearly the same level of theoretical thrust, that thrust is much more likely to be achieved or approached in the real flow. Within limits, the required pressure levels for the achievement of

a distributed thrust nearly equivalent to that of the flat wing singularity can be controlled by selection of the flap chords and deflections. Even with flow separation, the thrust force is preserved if reattachment takes place at or ahead of the hinge line and if no hinge-line separation occurs.

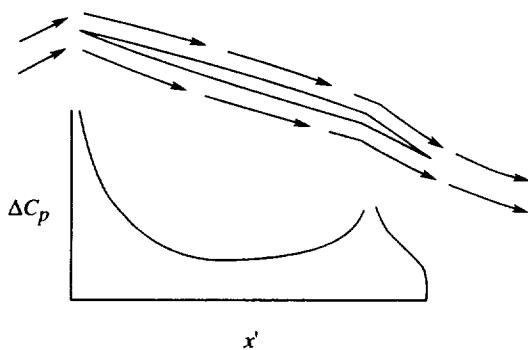
A trailing-edge flap can also be used to improve real flow wing performance. As shown in sketch 7-13, a deflected trailing-edge flap can increase the wing loading so that the required lift can be generated at a lower angle of attack. This in turn reduces the required loading and singularity strength at the leading edge and thus decreases the chance of separation in the real flow. In a sense, the trailing-edge flap causes the remainder of the wing section to act as a large-chord leading-edge flap.

As shown in sketch 7-14, the effects of leading-edge and trailing-edge flaps can be combined to further reduce the theoretical pressure peaks and decrease the chances for real-flow separation. Now there are three singularities associated with the turning of the flow, and for properly selected deflection angles, pressures in the vicinity of singularities can be made comparable in strength. Possibilities for attached flow are further enhanced by a small leading-edge radius and an effective radius at the hinge lines (created in part by the boundary layer). As discussed previously, even with flow separation at the leading edge, good performance of the leading-edge flap

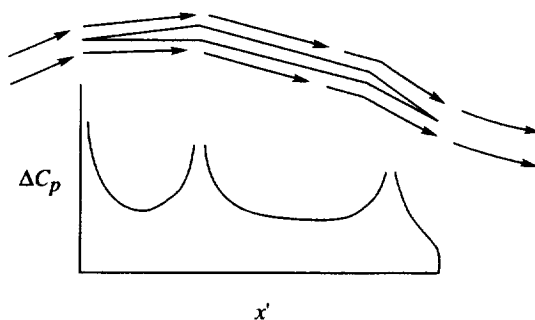
may be retained if the separation is sufficiently localized. Such flow patterns are termed "predominantly attached." As discussed in section 11.2, flow separation over the trailing-edge flap area only is not likely to be nearly as detrimental as separation at the wing leading edge.

An extension of the preceding arguments for the use of leading- and trailing-edge flaps would lead to multi-segmented flaps fore and aft and an approach to the continuously curved camber surface illustrated in sketch 7-15. Such a surface, which may be derived from the WINGDES code, provides for the complete elimination of singularities and an approach to a uniform pressure distribution which should maximize the possibilities for a fully attached flow. Therefore, it is reasonable to use such a wing design solution as a guide in the selection of flap chords and deflections to approximate that surface, its loading, and its aerodynamic performance.

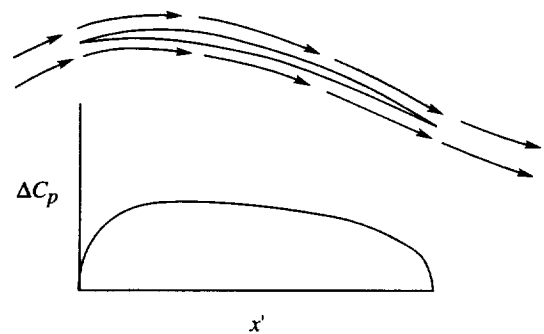
Use of the flap design feature may be illustrated with the aid of figure 19. For flap selection, a mission adaptive or restricted area design is performed. Leading-edge and trailing-edge modification surfaces must be employed, but no general surfaces are used. The chords of these surfaces should be input as the chords of the flaps themselves. The code then designs a restricted area camber surface for leading- and trailing-edge areas whose chords are set to 1.5 times the flap chords. The original camber surface (a flat surface or a milder camber design such as for supersonic cruise) is then superimposed by rotation and translation on the new design. Differences in leading- and trailing-edge ordinates are then used to calculate flap deflections which approximate the designed camber surface. The flap deflections thus obtained are not necessarily optimum deflections but only approximations. Iterative use of the AERO2S evaluation code can help provide a better estimate of true optimum deflections. Generally, the code user finds it necessary to modify the code-generated spanwise deflection schedules to correspond to practical flap segmentation schemes.



Sketch 7-13



Sketch 7-14



Sketch 7-15

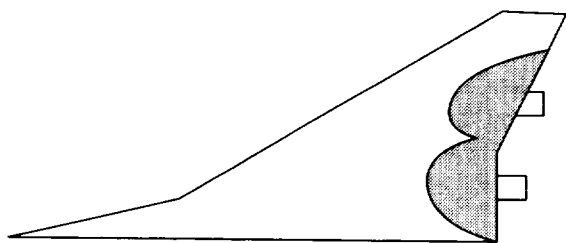
7.9. Design in Presence of Interference Flow Fields

The WINGDES computer code now permits the design of a wing lifting surface with flow fields of other airplane components such as fuselage, nacelles, or canards taken into account. This design may be accomplished by the addition of a table describing the interference pressure distribution on the wing surface generated by the other airplane components. This pressure field enters into the optimization process but, unlike the other loadings, remains unchanged throughout the design process.

The interference pressure field must be supplied by the user. Normally, these pressures are found by the use of some other aerodynamic analysis code capable of handling the designated airplane components. Most times, two computer runs of this other code are required; one has all the airplane components represented, and the other has only a mean camber surface that matches as closely as possible the fixed input camber surface (surface 1) of the wing design code. The interference pressure field for the wing design code is then defined as the difference between these two loadings. By using the appropriate WINGDES options, the design surface may include only the wing outboard of the wing-body juncture or it may include the complete lifting surface, in which case a new fuselage camber surface is generated.

When an interference pressure field is employed in the lifting surface design, normal forces generated by that field influence the wing design and are included in the listed wing forces and moments for the code design mode. For the code evaluation mode, these forces are excluded. Proper values of lift, drag, and suction parameter for the more complete configuration can be found only if all forces generated by the additional component are taken into account. In the absence of accurate axial-forces as well as normal-force increments, exclusion of both increments can be expected to give a more realistic performance estimate than inclusion of one or the other.

A special code option provides for the design of a reflexed surface in the vicinity of engine nacelles to take advantage of the nacelle pressure field. This option is



Sketch 7-16

intended for use at supersonic speeds where the influence of the nacelles is confined to a relatively small area of the wing near the trailing edge as shown in sketch 7-16. The reflex design is performed by use of trailing-edge surfaces corresponding to the affected area which must be specified by the user. When the reflex surface design option is used, the usual surface ordinates are replaced by a set more tailored to this particular problem. For this design, trailing-edge camber surface ordinates are defined by

$$z = k_s(c_{te})^{e_y}(x' - c + c_{te})^{e_x}$$

The code exponent defaults are as given in the following table:

Surface	e_y	e_x
11	1.0	1.5
12	1.0	2.0
13	2.0	1.5
14	2.0	2.0

This definition provides a design reflex surface reasonably well matched to the pressure fields generated by nacelles with a continual growth in cross-sectional area from the lip to the last station affecting the wing surface. With the choice of only four candidate surfaces, a detailed design cannot be expected. Actually, a detailed design with more undulations in the surface may be self defeating if it leads to boundary-layer separation.

7.10. Supersonic Empirical Corrections

A study of the application of the WINGDES code to the design and analysis of wings for supersonic speeds reported in reference 6 led to the development of empirical corrections which have now been incorporated in the code. Extensive comparisons of theory and experiment for twisted and cambered wings reveal a consistent pattern in which maximum suction parameter is overestimated by the linearized theory, and the required surface for given flight conditions is less severe than that given by the linearized theory. Analysis of data including pressure distributions indicates that an unrealistic theoretical prediction of the magnitude of the wing upwash field is the primary cause of the discrepancy and that the use of a theoretical design lift coefficient less than the desired operational lift coefficient offers an appropriate correction for linearized theory design methods. A further analysis of the data led to the development of an empirical method for the selection of the proper design lift coefficient and for the estimation of achievable aerodynamic performance. The empirical factors derived in reference 6 are shown in figure 20.

Use of the plots of figure 20 in selecting a design lift coefficient and estimating wing performance may be summarized as follows. First, for the selected design Mach number, use the factor K_{des} from the top plot to define a replacement design lift coefficient:

$$(C_{L,des})_{rep} = K_{des} C_{L,des}$$

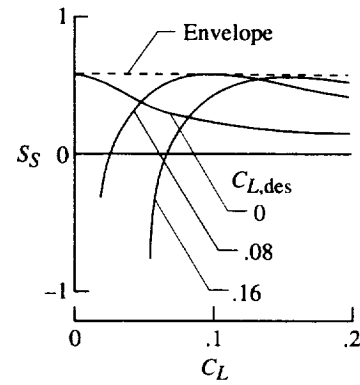
for use in the computer code definition of the lifting surface ordinates and theoretical performance including $(S_{S,max})_{th}$. Then use K_S from the bottom plot to estimate the maximum suction parameter

$$(S_{S,max})_{emp} = K_S(S_{S,max})_{th,b} + [S_{S,th} - (S_{S,th})_b] \Big|_{K_{des} C_{L,des}}$$

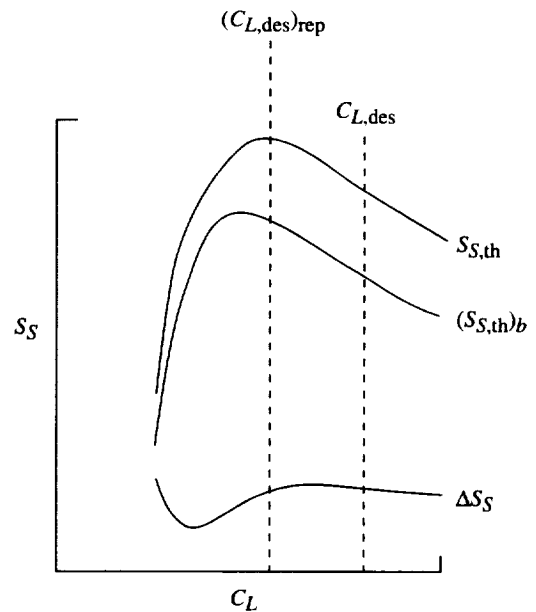
that can actually be achieved. The code value of $(S_{S,max})_{th,b}$ used in this expression is taken as the value at $(C_{L,des})_{rep}$ even though $(C_{L,des})_{rep}$ differs from $C_{L,des}$. As illustrated in sketch 7-17 for a wing design family of various values of $C_{L,des}$, there is very little variation of $S_{S,max}$ with C_L . This expression is somewhat different from that used in reference 6. The changes were made to make the empirical correction more appropriate for wings designed to take advantage of attainable thrust. Such designs have less severe camber surfaces and can be expected to have less severe drag penalties than those given by the original method.

The first change is the application of K_S to a suction parameter that represents only forces due to the basic pressure loading, not the total forces with attainable thrust and vortex forces included. The wing designs employed in wind tunnel tests that supplied data for establishment of K_S did not account for the presence of thrust or vortex forces and, in fact, prevented the attainment of any significant contribution of these forces at design conditions. The wing twist and camber were designed to produce leading-edge surfaces aligned with the local upwash. For the less severe camber surfaces that result from inclusion of attainable thrust benefits in the design process, the drag penalties should be less severe. The empirical estimate takes this into account by applying the factor to a suction parameter representing only the basic pressure forces and by handling thrust and vortex contributions separately.

The second term in the previous expression represents the contribution of thrust and vortex forces. As shown in sketch 7-18, which depicts typical code results, suction parameter increases (drag decreases) due to the presence of attainable thrust at the code replacement design lift coefficient. For an idealized design, attainable thrust is equal to theoretical thrust for a limited range of lift coefficients up to $(C_{L,des})_{rep}$. Beyond that point,



Sketch 7-17



Sketch 7-18

theoretical leading-edge thrust begins to be lost (K_t less than 1.0) and vortex forces begin to develop. The net result is that a maximum theoretical suction parameter is achieved at or near $(C_{L,des})_{rep}$. At the design condition $C_{L,des}$, where the wing with reduced twist and camber resulting from attainable thrust considerations actually operates, the drag reduction due to attainable thrust and vortex force contributions is even greater than at $(C_{L,des})_{rep}$. At the higher C_L , the stronger upwash field results in a larger theoretical leading-edge thrust. The decreasing attainable thrust factor K_t and the increasing theoretical thrust compensate in such a way that keeps the suction parameter increment nearly constant. Thus as shown by the typical code results of sketch 7-18, the drag reduction of the design lift coefficient can be approximated by assuming the suction parameter increment $S_{S,th} - (S_{S,th})_b$ at $(C_{L,des})_{rep}$ is applicable at $C_{L,des}$ as well.

This revised empirical method for estimating achievable suction parameters should provide a better estimate for wings designed to take advantage of attainable leading-edge thrust. For wings designed without thrust considerations (leading-edge surfaces aligned with local upwash), the revised method gives results that are little different from those obtained by use of the original method.

The empirically corrected drag coefficient at the design lift coefficient can be estimated by use of the expression

$$(C_{D,des})_{emp} = C_{D,0} + \frac{C_{L,des}^2}{\pi AR} + [1 - (S_{S,max})_{emp}] \times \left(C_{L,des} \tan \frac{C_{L,des}}{C_{L\alpha}} - \frac{C_{L,des}^2}{\pi AR} \right)$$

which is derived from a rewriting of the suction parameter definition. The lift-drag polar near the cruise lift coefficient may be approximated as

$$C_{D,emp} = C_{D,0} + \frac{C_L^2}{\pi AR} + (1 - S_{S,emp}) \left(C_L \tan \frac{C_L}{C_{L\alpha}} - \frac{C_L^2}{\pi AR} \right)$$

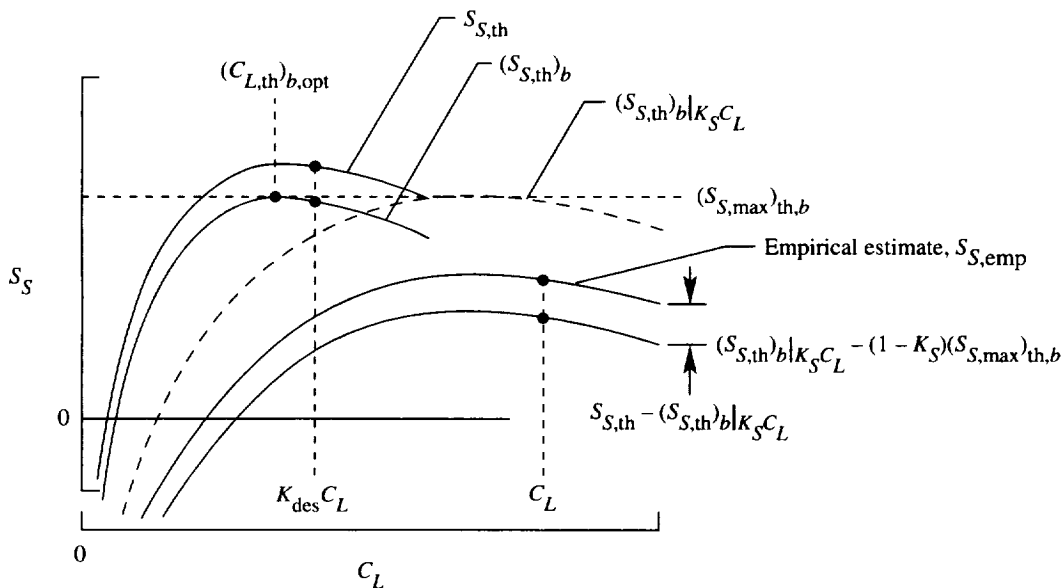
where for any C_L the suction parameter $S_{S,emp}$ is found from the curve for the uncorrected code $(S_{S,th})_b$ for a value of C_L equal to K_{des} times the actual C_L . The parameter is corrected for the overestimation tendency by subtracting an increment between the theoretical and

empirical suction parameter (assumed to be constant over a range of C_L) and by adding an incremental suction parameter representing the attainable thrust and vortex force contribution. In equation form,

$$S_{S,emp} = (S_{S,th})_b \Big|_{K_{des} C_L} - (1 - K_S)(S_{S,max})_{th,b} + [S_{S,th} - (S_{S,th})_b] \Big|_{K_{des} C_L}$$

As indicated by this expression, for a given C_L , both the suction parameter associated with basic pressure loadings and the increment associated with attainable thrust and vortex force contributions are found from code results for a different and lower lift coefficient $K_{des} C_L$. This correction is now implemented in the WINGDES code, for both the design and evaluation mode, incorporates a procedure to identify the optimum lift coefficient $(C_{L,th})_{b,opt}$ and the maximum suction parameter $(S_{S,max})_{th,b}$ used in defining the empirical correction. This procedure is used to represent as accurately as possible the aerodynamics of the surface being analyzed, which in the design mode may not represent a fully optimized surface for the specified design conditions. Sketch 7-19 illustrates a typical application of the procedure.

When applied to wings designed without consideration of attainable thrust or vortex forces (including the wings used to supply data for establishment of the empirical corrections), the revised method gives only slightly higher estimates of performance than the original method but still has good agreement with experimental data. For



Sketch 7-19

wings designed to take advantage of attainable thrust, the revised method predicts performance noticeably greater than that given by the original method. This expectation is reasonable because the milder surface of that design would be expected to suffer less from nonlinear penalties associated with twist and camber. However, additional wind tunnel data are needed to validate the application of the present correction to that type of design.

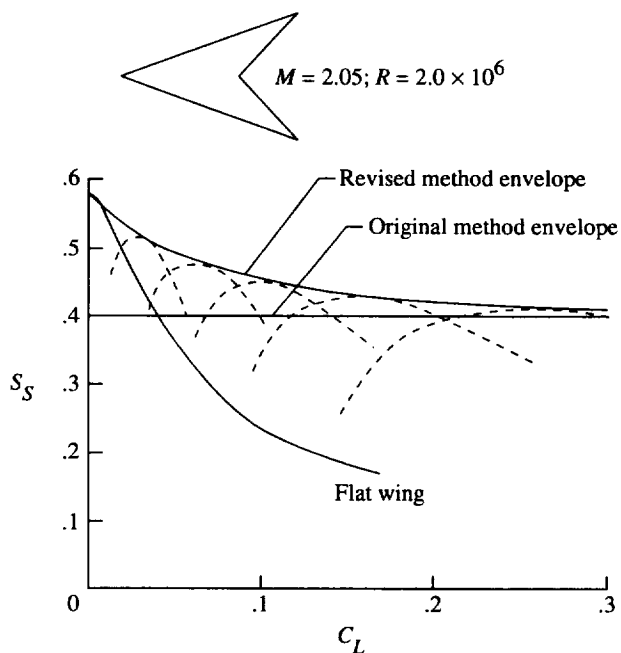
The nature of the differences between the revised and original empirical method for typical code results may be seen in sketch 7-20. The data shown are for a 70° swept leading-edge arrow wing designed for a series of design lift coefficients at a Mach number of 2.05. The wing sections had a maximum thickness ratio of 0.03 at the 50-percent-chord station, and a standard leading-edge radius index of 0.3. Dashed-line curves show code-revised empirical estimates for design lift coefficients of 0.04, 0.08, 0.12, 0.16, and 0.24. The solid-line curve labeled "Revised method envelope" shows the dependence of the estimated suction parameter on the severity of the twist and camber as dictated by the design lift coefficient. For the original method, the envelope gives a constant value of about 0.4 for all design lift coefficients including 0.0, which corresponds to a flat wing. But, code evaluation results for a flat wing show suction parameters at low lift coefficients that are considerably greater. With the original method, the user was advised to use discretion as shown by the following quote from reference 6:

"For small values of $C_{L,des}$, the factor will properly define the mild surface required, but application of the factor K_S may underestimate the performance. The suction parameter for a properly designed twisted and cambered wing will not be less than S_S for a flat wing at the same C_L . For a better performance estimate, use whichever value is greater."

The revised method eliminates the need for user intervention by providing a transition from the results for a flat wing at and near $C_L = 0$ to the corrected results at large design lift coefficients. A proper empirical correction should provide such a transition; only the shape of the curve in the intermediate range of lift coefficients is in question. The revised method seems to give a reasonable shape for this curve.

If the need to impose moment constraints on an optimum combination of loadings arises, the following expression can be used to define a replacement design moment coefficient for use in the design code:

$$(C_{m,des})_{rep} = C_{m,des} - \frac{\partial C_m}{\partial C_L} [C_{L,des} - (C_{L,des})_{rep}]$$



Sketch 7-20

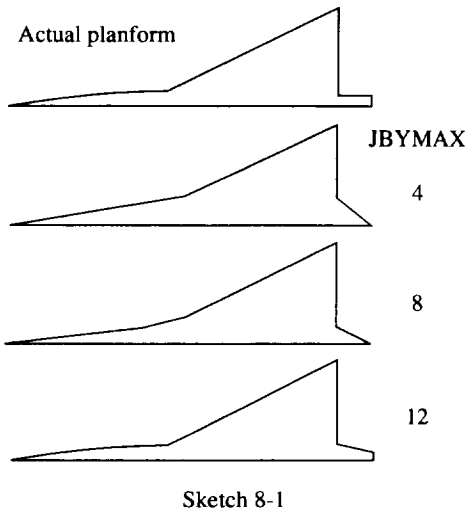
This strategy provides a design moment at $(C_{L,des})_{rep}$, which in combination with a moment increment due to the difference between $C_{L,des}$ and $(C_{L,des})_{rep}$ yields the desired $C_{m,des}$ at $C_{L,des}$.

Although wing design codes provide for the design of surfaces meeting specified moment constraints, this capability should be used cautiously for supersonic cruise vehicles. The imposition of seemingly mild constraints for $C_{m,des}$ can have large detrimental effects on lifting efficiency.

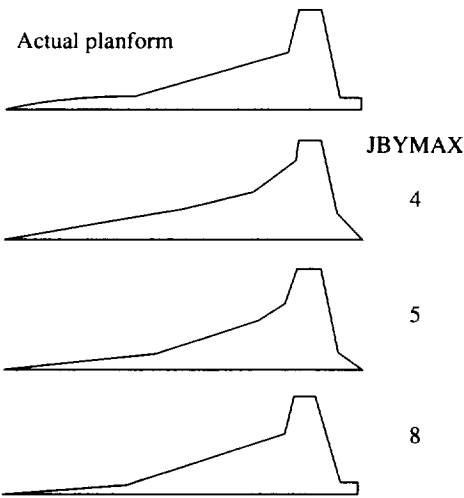
The empirical corrections outlined in this section have now been incorporated in the WINGDES code as a user option. In the design mode, K_{des} is used in the selection of a replacement design lift coefficient and K_S is used as a correction in the estimation of realistically achievable aerodynamic performance. This option may also be used in the evaluation mode to provide corrected performance estimates for wings designed by other methods. The correction is applicable to any wing design based on wing shaping to utilize the upwash field in the recovery of leading-edge thrust that otherwise would be lost. When using this correction to aerodynamic performance, remember that the correction is primarily applicable for a narrow range of lift coefficients on either side of the one where maximum suction parameter is achieved.

8. AERO2S Computer Code and Its Use

The theoretical concepts and the numerical methods outlined in sections 2 through 7 have been incorporated



Sketch 8-1



Sketch 8-2

into two computer codes: one primarily for analysis and the other primarily for design. This section discusses the analysis code and its use.

The wing analysis computer code AERO2S provides a subsonic analysis of wing-canard and wing-horizontal tail combinations that may employ wing leading- and trailing-edge flaps. The numerical method is based on linearized theory potential flow solutions for a lifting surface with zero thickness represented by an array of horseshoe vortices. A solution by iteration rather than by matrix inversion is used. The code also provides for an estimate of attainable leading-edge thrust and the forces caused by separated leading-edge vortices. A description of the code input and output data is given in appendix A.

8.1. Wing Surface Numerical Representation

Effective use of the AERO2S code requires that the user make an intelligent choice of the numerical model

used to represent the wing lifting surface. The number and distribution of code elements are controlled by the entries JBYMAX and ELAR. Figure 21 shows the results of a study of the sensitivity of the AERO2S code numerical solution to the wing planform representation for an aspect ratio 2 wing-body used for theoretical-experimental correlations to be presented later. In this figure, drag coefficient at a Mach number of 0.60 and a represented lift coefficient of 0.30 are shown as a function of the element spacing in the spanwise direction, JBYMAX, and the element spacing in the chordwise direction, ELAR. The scale chosen for this presentation is linear in the inverse of these quantities to enable an extrapolation of results to those presumably attainable with a very large number of elements approaching infinity. For some selected data points, the number of elements representing the complete wing (right- and left-hand panels) is shown in parentheses. As shown at the left of the figure, a reasonably stabilized solution is obtained with JBYMAX of 12 or greater with the element aspect ratio set at 2.0. As shown in sketch 8-1, a JBYMAX value of 12 gives a much closer approximation to the actual planform of the wing-body than does either a value of 4 or 8. The planform representation should be a primary concern in selection of an appropriate JBYMAX value. At the right of the figure, an ELAR value of 2.0 to 4.0 is seen to be sufficient to give a reasonably converged solution for both the flat and twisted

and cambered configurations. Additional information on choice of wing numerical representation was obtained for a cranked-wing supersonic fighter used in a later example of theoretical-experimental correlation. In a manner similar to that for the previous configuration, a study of the sensitivity of the numerical solution to the lifting surface representation was conducted. As shown in figure 22, a JBYMAX value of 8 and an ELAR value of 4.0 were found to be sufficient to give a reasonable approach to converged drag coefficient values for the representative lift coefficient of 0.8 at a Mach number of 0.50. Sketch 8-2 confirms the conclusion that a JBYMAX of at least 8 is required for planform representation. The selected ELAR of 4.0 in conjunction with a JBYMAX of 8 places an average of 4.3 elements between the wing leading edge and the flap hinge line. Generally two or more elements should be placed within the smaller flap chords of a given configuration. A formula given in appendix A provides a means of estimating the average number of elements in a given chord.

For wing-body configurations, the code generally gives better results, particularly in pitching moment, when the body (or fuselage) is modeled as part of the lifting surface planform. The body camber is believed to be modeled best by mean camber surface ordinates—the

same representation used for the wing. This representation generally requires some graphical work to define stations and ordinates for an airfoil section to represent the lifting surface inboard of the wing-body juncture. The mean camber surface ordinate is simply the halfway point between the body upper and lower surfaces. This procedure was used in generating numerical models for the theoretical-experimental correlations shown later.

8.2. Vortex Force Options

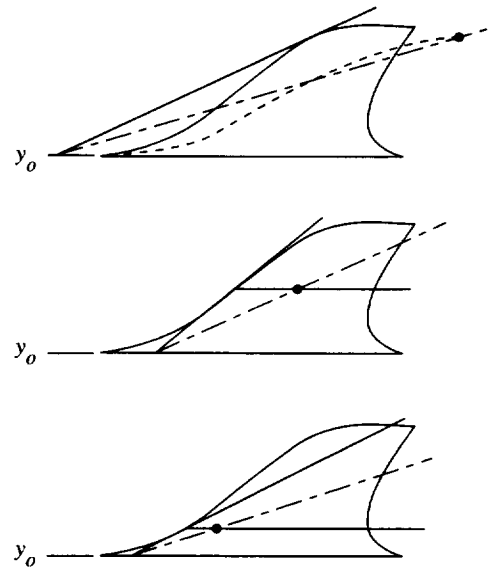
The vortex force created when the flow about the wing can no longer remain attached beyond the leading edge can have a significant impact on aerodynamic performance. The code user has some options for the calculation of this force, which are outlined in appendix A. The default option (IVOROP = 1) has been found to generally give a vortex force prediction in better agreement with experimental data than the other two options for wings with more than moderate sweep. However for unswept wings and for two-dimensional wing sections, option 0, in which the force acts at the leading edge, is the appropriate choice.

The code user can also exercise a degree of control over the spanwise location of the vortex flow-field origin which can provide a better modeling of the vortex field for special planforms such as sweptforward wings. For a typical sweptback wing with a curved leading edge, the default option (YAPEX = 0.0) gives a vortex location as shown in sketch 8-3. As shown, the vortex center (indicated by the dot) moves away from the leading edge as it progresses from inboard to outboard locations. As can happen in real flow, for the most outboard station shown, the vortex center is aft of the wing trailing edge. A vortex center track, the dashed line, can be formed by connecting the dots. For sweptforward and M-wings, a better representation of the vortex is given by using the proper value of YAPEX as shown in sketch 8-4. Because the vortex center track extends on both sides of the YAPEX location, this option cannot be used indiscriminately.

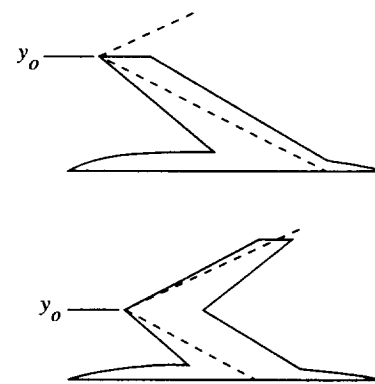
The AERO2S code has recently been modified to provide a solution for two-dimensional airfoil sections. The primary purpose of the modification is to provide a simplified means of recalibrating the method for predicting attainable thrust should the need and opportunity arise. The procedures used to conduct such a recalibration are thoroughly discussed in reference 7 and are treated briefly in appendix A.

8.3. Optimization Capabilities

The AERO2S code does not provide any direct design capability; however, information supplied by the code may be used in an optimization process for the selection of leading- and trailing-edge flap deflections.



Sketch 8-3

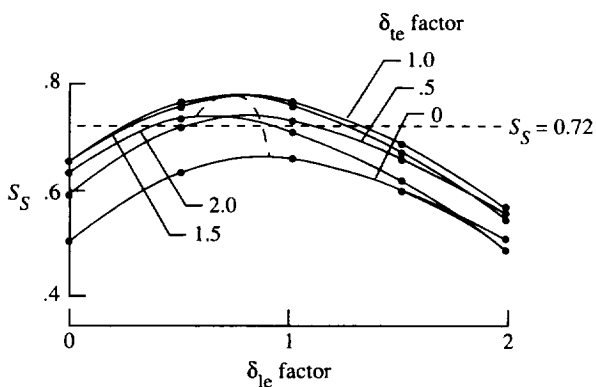


Sketch 8-4

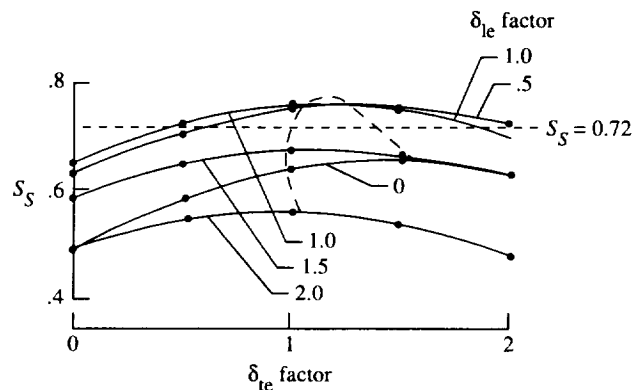
The optimization process involves the construction of performance contour maps with data from multiple runs of the code covering a matrix of deflection-angle schedules. For wings which have only a single leading-edge flap angle and a single trailing-edge flap angle, the matrix may represent the angles themselves. If the flap deflections are described by a schedule of flap angles that vary with spanwise position, the matrix should be composed of multipliers of the tangents of the angles which are used to create flap-angle schedules. Generally, a new computer code run should be made each time the angle (or the angle schedule) is changed. The code provides for generation of a matrix of data in a single run as outlined in appendix A. This capability, however, should be used only for small flap deflections—angles small enough so that little difference exists between the tangent of the angle and the sine of the angle. Where there is doubt, the safe approach is to use multiple runs.

The first step in the construction of performance contour maps is the preparation of plots such as those shown in sketches 8-5 and 8-6. Suction parameter S_S is plotted as a function of both leading- and trailing-edge factors. Data points from the code represented by the dots are faired to provide a family of curves. These two plots, in combination rather than a single plot, provide more data for construction of contour maps and also aid in the detection of errors which might mar the results. The dashed-line curve in the sketches connects maximum suction parameter points from each of the faired curves. The maximum value of the dashed-line curve indicates the peak suction parameter and the deflection angle at which it is reached. Sometimes this may be the only optimization information needed. If however, as is generally true, there are constraints on the design (for example, c_m or α), contour maps are also required.

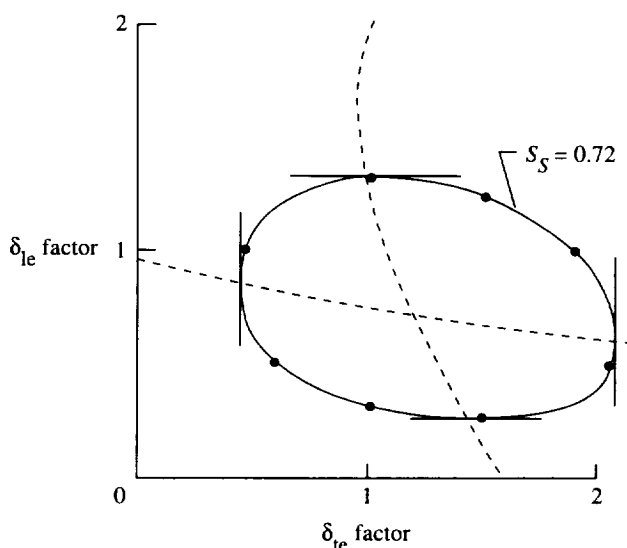
Sketch 8-7 illustrates the construction of one contour line that would appear in a complete map. This sketch shows, as an example, a contour line for $S_S = 0.72$. The dots represent points for $S_S = 0.72$, which were taken from sketches 8-5 and 8-6 at the intersection of each curve with the line for $S_S = 0.72$. These points alone sufficiently define a closed circuit along which the suction parameter remains constant at $S_S = 0.72$. In other situations where the dot array is meager, the dashed-line curves of sketches 8-5 and 8-6 provide additional information to help define the contour. These dashed-line curves transposed to sketch 8-7 show locations where the contour line when crossing the location must be parallel to the plot axes. Other contour lines are constructed in a similar manner to produce complete maps such as those shown in section 11.2. These maps permit identification of the estimated maximum suction parameter and the required deflection angles. As shown in one of the examples of code application, other contour lines such as pitching moment or angle of attack can be added to the plots to provide for the selection of maximum performance subject to appropriate design constraints.



Sketch 8-5



Sketch 8-6



Sketch 8-7

9. WINGDES Computer Code and Its Use

The theoretical concepts and the numerical methods outlined in sections 2 through 7 have been incorporated into two computer codes: one primarily for analysis and the other primarily for design. This section discusses the design code WINGDES and its use.

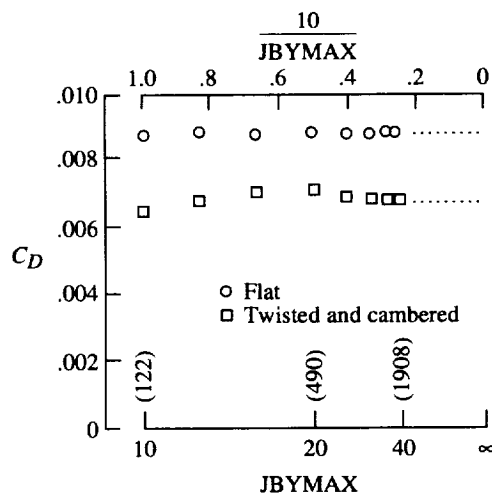
The wing-design code WINGDES generates an optimized twisted and cambered lifting surface for a given wing planform operating at specified flight conditions, provides the corresponding lifting pressure distribution, and gives wing force and moment data. The code provides an analysis of the designed surface and may be operated in an analysis-only mode. Supersonic and subsonic speeds can be handled, but it is not a code for transonic speeds. Because the solution is based on the use of candidate surfaces, it can provide a twisted and cambered surface restricted to specified wing regions (a mission adaptive design) as well as whole-wing design. The code

also provides for the design of leading- and trailing-edge flaps to approximate the shape of mission adaptive camber surface designs and to approach their performance. The actual performance of wings with flaps should be evaluated by use of the AERO2S code, which is not limited by the mild camber surface assumptions necessary for the design code.

The numerical method is based on linearized theory potential flow solutions for a lifting surface with zero thickness represented by an array of horseshoe vortices. A solution by iteration rather than by matrix inversion is used. The code also provides for an estimate of attainable leading-edge thrust and of the forces caused by separated leading-edge vortices. Attainable leading-edge thrust considerations play a direct part in the design process, but vortex force estimates do not except for a reduction of design lift coefficient (and camber surface severity) caused by the vortex lift contribution. A description of the code input and output data is given in appendix B.

9.1. Wing Surface Numerical Representation

As with the AERO2S code, the user must make an informed choice of the numerical model used to represent the wing lifting surface. For subsonic speeds, the controlling code entries JBYMAX and ELAR may be selected according to the guidelines for the AERO2S code offered in section 8. For supersonic speeds the user has no control over ELAR which is set to a default value of $1.0/\beta$. The remaining control, JBYMAX, must be set to a value large enough to ensure convergence, which typically is much larger than that required for subsonic speeds. Sketch 9-1 shows results of a sensitivity study for a supersonic transport wing used for theoretical-experimental correlations in section 11.4. In this sketch,



Sketch 9-1

drag coefficients at a Mach number of 2.40 for a representative lift coefficient of 0.12 are shown as a function of element spacing in the spanwise direction. For both the flat and the twisted and cambered wing, a reasonable convergence is obtained for JBYMAX of 25 or more. For this example, JBYMAX of 40 was used. A safe procedure is to use the code maximum value of 50. The supersonic solution runs quite fast and there usually is little time penalty for the additional spanwise elements.

The design procedure employed in the code is intended to provide the mildest possible camber surface that yields an aerodynamic lifting efficiency comparable with that of a flat wing with full theoretical leading-edge thrust by using to the fullest extent any thrust that may actually be developed. For such a design, the upper limit of the range of full thrust is made to coincide with the design angle of attack. For a more conservative design, one more comparable with previous design methods such as reference 10, an alternate approach may be taken. In this alternate approach, the wing design is performed with TBTOC and TBROC set to zero for the entire semi-span. After the design run, a second run with actual values of TBTOC and TBROC is performed to estimate the wing performance. For this design, the range of attainable thrust provides a factor of safety on either side of the design to minimize the effect of failures of the design procedures to properly match the surface to the upwash field in the vicinity of the leading edge.

For wing spanwise stations at which the leading edge is supersonic ($\beta \cot \Lambda_{le} > 1$), no theoretical leading-edge thrust is developed and the range of full thrust is zero. In the design process, however, the code still makes use of the calculated α_{zt} , which for a twisted and cambered wing is generally not zero. For this situation the value of α_{zt} may be considered to represent the zero leading-edge loading condition resulting from an alignment of the leading-edge surface with the local flow ahead of it. Maintenance of the same flow alignment condition, as for subsonic leading edges ($\alpha_{zt} + \alpha_{ft} = \alpha_{des}$), was found to yield a more efficient surface than other strategies and was adapted for supersonic leading edges also.

9.2. Design Surface Options

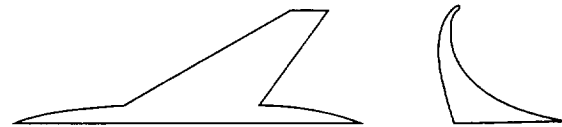
For the design code, the body (or fuselage) may be modeled as part of the lifting surface, a procedure described in section 11. This modeling generally provides a more accurate pitching-moment prediction for analysis purposes. However, for design problems, the highly swept leading edge at the wing apex and the large root chord can introduce exaggerated wing surfaces that are not practical for realistic airplanes. Sketch 9-2 illustrates the nature of the design surface obtained by use of code default options for a wing-body design problem.

The leading-edge surfaces cover all the planform with a chord equal to the wing root chord at all span stations (the code default). General camber surfaces also cover the entire planform. No trailing-edge surfaces are used. As shown in the sketch, for a normal design, the wing root chord has a larger incidence than that of a flat wing developing the same lift. This larger incidence occurs because the leading-edge surface changes required for thrust recovery also result in a loss of lift that must be compensated for by increasing lifting forces elsewhere.

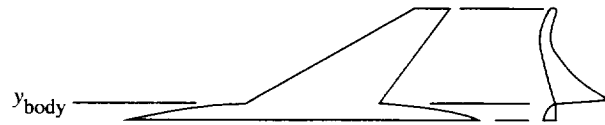
The wing code provides a number of options which can be used to control the character of the designed surface. For special design problems, the user may want to explore various alternate design approaches. For example, to reduce the incidence of the wing root chord and the cabin floor angle, the general design surfaces may be restricted to the wing outboard of the wing-body juncture by use of the entry YFUS. As shown in sketch 9-3, this results in a much reduced body incidence. If the leading-edge surface default chords are retained, as in this example, the body centerline actually has a slightly negative local angle of attack relative to the wing reference plane. However the local angle of attack of the wing surface just outboard of the wing-body juncture may be larger than that of the original design to compensate for the loss of lift generated by the body. This alternate design procedure can be expected to produce a drag penalty, and a problem may occur in the mating of the wing and body.

Another design option that may be explored is illustrated in sketch 9-4. For this design, the general surfaces are completely eliminated by setting NGCS = 0, and trailing-edge surfaces are substituted to perform their functions. Trailing-edge surface chords can be selected as zero inboard at the wing-body juncture and to change from zero at that location to values approaching or equaling the local wing chord at more outboard stations. Likewise, leading-edge surface chords can be selected to be zero inboard of the wing-body juncture and to change from zero at that point to larger values at more outboard stations. As shown in sketch 9-4, the leading-edge chords may be larger than the local wing chords. In fact, large leading-edge area chords are generally desirable. The code default gives values equal to the wing root chord. Although these values are probably larger than those for a true optimum, they produce good performance and avoid problems that might occur with chords that are too small. As shown in the sketch, this procedure alters the character of the design surface and offers another design choice with its own drag penalty.

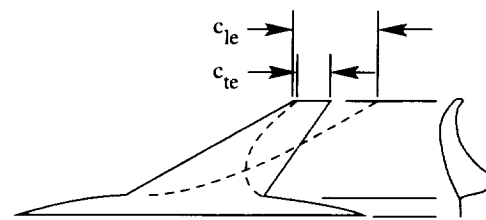
Another strategy the code user may employ to control the shape of the wing surface is use a table of increments for wing trailing-edge surface ordinates to alter the



Sketch 9-2



Sketch 9-3

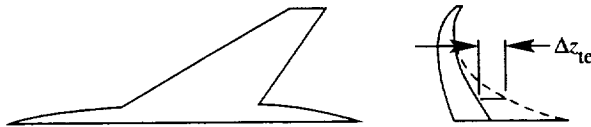


Sketch 9-4

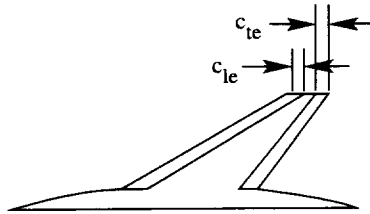
lifting surface after the design of the surface and before evaluation. As described in appendix B, a table of changes for wing trailing-edge ordinates, TDELZTE, alters wing airfoil sections to produce a desired trailing-edge shape without appreciably affecting the leading-edge thrust recovery design. An example of such a change in trailing-edge shape is shown in sketch 9-5. This procedure offers a powerful means of controlling the wing shape but again with possibly large drag penalties.

9.3. Mission Adaptive Design

The WINGDES code provides for an automated design of mission adaptive wing surfaces. In this design process, only portions of the wing defined by leading-edge and trailing-edge design areas enter into the design. The rest of the wing remains as defined by the camber surface input tables. This original camber surface may be input by the user, may have been retained from a previous design run, or may be the program default (a flat surface). Sketch 9-6 shows a wing-body with designated leading- and trailing-edge design areas. The numerical representation of the wing surface (JBYMAX and ELAR) should be chosen so that a sufficient number of elements are within the leading-edge surface chords and the trailing-edge surface chords to adequately define the sometimes highly curved designed camber surfaces. The smallest nonzero chords should accommodate two or more elements. Appendix B gives a formula which may



Sketch 9-5



Sketch 9-6

be used to estimate the number of elements in a given chord. For the mission adaptive design, the number of general surfaces must be set to zero to prevent camber surface changes outside the designated design areas.

9.4. Flap System Design

The WINGDES code may also be used in the design of low-speed flap systems. This option (activated by setting $IFLPDES = 1$) uses an automated flap-fitting technique, which is described in reference 3 and in section 7.8, applied to an appropriate mission adaptive design. When the flap design feature is used, leading-edge and/or trailing-edge design surfaces must be used, and NGCS must be set to zero. The chords of these surfaces are input as the chords of the flaps. The code then designs a restricted area camber surface for leading- and trailing-edge areas whose chords are set at 1.5 times the flap chords. The original camber surface (a flat surface or a milder camber design such as for supersonic cruise) is then superimposed by rotation and translation on the new design. Differences in leading- and trailing-edge ordinates are used to calculate flap deflections which approximate the designed camber surface. Note that the flap deflections thus obtained are not necessarily optimum deflections but only approximations. The code aerodynamic characteristics do not apply to the configuration with flaps but to the smooth designed surface from which the flap geometry was derived. For subsonic cases, use of the AERO2S code can help provide a better estimate of true optimum deflections and the flap system aerodynamic characteristics. See table II(e) for an example of flap design code input.

For the design of mission adaptive surfaces and the selection of flap geometry, a straightforward application of the code tends to underemphasize the contribution of loadings provided by the camber surface or flaps in the

region of the wing trailing edge. This underemphasis results in only a small penalty in theoretical performance because the wing leading-edge shape is still proper for the design conditions. As a practical matter, however, additional loading of the trailing-edge surfaces reduces the need for leading-edge camber which introduces drag penalties not fully covered by the linearized theory. A recommended procedure that uses trailing-edge camber and/or flap deflections to increase the theoretical performance and produce a more practical design is as follows:

1. Perform a whole-wing design for the entire wing planform at the design lift coefficient, Mach number, and Reynolds number. Use no moment restraint if performance alone is the concern but specify a design moment if trim conditions must also be considered. This design provides an indication of performance potential and aids in the selection of local design area chords within limitations imposed by wing structural restraints. Generally, chords should be as large as structural considerations allow; however, the whole-wing solution sometimes shows areas where leading-edge design area or flap chords may be reduced or eliminated.
2. Perform a restricted area wing design for the same flight conditions and for a moment coefficient $C_{m,des}$ at the design lift coefficient as given by the whole-wing solution. Imposition of the design moment ensures that adequate consideration is given to trailing-edge contributions to lifting efficiency. For a mission adaptive design, input the desired area chords subject to the considerations discussed in the first step. To perform a flap design, input a design area chord equal to the actual flap chord and activate the flap design (FLPDES) feature of the code to provide a spanwise flap deflection schedule.
3. For flap designs, examine the code output flap deflection schedule and modify it as necessary to meet design restraints such as those imposed by spanwise segmentation. Also, because the theoretically recommended deflections are only approximations and not true optimums, experience may be applied in modifying results, particularly in reducing large indicated angles. For subsonic speed, application of the wing evaluation code AERO2S to the selected flap system helps in defining more accurately the optimum deflections and the flap system performance.

An alternate process for making the design moment selection is given for the supersonic transport low-speed flap design in section 12.2.

9.5. Design by Iteration

In addition to the preceding strategies, the code user may make wholesale changes in the wing surface by creating a new set of wing surface ordinates with extensive modifications evaluated by using the analysis mode of the WINGDES code. Design by iteration using the analysis mode of the WINGDES code is highly recommended. The results of the analysis mode, not the design mode, must be accepted as the better estimate of actual aerodynamic performance. The design method provides candidate designs but sometimes candidate design with serious deficiencies for practical incorporation into practical airplane configurations. The two modes of the code used in combination can help the designer evaluate designs in which aerodynamic performance is compromised as little as possible to satisfy other restraints.

9.6. Leading-Edge Surface Control

Code-determined weighting factors for the leading-edge modification surfaces are subject to numerical inaccuracies which may produce z ordinates that do not have a smooth variation with respect to the y dimension. In addition to the leading-edge surface weighting factors used in the design, the code also provides a listing of suggested replacement values that, as described in reference 5, may lead to improved performance. By using this option (IAFIX = 1), the user may substitute a smoothed set of leading-edge surface factors (TAFIX) for the code-tabulated values. With the present code, two runs are required: the first finds the nonsmoothed values and the second operates with the smoothed values.

The table of suggested TAFIX values may sometimes show negative values. Negative values are provided to apply to design cases in which the initial surface is already twisted and cambered. If this initial surface has too severe a leading-edge camber for the new design conditions, it may need to be reduced, and a negative factor is appropriate. For the usual designs (the code default, for example), occasional negative values should be disregarded.

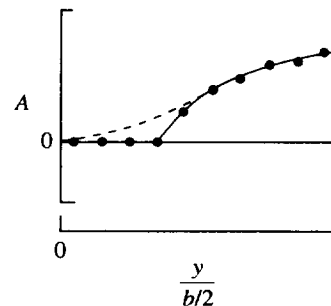
When using the suggested replacement leading-edge surface weighting factors TAFIX, one particular situation requires an additional explanation. For the standard automated design process which attempts to achieve a surface with minimum distortion from a flat surface, suggested redesign TAFIX values may take on the appearance shown in sketch 9-7. Strict adherence to the suggested distribution would produce a surface slope discontinuity that is neither necessary nor desirable. A better distribution is indicated by the dashed line. This distribution not only provides a smoother surface but also represents a design with a greater margin of safety. The suggested TAFIX values shown in sketch 9-7 result from

a wing design with values of α_{zt} and $\Delta\alpha_{ft}$ shown in sketch 9-8. Inboard of the 30-percent-semispan station, the range of full thrust $\Delta\alpha_{ft}$ is greater than the design angle of attack, and no camber or twist is required. However, a moderate amount of camber and twist dictated by the TAFIX distribution shown by the dashed line gives an equally good design phase aerodynamic efficiency and provides a design surface that does not suffer as severe performance penalties if evaluation phase results do not completely meet the design goals.

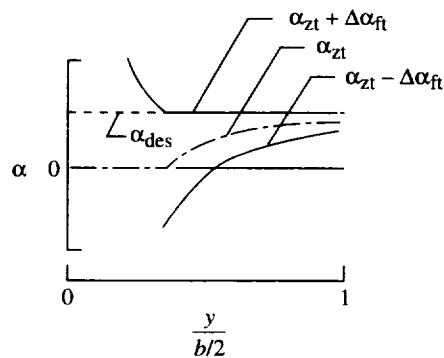
9.7. Design With Moment Restraints

For the design of a camber surface covering the whole-wing planform in which moment restraints are imposed, a straightforward application of the code yields a reasonable solution. However, for more than mild moment restraints a somewhat better performance is obtained by using the following steps:

1. Perform whole-wing design at design lift coefficient, Mach number, and Reynolds number but impose no moment restraint.
2. Perform second whole-wing design at same conditions but with desired moment restraint; for this case, also impose set of leading-edge surface



Sketch 9-7



Sketch 9-8

weighting factors TAFIX as defined in table of suggested values given by first design (with appropriate smoothing).

This process will produce a more nearly optimum surface in the critical leading-edge region. The required moment increment is supplied by the general surfaces covering the entire wing. The leading-edge surface is thus compromised to a lesser degree by the moment requirement.

9.8. Interference Flow-Field Design

The computer code permits the design of a wing lifting surface with flow fields of other airplane components, such as fuselage, nacelles, or canards, taken into account. This design may be accomplished by the addition of a table TCP and associated input data (appendix B) describing the interference lifting pressure distribution on the wing surface generated by the other airplane components. This pressure field and the surface on which it acts, described by an input table, enter into the optimization process but, unlike the other surfaces and loadings, remain unchanged throughout the design.

The interference pressure field must be supplied by the user; normally, it is found by the use of some other aerodynamic analysis code capable of handling the desired airplane components. Most times, two computer runs of this other code are required: one has all the airplane components represented and the other has only a mean camber surface that matches as closely as possible the fixed input camber surface (surface 1) of the wing design code. The wing design code interference lifting pressure field is then defined as the difference between these two loadings. By using the appropriate wing design code options, the design surface may include only the wing outboard of the wing-body juncture or may include the complete lifting surface, in which case a new fuselage camber surface is generated.

The code permits a design of the wing camber surface in the vicinity of nacelles which further optimizes the lifting efficiency of the wing by taking advantage of the pressure field created by the presence of the nacelle. The pressure field must be known and input as an interference flow field TCP and associated input. (See appendix B.) The design is accomplished by employment of trailing-edge wing surfaces TBTEC and associated input (appendix B) which represent in general the boundaries of the interference flow field. Trailing-edge surface chords which adequately define effective boundaries of the pressure field must be supplied by the user. This option is used primarily for the design of supersonic cruise wing surfaces. In this case, the intersection of an envelope of Mach cones emanating from the nacelle lip with a plane representing an average wing camber

surface provides an adequate definition. This option is activated by input of the index IREFL = 1.

9.9. Empirical Correction

An empirical method for selection of design lift coefficient and estimation of achievable aerodynamic performance for supersonic speeds described in reference 6 and in section 7.10 may be included in the code calculations by input of the following index:

IEMPCR empirical correction index (this index set to 1 implements empirical corrections; index set to 0, code default, bypasses this feature)

This correction adjusts the design lift coefficient to account for the tendency of linearized theory to overestimate the magnitude of the upwash field for supersonic speeds. It also corrects the estimated aerodynamic performance to compensate for the tendency of the theory to be overly optimistic.

10. Drag Synthesis

Use of the WINGDES and AERO2S codes to predict aerodynamic performance for complete airplane configurations is based on the assumption that estimates of other drag contributions may be obtained separately and combined with estimates of drag due to lift in a simple additive fashion. The most accurate drag estimate of the complete configuration would seem to require that all major drag contributions and possible interactions be taken into account. However, reasonable estimates of the drag may often be found without consideration of interactions because as discussed later the interactions are often negligible or tend to compensate for one another.

Sketch 10-1 depicts a typical lift-drag polar curve and shows the main contributions to the drag. For efficient flight at a lift coefficient which maximizes the lift-drag ratio, the drag due to lift is about one half the total. This contribution is estimated by the WINGDES and AERO2S codes. The codes evaluate the drag by an integration of pressures acting on the lifting surface and a computational process which accounts for leading-edge thrust forces. Linearized theory concepts also allow the drag due to lift to be separated into two fundamental components: (1) vortex drag associated with the spanwise distribution of the lifting force and the resultant downwash behind the wing and (2) wave drag due to lift associated with the longitudinal distribution of lift and the resultant disturbance waves propagating into the surrounding air. This separation of drag-due-to-lift contributions can be of value in analysis of wing performance and in the search for optimum designs; however, it is not a part of the drag breakdown employed in the system discussed herein. A discussion of the use of far field or area

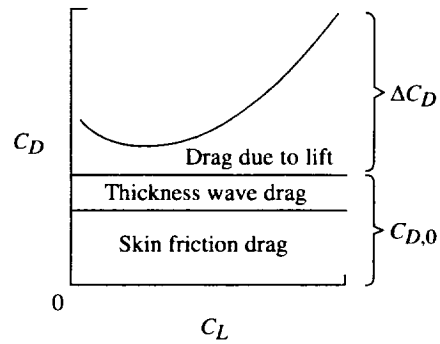
rule concepts in design for drag minimization and for estimating minimum achievable values of drag is given in appendix C.

The WINGDES and AERO2S codes actually work with forces perpendicular and tangent to a wing reference plane rather than lift and drag directly. The relationship between these forces is depicted in sketch 10-2. The use of C_N and C_A rather than C_L and C_D permits a more elementary separation of the contributions to wing forces. As shown in subsequent analysis, curves of C_A versus α are particularly useful in comparisons of the performance of a twisted and cambered wing with that of the corresponding flat wing. The drag-due-to-lift contribution is calculated by the WINGDES and AERO2S codes for lifting surfaces with zero thickness which may employ twist and camber and deflected flaps. Wing section thickness enters into the determination of attainable leading-edge thrust but is considered to generate no drag attributable to the generation of lift.

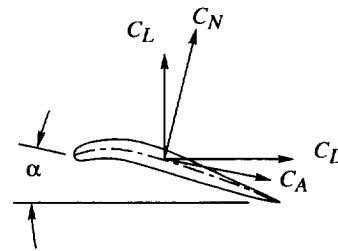
The thickness- or volume-induced drag is considered separately (not in the WINGDES or AERO2S codes). This drag arises from thickness-generated pressure fields acting on the configuration surfaces. It is generally calculated for a configuration without twist and camber at zero angle of attack. Thickness pressure drag generally arises only when the speed of sound is exceeded in some part of the flow field.

For low subsonic speeds, the thickness pressure distributions on airfoils tend to have the form depicted in sketch 10-3. Pressure distributions on bodies of revolution have a similar form. Because the airfoil generates pressure disturbances that travel at the speed of sound, its presence is felt well upstream of the airfoil itself. A stagnation point (zero velocity) at the leading edge is followed immediately by an acceleration of the flow around the leading edge. The low speeds in the vicinity of the leading edge create the pressure peak shown in the sketch. A second stagnation point at the trailing edge which makes its presence felt well upstream decelerates the flow to create maximum velocities and minimum pressures near the airfoil midchord. The distribution of pressures acting on the airfoil surface creates a thrust force on the aft portion of the airfoil which counteracts the drag force created by the forward portion. Thus in idealized inviscid flow, no thickness pressure drag occurs at subsonic speeds.

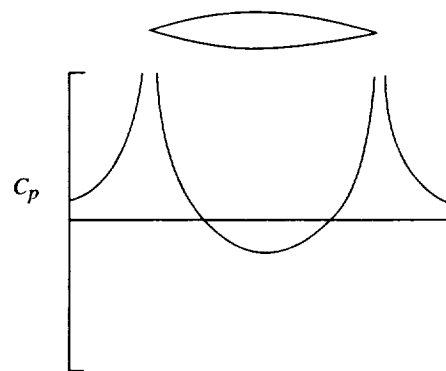
For supersonic speeds, the pressure distributions on airfoils and bodies of revolution have a completely different character as depicted in sketch 10-4. The airfoil shape shown here is similar to that shown in sketch 10-3 except for the elimination of any bluntness so that stagnation points are avoided to give a flow that is supersonic everywhere. Here the pressure change associated with



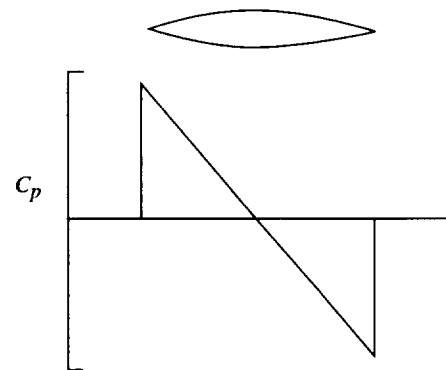
Sketch 10-1



Sketch 10-2



Sketch 10-3



Sketch 10-4

the airfoil leading edge cannot propagate upstream against the supersonic free stream to influence the flow ahead of the airfoil. Beyond the airfoil leading edge, the flow accelerates to higher velocities and lower pressures. In contrast to that for subsonic flow, this acceleration continues all the way to the rear of the body or airfoil because pressures generated by the trailing-edge deceleration cannot propagate upstream; no warning of the coming change is given. For an airfoil with fore and aft symmetry, the pressure jump or shock at the rear is equal to that at the nose. For supersonic flow, no aft surface thrust is available to counteract the forward surface drag, and a substantial thickness pressure drag is created. Because the discontinuous rise in pressure which propagates into the flow field surrounding the airfoil or body resembles the bow wave created by a boat, this drag contribution is often called wave drag.

The thickness or wave drag contribution may be calculated by methods described in reference 13. The complex of computing codes described in references 14 to 17 contains a code implementing the method of reference 13. A new and efficient implementation of this method is available from the same source as AERO2S and WINGDES.

The skin friction drag which must be taken into account for both supersonic and subsonic speeds may be calculated by methods described in reference 18, which also are implemented in the complex of computing codes of references 14 to 17.

The simplified analysis and synthesis of drag represented in sketch 10-1 excludes interactions which generally are not large enough to be the cause of serious concern. For example, all the experimental-theoretical correlations of references 2 to 9 were made without consideration of possible interactions between drag due to lift and either thickness pressure drag or skin friction drag. The following discussion helps to show why in many cases these effects are negligible.

The interaction between drag due to lift and thickness pressure drag is generally negligible for configurations with near vertical symmetry. Thickness-induced pressure fields on the wing tend to be of equal magnitude for the upper and lower surface. Any loss of lift on the upper surface is counteracted by an almost equal gain on the lower surface. Even for arrangements without vertical symmetry, opposing forces are at work that result in only small interaction forces. Consider a body of revolution located below a lifting wing surface. For a body with a continually increasing radius, the thickness-induced pressure field acting on the wing could create an appreciable lifting force leading to a significant reduction in drag due to lift. However, the positive pressure field below the wing associated with the generation of lift

acting on the body surface would lead to a counteracting increase in body pressure drag. The compensation might not be exact, but only a careful estimate of both of the opposing effects would yield a better estimate than neglecting the interactions.

Skin friction drag and the associated boundary layer does not normally have a direct interaction with drag due to lift. The primary influence of the boundary layer is generally to alter the thickness-induced pressure fields, which, as just shown, tend to have only a small effect.

However, under some circumstances, the normally attached boundary layer may separate from the configuration surface. Such a major change in flow conditions could have strong implications concerning the applicability of prediction methods derived with an attached flow assumption. The most severe flow separation tends to occur at wing leading edges for wings without flaps at large lift coefficients and for wings with deflected leading-edge flaps at low lift coefficients. Correlations of experiment and theory (refs. 3 to 9) sometimes show significant discrepancies for these conditions. But for an efficient flap system with deflections selected to minimize separation, the predicted performance generally agrees reasonably well with the measured results. Subsequent discussions of some sample correlations show why an attached flow method can be applicable to detached flow provided that the separation is mild and localized.

11. Examples of Prediction of Aerodynamic Performance

Extensive correlations of code theoretical results with wind tunnel experimental results given in references 2 to 9 have provided a validation of the WINGDES and AERO2S codes. A few correlations are repeated herein to provide the reader with examples that serve to illustrate the application of the codes to practical problems of interest. Where necessary, theoretical results have been updated to reflect the present status of codes which have undergone continuous improvement.

In the correlation figures, an attached-flow computer-code solution that includes no leading-edge thrust forces and no separated leading-edge vortex forces is shown by the short-dashed line. Code-estimated forces, which include attainable thrust and the effects of a separated vortex whose strength is determined by the Polhamus leading-edge suction analogy and whose location is given by delta wing empirical data (vortex option 1), are shown by the solid line. For reference, drag upper and lower bounds are also shown. The theoretical lower bound $C_{D,0} + (C_L^2/\pi AR)$ is the drag for a wing with an elliptical span load distribution and full

theoretical leading-edge thrust. A theoretical upper bound $C_{D,0} + C_L \tan(C_L/C_{L\alpha})$ is the drag for a flat wing with no leading-edge thrust and no vortex forces. The drag at $\alpha = 0^\circ$ for a flat wing $C_{D,0}$ was obtained from experimental data wherever possible.

11.1 Aspect Ratio 2 Wing–Body

A comparison of code results with experimental data from reference 19 for both a flat and a twisted and cambered delta wing of aspect ratio 2 in combination with a simple body of revolution is shown in figure 23. The wing incorporated a symmetrical 5-percent-thick NACA 0005-63 airfoil section. The twisted and cambered wing was designed for a trapezoidal spanwise load distribution at a Mach number of 1.53 and a design lift coefficient of 0.25. The data presented are for a Mach number of 0.61 and a Reynolds number of 3.0×10^6 . Input data used in the AERO2S code analysis are given in table I(a). The WINGDES code could also have been used for this example. Theoretical data shown in figure 23 was obtained for JBYMAX = 12 and ELAR = 4.0.

The drag of a flat wing configuration at $\alpha = 0^\circ$, $C_{D,0}$, used in the theoretical analysis was obtained from the axial-force data presented in figure 23(a). A proper value of $C_{D,0}$ will reflect the type of flow (laminar-turbulent balance) present at lifting conditions. The experimental C_D (and C_A) at $\alpha = 0^\circ$ of about 0.005 does not provide such a value. Likely a substantially greater extent of laminar flow is present than at larger lift coefficients. However, as shown in the axial-force plot, an appropriate $C_{D,0}$ can be found by fitting the theoretical curve given by the code to the experimental data over a range of angle of attack near $\alpha = 0^\circ$. The value $C_{D,0} = 0.0073$ given by this process was used in the theoretical predictions. See reference 7 for a more complete discussion of the process used to find $C_{D,0}$ from experimental data and examples of its application in theoretical-experimental correlations.

In examining the axial force for the flat wing, nearly full thrust is seen to develop over only a small range of angle of attack, and only a small portion of the theoretical thrust develops at the largest angles shown. The present method gives a reasonable estimate of the thrust actually produced. Because of the failure to produce thrust, a separated leading-edge vortex would be expected which in turn would produce a nonlinear increase in normal force. The normal-force data indicate that such a vortex force actually is present and is predicted by the present method. The present method is seen to provide a good estimate of the lift-drag performance of this wing–body combination. The limits for no thrust and full thrust provide a broad range of aerodynamic performance possibilities, and thus a reasonably accurate

determination of attainable thrust is a critical part of the estimation process.

For the twisted and cambered wing (fig. 23(b)), the axial-force curve is quite different. It is no longer symmetrical and has more negative values of the coefficient at moderate and large angles of attack. The theory indicates that even without thrust, negative values of axial force could be achieved. As might be expected, for equal values of theoretical thrust, the fraction attainable for the cambered wing is not much different than that for the flat wing. The experimental increment in axial force at $\alpha = 0^\circ$ is seen to be larger than the increment predicted by the code. As for the flat wing, there is a vortex contribution to the normal force. Again the theoretical and experimental data have good correlation.

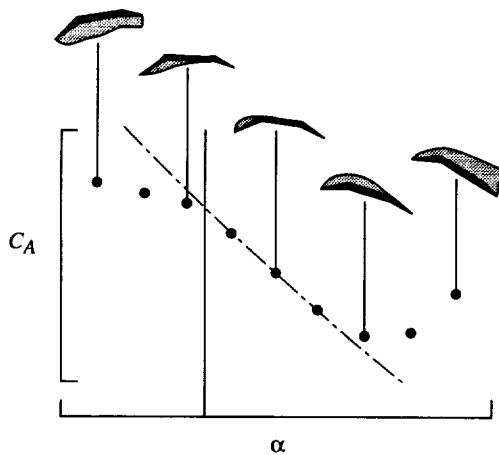
11.2. Cranked-Wing Supersonic Fighter

Reference 20 provides subsonic maneuver performance data for a cranked-wing supersonic fighter configuration that employs deflected flaps rather than wing twist and camber to enhance performance at high lift coefficients. Data were obtained for a matrix of leading- and trailing-edge flap deflection angles so that maximum suction parameters and optimum flap settings can be ascertained and compared with theoretical predictions. The wind tunnel tests were conducted in the Langley 7- by 10-Foot High-Speed Tunnel at Mach numbers of 0.30, 0.50, and 0.70. The experimental-theoretical correlations presented in the present report are for data gathered at a Mach number of 0.50 and a Reynolds number of 2.9×10^6 . The presence of flaps dictates the use of the AERO2S code, and the AERO2S input data are given in table I(b).

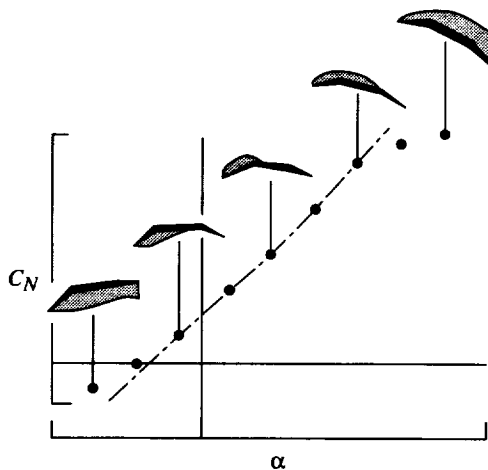
Figure 24 provides representative data for the longitudinal aerodynamic characteristics for the flap system depicted in the sketch at the top of the figure with leading-edge flap deflections of 0° , 15° , and 30° and trailing-edge flap deflections of 0° , 10° , and 20° . The flap deflection pairings shown in figures 24(a), (b), and (c) were selected to give near optimum performance (subject to limitations imposed by the constant leading-edge deflection angle measured normal to the flap hinge line) at lift coefficients of about 0, 0.4, and greater than 0.8, respectively.

The theory generally predicts the measured performance reasonably well for the undeflected and moderately deflected flaps (figs. 24(a) and (b)). However, for the severely deflected flaps (fig. 24(c)), noticeable discrepancies appear between experiment and theory for both high and low lift coefficients. The following discussion helps explain the sources of discrepancies between theory and experiment that can sometimes arise.

In the actual flow about flap systems, there may be serious departures from the idealized flap behavior discussed in section 7 which outlined wing camber surface and flap system design. These departures may be greater than those caused by mild leading-edge flow separation, which permits a predominantly attached flow. An example of the use of axial- and normal-force data in assessing the nature of departures from attached flow with vortex separation as calculated by the AERO2S computer code may be described with the aid of sketches 11-1 and 11-2. These data represent a wing-flap system that is operating in a predominantly attached-flow manner for the middle portion of the range of angle of attack shown. However, more severe flow separation occurs at higher and lower angles of attack. At an angle of attack large enough to cause the separated flow on the upper surface to reattach aft of the leading-edge flap hinge line but ahead of the trailing edge, a decrease in distributed thrust on the leading-edge flap surface and an increase in axial force



Sketch 11-1



Sketch 11-2

occur; however, there is little or no loss of normal force. At angles of attack large enough to prevent reattachment ahead of the trailing edge for much of the wing, a loss of normal force as well as an increase in axial force occurs. These changes bring about drastic losses in performance. At an angle of attack sufficiently low to cause a separation on the lower surface that originates at the wing leading edge and reattaches ahead of the trailing edge, axial force is reduced but normal force has little or no change. For this situation, performance with separated flow may be better than theoretical performance with attached flow. At even lower angles of attack, the separated flow may not reattach ahead of the trailing edge and the normal force is more positive than for attached flow. In the numerous examples of theoretical and experimental data correlation given in references 3, 4, and 9, there is only limited evidence (primarily the present case) of separation at high angle of attack for reasonably efficient flap systems at lift coefficients below about 0.8. An analysis conducted in reference 3 indicated that $\delta_{le,n} = 20^\circ$ and $\delta_{te,n} = 15^\circ$ would be more nearly optimum for the $C_L = 0.8$ design condition. This example with $\delta_{le,n} = 30^\circ$ and $\delta_{te,n} = 20^\circ$ was chosen specifically to demonstrate the nature and causes of discrepancies that can occur. The collection of theoretical-experimental correlations in the references showed many examples of separation at low angles of attack for highly deflected flaps.

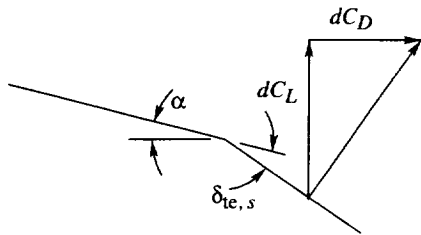
The data in reference 20 provide sufficient information for the construction of an experimental performance map for comparison with an analysis code performance map as shown in figure 25. The contours represent suction parameters for a lift coefficient of 0.45. The code predicts reasonably well the peak suction parameter and the deflection angle at which it occurs. Both leading- and trailing-edge deflections are required for peak performance. At the larger leading-edge flap deflection angles, the experiment shows poorer performance, perhaps because of hinge-line separation. Also, a poorer measured performance occurs for the wing with undeflected flaps than is predicted by the code. This discrepancy may be caused by, at least in part, a failure of the leading-edge separated flow to reattach ahead of the wing trailing edge, particularly on the wing outer panel. The important point, however, is that at $C_L = 0.45$ the flap system performance almost matches theoretical expectations; this indicates that the flow there is predominantly attached.

The behavior of the contour map data for this wing points out a difference in the effects on performance of separated flow in the leading-edge flap region and separated flow in the trailing-edge flap region. Flow separation from the trailing-edge flap surface is much less likely to cause performance penalties than flow

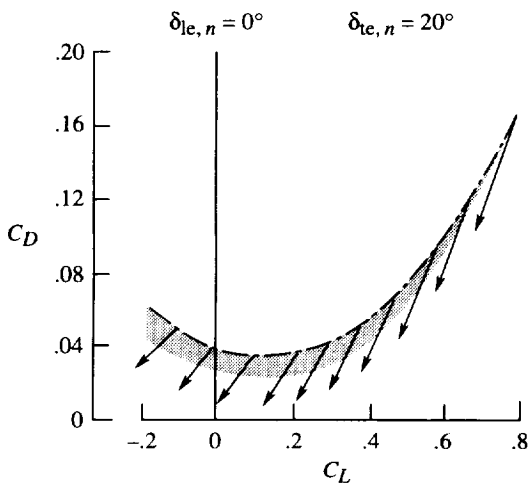
separation from the leading-edge flap surface; this can be illustrated through the use of sketches. Sketch 11-3 shows the relationship between lift and drag changes on the wing as a whole to be the result of a change in the trailing-edge flap loading. If changes in flow conditions such as those induced by changes in Reynolds number cause loading changes restricted to the flap itself, incremental changes in lift and drag are related according to the expression

$$\frac{dC_D}{dC_L} = \tan(\alpha + \delta_{te,s})$$

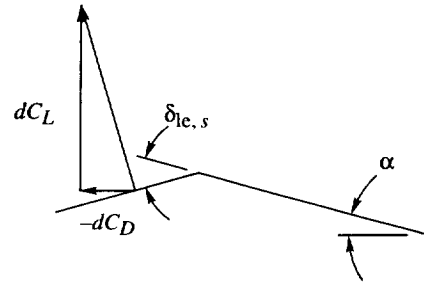
These considerations cause a loss in flap loading due to separation to bring about a loss in lift, which is accompanied by a decrease in drag. The net result is that the lift-drag ratio for an optimally deflected flap at a given lift coefficient is changed very little. An illustration of the effect of trailing-edge flap separation for the present configuration is given in sketch 11-4. The arrows show the direction of the relative change in lift and drag caused by a loss in loading on the trailing-edge flap itself. The hatched area indicates the magnitude of the change if 50 percent of the theoretical loading is lost. With no leading-edge flap deflection, the trailing-edge flap deflection of 20° is optimum for a $C_L \approx 0.8$. At this



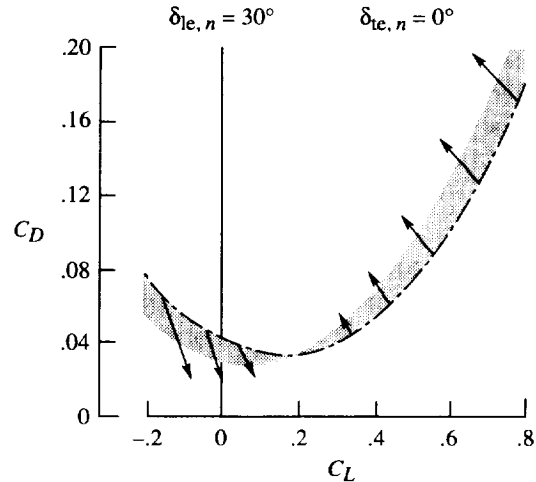
Sketch 11-3



Sketch 11-4



Sketch 11-5



Sketch 11-6

condition, changes in lift and drag tend to occur along a tangent to the polar curve; thus, little or no performance penalty occurs. Actually, penalties (drag increases) occur only for the lift coefficients in excess of 0.8. For lift coefficients less than that at which the deflection is optimum, the separation brings about a decrease in drag, an effect noted in the experimental data. This drag reduction is relative to the excessive drag of a surface deflected beyond the optimum for that lift coefficient. Separation would not be expected to lead to a drag lower than that of an optimally deflected surface.

The relationship between lift and drag changes on the wing as a whole because of a change in leading-edge flap loading alone, illustrated in sketch 11-5, may be expressed as

$$\frac{dC_D}{dC_L} = \tan(\alpha - \delta_{le,s})$$

Because of the negative sign, a loss in lift coefficient caused by a reduction of leading-edge flap loading is generally accompanied by an increase in drag. When applied to the present example, changes such as those shown in sketch 11-6 result. The arrows show the

relative change in lift and drag caused by a loss in loading on the leading-edge flap itself, and the hatched area indicates the magnitude of the change if 50 percent of the theoretical loading is lost. Obviously, severe penalties are associated with the failure of the leading-edge flap to produce the anticipated loading.

11.3. Subsonic Transport

The data of reference 21 provide an opportunity to compare AERO2S code results with measured data for a highly efficient subsonic transport configuration. Generally little need exists for application of the attainable thrust prediction method to such a design as this which is expected to develop almost all the theoretical leading-edge thrust. The example, however, serves to demonstrate the applicability of the method to a continuum of designs from ones certain to generate extensive separated flow as in the previous example to ones almost certain to maintain fully attached flow.

Data for the subsonic transport wing-body tested at a Mach number of 0.55 and a Reynolds number of 2.25×10^6 is shown in figure 26(a). AERO2S code input data are listed in table I(c). The WINGDES code also is capable of handling this example. Generally theory and experiment have good agreement for all data shown except pitching moment. The axial-force data follow a curve corresponding to full theoretical leading-edge thrust over the whole range of angle of attack shown. Some of the pitching-moment discrepancy may be attributable to a rather large strut used to mount the model. Data for a more complete configuration with a horizontal and vertical tail are shown in figure 26(b). The only difference in the theory shown in the two parts of the figure is because of an estimated increase in $C_{D,0}$ of 0.0042 caused by addition of the tail surfaces.

11.4. Supersonic Transport Wing

Data from reference 22 for a supersonic transport wing tested at a Mach number of 2.40 and a Reynolds number of 3.4×10^6 are shown in figure 27. Results for a flat wing in figure 27(a) may be compared with results for a twisted and cambered wing designed for a Mach number of 2.4 and a lift coefficient of 0.08 without constraints on leading-edge pressures. The selected design lift coefficient was chosen through use of a rule of thumb in an effort to maximize performance at a cruise C_L of 0.12. The supersonic test Mach number requires that the theory be obtained through the use of the WINGDES code (in its evaluation mode) rather than the AERO2S code which was used for the previous examples. Code input data are given in table II(a).

As shown in figure 27(a), for the flat wing there is a good prediction of all the aerodynamic characteristics,

even pitching moment. For the twisted and cambered wing (fig. 27(b)) the prediction is still good. But as shown in the suction parameter plot, employment of the empirical estimate feature of the code (which is described in detail in section 9.9) brings about a slight improvement in prediction of the lifting efficiency. Note that the suction parameter reaches a maximum near the intended cruise lift coefficient of 0.12.

11.5. Supersonic Transport Wing-Body-Horizontal Tail

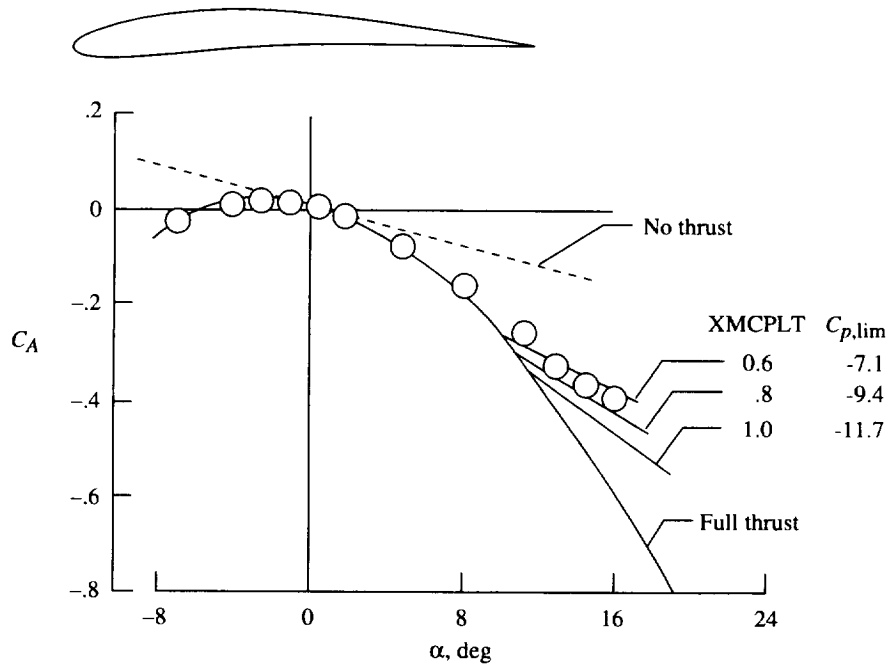
The application of the computer code to a highly swept arrow wing supersonic transport with a horizontal tail may be examined with the aid of figure 28. Experimental results for this configuration were obtained from reference 23. The wing is twisted and cambered for supersonic cruise at a Mach number of 2.20 (wing W_2 of ref. 24) and is equipped with leading- and trailing-edge flaps. The leading-edge flap is full span and is broken into six segments. The trailing-edge flap system is composed of inboard and outboard segments of single-slotted flaps (ref. 24). AERO2S code input data are given in table I(d). The tests were run in the Langley 30- by 60-Foot Tunnel at $M = 0.09$ and $R = 4.19 \times 10^6$ (based on \bar{c}).

The data shown in figure 28(a) are for undeflected leading- and trailing-edge flaps. The horizontal tail deflection is -5° which was found to be a near optimum setting for drag minimization. The theory gives a good prediction of aerodynamic characteristics with the exception of pitching moment for lift coefficients greater than 0.04. The axial-force calculations show the effect of the attainable leading-edge thrust, and the normal-force calculations show the effect of the vortex force. The mildness of the wing twist and camber is shown by the slight slope in the axial force without attainable leading-edge thrust and vortex force.

The data for deflected leading- and trailing-edge flaps in figure 28(b) show a considerable increase in lifting efficiency for lift coefficients of about 0.5 to 0.7 (suction parameters of 0.65 or more). The drag and suction parameter are well predicted in spite of some discrepancies in axial- and normal-force correlation. Again, pitching moment is not well predicted. Reference 4 provides a more detailed study of the prediction of the aerodynamic performance of this and other configurations with two lifting surfaces.

11.6. Two-Dimensional Airfoil

The AERO2S code has recently been modified to provide a solution for two-dimensional airfoil sections. The primary purpose of the modification is to provide a simplified means of recalibrating the method for



Sketch 11-7

predicting attainable thrust should the need and opportunity arise. The procedures used to conduct such a recalibration are thoroughly discussed in reference 7 and are treated briefly in appendix A.

To illustrate the use of this code feature, an NACA 4409 airfoil has been subjected to a code analysis. The airfoil description and test data are taken from reference 25. In the development of the attainable thrust method only symmetrical airfoils were employed, and that restriction is still recommended. However for this example, an airfoil with camber was selected to show that, if necessary, such airfoil data are also applicable. The code input data are presented in table I(e), and code results are compared with experimental data in sketch 11-7. As shown in the sketch, code results were obtained with values of XMCPLT of 1.0, 0.8, and 0.6. The object of this exercise is to find the limiting pressure curve which best matches the experimental data in the vicinity of the breakaway from the full thrust curve. For this example $C_{p,lim} \approx -8.5$ becomes a candidate to replace $C_{p,lim} \approx -11.7$ now used in the attainable thrust method for a Mach number of 0.06 and a Reynolds number of 8.0×10^6 . The section camber causes the slope in the no-thrust axial-force curve. This slope results in some additional uncertainty regarding the curve fit and the selection of the appropriate limiting pressure to match the experimental data. A collection of data such as these covering various airfoils and a wide range of Mach numbers and Reynolds numbers could provide a new and

hopefully more accurate calibration of the attainable thrust system.

12. Examples of Design for Aerodynamic Performance Optimization

In section 11, which dealt with prediction of aerodynamic performance, the AERO2S code was employed for all examples except those for supersonic Mach numbers. The design examples treated in this section require use of the WINGDES code. Only for one example, which requires evaluation of a previously designed low-speed flap system, is the AERO2S code employed.

12.1. Supersonic Transport Cruise Surface Design

As an example of the use of the WINGDES code in the design mode, the supersonic transport configuration shown in figure 29 has been subjected to a multistep design process. This configuration was derived from the SST wing treated in section 11.4. The process begins with a standard wing design for a supersonic cruise Mach number of 2.40 and a lift coefficient of 0.12. This step is followed by a design of a wing reflex surface to take advantage of the nacelle pressure field at the supersonic cruise Mach number. Next, in section 12.2 the reflexed wing surface designed for supersonic cruise is subjected to a mission adaptive (or restricted area) design to define a candidate flap system for a subsonic design point, $M = 0.30$ and $C_L = 0.6$. Finally the AERO2S code is

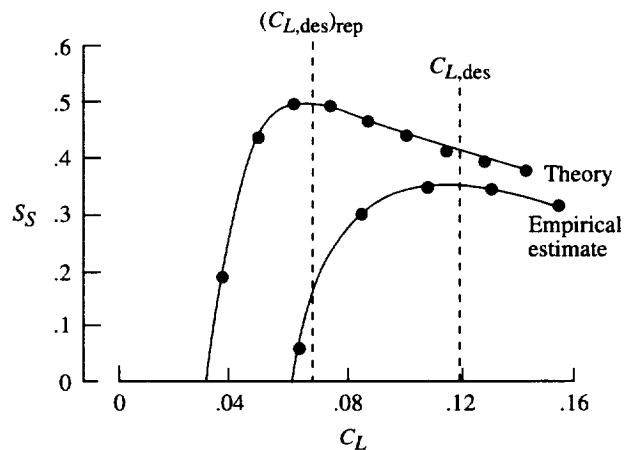
employed to create a performance contour map showing the effect of variation of flap settings on subsonic performance.

As a first step, the wing-body planform of figure 29 was subjected to a design for a cruise Mach number of 2.40 to optimize the aerodynamic performance for $C_{L,des} \approx 0.12$ with no moment restraint. The WINGDES code input is shown in table II(b). This design is characterized as a "whole-wing design." The design starts with a flat wing ($z = 0$ everywhere), and all regions of the planform are free to be reshaped as necessary. Much of the required code input data such as the initial camber surface and the selection of candidate design surfaces is covered by code defaults. The supersonic empirical design corrections described in reference 6 are also implemented as part of the default.

The critical parameters of the design are shown in figure 30. At the top of the figure is shown a plot of angle of attack as a function of spanwise position. (The plot shows 37 spanwise locations rather than 40, as might be expected, because the input JBYMAX of 40 was reduced by a code automatic feature to keep the total number of elements within code limits.) As explained in section 7, the purpose of the design is to match the upper limit of the range of full thrust ($\alpha_{zt} + \Delta\alpha_{ft}$) with the angle of attack corresponding to the design lift coefficient. In this way, theoretical leading-edge thrust that is not realized as attainable leading-edge thrust is recovered as a distributed thrust on the wing camber surface, primarily in the region just behind the leading edge. For this supersonic design, which employs an empirical correction discussed in section 9.9, $(C_{L,des})_{rep}$ is given by $K_{des}C_{L,des}$ with $K_{des} = 0.57$, and the angle of attack for the replacement design lift coefficient is about 2.7° . The plot shows that the design matchup has essentially been achieved. The large spread of the range of full thrust for the inboard stations simply shows that little or no modification of the input surface is required there. The suction parameter plot (middle of fig. 30), however, indicates that the performance at the cruise lift coefficient could be improved to a slight degree by a redesign which would place the maximum S_S closer to $C_{L,des}$. Actually for this design problem, retaining the first design would be advisable because of the advantage of its relatively mild camber surface and the very slight gain a more severe surface might produce in practice. However, to illustrate the use of the adjustment procedure for cases where it may be required, a revised design has been undertaken. The plot of leading-edge surface weighting factors (bottom of fig. 30), given as a part of the code output, shows the factors used in the design and also shows revised values that should lead to improved performance. Because there are inherent inaccuracies in the numerical solution, and because the code-recommended values would lead to

surface irregularities, a fairing of these data is used instead. The fairing as shown by the dashed line was used in a redesign with the data of table II(c) being substituted for the data of table II(b). For this rerun, code-calculated leading-edge surface factors are replaced by those given in the TAFIX table; otherwise the design process is the same. The results of the revised design are shown in figure 31. Figure 31(a) shows the new design parameters and figure 31(b) shows the wing camber surface generated by the code. The peak suction parameter shown in figure 31(a) has not been increased, but it does occur closer to the cruise lift coefficient. The computer-generated plots of the wing surface show a relatively small amount of twist and camber.

The wing design may also incorporate a reflexed trailing-edge surface to take into account the presence of an interference pressure field induced by nacelles or other components which are not considered as variables in the design process. To implement this option, the user must supply the pressure field information and specify an index ($ICP = 1$) to indicate that an interference pressure field is to be taken into account. The user must also specify wing trailing-edge design surfaces corresponding in general to the areas of the wing influenced by the pressure field. An example of the code input for such a design is given in table II(d). The only differences between this table and table II(b) are the entries required to substitute a design incorporating reflexing for a standard design. Results for this design, shown in figure 32, are similar to results for the initial whole-wing design shown in figure 30. When the A_{1e} fairing of figure 32 is employed in a redesign, the peak suction parameter given by the empirical estimate occurs close to the cruise lift coefficient as shown in sketch 12-1. At the cruise lift coefficient of 0.12, the corrected suction parameter given by the code is about 0.34, which is less than the value of



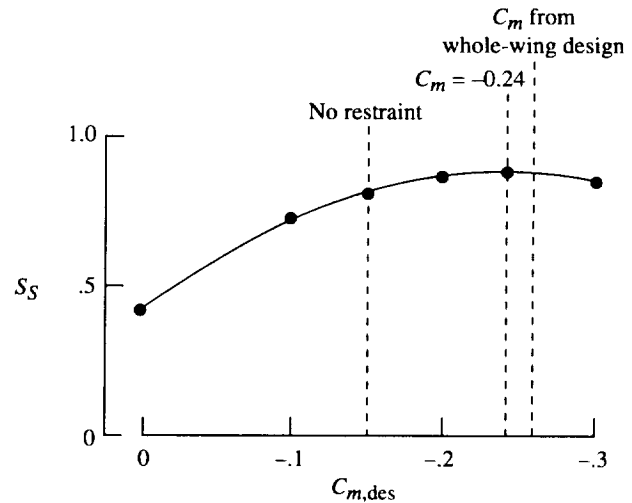
Sketch 12-1

0.37 for the previous design which did not include the interference pressure field. The code evaluation of the suction parameter does not include the beneficial effect of the increase in lift caused by the pressure field. If the increase in lift had been taken into consideration, the suction parameter would have been greater than 0.40, an obviously optimistic value. Proper values of lift, drag, and suction parameter for the more complete configuration can be found only if all forces generated by the additional component are taken into account. In the absence of accurate axial-force as well as normal-force increments, exclusion of both increments can be expected to give a more realistic performance estimate than inclusion of one or the other. A pictorial representation of the reflexed wing surface design is given in figure 33.

12.2. Supersonic Transport Low-Speed Flap Design

An attractive feature of the WINGDES code is the capability for performing runs in succession. For example, a supersonic design run could be followed by an evaluation of that surface at other Mach numbers—either supersonic or subsonic—or a second design run. An example of a supersonic surface design with nacelle reflexing followed by a subsonic design to determine a mission adaptive surface and flap deflections to approximate that surface is given. Table II(e) shows the code input for the supersonic reflex surface design treated earlier but now with provision for a subsequent run for the design of a flap system for a subsonic Mach number of 0.30 and a lift coefficient of 0.6. Note the quantities that must be reset when consecutive design runs are performed as specified in appendix B. The supersonic design input of table II(e) is the same as that of table II(d) with the exception of the TAFIX table addition, which is very similar to the TAFIX table used in the whole-wing design.

For the subsonic mission adaptive surface design, $C_{m,des} = -0.24$ is imposed. For mission adaptive designs, it is always advisable to employ a $C_{m,des}$ that has been selected carefully. Applications of the mission adaptive design option have shown that the numerical solutions tend to call for greater use of leading-edge surfaces and less use of trailing-edge surfaces than would a true optimum design. The problem does not arise to any appreciable extent for the whole-wing design but does affect results for the mission adaptive design, where relatively large surface slopes are needed to generate the required loadings on restricted areas. An improved design can be found by running the mission adaptive design code for a selected series of design pitching-moment coefficients and using a plot such as that shown in sketch 12-2. The unrestrained design provides a suction parameter of



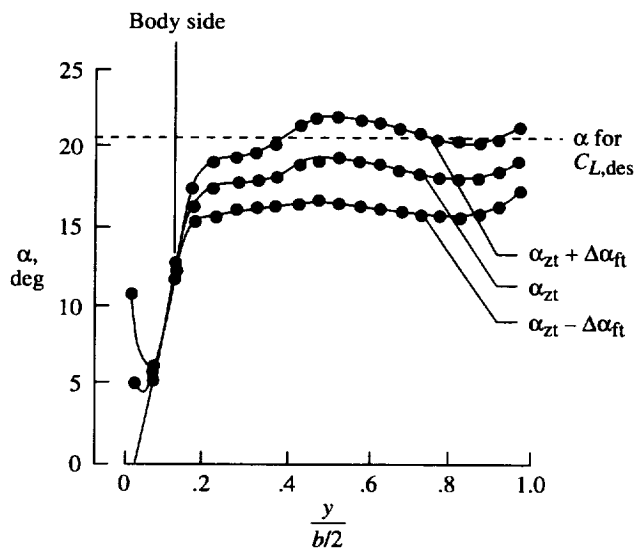
Sketch 12-2

about 0.80 and $C_{m,des} \approx -0.15$, whereas an optimum suction parameter of about 0.87 occurs for $C_{m,des} = -0.24$. This large negative moment might present a trim drag problem in an airplane design project. When horizontal tail contributions or canard trim contributions are considered in the definition of a desired wing moment coefficient and when that moment is specified as a wing design code input, a better overall design should result. Then the previously described search for optimum performance of the wing alone is avoided. An alternate selection of a design pitching moment can be obtained by using C_m generated by a whole-wing design (with either a flat surface or the supersonic cruise surface as an input) at $C_{L,des}$. This procedure gives $C_{m,des} \approx -0.26$.

For this design, $C_{m,des} = -0.24$ was used. Results of the subsonic mission adaptive surface design are shown in figure 34. These data show the leading-edge α matchup, an indicated maximum suction parameter of 0.88, and the leading-edge factors as used and as suggested for redesign. This pair of back-to-back runs was repeated with a TAFIX table for the subsonic design as represented by the dashed line. For this example, the selected fairing of the leading-edge surface weighting factors is only slightly greater than the as-used values because the leading-edge matchup conditions were almost met and because the suction parameter at $C_{L,des}$ is only slightly less than the maximum. Wherever possible, design surfaces more severe than necessary should be avoided. Results of this repeat run are shown in figure 35. As shown in figure 35(a), the leading-edge α matchup and the suction parameters are changed only slightly from figure 34. Note the design fails to completely match the design angle of attack at inboard span positions near the wing-body juncture. This problem is associated with the small number of spanwise elements.

As shown in sketch 12-3, a new design doubling the spanwise elements ($JBYMAX = 20$) gives a much better matchup in the region of the wing-body juncture. However, with present code limitations, this increase in spanwise representation can be accommodated only with a decrease in element aspect ratio and a corresponding decrease in chordwise shape representation. When technology advances permit, an increase in the number of elements the code can handle would be highly recommended. The computer-generated plot of figure 35(b) shows a mission adaptive design surface much more severe than the mild supersonic cruise surface. At the bottom of figure 35(a) is shown the leading- and trailing-edge flap deflections provided by the code to approximate the designed mission adaptive surface. The solid line represents selected flap segmentation and deflection schedules for use at the subsonic design conditions.

The final step in this exercise involving the SST design is an evaluation of the performance of the flap system at the subsonic design conditions. For this purpose, the AERO2S code must be used. An example of the required input is shown in table I(f). Results of the flap system evaluation for the nominal flap deflection schedules of figure 35 are shown in figure 36. As shown at the top of the figure, the upper limit of the range of full thrust falls short of the angle of attack for $C_{L,des} = 0.6$ by 5° or more; this is in contrast to the matchup for the mission adaptive surface. This difference is to be expected because the flaps are only a poor approximation of the camber surface. The idea is to balance flow separation tendencies at the leading edge with those at the hinge line so that separation is not excessive at either location. The



Sketch 12-3

mismatch of 5° at the leading edge is expected to result in the formation of separated leading-edge vortices. But the separation is hoped to be mild enough so that reattachment occurs at or ahead of the hinge line and performance losses relative to fully attached flow are small. The suction parameter plot shows a suction parameter of about 0.77 at $C_{L,des} = 0.6$. This value is significantly less than the value of 0.88 for the continuous mission adaptive surface but nevertheless is a reasonable level for flap system performance.

Multiple additional runs using input data such as those of table I(f) with other values of flap deflection angles can be used in the construction of performance contour maps as illustrated in figure 37. The deflection angles are defined as those whose tangents are obtained by multiplying the tangents of the nominal angles by a set of factors, 0, 0.5, 1.0, 1.5, and 2.0. The map of figure 37(a) was obtained by applying these factors to the nominal leading- and trailing-edge flap deflection schedules to create input data for a series of code runs. Construction of this map required 16 individual runs. The 5 by 5 matrix does not require 25 individual runs because, as described in appendix A, a single run which utilizes TXMLEFD and TXMTEFD values of 0.0 gives valid data for 4 data points (the nominal leading-edge deflections in combination with the nominal trailing-edge deflections, the nominal leading-edge deflections in combination with zero trailing-edge deflections, the nominal trailing-edge deflections in combination with zero leading-edge deflections, and zero deflection of both leading and trailing edges).

If desired, a full set of data for the construction of contour maps can be obtained in a single run. For this purpose, a full set of TXMLEFD and TXMTEFD values (5 values of each) may be employed in that one run. The results, however, are not as accurate as those of the multiple run process. A map constructed in this way for the same configuration is shown in figure 37(b). Some obvious discrepancies are seen, particularly for leading-edge deflection factors greater than 1.0. This discrepancy is clearly an example of a case where the simple single run approach is not applicable and should have been anticipated since leading-edge flap deflections are as high as 56° . The single run approach has been used successfully for smaller deflection angles—angles small enough so that there is little difference between the tangent of the angle and the sine of the angle. When in doubt, the safe approach is to use multiple runs.

The contour map obtained from multiple runs in figure 37(a) shows, for $C_{L,des} = 0.6$, a maximum suction parameter of about 0.77 for a leading-edge flap deflection factor of about 0.8 and a trailing-edge flap deflection

factor of about 1.2. Thus, for this example, the optimum flap settings for $C_L = 0.6$ are estimated to be

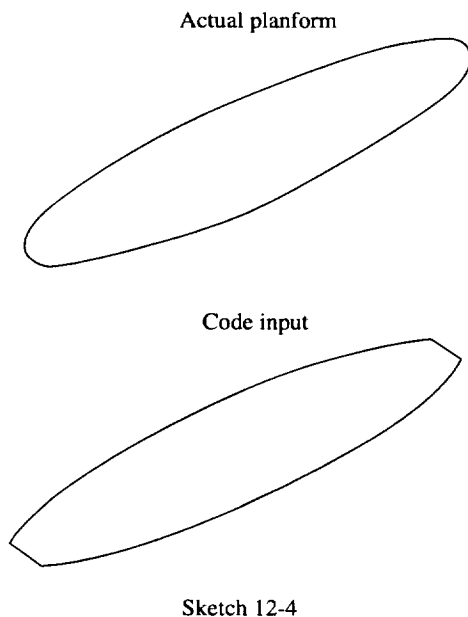
$$\delta_{le,s} \approx 21^\circ/26^\circ/30^\circ$$

$$\delta_{te,s} \approx 16^\circ/16^\circ/19^\circ$$

This map also has contour lines for pitching-moment coefficients to enable selection of optimum flap settings subject to constraints.

12.3. Nonsymmetrical Wing Cruise Surface Design

A relatively new addition to the WINGDES code is the capability for the design of optimized surfaces for nonsymmetrical wings such as that shown in sketch 12-4. As an example of nonsymmetrical wing design, an optimum surface for this elliptical planform was designed for a lift coefficient of 0.16 at a cruise Mach number of 1.40. Code input data are shown in table II(f). The rolling moment was constrained to be zero about an assumed center of gravity at the midspan. Figure 38 shows the design results. Figure 38(b) presents a computer drawing of the wing camber surface. This surface displays considerable camber and a pronounced twist distribution to take advantage of the increasing upwash along the leading edge. The plot of angle of attack at the top of figure 38(a) shows a close matchup of the upper limit of the range of full thrust with α for $(C_{L,des})_{rep}$. The small part of the span that has a zero range of full thrust results from the local supersonic leading edge. As shown in the middle plot, a maximum suction parameter for the curve with the empirical correction occurs at a lift coefficient just below $C_{L,des}$. For this design there is no need for a redesign



with modified leading-edge surface weighting factors. As shown at the bottom of the figure, the code solution gives a nearly elliptical span load distribution. The AERO2S code has recently been modified to provide the capability for analysis of a nonsymmetrical wing.

13. Concluding Remarks

A pair of computer codes, AERO2S and WINGDES, is now widely used for the analysis and design of airplane lifting surfaces under conditions that tend to induce flow separation. These codes have undergone continued development to provide additional capabilities since the introduction of the original versions over a decade ago. This code development has been reported in a variety of publications (NASA technical papers, NASA contractor reports, and journal articles). Some modifications have not been publicized at all. Users of these codes have suggested the desirability of combining in a single document, descriptions of the code development, an outline of the particular features of each code, and suggestions for effective code usage. This report is intended to supply that need.

This report describes the development of numerical solutions of linearized theory for both subsonic and supersonic speeds that are performed by iteration (rather than by matrix inversion) and thus are easily adaptable to provide increased accuracy as more advanced computers become available. Another important feature of the theoretical solutions is a separation of loading components with and without the presence of singularities, so that each may be handled in an appropriate manner to increase the accuracy of integration techniques used to evaluate forces and moments. The numerical solutions also provide for the estimation of attainable leading-edge thrust which has a powerful effect on the aerodynamic lifting efficiency that can actually be achieved.

Discussions of the application of the computer codes to problems of practical interest show how attached flow theoretical predictions are actually applicable to flows with detached regions provided that the separation is mild and localized. Code results are shown to be more accurate for configuration arrangements which, through the use of wing twist and camber or flap systems, promote predominantly attached flows and high levels of aerodynamic efficiency. Design features of the codes permit the definition of efficient wing camber surfaces and flap system deflection schedules to minimize separation and maximize performance.

NASA Langley Research Center
Hampton, VA 23681-2199
April 8, 1997

Appendix A

AERO2S Code Input and Output

The AERO2S computer code is written in generic FORTRAN 77 for use on virtually any computer system with a Fortran compiler having namelist capability. The first record in the input is a code run identification (title) that accepts up to 80 characters. The remainder of the input is placed in namelist format under the name INPT1. The code is constructed so that successive runs may be made with a given code entry. To make additional runs, it is necessary only to add an identification record and namelist data that are to be changed from the previous run.

A1. Wing Planform—Required Input

The wing planform information is specified by a series of leading-edge and trailing-edge breakpoints for a right-hand wing panel. Up to 30 pairs of coordinates may be used to describe the leading edge and up to 30 pairs to describe the trailing edge. The planform input data in code terminology are as follows:

NLEY	number of leading-edge breakpoints (limit of 30)
TBLEY	table of leading-edge y values; beginning at $y = 0$; increasing order of y from root to tip
TBLEX	table of leading-edge x values that corresponds to TBLEY table
NTEY	number of trailing-edge breakpoints (limit of 30)
TBTEY	table of trailing-edge y values; beginning at $y = 0$; increasing order of y from root to tip
TBTEX	table of trailing-edge x values that corresponds to TBTEY table
XMAX	largest x ordinate anywhere on planform; includes second surface if present
SREF	wing reference area for use in aerodynamic force and moment coefficients
CBAR	wing reference chord for use in aerodynamic moment coefficients
XMC	x location of moment reference center
JBYMAX	integer designating number of elements in spanwise direction (limit of 41)
ELAR	element aspect ratio

The size of the wing in code dimensions is controlled by the entry JBYMAX. The necessary scaling is done within the code by use of a scale factor $2(JBYMAX)/\beta y$.

The number of complete wing elements N corresponding to a given JBYMAX may be approximated as

$$N = 4(JBYMAX)^2 \left(\frac{ELAR}{AR} \right)$$

The code has been written to accommodate 4000 right-hand panel elements. Generally, the JBYMAX integer is much less than the limit of 41. The normal range is 8 to 20. Computational costs tend to increase as the square of the number of elements.

For flat and mildly cambered wings, an element aspect ratio approximately equal to the full-wing aspect ratio is recommended. For small chord leading- or trailing-edge flaps, the use of a large element aspect ratio may be necessary to place two or more elements within the chord. The number of elements in a given chord, c_{le} or c_{te} , may be approximated as

$$N = \frac{c_{le}}{b/2} (JBYMAX)(ELAR)$$

or

$$N = \frac{c_{te}}{b/2} (JBYMAX)(ELAR)$$

Because computational costs tend to increase as the fourth power of JBYMAX and the second power of ELAR, an increase in the element aspect ratio is the more efficient means of providing improved definition.

A2. Wing Planform—Optional Input

The code permits the design or analysis of an asymmetrical lifting surface. For this option, the spanwise geometric data (i.e., TBLEY, TBTEY, TBYC, TBYR) are input from wingtip to wingtip as positive values beginning at a span station of zero. The entire wing is confined to what otherwise would be only a right-hand panel. To implement this feature, input the index

NSYM nonsymmetrical planform index (set this index to 1 for asymmetrical planform, code defaults to 0 to provide a symmetrical planform by construction of additional mirror image left-hand panel)

A3. Wing Camber Surface—Required Input

The wing mean camber surface must be specified by exactly 26 chordwise ordinates at up to 52 span stations. When fewer than 26 camber coordinates are used to define the sections, the ordinate tables must be filled with enough zeros to complete the list of 26. The necessary section information is as follows:

NYC	number of spanwise stations at which chordwise sections are used to define mean-camber surface (limit of 52)	= 1 vortex center given by empirical relationships derived from delta wing experimental data (default)
TBYC	table of y values for chordwise camber-surface sections; beginning at $y = 0$; increasing order of y from root to tip	= 2 vortex center given by method of Lan and Chang (ref. 12)
NPCTC	number of chordwise stations used in definition of mean camber surface (limit of 26)	
TBPCTC	table of chordwise stations, in percent chord, at which mean camber surface ordinates are defined; increasing order from leading edge to trailing edge	
TZORDC	table of mean camber surface z ordinates that corresponds to TBPCTC table; full 26 values for root chord (including zeros for values in excess of NPCTC) are given first, followed by similar information for all spanwise stations in increasing order of y	
TZSCALE	multiplying factor applied to TZORDC table to change camber surface ordinates; default 1.0	

The TZORDC table may be multiplied by a scale factor TZSCALE. This factor may be useful if the original tabulated ordinates are nondimensionalized with respect to a single measurement (e.g., the wing root chord) or if it is necessary to evaluate the effect of a change in camber surface severity.

A4. Section Parameters for Attainable Thrust Calculation—Required Input

The following wing section information is required for the calculation of attainable leading-edge thrust and leading-edge separation forces:

NYR	number of spanwise stations at which information on airfoil sections is supplied (limit of 30)
TBYR	table of y values for airfoil section information; beginning at $y = 0$; increasing order of y from root to tip
TBTOC	table of airfoil maximum thickness as fraction of chord, $(\tau/c)_{\max}$
TBETA	table of section locations of maximum thickness as fraction of chord, η
TBROC	table of leading-edge radii as fraction of chord, r/c
IVOROP	vortex location option as follows: = 0 full vortex force acts normal to wing reference plane at wing leading edge; does not contribute to axial force

A5. Flight Conditions—Required Input

The flight or test conditions are specified as follows:

XM	free-stream Mach number
RN	free-stream Reynolds number (based on \bar{c}) $\times 10^{-6}$
NALPHA	number of angles of attack to be calculated (limit of 40)
TALPHA	table of angles of attack to be calculated, deg
NADRN	number of additional Reynolds numbers (default 0)
TADRN	table of additional Reynolds numbers (limit of 3)

The commonly accepted practice of performing subsonic calculations for a Mach number of 0 is not appropriate for this code. Realistic estimates of attainable thrust can be made only if both the Mach number and the Reynolds number correspond to actual conditions. In fact, the code stops and writes an error message when $XM = 0$ is input.

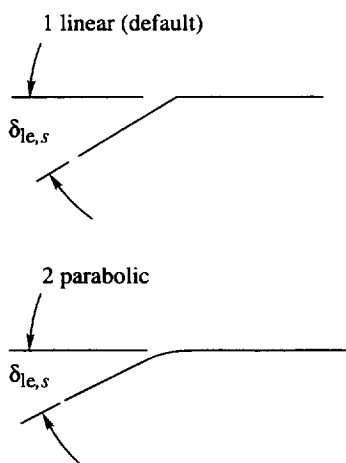
A6. Leading- and Trailing-Edge Flaps—Optional Input

The following information makes possible the calculation of loadings and forces on deflected leading-edge and trailing-edge flaps. If flap data are not desired, simply omit these entries.

NLEFY	number of breakpoints in leading-edge flap chord distribution (limit of 30)
TBLEFY	table of y values at breakpoints in leading-edge flap chord distribution; beginning at $y = 0$; increasing order of y from root to tip
TBLEFC	table of streamwise leading-edge flap chords that corresponds to TBLEFY table
TBLEFD	table of flap deflections in degrees (positive for leading edge down) that corresponds to TBLEFY table

NADLEFD	number of leading-edge flap deflection multipliers other than 1.0 (limit of 4) (default 0)
TXMLEFD	table of leading-edge flap deflection multipliers (applied as multiplier of tangents of input flap deflections)
LEFTYPE	type of leading-edge deflection as shown in sketch A-1
NTEFY	number of breakpoints in trailing-edge flap chord distribution (limit of 30)
TBTEFY	table of y values at breakpoints in trailing-edge flap chord distribution; beginning at $y = 0$; increasing order of y from root to tip
TBTEFC	table of streamwise trailing-edge flap chords that corresponds to TBTEFY table
TBTEFD	table of flap deflections in degrees (positive for trailing edge down) that corresponds to TBTEFY table
NADTEFD	number of trailing-edge flap deflection multipliers other than 1.0 (limit of 4) (default 0)
TXMTEFD	table of trailing-edge flap deflection multipliers (applied as multiplier to tangents of input flap deflections)
CLDES	additional lift coefficient for which flap system aerodynamic performance is to be specified; code aerodynamic characteristics are given only for angles of attack in input TALPHA table unless CLDES is specified

Spanwise tables must begin with $y = 0$ and extend to $y = b/2$ (with chords of 0 where there are no flaps). At spanwise positions where there are discontinuities in



Sketch A-1

either flap chord or deflection, it is necessary to make closely spaced tabular entries inboard and outboard of the discontinuity.

The code requires flap deflection angles measured in the X - Z plane. Flap deflection angles measured normal to the flap hinge line may be converted to code input angles by

$$\delta_{le,s} = \tan^{-1} (\cos \Lambda_{h,le} \tan \delta_{le,n})$$

$$\delta_{te,s} = \tan^{-1} (\cos \Lambda_{h,te} \tan \delta_{te,n})$$

The code provides solutions for wing surfaces composed of all possible combinations of leading-edge and trailing-edge flap settings provided by the original deflections (TBLEFD and TBTEFD) and by the flap deflection multipliers (TXMLEFD and TXMTEFD). Up to 25 pairs of leading-edge and trailing-edge flap deflection schedules may thus be treated simultaneously. Solutions obtained by using the multipliers (values other than 0 or 1) are determined by a perturbation process; thus, they are not as accurate as solutions for the original or nominal input deflections. When increased accuracy is required, or when the change in performance with the change in deflection must be evaluated—as in the construction of suction parameter contour maps—individual solutions without recourse to multipliers are generally required.

The code also provides an improved accounting of hinge-line singularities in determination of wing forces and moments. The technique used is described in appendix B of reference 3. See table I(b) for an example of leading- and trailing-edge flap input data.

A7. Solution Convergence Criteria—Optional Input

To determine lifting-surface perturbation velocity distributions, the code provides for a maximum of 70 iterations. If this number is reached without the convergence criteria being met, the results for the 70th iteration are printed with a warning of the failure to meet the criteria. The maximum number of iterations may be increased or decreased by the entry

ITRMAX maximum number of perturbation velocity iterations (default 70)

The code convergence criteria are met when, for all four wing surfaces and for two successive iterations, the average difference in perturbation velocity between iterations is less than half of 1 percent of the average velocity over the wing. If the average velocity for the camber surface or either of the flap surfaces is less than the average velocity for the flat surface at $\alpha = 1^\circ$, the flat wing surface value is used instead. In many instances, these

criteria may be more stringent than necessary. If desired, the convergence criteria may be changed by the entry

CNVTST perturbation velocity convergence criteria (default 0.005)

A8. Canard or Horizontal Tail—Optional Input

The following set of input data is required for the handling of wing-canard or wing-horizontal tail configurations. If wing-along solutions are desired, simply omit these entries.

ILS2 second surface identifier
 = 0 no second surface (default)
 = 1 canard
 = 2 horizontal tail

If a second surface is employed (ILS2 = 1 or 2), the following planform information must be supplied:

NLEY2 number of leading-edge breakpoints (limit of 21)
 TBLEY2 table of leading-edge y values; need not begin at y = 0; increasing order of y
 TBLEX2 table of leading-edge x values that corresponds to TBLEY2 table
 NTEY2 number of second surface trailing-edge breakpoints (limit of 21)
 TBTEY2 table of trailing-edge y values; need not begin at y = 0 but initial and final values must be same as TBLEX2 initial and final values; increasing order of y
 TBTEX2 table of trailing-edge x values that corresponds to TBTEY2 table

For the second surface, the mean camber surface must be specified by exactly 26 chordwise ordinates at up to 21 span stations. When fewer than 26 camber coordinates are used to define the sections, the ordinate tables must be filled with enough zeros to complete the list of 26. The necessary section information is as follows:

NYC2 number of spanwise stations at which chordwise sections are used to define mean camber surface (limit of 21)
 TBYC2 table of y values for chordwise camber surface sections; increasing order of y
 NPCTC2 number of chordwise stations used in definition of mean camber surface (limit of 26)
 TBPCTC2 table of chordwise stations, in percent chord, at which mean camber surface ordinates are defined; increasing order from leading edge to trailing edge

TZORDC2 table of mean camber surface z ordinates that corresponds to TBPCTC2 table; the full 26 values for the root chord (including zeros for values in excess of NPCTC2) are given first, followed by similar information for all spanwise stations in increasing order of y

TZSCAL2 multiplying factor applied to TZORDC2 table to change camber surface ordinates (default 1.0)

The following canard or horizontal tail section information is required for the calculation of attainable leading-edge thrust and leading-edge separation forces:

NYR2 number of spanwise stations at which information on airfoil sections is supplied (limit of 21)
 TBYR2 table of y values for airfoil section information; increasing order of y
 TBTOC2 table of airfoil maximum thickness as fraction of chord, $(\tau/c)_{\max}$
 TBETA2 table of section locations of maximum thickness as fraction of chord, η
 TBROC2 table of leading-edge radii as fraction of chord, r/c
 YAPEX2 spanwise location of second surface vortex flow-field origin
 For special planforms such as forward-swept surfaces or other surfaces with apex away from centerline, this input can help provide a better estimate of vortex-induced flow fields and forces; default is YAPEX2 = 0.0.
 DELTA2 incidence of second surface with respect to wing reference plane, deg (default DELTA2 = 0.0), positive for leading edge up

See table I(d) for an example of horizontal tail input data.

A9. Optional Two-Dimensional Airfoil Solution

The code has been modified to provide solutions for two-dimensional airfoil sections. As described in reference 7, this capability may be useful in recalibration of the attainable thrust prediction method when additional experimental data covering a wider range of Mach numbers and Reynolds numbers become available. An input of JBYMAX = 1 signals a two-dimensional airfoil solution. For this purpose, tables of airfoil section characteristics defining the camber surface and the thickness distribution with identical listings for a root- and tip-chord station must be provided.

A recalibration of the limiting pressure coefficients used in the attainable thrust prediction method requires

an iterative approach. Repetitive solutions with various values of the following limiting pressure multiplier are required:

XMCPLT limiting pressure multiplier (default 1.0)

This quantity acts as a multiplier of the limiting pressure formula presently used in the code. For each code run, the output listing includes the limiting pressure coefficient used in that run. As described in reference 7, the iteration is continued until the best match of code and experimental axial-force data is obtained. The listed limiting pressure coefficient then becomes a revised value for the specified Mach number and Reynolds number to be used in formulation of new limiting pressure relationships. See table I(e) for an example of two-dimensional airfoil code input.

A10. Code Output Data

The printed code results include

1. Iteration-by-iteration history of convergence parameters
 2. Listing of theoretical pressure distributions for combined camber surface at $\alpha = 0^\circ$ and for combined flat surface at $\alpha = 1^\circ$; for each code spanwise station (controlled by JBYMAX), interpolated or extrapolated pressure coefficients are given for a set of chordwise stations
 3. Listing of spanwise distribution of section normal-force, axial-force, and pitching-moment coefficients for combined cambered surface at $\alpha = 0^\circ$ and for combined flat surface at $\alpha = 1^\circ$; interference axial-force coefficient caused by flat surface loading acting on camber surface and theoretical thrust parameters are also printed
 4. Listing of overall theoretical aerodynamic coefficients C_N , C_A , C_m , and C_D with no thrust and with theoretical thrust as function of angle of attack
 5. Listing of spanwise distribution of flat wing angle-of-attack range for full theoretical leading-edge thrust (for wing-alone solution only)
 6. Listing of overall estimated aerodynamic coefficients including C_N , C_A , and C_m for basic pressure loading, ΔC_N and ΔC_A for attainable thrust and vortex-force increments, and C_N , C_A , C_m , C_L , C_D , and S_S for total loading
- Additional tabulated output data may be selected by using the following print options:
- IPRCPD = 1 theoretical pressure distributions for each selected angle of attack
- IPRSLDT = 1 theoretical span load distribution of C_N , C_A , C_m , and C_D with no thrust and with full theoretical thrust for each selected angle of attack
- IPRSLDA = 1 estimated span load distribution of C_N , C_A , C_m , and C_D with attainable thrust and vortex-force effects for each selected angle of attack
- IPRALL = 1 preceding print control options apply only to first set of flap deflections; select this option if three preceding options are to apply to all flap deflection combinations; selection of this option could result in very large volume of printed output

Appendix B

WINGDES Code Input and Output

The WINGDES code is written in generic FORTRAN 77 for use on virtually any computer system with a Fortran compiler having namelist capability. The first record in the input is a code run identification (title) that accepts up to 80 characters. The remainder of the input is placed in namelist format under the name INPT1. The code is constructed so that successive runs may be made with a given computer entry. To make additional runs, it is only necessary to add an identification record and namelist data that change from the previous run. An additional capability is provided by the entry NEWDES. When the code is run in the design mode and NEWDES is set to 1, a design camber surface is found, the input set of camber surface ordinates is replaced by camber surface ordinates for the new design, and this new design is treated as an evaluation case. In the original code, the default for the entry NEWDES was 0, which provided for a design of the wing surface but not for a subsequent evaluation. Now, however, because this feature was found so useful, the default was changed to NEWDES = 1. When the NEWDES option is used, successive runs may be employed to evaluate the new surface at off-design conditions.

B1. Wing Planform—Required Input

The wing planform information is specified by a series of leading-edge and trailing-edge breakpoints for a right-hand wing panel. Up to 30 pairs of coordinates may be used to describe the leading edge and up to 30 pairs to describe the trailing edge. The planform input data in code terminology are as follows:

NLEY	number of leading-edge breakpoints (limit of 30)
TBLEY (NLEY)	table of leading-edge y values; beginning at y = 0; increasing order of y from root to tip
TBLEX (NLEY)	table of leading-edge x values that corresponds to TBLEY table
NTEY	number of trailing-edge breakpoints (limit of 30)
TBTEY (NTEY)	table of trailing-edge y values; beginning at y = 0; increasing order of y from root to tip
TBTEX (NTEY)	table of trailing-edge x values that corresponds to TBTEY table
XMAX	largest x ordinate anywhere on planform

SREF	wing reference area for use in aerodynamic force and moment coefficients
CBAR	wing reference chord for use in aerodynamic moment coefficients
XMC	x location of moment reference center
ELAR	element aspect ratio (default 1.0 for subsonic cases, $1.0/\beta$ for supersonic cases)
JBYMAX	integer designating number of elements in spanwise direction (limit of 50)

For subsonic speeds, the element aspect ratio ELAR is chosen by the user (default 1.0). At supersonic speeds, a fixed value of $ELAR = 1.0/\beta$ is imposed to avoid computational difficulties, and the user has no option. For flat and mildly cambered wings at subsonic speeds, an element aspect ratio one half the full wing aspect ratio or greater is recommended. For wings with small chord leading-edge or trailing-edge design areas, using a large element aspect ratio may be necessary to place at least two elements within the chord. The number of elements in a given chord, c_{le} or c_{te} , may be approximated as

$$N = \frac{c_{le}}{b/2} (JBYMAX) (ELAR)$$

or

$$N = \frac{c_{te}}{b/2} (JBYMAX) (ELAR)$$

Because computational costs tend to increase as the fourth power of JBYMAX and the second power of ELAR, an increase in the element aspect ratio is the more efficient means of providing improved definition. At supersonic speeds, where ELAR is fixed, the only recourse is to increase JBYMAX. This parameter controls the size of the wing in code dimensions.

The necessary scaling is done within the code by use of a scale factor, $2(JBYMAX)/[SPAN(\beta)]$. The number of complete wing elements N corresponding to a given JBYMAX may be approximated as

$$N = 4(JBYMAX)^2 \left(\frac{ELAR}{AR} \right)$$

The code has been written to accommodate 1000 right-hand panel elements (2000 complete wing elements). Generally, the JBYMAX integer is less than the limit of 50. The normal range is 8 to 20 for subsonic speeds and 20 to 50 for supersonic speeds. Computational costs tend to increase as the square of the number of elements.

B2. Wing Planform—Optional Input

The code permits the design or analysis of an asymmetrical lifting surface. For this option, the spanwise geometric data (i.e., TBLEY, TBTEY, TBYC, TBYR) are input from wingtip to wingtip as positive values beginning at a span station of zero. The entire wing is confined to what otherwise would be only a right-hand panel. To implement this feature, input the index

NSYM nonsymmetrical planform index (set this index to 1 for asymmetrical planform, code defaults to 0 to provide symmetrical planform by construction of additional mirror image left-hand panel)

Also see section B8 for YCG, CRTST, and CRNSYM entries. In addition, often specifying NLEC, TBLECY, and TBLEC input data is necessary rather than allow the default values to be used. For example, the nonsymmetrical wing example of this report (table II(f)) has a chord of nearly zero at $y = 0$, which if used as the default for the leading-edge surface chord would not produce an acceptable design.

B3. Wing Camber Surface—Optional Input

A wing mean camber surface may be specified by a set of tabular entries. However, if a flat wing analysis is performed or if a flat wing is used as the initial surface in a design process, these entries are not required. If a wing surface is input, the section mean camber surface must be specified by exactly 26 chordwise ordinates at up to 52 span stations. When fewer than 26 camber coordinates are used to define the sections, the ordinate tables must be filled with enough zeros to complete the list of 26. The necessary section information is as follows:

NYC number of spanwise stations at which chordwise sections are used to define mean camber surface (limit of 52)

TBYC (NYC) table of y values for chordwise camber surface sections; beginning at $y = 0$; increasing order of y from root to tip

NPCTC number of chordwise stations used in definition of mean camber surface (limit of 26)

TBPCTC (NPCTC) table of chordwise stations, in percent chord, at which mean camber surface ordinates are defined; increasing

order from leading edge to trailing edge

TZORDC (NPCTC,NTC) table of mean camber surface z ordinates that corresponds to TBPCTC table; the full 26 values for root chord (including zeros for values in excess of NPCTC) are given first, followed by similar information for NYC spanwise stations in increasing order of y

TZSCALE multiplying factor applied to TZORDC table to change camber surface ordinates

The TZORDC table may be multiplied by a scale factor TZSCALE. This factor may be useful if the original tabulated ordinates are nondimensionalized with respect to a single measurement (e.g., the wing root chord) or if it is necessary to evaluate the effect of change in camber surface severity. See table II(a) for an example of wing camber surface code input.

B4. Section Parameters for Attainable Thrust Calculation—Required Input

The following wing section information is required for the calculation of attainable leading-edge thrust and leading-edge separation forces:

NYR number of spanwise stations at which information on airfoil sections is supplied (limit of 30)

TBYR (NYR) table of y values for airfoil section information; beginning at $y = 0$; increasing order of y from root to tip

TBTOC (NYR) table of airfoil maximum thickness as fraction of chord, t/c

TBETA (NYR) table of section locations of maximum thickness as fraction of chord, η

TBROC (NYR) table of leading-edge radii as fraction of chord, r/c

IVOROP vortex location option as follows:
 = 0 full vortex force acts normal to wing reference plane at wing leading edge; does not contribute to axial force
 = 1 vortex center given by empirical relationships derived from delta wing experimental data (default)

= 2 vortex center given by method of Lan and Chang (ref. 12)

YAPEX spanwise location of vortex flow-field origin (default 0.0)

For special planforms such as forward-swept wings or other wings with apex away from centerline, this input can help provide better estimate of vortex-induced flow fields and forces.

B5. Flight Conditions—Required Input

The flight or test conditions are specified as follows:

XM free-stream Mach number
 RN free-stream Reynolds number (based on \bar{c}) $\times 10^{-6}$
 NALPHA number of angles of attack to be calculated (limit of 19)
 TALPHA table of angles of attack to be calculated, deg

The commonly accepted practice of performing subsonic calculations for a Mach number of 0 is not appropriate for this code. Realistic estimates of attainable thrust can be made only if both the Mach number and the Reynolds number correspond to actual conditions. In fact, the code stops and writes an error message when $XM = 0$ is input. The TALPHA table must begin with the smallest angle (most negative) and continue with increasingly larger angles up to the largest angle. A wide range of angle of attack is required in order to use the code in the design mode. This range must cover the angle of attack for $C_{L,des}$ of the original and all subsequent surfaces. An error message is written when the angle-of-attack range is too small.

B6. Solution Convergence Criteria—Optional Input

To determine perturbation velocity distributions for the input camber surface, the flat wing surface at an angle of attack of 1° , and the candidate camber surfaces used in the design mode, a maximum of 70 iterations are provided. If this number is reached without the convergence criteria being met, the results for the 70th iteration are printed with an appropriate message. The maximum number of iterations may be changed by the entry

ITRMAX maximum number of perturbation velocity iterations (default 70)

The code convergence criteria are met when, for all wing surfaces, the average difference in perturbation velocity between successive iterations is less than one half of 1 percent of the average velocity over the wing. If the average velocity for any wing surface is less than the

average velocity for the flat surface at $\alpha = 1^\circ$, the value for the flat wing surface is used instead. In many instances, these criteria may be more stringent than necessary. If desired, the convergence criteria may be changed by the entry

CNVGTST perturbation velocity convergence criteria (default 0.005)

The code wing surface design is also the result of an iterative process. The iteration is terminated when, from one iteration to the next, the design angle of attack changes by less than 0.01° and the design pitching-moment coefficient changes by less than 0.001. If desired, these criteria may be made more or less stringent by use of the following entries:

ALPTST angle-of-attack convergence test (default 0.01)

CMTST pitching-moment convergence test used when a design pitching-moment constraint is specified (default 0.001)

B7. Design Specifications—Required Input for Design Mode

The following entries control the solution for the optimized surface in the code design mode. For the analysis of a specified wing surface, omit the following entries:

CLDES design lift coefficient (if CLDES is not specified, the code defaults to 0.0, which triggers an analysis-only solution)

CMDES design pitching-moment coefficient (if CMDES is not specified, the code defaults to 1000.0, which triggers an optimization solution without moment restraint)

ITRDESM maximum number of design iterations (default 20)

See section 7.10 for comments on performance penalties that can result from imposition of CMDES restraints. This capability should not generally be used for supersonic cruise designs.

In attempting to meet the convergence criteria for wing design, the code provides for a maximum of 20 iterations. If this number is reached without the convergence criteria being met, the results for the 20th iteration are printed with a warning of the failure to meet the criteria. If desired, the maximum number of design iterations may be increased or decreased by the ITRDESM entry.

B8. Design Specifications—Optional Input for Design Mode

The rest of the design mode entries are optional. These can be valuable for code user control of the design process but are covered by code defaults if the user chooses not to exercise the options. Code defaults provide candidate surfaces which generally provide a camber surface design with good aerodynamic efficiency. The code user, however, may want to tailor a camber surface solution more appropriate to the problem at hand and may want to search for solutions offering greater efficiency.

The user may select the number of general camber surfaces to be used in the optimization process as follows:

NGCS number of general camber surfaces covering entire wing (limit of 8, default 8)

In addition, the user may select exponents that control the shape of the various general camber surfaces by use of the following entries:

EXPY1, EXPY2, EXPY3, EXPY4 exponents of y used in definition of general camber surfaces (defaults: EXPY1 = 0.0, EXPY2 = 1.0, EXPY3 = 2.0, and EXPY4 = 3.0)

EXPX1, EXPX2 exponents of x' used in definition of general camber surfaces (defaults: EXPX1 = 1.5, EXPX2 = 2.0)

To preserve the original surface between the leading-edge modification surfaces and the trailing-edge modification surfaces for a mission adaptive design, NGCS may be set to zero. In this case, user options for both leading-edge and trailing-edge modifications must be employed.

The following entries control the region of the wing affected by the leading-edge modification surfaces. Because wing aerodynamic performance is critically dependent on the surface shape and pressure loading in the leading-edge region, these surfaces are essential to the optimization process.

NLEC number of breakpoints used in definition of area of wing affected by leading-edge modification surfaces (limit of 30, default 2)

TBLECY (NLEC) table of y values at breakpoints used in definition of area of wing affected by leading-edge modification surfaces; increasing order of y from root to tip (default 0.0, TBLEY (NLEY))

TBLEC (NLEC) table of c_{le} values that corresponds to TBLECY table (default

TBTEX(1) – TBLEX(1) for both entries); see discussion for ELAR (p. 58) regarding definition of leading-edge areas; may be necessary to change ELAR or to place limits on nonzero c_{le} values

The code employs linear interpolation of tabular chord inputs to define chords at the required code span locations.

The following entries control the region of the wing affected by the trailing-edge modification surfaces and the streamwise section shape of these surfaces. The code defaults exclude these surfaces.

NTES number of trailing-edge modification surfaces (limit of 4) (see fig. 18 for examples); does not represent number of trailing-edge design areas or flap surface areas which are controlled by TBTECY and TBTEC inputs

NTEC number of breakpoints used in definition of area of wing affected by trailing-edge modification surfaces (limit of 30)

TBTECY (NTEC) table of y values at breakpoints used in definition of area of wing affected by trailing-edge modification surfaces; increasing order of y from root to tip

TBTEC (NTEC) table of c_{te} values that corresponds to TBTECY table; see discussion for ELAR (p. 58) regarding definition of trailing-edge areas; may be necessary to change ELAR or to place limits on nonzero c_{te} values

EXPXTE exponent of $x' - (c - c_{te})$ used in definition of trailing-edge modification surfaces (exponents of y are same as used in definition of general camber surfaces) (default 1.5)

Leading- and trailing-edge modification surface chords must be specified for the entire wing semispan even if the chords are zero. Where an abrupt change in chord occurs, values of the chord should be specified for semispan stations just inboard and just outboard of the break. See table II(e) for an example of leading- and trailing-edge design surface code inputs.

B9. Additional Optional Input

If desired, the design twist and camber may be confined to the wing outboard of the fuselage. The limit of the general surfaces is controlled by the following input:

YFUS spanwise station of wing-body juncture; this entry limits wing general camber surfaces to values of y greater than specified (default 0.0)

Leading- and trailing-edge camber surfaces may be limited by existing options; use of these limitations yields a design lifting surface confined to the wing outboard of the fuselage.

For an asymmetrical wing design, a design restraint to eliminate rolling moment may also be applied as follows:

YCG lateral center-of-gravity and rolling-moment center as fraction of wingspan (default 1000.0 imposes no restraint)

CRTST absolute value of maximum allowable rolling moment (default 0.01)

An asymmetric wing reference root chord may be input if desired as follows:

CRNSYM reference root chord of asymmetric wing (default computed by code as chord at midspan)

The code allows for modifications to the designed lifting surface after generation of the design and before evaluation of that surface. This option permits an assessment of the effect of practical considerations on wing aerodynamic performance.

Wing trailing-edge ordinates may be altered to provide less severe lateral surface slopes and to reduce the incidence of the lifting surface representing the fuselage. The modification could also be used to provide a straight line portion of the camber surface at the wing trailing edge or at trailing-edge flap hinge-line location. The airfoil section camber lines are altered by use of a formulation that does not change surface slopes at the wing leading edge so that the design leading-edge thrust condition is preserved as much as possible.

TDELZTE table of changes in wing trailing-edge ordinates expressed as fraction of wing root chord

This table is used in generation of trailing-edge ordinates to replace those listed in code-generated table of surface ordinates; entry required for each span station listed in code output in same order of increasing span stations.

B10. Reflex Surface Design—Optional Input for Design Mode

The code permits a design of the wing camber surface in the vicinity of nacelles which further optimizes the lifting efficiency of the wing by taking advantage of the pressure field created by the presence of the nacelle. This option is activated by the input

IREFL reflex surface design index (set this index to 1 if code is used to define reflexed camber surface in vicinity of nacelles; use of this option requires proper definition of input interference pressure field and corresponding trailing-edge design surface; code defaults to index of 0, which bypasses reflex design feature)

See table II(d) for an example of reflex surface design code input.

B11. Flap Design—Optional Input for Design Mode

The code provides an automated graphical flap-fitting technique, described in reference 3, which is activated by the following input:

IFLPDES flap design index (set this index to 1 if code is used to define spanwise distribution of leading- and trailing-edge flap deflections which approximate designed camber surface; use this option only for design in which leading- and trailing-edge modification surfaces are specified; code defaults to index of 0, which bypasses flap design feature)

When the flap design feature is used, leading-edge and/or trailing-edge design surfaces must be used, and NGCS must be set to zero. The chords of these surfaces are input as the chords of the flaps. The code then designs a restricted area camber surface for leading- and trailing-edge areas whose chords are set at 1.5 times the flap chords.

B12. Design Surface Smoothness Control—Optional Input

The following user option provides a degree of control over the smoothness of the camber surface solution:

IAFIX smoothing operation indicator; set IAFIX = 1 if smoothed values are supplied (default 0)

TAFIX (JBYMAX) table of smoothed surface weighting factors replacing code-generated table in same order of increasing span stations

See table II(c) for an example of surface smoothness control code input.

B13. Interference Flow Field—Optional Input

The following additional input data provide for a wing design with pressure fields induced by other airplane components taken into account. For normal code operation, simply omit these entries. If an interference pressure field is input, the distribution must be specified by exactly 26 chordwise positions at up to 52 span stations. When fewer than 26 chordwise positions are used to define the interference pressure field, the table for ΔC_p must be filled with enough zeros to complete the list of 26.

ICP	other airplane component-induced pressure field indicators; set ICP = 1 if this option is used (default 0)
NYCP	number of spanwise stations at which chordwise sections are used to define interference pressure field (limit of 52)
TBYCP (NYCP)	table of y values for interference pressure field chordwise sections; beginning at y = 0; increasing order of y from root to tip
NPCTCP	number of chordwise stations used in interference pressure field definition (limit of 26)
TBPCTCP (NPCTCP)	table of chordwise stations, in percent of chord, at which interference pressure field distributions are defined; increasing order from leading edge to trailing edge
TCP (NPCTCP, NYCP)	table of interference pressure field coefficients that corresponds to TBPCTCP table; full 26 values for root chord (including zeros for values in excess of NPCTCP) are given first, followed by similar information for spanwise stations in increasing order of y
PFMULT	multiplier of input pressure field coefficients (default 1.0)

See table II(d) for an example of a reflex surface design with an interference pressure field code input.

B14. Empirical Corrections—Optional Input

An empirical method for selection of design lift coefficient and estimation of achievable aerodynamic

performance for supersonic speeds described in reference 6 and in section 7.10 may be included in the code calculations by input of the index

IEMPCR empirical correction index (this index set to 1 implements empirical corrections; index set to 0, code default, bypasses this feature)

This correction adjusts the design lift coefficient to account for the tendency of linearized theory to overestimate the magnitude of the upwash field for supersonic speeds. It also corrects the estimated aerodynamic performance to compensate for the tendency of the theory to be overly optimistic.

B15. Code Output Data

The code is constructed so that successive runs may be made with a given computer entry. To make additional runs, it is only necessary to add an identification record and namelist data that change from the previous run. An additional capability is provided by the entry NEWDES. When the code is run in the design mode and NEWDES is set to 1, a design camber surface is found, the input set of camber surface ordinates is replaced by camber surface ordinates for the new design, and this new design is treated as an evaluation case. In the original code, the default for the entry NEWDES was 0, which provided for a design of the wing surface but not for a subsequent evaluation. Now, however, because this feature was found so useful, the default has been changed to NEWDES = 1. When the NEWDES option is used, successive runs may be employed to evaluate the new surface at off-design conditions.

The wing-design camber surface ordinates are printed for a reference angle of attack defined by an entry of ALPZPR (reference angle of attack) or CLZPR (reference lift coefficient). The default is ALPZPR = 0.0. When CLZPR is specified, the code calculates the corresponding ALPZPR and uses it in the determination of ordinates.

If the code user desires, span load distribution data may be printed. If the index IPRSLD is set to 1, section aerodynamic characteristics, including the separate contributions of basic pressure loadings, attainable thrust, and vortex forces for each entry in the angle-of-attack table, are printed. These data are printed only for the evaluation mode or when the NEWDES option is used in the design mode.

The printed code results include the following items:

1. Iteration-by-iteration history of convergence parameters for longitudinal perturbation velocity solution; in design mode, data given only for most critical surface of up to 64 surfaces used and for

- flat surface at $\alpha = 1^\circ$; for supersonic solution in which iteration not used, printout is omitted
2. Listing of spanwise distribution of leading-edge surface factor, angle-of-attack range for full thrust, and angle of attack for zero thrust; these data given for evaluation mode and for all iterations in design mode from first (input surface) to last (optimized surface); for evaluation mode, leading-edge surface factors all zero
 3. Listing of overall theoretical aerodynamic coefficients C_N , C_A , C_m , C_L , and C_D with no thrust and with full theoretical thrust as function of angle of attack
 4. Listing of overall estimated aerodynamic coefficients including C_N , C_A , and C_m for basic pressure loading, ΔC_N and ΔC_A for attainable thrust and vortex-force increments, and C_N , C_A , C_m , C_L , C_D , and S_S for total loading as function of angle of attack; these data given for evaluation mode and for all iterations in design mode from first (input surface) to last (optimized surface)
 5. Additional listing of overall wing aerodynamic characteristics including empirical corrections for optimized surface when IEMPCOR empirical correction option employed for supersonic design and evaluation
 6. Listing of spanwise distribution of wing-section aerodynamic characteristics, including separate contributions of basic pressure loadings, attainable thrust, and vortex forces; these data given only for evaluation mode (or when NEWDES option used in design mode) and given only if print option IPRSLD set to 1
 7. Listing of wing-surface ordinates as function of chord position for each of span stations used in code solution
 8. Listings of lifting pressure distributions for camber surface at $\alpha = 0^\circ$ and for flat surface at $\alpha = 1^\circ$
 9. Listing of leading-edge surface factors used in design and listing of suggested replacement values which may lead to improved performance when NEWDES option used; generally, need for this replacement arises only when not possible to provide sufficiently detailed numerical representation of wing to give closely matched aerodynamic characteristics in design and evaluation modes
 10. Listing of suggested spanwise distribution of flap deflection angles to approximate designed camber surface and to approach its aerodynamic performance when IFLPDES option used and flap chord information supplied
- As discussed at the beginning of this section, provision has been made for successive runs of the code with a single computer entry. Under some circumstances, the following input data quantities may be changed during a computer run. The new values are used for subsequent runs unless reset by the code user.
- | | |
|---------|--|
| JBYMAX | may be reduced to keep number of elements within code limits; new value which depends on Mach number retained unless respecified |
| CLDES | reset to 0.0 after design run performed; subsequent runs for evaluation only unless CLDES respecified |
| NEWDES | reset to 0 after evaluation of newly designed surface is performed; original input camber surface description ($z = 0$ everywhere for default) is replaced with new values of NYC, TBYC, NPCTC, TBPCTC, and TZORDC for designed surface which are retained unless respecified |
| TZSCALE | reset to 1.0 after rescaling operation performed; any subsequent rescaling activated by setting TZSCALE to value other than 1.0 applied to newly rescaled surface |
| TBLEC | values multiplied within code by 1.5 when flap design option (IFLPDES = 1) is employed; this new table replaces original input; TBLEC must be respecified if subsequent design performed |
| CLZPR | reset to 1000 at completion of each computer run; for following run, camber surface ordinates printed for angle of attack of 0° unless CLZPR respecified |

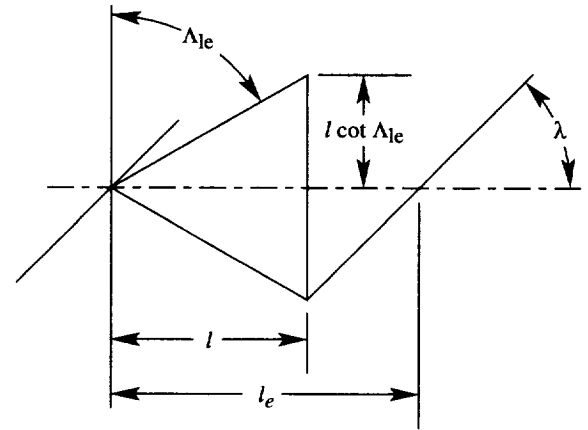
Appendix C

Estimation of Idealized Minimum Drag and Maximum Suction Parameter

For both the AERO2S and WINGDES codes, the suction parameter is employed as a means of rating the relative aerodynamic efficiency of wing lifting surfaces. In this parameter, the drag of a given wing surface is compared with that of a flat wing without leading-edge thrust or vortex forces $C_L \tan (C_L/C_{L\alpha})$ and with that of a wing with an elliptical span load distribution and a corresponding uniform downwash $C_L^2/\pi AR$. This means of rating performance is quite appropriate for subsonic speeds where the vortex drag due to lift with its theoretical minimum of $C_L^2/\pi AR$ is the only appreciable contribution. However, at supersonic speeds and whenever the local flow becomes anywhere supersonic, a new source of drag—wave drag due to lift—is introduced. As a matter of convenience, the suction parameter definition used for supersonic speeds is the same as that used for subsonic speeds because, for wave drag due to lift, there is no simple means of estimating minimum values and the limits used in the subsonic form are easily reproducible and not subject to problems of interpretation. The terms are dependent only on geometric properties and on a flat surface lift-curve slope, which can be evaluated by any valid numerical solution of linearized theory. Use of the same form for both speed regimes, however, means that supersonic suction parameters cannot approach a limiting value of 1.0 as they do for low subsonic speeds. However, a process although somewhat complicated may be used to estimate minimum wave drag due to lift and an upper limit of suction parameter for supersonic speeds.

In reference 26, Hayes developed a method of calculating wave drag due to lift by consideration of the flow field created at large distances from the object generating the lift. The method is closely related to the well-publicized area rule concept for the calculation of wave drag generated by the volume or thickness of bodies and wing-body combinations. Calculations begin with the creation of a series of equivalent bodies of revolution, each corresponding to a particular portion of the flow field propagating away from the body along azimuth angles ϕ as shown in figure C1. Each of these bodies has an equivalent cross-sectional area development related to the summation of the component of lift-generated forces acting along that azimuth angle. The drag of each of these bodies may be calculated by use of formulas,²

²A presentation of these integral formulas is not necessary for the purpose of this analysis because the drag need be found only for very specialized cases for which analytic solutions have already been published.



Sketch C-1

which take into account the second derivative of the cross-sectional area with respect to the longitudinal distance from the body nose. Hayes shows that the drag due to lift of the system as a whole may be represented as the average drag of the series of bodies covering azimuth angles from 0° to 360° .

At a given point along the axis of an equivalent body for a given azimuth angle, the equivalent cross-sectional area is the result of an accumulation of the component of lifting forces directed along the azimuth line. The summation includes all lifting forces generated by the object forward of the intersection with the object of a fore Mach cone from the specified field point as shown in figure C1.

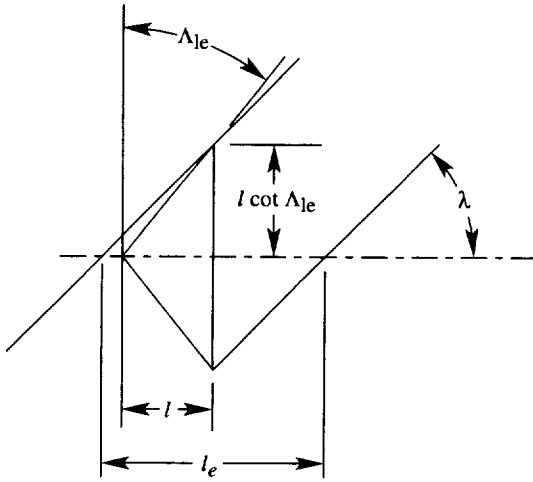
For simplicity, the lifting object shown in the figure is a thin delta wing without twist and camber at a very small angle of attack. As shown in the plan view, the fore Mach cone intersection with the wing plane has a parabolic shape. For large distances, this intersection is essentially a straight line with an intersection angle λ . Through use of some trigonometry, the intersection angle may be given as

$$\lambda = \tan^{-1} \left(\frac{1}{\beta \cos \phi} \right)$$

For delta wings with subsonic leading edges $\beta \cot \Lambda_{1e} < 1$, length of each body up to the point at which all the forces are accumulated as shown in sketch C-1 is

$$\begin{aligned} l_e &= l \left(1 + \frac{\cot \Lambda_{1e}}{\tan \lambda} \right) \\ &= l (1 + \beta \cot \Lambda_{1e} \cos \phi) \end{aligned}$$

Beyond this point the equivalent cross-sectional area is constant, and no more drag is created. For delta wings



Sketch C-2

with supersonic leading edges $\beta \cot \Lambda_{1e} > 1$ shown in sketch C-2, the equivalent body length is

$$l_e = l(2\beta \cot \Lambda_{1e} \cos \phi)$$

Hayes (ref. 26) shows that the equivalent cross-sectional area of any point on a body for a given azimuth angle is given by the relationship

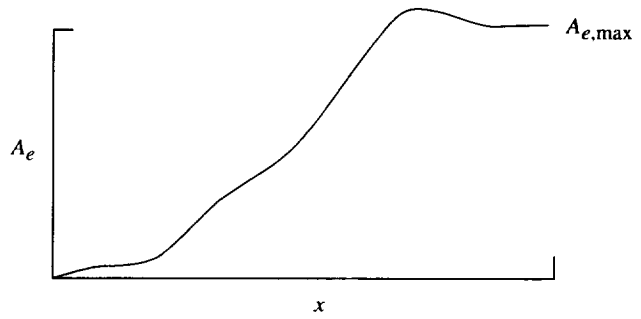
$$A_e = \frac{\beta}{2q} \int_0^x F'_L dx$$

where F'_L is the rate of growth of the lifting force with increasing distance (for example, lift in pounds per foot of distance). At the distance l_e , the point at which all the lifting force has been taken into account, the cross-sectional area will be

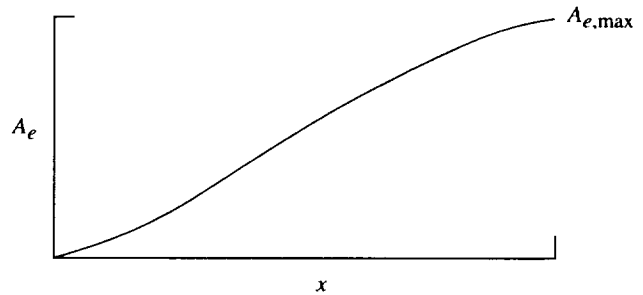
$$A_{e,\max} = \frac{-\beta}{2} C_L S \sin \phi$$

The negative sign accounts for the occurrence of the maximum force directly below the lifting object at $\phi = -90^\circ$. The actual distribution of the equivalent area with longitudinal distance is dependent on the wing geometry and the loading distribution. As shown in sketch C-3, the development may have a quite arbitrary shape and the drag of a given body may in some instances be very large. One way of estimating minimum achievable wave drag due to lift is to assume that the wing may be shaped to provide an optimum equivalent area distribution and a corresponding minimum drag for each equivalent body required for the drag calculation. Such a limit may not be realistically attainable, but it does represent an idealized nonzero goal.

An optimum body of revolution and its minimum drag suitable for this study is given in reference 27. The



Sketch C-3



Sketch C-4

Sears-Haack body for minimum drag for a given length and maximum cross-sectional arc has an area distribution for its front half (up to the maximum area) as shown in sketch C-4. The drag coefficient of this half-body is given by

$$C_{D,\min} = \frac{\pi}{2} \frac{A_{\max}^2}{l^2}$$

This formula may be used to define a minimum wave drag due to lift for each equivalent body associated with a given azimuth angle. First the minimum drag equation is changed to provide a coefficient based on the wing reference area rather than the body maximum area as follows:

$$C_{D,\min} = \frac{\pi}{2S} \frac{A_{\max}^2}{l^2}$$

Then with the substitution of the previously defined effective area $A_{e,\max}$ and the effective length l_e for the body area and length,

$$C_{D,\min} = \frac{\pi}{8} \beta^2 C_L^2 S \left(\frac{\sin \phi}{l_e} \right)^2$$

or

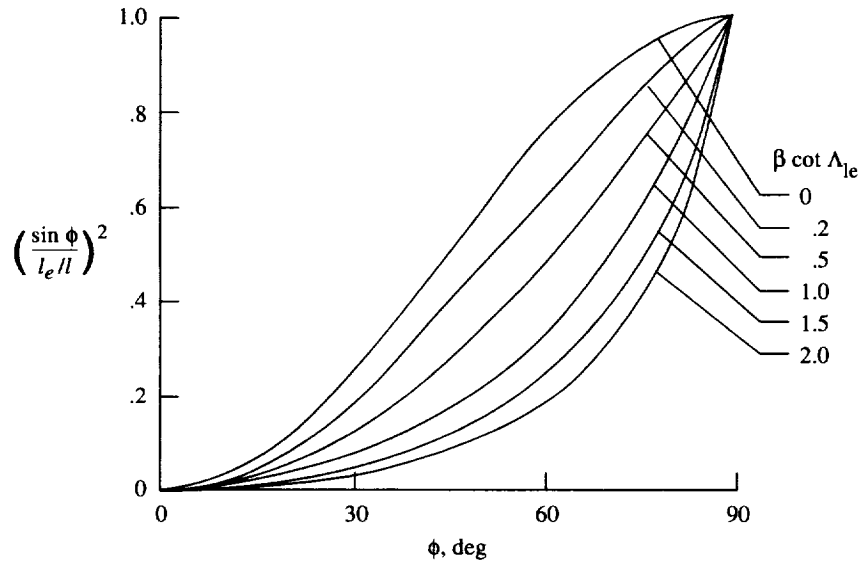
$$C_{D,\min} = \frac{\pi}{8} \beta^2 C_L^2 \frac{S}{l^2} \left(\frac{\sin \phi}{l_e/l} \right)^2$$

To find the average drag coefficient for the series of bodies corresponding to values of ϕ from 0° to 360° , integrating the term containing $\sin \phi$ and l_e is necessary. As noted previously, l_e is dependent on the leading-edge sweep parameter as well as the angle ϕ . Because of symmetry, the average drag can be found by an integration

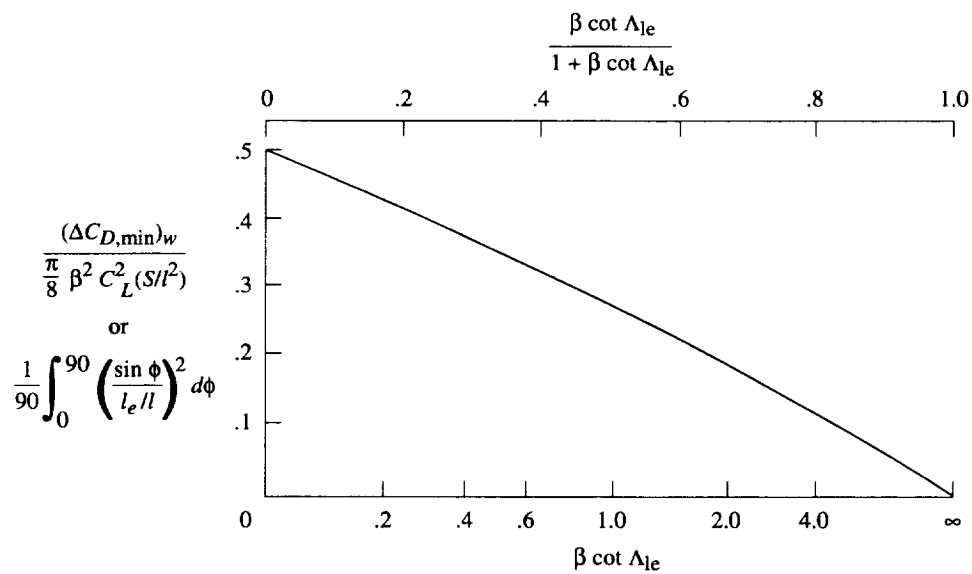
from $\phi = 0^\circ$ to 90° . The minimum wave drag due to lift is thus

$$(\Delta C_{D,\min})_w = \frac{\pi}{8} \beta^2 C_L^2 \frac{S}{l^2} \frac{1}{90} \int_0^{90} \left(\frac{\sin \phi}{l_e/l} \right)^2 d\phi$$

Sketch C-5 shows a plot of the integrand term as a function of the azimuth angle ϕ for delta wings with various values of the leading-edge sweep parameter. A numerical integration of these curves permits the calculation of an average drag for each of the selected $\beta \cot \Lambda_{le}$ values. Results of the integration are shown in sketch C-6. This



Sketch C-5



Sketch C-6

plot uses a scale for the leading-edge sweep parameter $\beta \cot \Lambda_{1e}$ that permits representation of the full range of values from zero to infinity. The quantity $\beta \cot \Lambda_{1e} / (1 + \beta \cot \Lambda_{1e})$ is plotted on a linear scale.

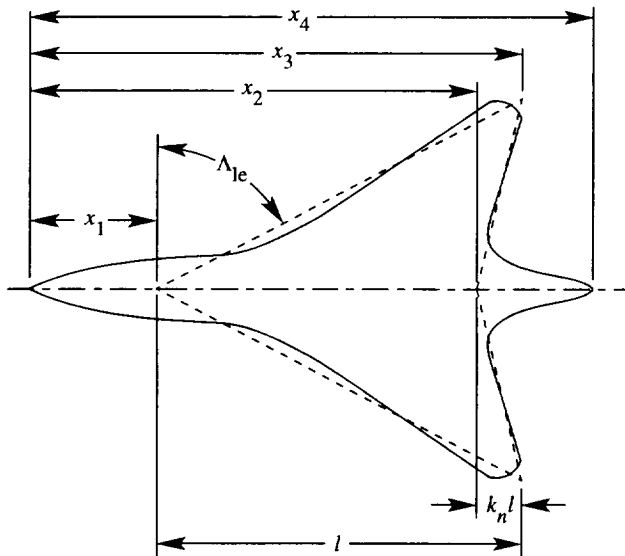
Although this technique for calculation of minimum wave drag was derived for a delta wing, it can also be applied to arrow wings. In fact, the calculation process may be employed in estimation of the minimum wave drag due to lift for wing-body configurations with wings of arbitrary planform by substitution of an appropriate arrow wing for the actual planform. Sketch C-7 helps to illustrate how such a replacement arrow wing may be found through a superposition of planforms. When, as shown in the sketch, the actual planform includes the fuselage, little weight should be given to the fuselage portion which typically generates little of the total lift. The length of the arrow wing should represent a longitudinal distance over which the lift may be developed in an efficient manner. Likewise, the span should represent a lateral distance over which a near-elliptical span load distribution may be achieved.

For an arrow wing as shown by the dashed line in sketch C-7, the wing reference area may be expressed as

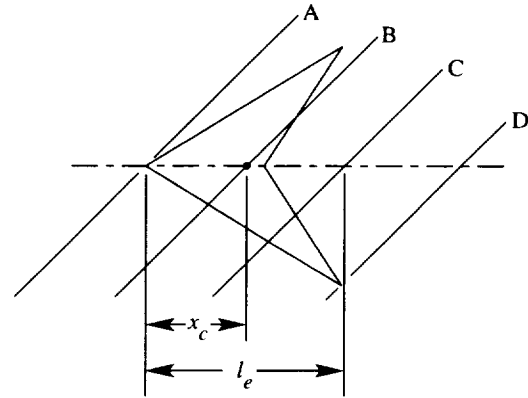
$$S = \frac{l^2}{\beta} (1 - k_n) (\beta \cot \Lambda_{1e})$$

The minimum wave drag due to lift for any arrow wing may thus be expressed as

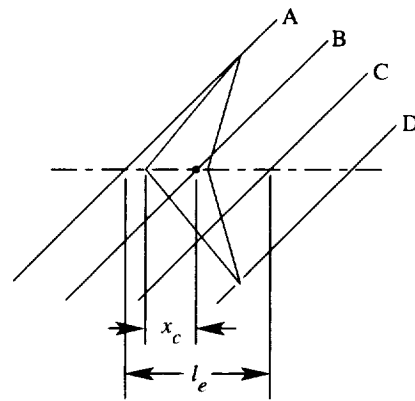
$$\frac{(\Delta C_{D,\min})_w}{C_L^2} = \frac{\pi}{8} \beta (1 - k_n) (\beta \cot \Lambda_{1e}) \frac{1}{90} \int_0^{90} \left(\frac{\sin \phi}{l_e/l} \right)^2 d\phi$$



Sketch C-7



Sketch C-8



Sketch C-9

If the actual wing reference area differs from the arrow wing reference area, the right-hand side of the equation should be multiplied by the ratio of the reference area to the arrow wing area.

The effective equivalent body lengths for use in the drag equation take on values defined in the following formulation which accounts for subsonic and supersonic leading edges and positive or negative notch ratios:

$$\begin{aligned} l_e &= x_2 - x_1 \\ l_e &= (x_3 - x_1)(1 + \beta \cos \Lambda_{1e} \cos \phi) \\ l_e &= (x_3 - x_1) + (x_3 - x_1)(\beta \cos \Lambda_{1e} \cos \phi - 1) \\ l_e &= (x_3 - x_1)(2\beta \cos \Lambda_{1e} \cos \phi) \end{aligned}$$

Use whichever length is greatest.

For some situations, for example, those shown in sketches C-8 and C-9, the belief that an optimum wing loading could be maintained over the lengths given by the formula is not reasonable. Optimum load distributions do not depart to any great degree from that given by uniform lifting pressures. A uniform load would have a

center of pressure of the centroid of area which for an arrow wing is

$$x_c = \frac{1}{3}(x_2 - x_1) + \frac{1}{3}(x_3 - x_1)$$

For the wing shown in sketch C-8, one half the total lift would be accumulated when the cutting plane intersection labeled B is reached. No matter how the load is distributed over the rest of the wing, the drag is not likely to be any lower than that of an equivalent body terminating at the cutting plane intersection C whose length is

$$l_e = 2x_c = \frac{2}{3}(x_2 + x_3)$$

If the arrow wing leading edge is supersonic, for some cutting plane intersections the equivalent body length may be greater than $2x_c$ as shown in sketch C-9 where

$$l_e = \frac{2}{3}(x_2 + x_3 - 2x_1) + 2(x_3 - x_1)(\beta \cot \Lambda_{le} \cos \phi - 1)$$

Whichever of these two body lengths is longer is taken to be a maximum not to be exceeded by lengths defined solely by cutting planes. By use of numerical evaluation of the integral in the equation for wave drag due to lift, the minimum wave drag due to lift for arrow wings may be represented by curves shown in figure C2. A value of zero for $\beta \cos \Lambda_{le}$ represents a wing of infinite length and no span which has no wave drag due to lift. On the other extreme, $\beta \cos \Lambda_{le} = \infty$ represents a wing of infinite span and no length which has an infinite wave drag due to lift.

The minimum vortex drag due to lift for arrow wings may also be represented by figure C2. The minimum vortex drag due to lift is simply

$$(\Delta C_{D,\min})_{\text{vor}} = \frac{C_L^2}{\pi AR}$$

For the arrow wing shown in the sketch at the top of figure C2, the span is

$$b = \frac{2l}{\beta}(\beta \cot \Lambda_{le})$$

and the aspect ratio is

$$AR = \frac{b^2}{S} = \frac{4}{\beta} \frac{\beta \cot \Lambda_{le}}{1 - k_n}$$

Thus the minimum vortex drag due to the lift is

$$\frac{(\Delta C_{D,\min})_{\text{vor}}}{C_L^2} = \frac{\beta}{4\pi} \frac{1 - k_n}{\beta \cot \Lambda_{le}}$$

In contrast to the wave drag, the vortex drag is zero for $\beta \cot \Lambda_{le} = \infty$, which represents a wing of infinite span, and is infinite for $\beta \cot \Lambda_{le} = 0$.

The minimum total drag due to lift obtained by an addition of these two curves occurs at $\beta \cot \Lambda_{le} \approx 0.8$ for the delta wings and at lower values of $\beta \cot \Lambda_{le}$ for more highly swept leading edges. An important drag contribution so far not discussed in this analysis that has a strong impact on the choice of leading-edge sweep angle is the wave drag due to the configuration thickness or volume. This contribution tends to increase with increasing values of the leading-edge sweep parameter $\beta \cos \Lambda_{le}$ in much the same way as does the wave drag due to lift. When this additional drag term is taken into account, the wing sweep angle for minimization of the complete configuration drag falls well within the subsonic leading-edge range. The optimum leading-edge sweep parameter $\beta \cos \Lambda_{le}$ must be evaluated on an individual basis for any given design exercise.

The maximum attainable suction parameter may be expressed as

$$S_{S,\max} = \frac{C_L \tan(C_L/C_{L_\alpha}) - [(C_{D,\min})_w + (C_L^2/\pi AR)]}{C_L \tan(C_L/C_{L_\alpha}) - (C_L^2/\pi AR)}$$

Through use of lift-curve slopes C_{L_α} evaluated by the WINGDES code, the maximum suction parameters shown in the plot at the bottom of figure C2 were obtained. This plot shows that high values of suction parameter comparable with those attainable at subsonic speed could be realized only if it were possible to use wings with high notch ratios. For more practical arrow wings approaching the delta wing planform, the potential for high values of suction parameter is much reduced. In addition, it must be recognized that the high values of maximum suction parameter for highly swept wings ($\beta \cos \Lambda_{le}$ approaching zero) are countered by high values of vortex drag which tend to negate the wave drag improvements. It should also be reiterated that the arrow wing performance maximums given here are, as mentioned previously, based on highly idealized assumptions.

Before using the plot for $S_{S,\max}$ in figure C2 to estimate achievable values of the suction parameter, an additional factor must be taken into account. Reference 6 has shown that as Mach number increases, linearized theory becomes less reliable as an indicator of aerodynamic performance. Achievable suction parameters were shown to decline with increasing Mach number. A plot of the ratio of achieved experimental suction parameters to theoretically indicated suction parameters from reference 6 are repeated in sketch C-10. A final realistic estimate of

maximum suction parameter may thus be found by applying the K_S factor for a given Mach number from sketch C-10 to the theoretical maximum suction parameter defined by the equation for $S_{S,max}$ or by the curves of figure C2.

The minimum wave drag due to volume may be estimated through use of another Sears-Haack body of revolution that gives minimum wave drag for a given length and volume. The drag coefficient of this body is

$$(C_{D,0,min})_w = \frac{128}{\pi} \frac{l^2}{S} \left(\frac{V}{l^3} \right)^2$$

or

$$(C_{D,0,min})_w = \frac{128}{\pi} \frac{l_{e,v}^2}{S} \left(\frac{V}{l_{e,v}^3} \right)^2$$

with $l_{e,v}$ representing an effective length for each equivalent body corresponding to a given azimuth angle ϕ . Then the minimum wave drag due to volume for a wing-configuration may be given as

$$(C_{D,0,min})_w = \frac{128}{\pi} \frac{l^2}{S} \left(\frac{V}{l^3} \right)^2 \frac{1}{180} \int_0^{180} \frac{1}{(l_{e,v}/l)^4} d\phi$$

If the actual wing reference area differs from the arrow wing area, the right-hand side of the equation should be multiplied by the ratio of the arrow wing area to the reference area.

The effective equivalent body lengths take on values of

$$l_e = x_4$$

$$l_e = x_1 + (x_3 - x_1)(1 + \beta \cot \Lambda_{le} \cos \phi)$$

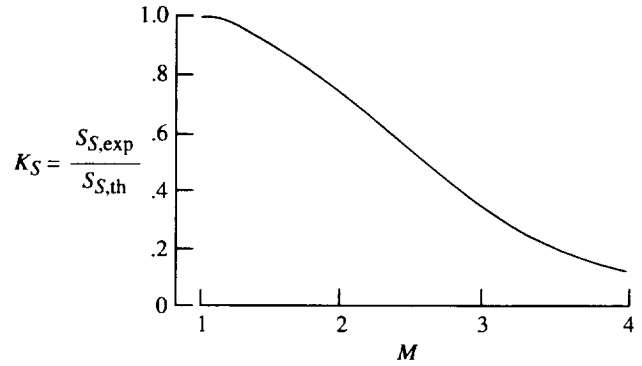
$$l_e = x_4 + (x_3 - x_1)(\beta \cot \Lambda_{le} \cos \phi - 1) - x_1$$

$$l_e = (x_3 - x_1)(2\beta \cot \Lambda_{le} \cos \phi)$$

Use whichever length is the greatest.

This collection of expressions for drag component idealized minimums in combination with estimates of the remaining skin friction drag may be used in studies aimed at setting performance limits. As an example, consider an arrow wing with all the volume contained within the planform. For such a configuration, the minimum wave drag due to volume may be expressed as

$$(C_{D,0,min})_w = \frac{128}{\pi \beta^2} [(1 - k_n) \beta \cot \Lambda_{le}]^2 \left(\frac{V^{2/3}}{S} \right)^3 \frac{1}{90} \int_0^{90} \frac{1}{(l_e/l)^4} d\phi$$



Sketch C-10

where the quantity $V^{2/3}/S$ is a measure of the configuration volume. Although the same parameters as seen in the expressions for $(\Delta C_{D,0,min})_w$ and $(\Delta C_{D,0,min})_{vor}$ reappear here, it is no longer possible to construct a plot covering the range of variables given in figure C2. However, for a given notch ratio and a selected Mach number and design lift coefficient, as well as a specified volume and skin friction drag coefficients, informative plots such as that shown in figure C3 may be prepared.

Figure C3 is intended only to serve as an example of the application of the minimum drag expressions. These results are for a simplified and not very practical case. Nevertheless, they do illustrate the character of the various drag components and the trade-offs involved in the search for optimized configurations. The design conditions are assumed to be

$$k_n = 0.0 \quad (\text{Delta wing})$$

$$M = 2.0$$

$$h = 50\,000 \text{ ft}$$

$$S = 8000 \text{ ft}^2$$

$$C_L = 0.12$$

$$\frac{V^{2/3}}{S} = 0.10$$

Again, the results are shown as a function of the leading-edge sweep angle parameter. Each minimum drag expression previously discussed is represented as is an estimate of skin friction drag. The total drag with an empirical drag correction term is given as follows:

$$\Delta C_{D,cor} = (S_{S,th} - S_{S,emp}) \left[C_L \tan \frac{C_L}{C_{L\alpha}} - \frac{C_L^2}{\pi AR} \right]$$

where $S_{S,emp}$ is an estimated achievable suction parameter obtained by application of K_S for a given Mach number to the theoretical maximum suction parameter. Some of the wing planforms represented are shown by

sketches. As shown by the curves for total C_D , an optimum planform will have a leading-edge swept well behind the Mach line. The optimum $\beta \cot \Lambda_{le}$ is strongly influenced by the contribution of wave drag due to volume.

These idealized minimum drag components could be valuable for parametric studies of aerodynamic performance dependence on fundamental configuration geometric parameters. They should also be useful in placing

limits on achievable performance for specific airplane designs to separate reasonable projections from outlandish claims. The strategies for the estimation of drag minima outlined in this appendix have been incorporated into a computer code, CDMIN. Although the code derivation as shown here is quite complex, the code itself is easy to use. The user is required to input only the Mach number, the wing reference area, the wing span, the configuration volume, and the dimensions x_1 to x_4 shown in sketch C-7.

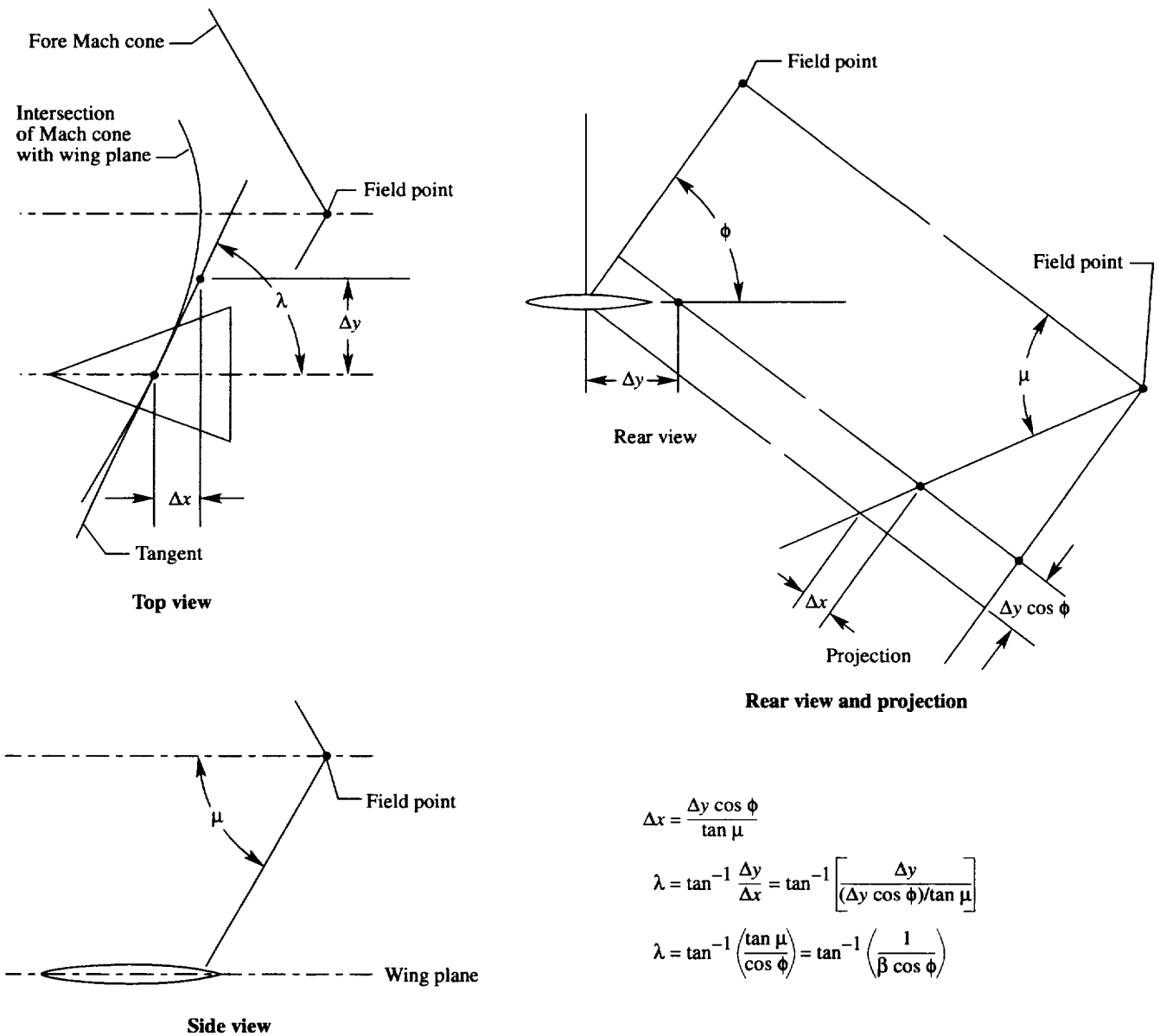


Figure C1. Illustration of area rule concepts.

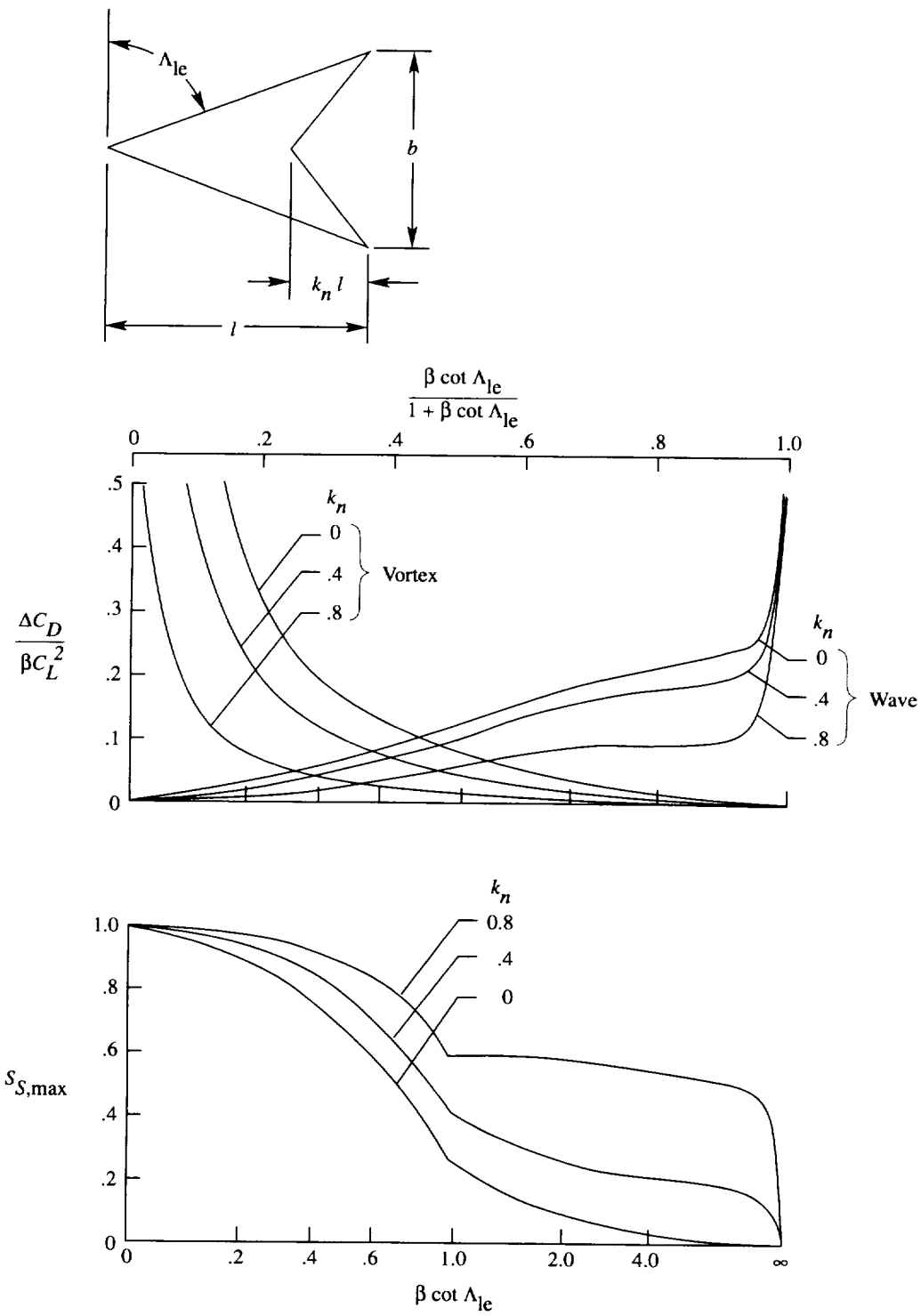


Figure C2. Idealized minimum drag due to lift for arrow wings.

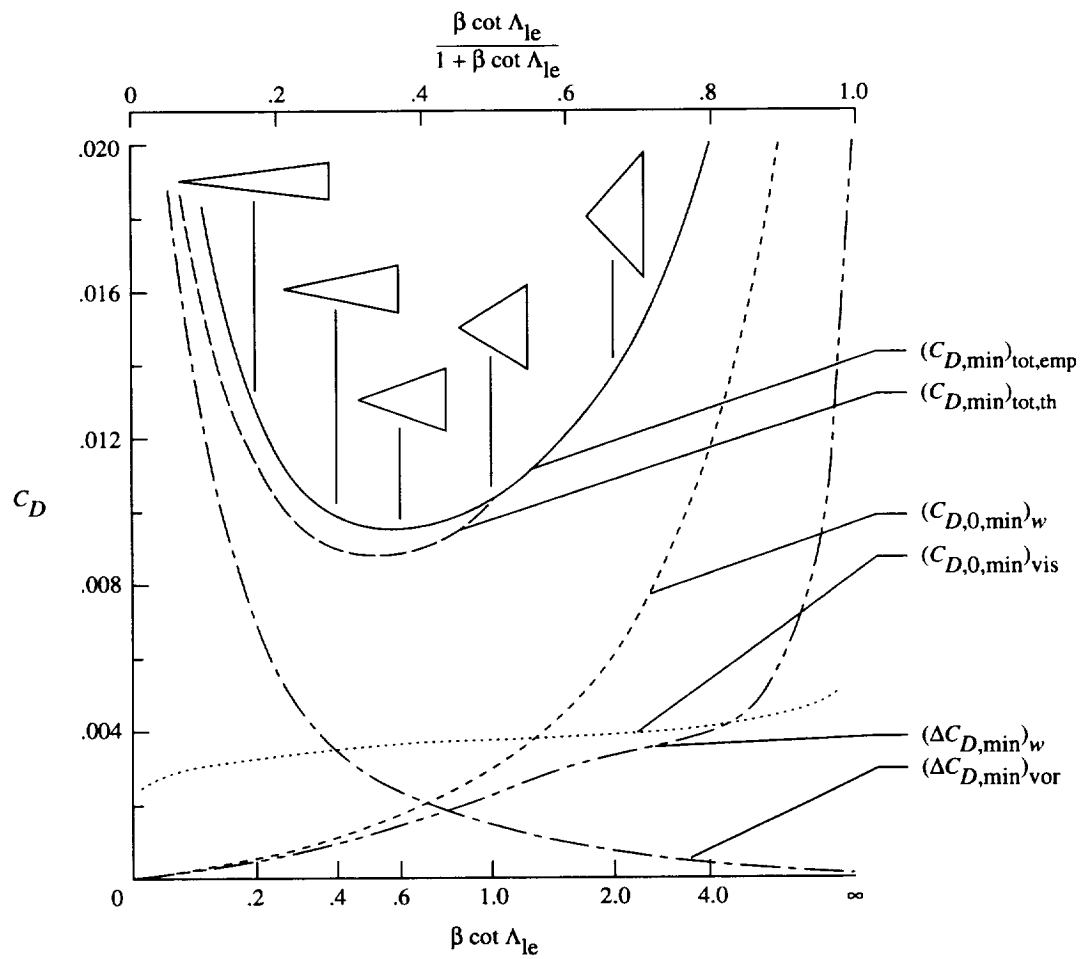


Figure C3. Idealized minimum total drag for delta wings. $M = 2.00$; $h = 50\,000$ ft; $C_L = 0.10$; $S = 8000$ ft²; $V^{2/3}/S = 0.10$.

References

1. Carlson, Harry W.; Mack, Robert J.; and Barger, Raymond L.: *Estimation of Attainable Leading-Edge Thrust for Wings at Subsonic and Supersonic Speeds*. NASA TP-1500, 1979.
2. Carlson, Harry W.; and Walkley, Kenneth B.: *A Computer Program for Wing Subsonic Aerodynamic Performance Estimates Including Attainable Thrust and Vortex Lift Effects*. NASA CR-3515, 1982.
3. Carlson, Harry W.; and Darden, Christine M.: *Validation of a Pair of Computer Codes for Estimation and Optimization of Subsonic Aerodynamic Performance of Simple Hinged-Flap Systems for Thin Swept Wings*. NASA TP-2828, 1988.
4. Carlson, Harry W.; Darden, Christine M.; and Mann, Michael J.: *Validation of a Computer Code for Analysis of Subsonic Aerodynamic Performance of Wings With Flaps in Combination With a Canard or Horizontal Tail and an Application to Optimization*. NASA TP-2961, 1990.
5. Carlson, Harry W.; and Walkley, Kenneth B.: *Numerical Methods and a Computer Program for Subsonic and Supersonic Aerodynamic Design and Analysis of Wings With Attainable Thrust Considerations*. NASA CR-3808, 1984.
6. Carlson, Harry W.; and Mann, Michael J.: *Survey and Analysis of Research on Supersonic Drag-Due-to-Lift Minimization With Recommendations for Wing Design*. NASA TP-3202, 1992.
7. Carlson, Harry W.; McElroy, Marcus O.; Lessard, Wendy B.; and McCullers, L. Arnold: *Improved Method for Prediction of Attainable Wing Leading-Edge Thrust*. NASA TP-3557, 1996.
8. Carlson, Harry W.; and Walkley, Kenneth B.: *An Aerodynamic Analysis Computer Program and Design Notes for Low Speed Wing Flap Systems*. NASA CR-3675, 1983.
9. Carlson, Harry W.; and Darden, Christine M.: *Applicability of Linearized-Theory Attached-Flow Methods to Design and Analysis of Flap Systems at Low Speeds for Thin Swept Wings With Sharp Leading Edges*. NASA TP-2653, 1987.
10. Carlson, Harry W.; and Miller, David S.: *Numerical Methods for the Design and Analysis of Wings at Supersonic Speeds*. NASA TN D-7713, 1974.
11. Polhamus, Edward C.: Predictions of Vortex-Lift Characteristics by a Leading-Edge Suction Analogy. *J. Aircr.*, vol. 8, no. 4, Apr. 1971, pp. 193–199.
12. Lan, C. Edward; and Chang, Jen-Fu: *Calculation of Vortex Lift Effect for Cambered Wings by the Suction Analogy*. NASA CR-3449, 1981.
13. Harris, Roy V., Jr.: *An Analysis and Correlation of Aircraft Wave Drag*. NASA TM X-947, 1964.
14. Middleton, W. D.; and Lundry, J. L.: *A System for Aerodynamic Design and Analysis of Supersonic Aircraft. Part 1—General Description and Theoretical Development*. NASA CR-3351, 1980.
15. Middleton, W. D.; Lundry, J. L.; and Coleman, R. G.: *A System for Aerodynamic Design and Analysis of Supersonic Aircraft. Part 2—User's Manual*. NASA CR-3352, 1980.
16. Middleton, W. D.; Lundry, J. L.; and Coleman, R. G.: *A System for Aerodynamic Design and Analysis of Supersonic Aircraft. Part 3—Computer Program Description*. NASA CR-3353, 1980.
17. Middleton, W. D.; and Lundry, J. L.: *A System for Aerodynamic Design and Analysis of Supersonic Aircraft. Part 4—Test Cases*. NASA CR-3354, 1980.
18. Sommer, Simon C.; and Short, Barbara J.: *Free-Flight Measurements of Turbulent-Boundary-Layer Skin Friction in the Presence of Severe Aerodynamic Heating at Mach Numbers From 2.8 to 7.0*. NACA TN 3391, 1955.
19. Hall, Charles F.: *Lift, Drag, and Pitching Moment of Low-Aspect-Ratio Wings at Subsonic and Supersonic Speeds*. NACA RM A53A30, 1953.
20. Campbell, Bryan A.; Hom, Kam W.; and Huffman, Jarrett K.: *Investigation of Subsonic Maneuver Performance of a Supersonic Fighter Cranked Wing*. NASA TP-2687, 1987.
21. Capone, Francis J.: *Longitudinal Aerodynamic Characteristics of a Twin-Turbofan Subsonic Transport With Nacelles Mounted Under the Wings*. NASA TN D-5971, 1970.
22. Leavitt, Laurence D.: *Effect of Empennage Location on Twin-Engine Afterbody Slant Nozzle Aerodynamic Characteristics at Mach Numbers From 0.6 to 1.2—Wind Tunnel Tests*. NASA TP-2116, 1983.
23. Yip, Long P.; and Parlett, Lysle P.: *Low-Speed Wind-Tunnel Tests of a 1/10-Scale Model of an Advanced Arrow-Wing Supersonic Cruise Configuration Designed for Cruise at Mach 2.2*. NASA TM-80152, 1979.
24. Radkey, R. L.; Welge, H. R.; and Felix, J. E.: *Aerodynamic Characteristics of a Mach 2.2 Advanced Supersonic Cruise Aircraft Configuration at Mach Numbers From 0.5 to 2.4*. NASA CR-145094, 1977.
25. Abbott, Ira H.; and Von Doenhoff, Albert E.: *Theory of Wing Sections—Including a Summary of Airfoil Data*. Dover Publ., Inc., 1959.
26. Hayes, Wallace D.: *Linearized Supersonic Flow*. Rep. No. AL-222, North American Aviation Inc., 1947.
27. Sears, William R.: On Projectiles of Minimum Wave Drag. *Q. Appl. Math.*, vol. IV, no. 4, Jan. 1947, pp. 361–366.

Table I. Sample Input Data for AERO2S Code

(a) Aspect ratio 2 wing-body

```

AR 2 DELTA - HALL, RM A53A30 5 PCT - TWISTED AND CAMBERED
$INPT1 XM=.61,RN=3.0,JBYMAX=12,ELAR=4.0,
SREF=578.0,CBAR=22.67,XMC=38.12,XMAX=60.44,
CLDES=.3,
NLEY=4,TBLEY=0.000,1.650,2.620,17.00,
      TBLEX=0.000,16.06,26.28,55.12,
NTEY=4,TBTEY=0.000,2.000,2.210,17.00,
      TBTEX=60.44,60.44,55.12,55.12,
NYC=12,TBYC=0.0,2.6,2.62,3.4,5.1,6.8,8.5,10.2,11.9,13.6,15.3,17.0,
NPCTC=9,
TBPCTC=0.000,2.500,5.000,10.00,20.00,40.00,60.00,80.00,100.0,
TZORDC=0.000,0.000,0.000,0.000,0.000,0.000,0.000,0.000,0.000,17*0.0,
      0.000,0.000,0.000,0.000,0.000,0.000,0.000,0.000,0.000,17*0.0,
      0.409,0.510,0.546,0.446,0.211,0.097,0.057,0.023,0.005,17*0.0,
      0.557,0.665,0.708,0.726,0.406,0.200,0.128,0.082,0.053,17*0.0,
      0.836,0.950,1.014,1.087,1.055,0.524,0.330,0.255,0.193,17*0.0,
      1.114,1.226,1.293,1.390,1.480,1.162,0.725,0.548,0.437,17*0.0,
      1.393,1.494,1.564,1.655,1.780,1.815,1.453,1.016,0.819,17*0.0,
      1.672,1.761,1.824,1.922,2.060,2.193,2.178,1.972,1.524,17*0.0,
      1.950,2.023,2.076,2.163,2.296,2.467,2.553,2.569,2.513,17*0.0,
      2.229,2.282,2.324,2.392,2.502,2.665,2.781,2.862,2.917,17*0.0,
      2.508,2.538,2.562,2.604,2.675,2.790,2.883,2.962,3.031,17*0.0,
      2.787,2.787,2.787,2.787,2.787,2.787,2.787,2.787,2.787,17*0.0,
NYR=4,TBYR=0.000,2.600,2.620,17.00,
      TBTOC=0.000,0.000,.0500,.0500,
      TBROC=0.000,0.000,.0028,.0028,
      TBETA=.3000,.3000,.3000,.3000,
NALPHA=13,TALPHA=-4.0,-2.0,0.0,2.0,4.0,6.0,8.0,10.0,12.0,14.0,
16.0,18.0,20.0,      $
AR 2 DELTA - HALL, RM A53A30 5 PCT FLAT
$INPT1 TZSCALE=0.0,      $

```

Table I. Continued
(b) Cranked wing supersonic fighter

SUPERSONIC CRUISE FIGHTER - CAMPBELL, TP 2687 - DLN=15,DTN=10
 \$INPT1 XM=0.50,RN=2.9,JBYMAX=8,ELAR=4.0,IVOROP=1,IPRSLDA=1,
 SREF=163.5,CBAR=12.4,XMC=20.64,XMAX=33.50,
 NLEY=8,TBLEY=0.000,0.470,0.870,1.160,1.190,1.200,5.510,9.550,
 TBLEX=0.000,2.000,4.000,6.000,6.540,12.88,26.37,27.84,
 NTEY=4,TBTEY=0.000,1.200,1.210,9.550,
 TBTEX=33.50,33.50,31.70,29.79,
 NYC=2,TBYC=0.00,9.55,NPCTC=2,TBPCTC=0.00,100.0,TZORDC=52*0.0,
 NYR=5,TBYR=0.000,1.200,5.510,5.520,9.550,
 TBTOC=0.000,.0160,.0400,.0400,.0400,
 TBROC=0.000,.0001,.0004,.0010,.0010,
 TBETA=.5000,.5000,.5000,.5000,.5000,
 NLEFY=5,TBLEFY=0.000,1.200,4.630,5.510,9.550,
 TBLEFC=0.000,0.000,3.310,1.080,.4870,
 TBLEFD=0.000,4.252,4.252,14.67,14.67,
 NTEFY=4,TBTEFY=0.000,1.540,1.550,9.550,
 TBTEFC=0.000,0.000,1.658,.4870,
 TBTEFD=0.000,0.000,9.972,9.972,
 NADLEFD=1,TXMLEFD=0.000,
 NADTEFD=1,TXMTEFD=0.000,
 NALPHA=14,TALPHA=-6.,-4.,-2.,0.0,2.,4.,6.,8.,10.,12.,14.,16.,
 18.,20., \$
 SUPERSONIC CRUISE FIGHTER - CAMPBELL,TP 2687 - DLN=30,DTN=20
 \$INPT1 TBLEFD=0.000,9.100,9.100,29.42,29.42,
 TBTEFD=0.000,0.000,19.94,19.94,NADLEFD=0,NADTEFD=0 \$

Table I. Continued
(c) Subsonic transport

SUBSONIC TRANSPORT WING BODY - CAPONE, TN D-5971
 \$INPT1 XM=.55,RN=2.25,JBYPX=10,ELAR=8.0,
 SREF=3674.3,CBAR=21.17,XMC=83.34,XMAX=171.2,
 NLEY=6,TBLEY=0.000,4.000,8.000,11.22,32.19,87.80,
 TBLEX=0.000,6.000,20.00,60.88,76.09,105.1,
 NTEY=6,TBTEY=0.000,4.000,8.000,11.22,32.19,87.80,
 TBTEX=171.2,160.0,142.0,98.11,98.11,114.8,
 NYC=10,TBYC=0.000,4.0,8.0,11.2,11.22,16.44,25.48,32.19,82.20,87.80,
 NPCTC=9,
 TBPCTC=0.000,2.500,5.000,10.00,20.00,40.00,60.00,80.00,100.0,
 TZORDC=0.000,0.488,0.943,1.752,2.970,3.965,4.645,7.172,12.56,17*0.0,
 0.610,1.010,1.400,2.100,3.100,4.000,4.600,6.300,10.30,17*0.0,
 1.900,2.150,2.400,2.800,3.400,4.000,4.400,5.400,7.650,17*0.0,
 3.800,3.820,3.840,3.880,3.960,4.120,4.280,4.440,4.600,17*0.0,
 0.659,0.700,0.720,0.685,0.505,0.380,0.270,0.160,0.000,17*0.0,
 0.294,0.460,0.495,0.512,0.472,0.375,0.270,0.160,0.000,17*0.0,
 0.000,0.170,0.240,0.340,0.390,0.340,0.255,0.125,0.000,17*0.0,
 0.000,0.128,0.206,0.295,0.347,0.304,0.247,0.131,0.000,17*0.0,
 0.000,0.063,0.101,0.145,0.170,0.149,0.110,0.064,0.000,17*0.0,
 0.000,0.056,0.090,0.129,0.152,0.133,0.108,0.057,0.000,17*0.0,
 NYR=6,TBYR=0.000,11.22,16.44,25.48,32.19,87.80,
 TBTOC=0.145,0.154,0.125,0.100,0.100,0.100,
 TBROC=0.013,0.038,0.018,0.004,0.005,0.005,
 TBETA=0.320,0.200,0.300,0.400,0.400,0.400,
 NALPHA=13,TALPHA=-2.0,-1.0,0.0,1.0,2.0,3.0,4.0,5.0,6.0,7.0,8.0,9.0,
 10.0, \$

Table I. Continued

(d) Supersonic transport wing-body-horizontal tail

SUPERSONIC TRANSPORT WITH DEFLECTED FLAPS AND HORIZONTAL TAIL - YIP, TM 80152
 \$INPT1 XM=0.09,RN=4.19,JBYMAX=10,ELAR=6.0,
 SREF=14400.0,CBAR=77.76,XMC=220.91,XMAX=372.0,
 NLEY=4,TBLEY=0.0000,7.0000,51.710,81.330,
 TBLEX=0.0000,104.70,234.55,280.20,
 NTEY=4,TBTEY=0.0000,7.0000,25.800,81.330,
 TBTEX=372.00,277.70,277.70,294.97,
 NYC=15,TBYC=0.0000,4.4090,13.482,20.899,23.218,27.202,29.498,
 38.294,47.061,49.819,53.701,56.458,67.509,76.399,
 81.330,
 NPCTC=10,
 TBPCTC=0.000,5.000,10.00,20.00,30.00,40.00,50.00,60.00,80.00,100.0,
 TZORDC=14.30,15.20,17.50,17.40,15.40,12.55,10.00,8.000,6.000,10.00,16*0.0,
 13.20,13.20,12.79,11.24,9.250,7.380,5.700,4.250,2.000,.6000,16*0.0,
 6.250,6.780,6.990,6.890,6.200,5.320,4.500,3.770,2.330,1.000,16*0.0,
 4.280,4.850,5.250,5.430,5.130,4.600,4.030,3.500,2.470,1.420,16*0.0,
 4.030,4.600,4.940,5.200,4.980,4.450,3.930,3.430,2.470,1.500,16*0.0,
 3.760,4.270,4.600,4.890,4.660,4.220,3.780,3.300,2.380,1.560,16*0.0,
 3.530,4.000,4.370,4.650,4.430,4.100,3.660,3.200,2.350,1.580,16*0.0,
 1.950,2.430,2.800,3.120,3.070,2.880,2.680,2.450,2.000,1.580,16*0.0,
 0.660,0.960,1.200,1.480,1.600,1.630,1.660,1.630,1.570,1.480,16*0.0,
 0.470,0.700,0.880,1.120,1.250,1.330,1.400,1.420,1.430,1.430,16*0.0,
 0.330,0.450,0.580,0.760,0.900,1.040,1.130,1.210,1.300,1.340,16*0.0,
 0.260,0.370,0.430,0.590,0.720,0.870,0.980,1.070,1.200,1.280,16*0.0,
 0.300,0.310,0.320,0.350,0.410,0.470,0.550,0.620,0.790,0.930,16*0.0,
 0.270,0.270,0.270,0.280,0.290,0.310,0.330,0.360,0.430,0.520,16*0.0,
 0.280,0.280,0.280,0.280,0.280,0.280,0.290,0.300,0.330,0.400,16*0.0,
 NYR=7,TBYR=0.00000,4.40900,20.8990,38.2940,51.7000,51.7100,81.3300,
 TBTOC=0.04000,0.02380,0.02870,0.03000,0.03000,0.03000,0.03000,
 TBROC=0.00000,0.00024,0.00050,0.00048,0.00040,.000003,.000013,
 TBETA=0.50000,0.66000,0.55000,0.58000,0.60000,0.60000,0.60000,
 NLEFY=10,TBLEFY=0.000,7.000,7.010,17.59,17.60,44.42,51.71,64.00,64.01,81.33,
 TBLEFC=0.000,0.000,18.84,18.80,18.80,18.78,8.370,6.770,6.770,4.510,
 TBLEFD=0.000,0.000,4.300,4.300,12.80,12.80,11.20,11.20,17.60,17.60,
 NTEFY=10,TBTEFY=0.000,17.00,17.01,25.80,25.81,36.59,36.60,61.00,61.01,81.33,
 TBTEFC=0.000,0.000,15.93,15.93,0.000,0.000,14.50,9.650,0.000,0.000,
 TBTEFD=0.000,0.000,30.00,30.00,0.000,0.000,30.00,30.00,0.000,0.000,
 NADLEFD=1,TXMLEFD=0.0,
 NADTEFD=1,TXMTEFD=0.0,
 ILS2=2,DELTA2=-5.0,
 NLEY2=2,TBLEY2=2.0000,23.700,
 TBLEX2=323.20,348.99,
 NTEY2=2,TBTEY2=2.0000,23.700,
 TBTEX2=361.00,355.39,
 NYC2=2,TBYC2=2.0000,23.700,NPCTC2=2,TBPCTC2=0.0000,100.0,
 TZORDC2=52*0.0,
 NYR2=2,TBYR2=2.000,23.70,
 TBTOC2=0.035,0.035,
 TBROC2=0.000,0.000,
 TBETA2=0.500,0.500,
 NALPHA=16,TALPHA=-6.0,-4.0,-2.0,0.0,2.0,4.0,6.0,8.0,10.0,12.0,14.0,
 16.0,18.0,20.0,22.0,24.0, \$

Table I. Continued
(e) Two-dimensional airfoil

NACA 4409 AIRFOIL, REPORT 586 - ATTAINABLE THRUST CALIBRATION
 \$INPT1 XM=.06,RN=8.0,JBYMAX=1,ELAR=25.0,IVOROP=0,
 XMCPLT=1.0,
 SREF=2.0,CBAR=1.0,XMC=0.25,XMAX=1.0,
 NLEY=2,TBLEY=0.000,1.000,
 TBLEX=0.000,0.000,
 NTEY=2,TBTEY=0.000,1.000,
 TBTEX=1.000,1.000,
 NYC=2,TBYC=0.0,1.0,NPCTC=10,
 TBPCTC=0.000,2.500,5.000,10.00,20.00,30.00,40.00,60.00,80.00,100.0,
 TZORDC=0.000,.0062,.0104,.0182,.0302,.0374,.0400,.0357,.0235,0.000,
 16*0.0,
 0.000,.0062,.0104,.0182,.0302,.0374,.0400,.0357,.0235,0.000,
 16*0.0,
 NYR=2, TBYR=0.000,1.000,
 TBTOC=0.090,0.090,
 TBROC=.0089,.0089,
 TBETA=.3000,.3000,
 NALPHA=13,TALPHA=-8.0,-6.0,-4.0,-2.0,0.0,2.0,4.0,6.0,8.0,10.0,12.0,
 14.0,16.0, \$
 XMCPLT=0.80
 \$INPT1 XMCPLT=0.80, \$
 XMCPLT=0.60
 \$INPT1 XMCPLT=0.60, \$

Table I. Continued

(f) Supersonic transport flap system evaluation

SUPERSONIC TRANSPORT EXAMPLE - FLAP EVALUATION
 \$INPT1 XM=.3,RN=2.0,JBYMAX=10,ELAR=4.0,
 SREF=2.65,CBAR=1.85,XMC=2.77,XMAX=5.47,
 CLDES=.6,
 NLEY=13,
 TBLEY=0.00,0.04,0.10,0.112,0.20,0.30,0.40,0.50,0.60,0.70,0.80,0.90,1.00,
 TBLEX=0.00,0.20,1.00,1.425,1.95,2.55,3.02,3.32,3.56,3.78,4.00,4.22,4.43,
 NTEY=13,
 TBTEY=0.00,0.04,0.10,0.112,0.20,0.30,0.40,0.50,0.60,0.70,0.80,0.90,1.00,
 TBTEX=5.47,5.15,4.28,4.075,4.11,4.18,4.26,4.34,4.43,4.51,4.60,4.68,4.76,
 NYR=4,TBYR=0.0000,0.5000,0.8000,1.0000,
 TBTOC=0.0300,0.0300,0.0300,0.0300,
 TBROC=.00030,.00030,.00050,.00050,
 TBETA=0.5000,0.5000,0.5000,0.5000,
 NYC=20,
 TBYC=0.0000,0.0405,0.0946,0.1486,0.2027,
 0.2568,0.3108,0.3649,0.4189,0.4730,
 0.5270,0.5811,0.6351,0.6892,0.7432,
 0.7973,0.8514,0.9054,0.9595,1.0000,
 NPCTC=13,
 TBPCTC=0.00,5.00,10.0,15.0,20.0,30.0,40.0,50.0,60.0,70.0,80.0,90.0,100.0,
 TZORDC=
 0.000000, -0.004681, -0.019204, -0.037864, -0.058624, -0.102124,
 -0.143945, -0.180760, -0.210323, -0.230986,
 -0.241472, -0.240753, -0.227979, 13*0.000000,
 0.000000, -0.000794, -0.008815, -0.020353, -0.034084, -0.065313,
 -0.098756, -0.132249, -0.164330, -0.193929,
 -0.220214, -0.242517, -0.260285, 13*0.000000,
 0.000000, 0.002250, 0.001000, -0.002214, -0.006841, -0.019173,
 -0.034445, -0.051759, -0.070511, -0.090256,
 -0.110650, -0.131416, -0.152325, 13*0.000000,
 0.000000, 0.002784, 0.003749, 0.003652, 0.002763, -0.000819,
 -0.006233, -0.013038, -0.020937, -0.029711,
 -0.039191, -0.049239, -0.047659, 13*0.000000,
 0.000000, 0.002826, 0.004374, 0.005197, 0.005492, 0.004920,
 0.003218, 0.000706, -0.002395, -0.005927,
 -0.009765, -0.006247, -0.006488, 13*0.000000,
 0.000000, 0.003150, 0.005279, 0.006864, 0.008072, 0.009720,
 0.010703, 0.011297, 0.011690, 0.012018,
 0.012749, 0.014052, 0.011896, 13*0.000000,
 0.000000, 0.003687, 0.006449, 0.008736, 0.010709, 0.014054,
 0.016938, 0.019622, 0.022285, 0.025056,
 0.028782, 0.032042, 0.032985, 13*0.000000,
 0.000000, 0.003996, 0.007093, 0.009734, 0.012077, 0.016207,
 0.019930, 0.023506, 0.027108, 0.030866,
 0.038234, 0.044912, 0.047363, 13*0.000000,
 0.000000, 0.004165, 0.007439, 0.010255, 0.012769, 0.017219,
 0.021225, 0.025039, 0.028834, 0.033458,
 0.040849, 0.046328, 0.048703, 13*0.000000,

Table I. Concluded

(f) Concluded

0.000000,	0.004015,	0.007141,	0.009803,	0.012153,	0.016236,
0.019821,	0.023154,	0.026402,	0.029545,		
0.032310,	0.034719,	0.036816,	13*0.000000,		
0.000000,	0.003587,	0.006314,	0.008581,	0.010531,	0.013782,
0.016472,	0.018834,	0.021203,	0.024716,		
0.027540,	0.029189,	0.029484,	13*0.000000,		
0.000000,	0.003272,	0.005721,	0.007716,	0.009387,	0.012037,
0.014042,	0.015617,	0.017326,	0.022147,		
0.026038,	0.027793,	0.026923,	13*0.000000,		
0.000000,	0.003022,	0.005289,	0.007120,	0.008629,	0.010923,
0.012492,	0.013523,	0.014141,	0.019504,		
0.025285,	0.028579,	0.028468,	13*0.000000,		
0.000000,	0.002919,	0.005129,	0.006919,	0.008392,	0.010606,
0.012064,	0.012933,	0.013328,	0.017458,		
0.022008,	0.027143,	0.029196,	13*0.000000,		
0.000000,	0.002687,	0.004845,	0.006657,	0.008188,	0.010546,
0.012104,	0.012968,	0.013209,	0.012882,		
0.016794,	0.022316,	0.026000,	13*0.000000,		
0.000000,	0.002574,	0.004769,	0.006690,	0.008372,	0.011099,
0.013056,	0.014303,	0.014880,	0.014816,		
0.014202,	0.017284,	0.020543,	13*0.000000,		
0.000000,	0.002450,	0.004689,	0.006741,	0.008613,	0.011840,
0.014391,	0.016282,	0.017520,	0.018114,		
0.018069,	0.017478,	0.018368,	13*0.000000,		
0.000000,	0.002307,	0.004567,	0.006734,	0.008790,	0.012535,
0.015754,	0.018420,	0.020515,	0.022024,		
0.022938,	0.023247,	0.022945,	13*0.000000,		
0.000000,	0.002143,	0.004383,	0.006618,	0.008811,	0.012994,
0.016828,	0.020254,	0.023230,	0.025728,		
0.027724,	0.029200,	0.030140,	13*0.000000,		
0.000000,	0.001989,	0.004165,	0.006396,	0.008634,	0.013030,
0.017221,	0.021127,	0.024697,	0.027894,		
0.030686,	0.033050,	0.034967,	13*0.000000,		

NLEFY=14,
TBLEFY=0.00, .111, .112, .200, .300, .399, .400, .500, .600, .699, .700, .800, .900, 1.00,
TBLEFC=0.00, 0.00, 0.00, .248, .248, .248, .248, .156, .123, .111, .111, .098, .086, .083,
TBLEFD=0.00, 0.00, 26.0, 26.0, 26.0, 26.0, 32.0, 32.0, 32.0, 32.0, 36.0, 36.0, 36.0, 36.0,
NTEFY=16,
TBTEFY=0.00, .111, .112, .189, .190, .310, .311, .389, .390,
.510, .511, .600, .700, .800, .900, 1.00,
TBTEFC=0.00, 0.00, .203, .234, 0.00, 0.00, .304, .276, 0.00,
0.00, .235, .213, .177, .153, .118, .083,
TBTEFD=0.00, 0.00, 14.0, 14.0, 0.00, 0.00, 14.0, 14.0, 0.00,
0.00, 16.0, 16.0, 16.0, 16.0, 16.0, 16.0, 16.0, 16.0, 16.0,
NADLEFD=1, TXMLEFD=0.0,
NADTEFD=1, TXMTEFD=0.0,
NALPHA=16, TALPHA=0.0, 2.0, 4.0, 6.0, 8.0, 10.0, 12.0, 14.0, 16.0, 18.0,
20.0, 22.0, 24.0, 26.0, 28.0, 30.0, \$

Table II. Sample Input Data for WINGDES Code

(a) Supersonic transport wing evaluation

```

CURVED L E WING - DARDEN, TP-2446 T & C NO CONSTRAINT
$INPT1 XM=2.4,RN=2.0,JBYMAX=40,IEMPCR=1,
SREF=2.5375,CBAR=1.686,XMC=1.43,XMAX=3.29,
NLEY=11,
TBLEY=0.00,0.10,0.20,0.30,0.40,0.50,0.60,0.70,0.80,0.90,1.00,
TBLEX=0.00,0.12,0.48,1.08,1.55,1.85,2.09,2.31,2.53,2.75,2.96,
NTEY=11,
TBTEY=0.00,0.10,0.20,0.30,0.40,0.50,0.60,0.70,0.80,0.90,1.00,
TBTEX=2.58,2.60,2.64,2.71,2.79,2.87,2.96,3.04,3.13,3.21,3.29,
NYR=4,TBYR=0.0000,0.5000,0.8000,1.0000,
      TBTOC=0.0300,0.0300,0.0300,0.0300,
      TBROC=.00010,.00030,.00050,.00050,
      TBETA=0.5000,0.5000,0.5000,0.5000,
NYC=11,TBYC=0.00,0.10,0.20,0.30,0.40,0.50,0.60,0.70,0.80,0.90,1.00,
NPCTC=9,
TBPCTC=0.000,5.000,10.00,20.00,30.00,40.00,60.00,80.00,100.0,
TZORDC=.1182,.1083,.0965,.0721,.0494,.0307,.0063,-.004,-.013,17*0.0,
      .1345,.1290,.1195,.0968,.0727,.0501,.0139,-.012,-.035,17*0.0,
      .1099,.1156,.1127,.0972,.0764,.0544,.0151,-.012,-.027,17*0.0,
      .0357,.0487,.0557,.0560,.0485,.0374,.0122,-.011,-.028,17*0.0,
      .0059,.0123,.0157,.0184,.0176,.0148,.0054,-.006,-.017,17*0.0,
      .0026,.0053,.0073,.0090,.0088,.0075,.0029,-.003,-.010,17*0.0,
      .0018,.0029,.0039,.0048,.0046,.0040,.0015,-.002,-.005,17*0.0,
      .0007,.0013,.0018,.0023,.0023,.0019,.0008,-.001,-.002,17*0.0,
      .0000,.0003,.0007,.0013,.0015,.0016,.0014,.0010,.0006,17*0.0,
      .0000,.0002,.0005,.0010,.0013,.0016,.0019,.0022,.0023,17*0.0,
      .0000,.0001,.0002,.0004,.0015,.0025,.0050,.0075,.0102,17*0.0,
CLZPR=.08,
NALPHA=17,TALPHA=-6.0,-5.0,-4.0,-3.0,-2.0,-1.0,0.0,1.0,2.0,3.0,
      4.0,5.0,6.0,7.0,8.0,9.0,10.0,      $
CURVED L E WING - DARDEN TP-2446 FLAT WING
$INPT1 TZSCALE=0.0,CLZPR=.08,IEMPCR=0,      $

```

Table II. Continued

(b) Supersonic transport cruise surface design

SUPERSONIC TRANSPORT EXAMPLE - WHOLE WING DESIGN-INC FUSE - M=2.4
 \$INPT1 XM=2.4, RN=2.0, JBYMAX=40, IEMPCR=1,
 SREF=2.65, CBAR=1.85, XMC=2.77, XMAX=5.47,
 NLEY=13,
 TBLEY=0.00, 0.04, 0.10, 0.112, 0.20, 0.30, 0.40, 0.50, 0.60, 0.70, 0.80, 0.90, 1.00,
 TBLEX=0.00, 0.20, 1.00, 1.425, 1.95, 2.55, 3.02, 3.32, 3.56, 3.78, 4.00, 4.22, 4.43,
 NTEY=13,
 TBTEY=0.00, 0.04, 0.10, 0.112, 0.20, 0.30, 0.40, 0.50, 0.60, 0.70, 0.80, 0.90, 1.00,
 TBTEX=5.47, 5.15, 4.28, 4.075, 4.11, 4.18, 4.26, 4.34, 4.43, 4.51, 4.60, 4.68, 4.76,
 NYR=4, TBYR=0.0000, 0.5000, 0.8000, 1.0000,
 TBTOC=0.0300, 0.0300, 0.0300, 0.0300,
 TBROC=.00030, .00030, .00050, .00050,
 TBETA=0.5000, 0.5000, 0.5000, 0.5000,
 CLDES=.12,
 NALPHA=19, TALPHA=-2.0, -1.5, -1.0, -0.5, 0.5, 1.0, 1.5, 2.0, 2.5,
 3.0, 3.5, 4.0, 4.5, 5.0, 5.5, 6.0, 6.5, 7.0, 7.5, \$

(c) Supersonic transport cruise surface design with imposed leading-edge surface factors

SUPERSONIC TRANSPORT EXAMPLE - WHOLE WING DESIGN-INC FUSE - M=2.4
 \$INPT1 XM=2.4, RN=2.0, JBYMAX=40, IEMPCR=1,
 SREF=2.65, CBAR=1.85, XMC=2.77, XMAX=5.47,
 NLEY=13,
 TBLEY=0.00, 0.04, 0.10, 0.112, 0.20, 0.30, 0.40, 0.50, 0.60, 0.70, 0.80, 0.90, 1.00,
 TBLEX=0.00, 0.20, 1.00, 1.425, 1.95, 2.55, 3.02, 3.32, 3.56, 3.78, 4.00, 4.22, 4.43,
 NTEY=13,
 TBTEY=0.00, 0.04, 0.10, 0.112, 0.20, 0.30, 0.40, 0.50, 0.60, 0.70, 0.80, 0.90, 1.00,
 TBTEX=5.47, 5.15, 4.28, 4.075, 4.11, 4.18, 4.26, 4.34, 4.43, 4.51, 4.60, 4.68, 4.76,
 NYR=4, TBYR=0.0000, 0.5000, 0.8000, 1.0000,
 TBTOC=0.0300, 0.0300, 0.0300, 0.0300,
 TBROC=.00030, .00030, .00050, .00050,
 TBETA=0.5000, 0.5000, 0.5000, 0.5000,
 IAFIX=1,
 TAFIX=0.00, 0.00, 0.00, 0.00, 0.00, 0.00, 0.00, 0.51, 1.04, 1.56,
 2.08, 2.60, 3.12, 3.64, 3.64, 3.64, 3.64, 3.64, 3.64, 3.64,
 3.64, 3.64, 3.64, 3.64, 3.64, 3.64, 3.64, 3.64, 3.64, 3.64,
 3.64, 3.64, 3.64, 3.64, 3.64, 3.64, 3.64,
 CLDES=.12,
 NALPHA=19, TALPHA=-2.0, -1.5, -1.0, -0.5, 0.5, 1.0, 1.5, 2.0, 2.5,
 3.0, 3.5, 4.0, 4.5, 5.0, 5.5, 6.0, 6.5, 7.0, 7.5, \$

Table II. Continued

(d) Supersonic transport cruise surface design with reflexing

SUPERSONIC TRANSPORT EXAMPLE - REFLEX DESIGN WITH NACELLE PRESSURES AT M=2.4
 \$INPT1 XM=2.4,RN=2.0,JBYMAX=40,IEMPCR=1,
 SREF=2.65,CBAR=1.85,XMC=2.77,XMAX=5.47,
 NLEY=13,
 TBLEY=0.00,0.04,0.10,0.112,0.20,0.30,0.40,0.50,0.60,0.70,0.80,0.90,1.00,
 TBLEX=0.00,0.20,1.00,1.425,1.95,2.55,3.02,3.32,3.56,3.78,4.00,4.22,4.43,
 NTEY=13,
 TBTEY=0.00,0.04,0.10,0.112,0.20,0.30,0.40,0.50,0.60,0.70,0.80,0.90,1.00,
 TBTEX=5.47,5.15,4.28,4.075,4.11,4.18,4.26,4.34,4.43,4.51,4.60,4.68,4.76,
 NYR=4,TBYR=0.0000,0.5000,0.8000,1.0000,
 TBTOC=0.0300,0.0300,0.0300,0.0300,
 TBROC=.00030,.00030,.00050,.00050,
 TBETA=0.5000,0.5000,0.5000,0.5000,
 NTES=4
 NTEC=13,
 TBTECY = 0.0,0.112,0.2,0.25,0.3,0.4,0.45,0.5,0.6,0.7,0.8,0.9,1.0,
 TBTEC=0.0,0.0,0.346,0.417,0.424,0.372,0.429,0.428,0.365,0.248,0.120,0.,0.,
 IREFL=1, ICP=1,
 NYCP=13,
 TBYCP= 0.0,0.112,0.2,0.25,0.3,0.4,0.45,0.5,0.6,0.7,0.8,0.9,1.0,
 NPCTCP = 20,
 TBPCTCP = 0.,50.,54.,58.,62.,66.,70.,74.,78.,80.,
 82.,84.,86.,88.,90.,92.,94.,96.,98.,100.,
 TCP= 0.00000,0.00000,0.00000,0.00000,0.00000,0.00000,0.00000,0.00000,
 0.00000,0.00000,0.00000,0.00000,0.00000,0.00000,0.00000,0.00000,
 0.00000,0.00000,0.00000,0.00000,0.00000,0.00000,0.00000,0.00000,
 0.00000,0.00000,0.00000,0.00000,0.00000,0.00000,0.00000,0.00000,
 0.00000,0.00000,0.00000,0.00000,0.00000,0.00000,0.00000,0.00000,
 0.00000,0.03775,0.06469,0.03930,0.00000,0.00000,0.00000,0.00000,
 0.00000,0.00000,
 0.00000,0.00000,0.00000,0.00000,0.00000,0.00000,0.00000,0.00000,
 0.00000,0.00000,0.00000,0.00000,0.00000,0.00000,0.00000,0.00000,
 0.00000,0.03775,0.06469,0.03930,0.00000,0.00000,0.00000,0.00000,
 0.00000,0.00000,
 0.00000,0.00000,0.00000,0.00000,0.00000,0.00000,0.00000,0.00000,
 0.00000,0.00000,0.00000,0.00000,0.00000,0.05550,0.04469,0.07734,0.04332,
 0.01874,0.01756,0.01616,0.00607,0.00000,0.00000,0.00000,0.00000,
 0.00000,0.00000,
 0.00000,0.00000,0.00000,0.00000,0.00000,0.00000,0.00000,0.00000,
 0.00000,0.05218,0.05195,0.04697,0.07535,0.04200,0.02145,0.01901,
 0.01793,0.00941,-.01186,-.04329,0.00000,0.00000,0.00000,0.00000,
 0.00000,0.00000,
 0.00000,0.00000,0.00000,0.00000,0.00000,0.00000,0.00000,0.00000,
 0.05156,0.04479,0.08583,0.05949,0.03513,0.02044,0.01760,0.01729,
 0.01273,0.04051,0.01629,0.01619,0.00000,0.00000,0.00000,0.00000,
 0.00000,0.00000,
 0.00000,0.00000,0.00000,0.00000,0.00000,0.00000,0.00000,0.04091,
 0.08278,0.10878,0.14220,0.10866,0.07703,0.04975,0.03432,0.03134,
 0.03108,0.02847,0.02141,0.00706,0.00000,0.00000,0.00000,0.00000,
 0.00000,0.00000,
 0.00000,0.00000,0.00000,0.00000,0.00000,0.06732,0.05093,0.09089,
 0.04847,0.03030,0.02231,0.01977,0.01964,0.01912,0.01517,0.00951,
 -.00241,-.02088,-.04112,-.06222,0.00000,0.00000,0.00000,0.00000,
 0.00000,0.00000,

Table II. Continued

(d) Concluded

0.00000,0.00000,0.00000,0.00000,0.05773,0.04634,0.08295,0.04924,
0.02014,0.01816,0.01809,0.01793,0.01747,0.01410,0.00862,0.00019,
-.01284,-.02787,-.04448,-.06110,0.00000,0.00000,0.00000,0.00000,
0.00000,0.00000,
0.00000,0.00000,0.00000,0.00000,0.04349,0.03549,0.06035,0.04847,
0.03186,0.02429,0.01719,0.01452,0.01338,0.01333,0.01331,0.01284,
0.01154,0.00860,0.00523,0.00022,0.00000,0.00000,0.00000,0.00000,
0.00000,0.00000,
0.00000,0.00000,0.00000,0.00000,0.00000,0.00000,0.03280,0.02813,
0.05134,0.04636,0.04137,0.03638,0.03140,0.02656,0.02229,0.01808,
0.01386,0.01122,0.01076,0.01073,0.00000,0.00000,0.00000,0.00000,
0.00000,0.00000,
0.00000,0.00000,0.00000,0.00000,0.00000,0.00000,0.00000,0.00000,
0.00000,0.00000,0.02296,0.02581,0.02451,0.02361,0.04242,0.04115,
0.03809,0.03503,0.03196,0.02890,0.00000,0.00000,0.00000,0.00000,
0.00000,0.00000,
0.00000,0.00000,0.00000,0.00000,0.00000,0.00000,0.00000,0.00000,
0.00000,0.00000,0.00000,0.00000,0.00000,0.00000,0.00000,0.00000,
0.00000,0.00000,0.00000,0.00000,0.00000,0.00000,0.00000,0.00000,
0.00000,0.00000,
0.00000,0.00000,0.00000,0.00000,0.00000,0.00000,0.00000,0.00000,
0.00000,0.00000,0.00000,0.00000,0.00000,0.00000,0.00000,0.00000,
0.00000,0.00000,0.00000,0.00000,0.00000,0.00000,0.00000,0.00000,
0.00000,0.00000,
CLDES=.12,
NALPHA=19, TALPHA=-2.0,-1.5,-1.0,-0.5,0.5,1.0,1.5,2.0,2.5,
3.0,3.5,4.0,4.5,5.0,5.5,6.0,6.5,7.0,7.5, \$

Table II. Continued

(e) Supersonic transport reflexed cruise surface design with imposed leading-edge surface factors followed by subsonic flap system design

SUPERSONIC TRANSPORT EXAMPLE - REFLEX DESIGN WITH NACELLE PRESSURES AT M=2.4
 \$INPT1 XM=2.4,RN=2.0,JBYMAX=40,IEMPCR=1,
 SREF=2.65,CBAR=1.85,XMC=2.77,XMAX=5.47,
 CLDES=.12,
 NLEY=13,
 TBLEY=0.00,0.04,0.10,0.112,0.20,0.30,0.40,0.50,0.60,0.70,0.80,0.90,1.00,
 TBLEX=0.00,0.20,1.00,1.425,1.95,2.55,3.02,3.32,3.56,3.78,4.00,4.22,4.43,
 NTEY=13,
 TBTEY=0.00,0.04,0.10,0.112,0.20,0.30,0.40,0.50,0.60,0.70,0.80,0.90,1.00,
 TBTEX=5.47,5.15,4.28,4.075,4.11,4.18,4.26,4.34,4.43,4.51,4.60,4.68,4.76,
 NYR=4,TBYR=0.0000,0.5000,0.8000,1.0000,
 TBTOC=0.0300,0.0300,0.0300,0.0300,
 TBROC=.00030,.00030,.00050,.00050,
 TBETA=0.5000,0.5000,0.5000,0.5000,
 NTES=4,
 NTEC=13,
 TBTECY = 0.0,0.112,0.2,0.25,0.3,0.4,0.45,0.5,0.6,0.7,0.8,0.9,1.0,
 TBTEC=0.0,0.0,0.346,0.417,0.424,0.372,0.429,0.428,0.365,0.248,0.120,0.,0.,
 IREFL=1, ICP=1,
 NYCP=13,
 TBYCP= 0.0,0.112,0.2,0.25,0.3,0.4,0.45,0.5,0.6,0.7,0.8,0.9,1.0,
 NPCTCP = 20,
 TBPCTCP = 0.,50.,54.,58.,62.,66.,70.,74.,78.,80.,
 82.,84.,86.,88.,90.,92.,94.,96.,98.,100.,
 TCP= 0.00000,0.00000,0.00000,0.00000,0.00000,0.00000,0.00000,0.00000,
 0.00000,0.00000,0.00000,0.00000,0.00000,0.00000,0.00000,0.00000,
 0.00000,0.00000,0.00000,0.00000,0.00000,0.00000,0.00000,0.00000,
 0.00000,0.00000,0.00000,0.00000,0.00000,0.00000,0.00000,0.00000,
 0.00000,0.00000,0.00000,0.00000,0.00000,0.00000,0.00000,0.00000,
 0.00000,0.03775,0.06469,0.03930,0.00000,0.00000,0.00000,0.00000,
 0.00000,0.00000,
 0.00000,0.00000,0.00000,0.00000,0.00000,0.00000,0.00000,0.00000,
 0.00000,0.00000,0.00000,0.00000,0.05550,0.04469,0.07734,0.04332,
 0.01874,0.01756,0.01616,0.00607,0.00000,0.00000,0.00000,0.00000,
 0.00000,0.00000,
 0.00000,0.00000,0.00000,0.00000,0.00000,0.00000,0.00000,0.00000,
 0.00000,0.05218,0.05195,0.04697,0.07535,0.04200,0.02145,0.01901,
 0.01793,0.00941,-.01186,-.04329,0.00000,0.00000,0.00000,0.00000,
 0.00000,0.00000,
 0.00000,0.00000,0.00000,0.00000,0.00000,0.00000,0.00000,0.00000,
 0.05156,0.04479,0.08583,0.05949,0.03513,0.02044,0.01760,0.01729,
 0.01273,0.04051,0.01629,0.01619,0.00000,0.00000,0.00000,0.00000,
 0.00000,0.00000,
 0.00000,0.00000,0.00000,0.00000,0.00000,0.00000,0.00000,0.04091,
 0.08278,0.10878,0.14220,0.10866,0.07703,0.04975,0.03432,0.03134,
 0.03108,0.02847,0.02141,0.00706,0.00000,0.00000,0.00000,0.00000,
 0.00000,0.00000,
 0.00000,0.00000,0.00000,0.00000,0.00000,0.06732,0.05093,0.09089,
 0.04847,0.03030,0.02231,0.01977,0.01964,0.01912,0.01517,0.00951,

Table II. Concluded
(f) Nonsymmetrical wing cruise surface design

```

NONSYMMETRICAL ELLIPTICAL WING DESIGN
$INPT1 XM=1.4,RN=2.0,JBYPMAX=40,IPRSLD=1,IEMPCR=1,
CLDES=.16,YCG=.5,
NSYM=1,
SREF=3.142,CBAR=2.0,XMC=2.0,XMAX=4.0,
NLEY=11,
TBLEY=0.000,.2000,.4000,.6000,.8000,1.000,1.200,1.400,1.600,1.800,2.000,
TBLEX=0.268,0.014,0.161,0.392,0.674,1.000,1.366,1.777,2.239,2.785,3.732,
NTEY=11,
TBTEY=0.000,.2000,.4000,.6000,.8000,1.000,1.200,1.400,1.600,1.800,2.000,
TBTEX=0.269,1.215,1.761,2.223,2.634,3.000,3.326,3.609,3.839,3.986,3.733,
NLEC=2,
TBLECY=0.0,2.0,
TBLEC =2.0,2.0,
NYR=4,
TBYR =0.000,.2000,1.800,2.000,
TBTOC=.0400,.0400,.0400,.0400,
TBROC=.0010,.0010,.0010,.0100,
TBETA=.4000,.4000,.4000,.4000,
NALPHA=14,
TALPHA=0.00,1.0,2.0,3.0,4.0,5.0,6.0,7.0,8.0,9.0,10.0,11.0,12.0,5.25,    $

```

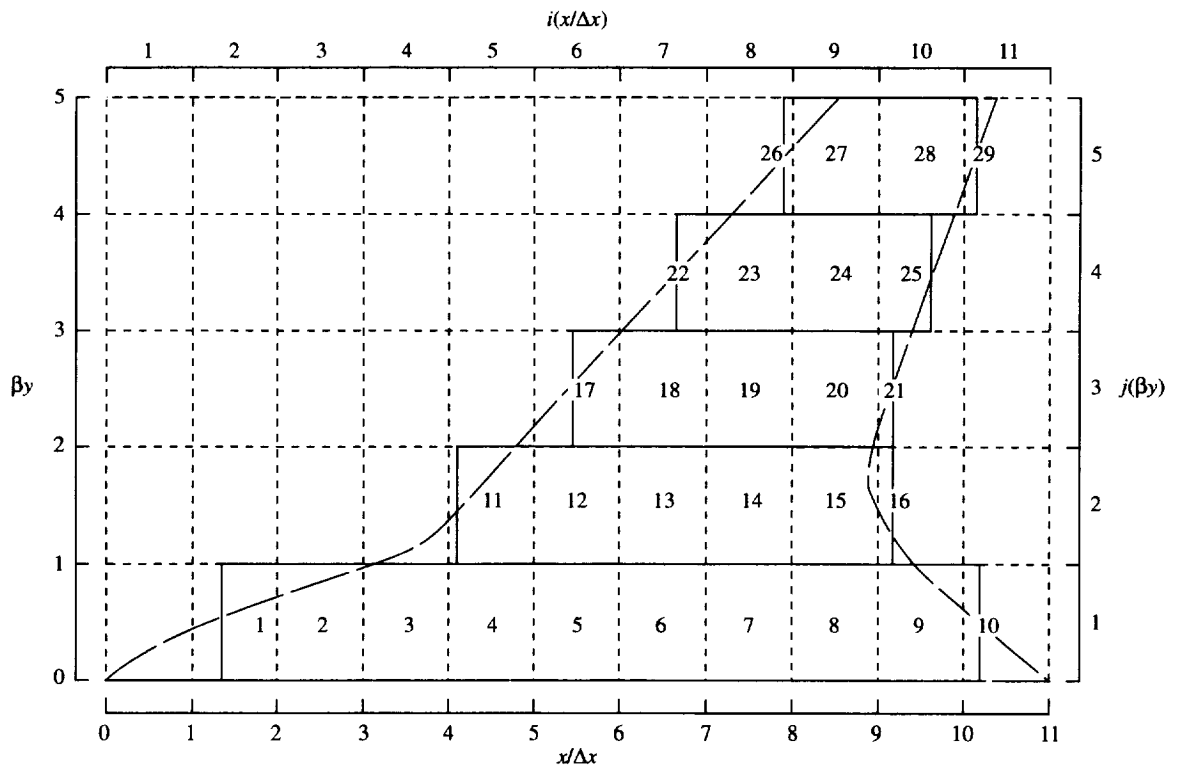
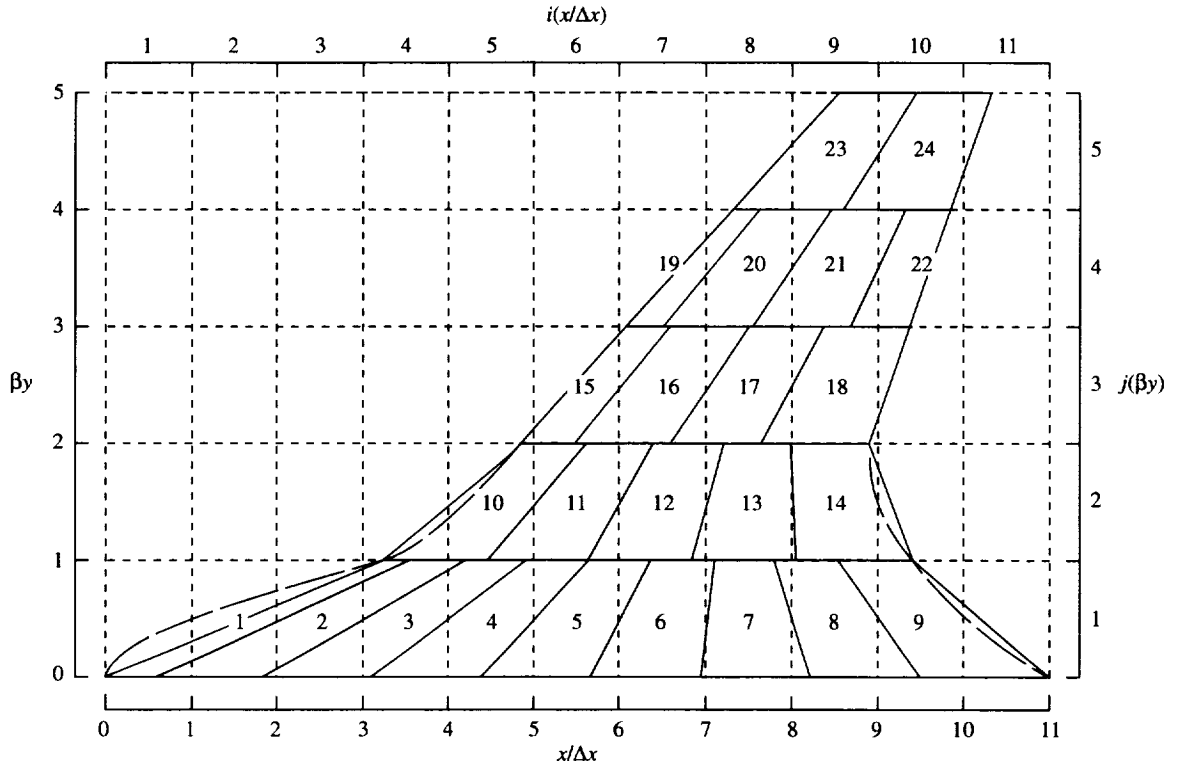


Figure 1. Grid system used in numerical solution of linearized theory.

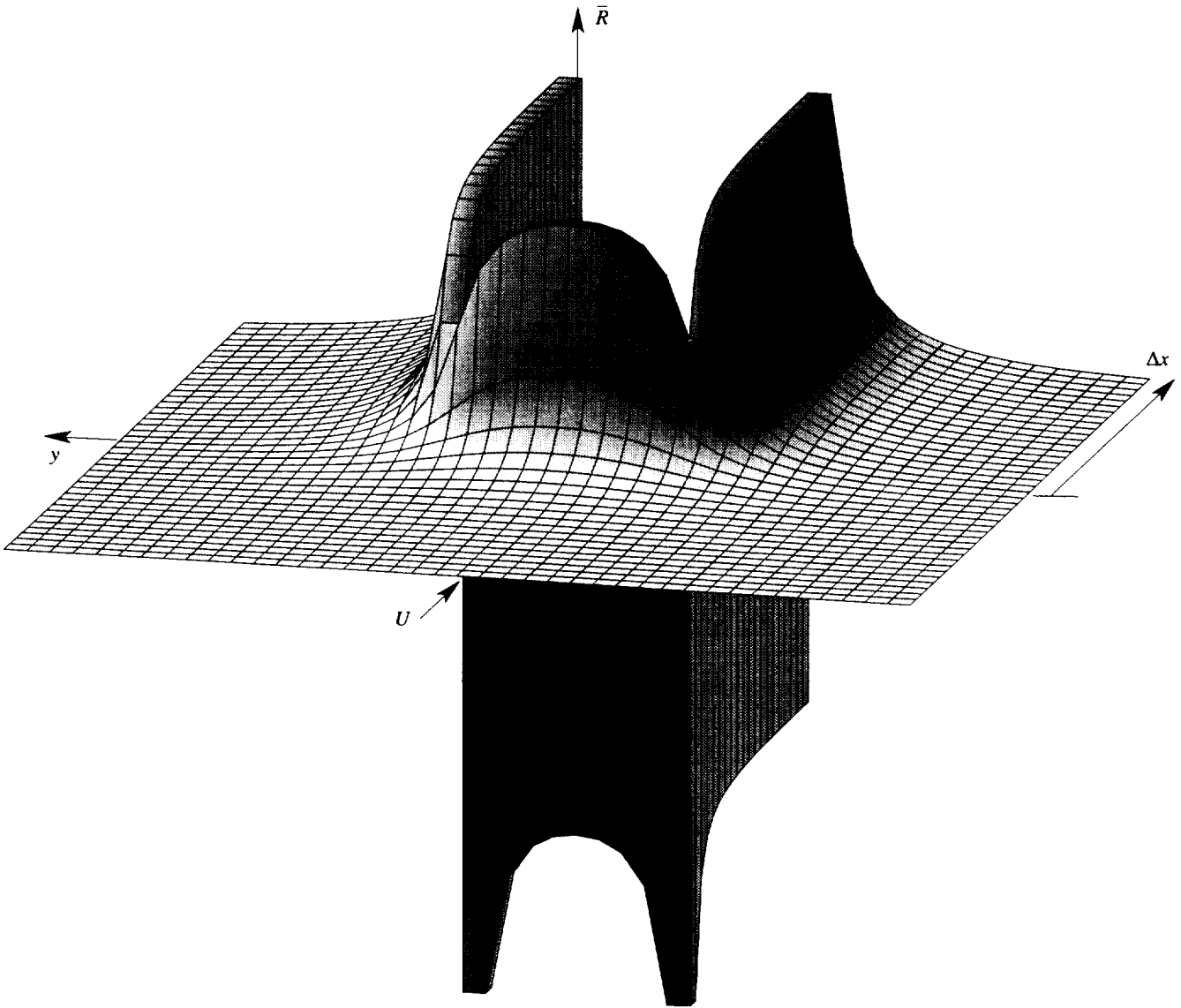


Figure 2. Subsonic influence function.

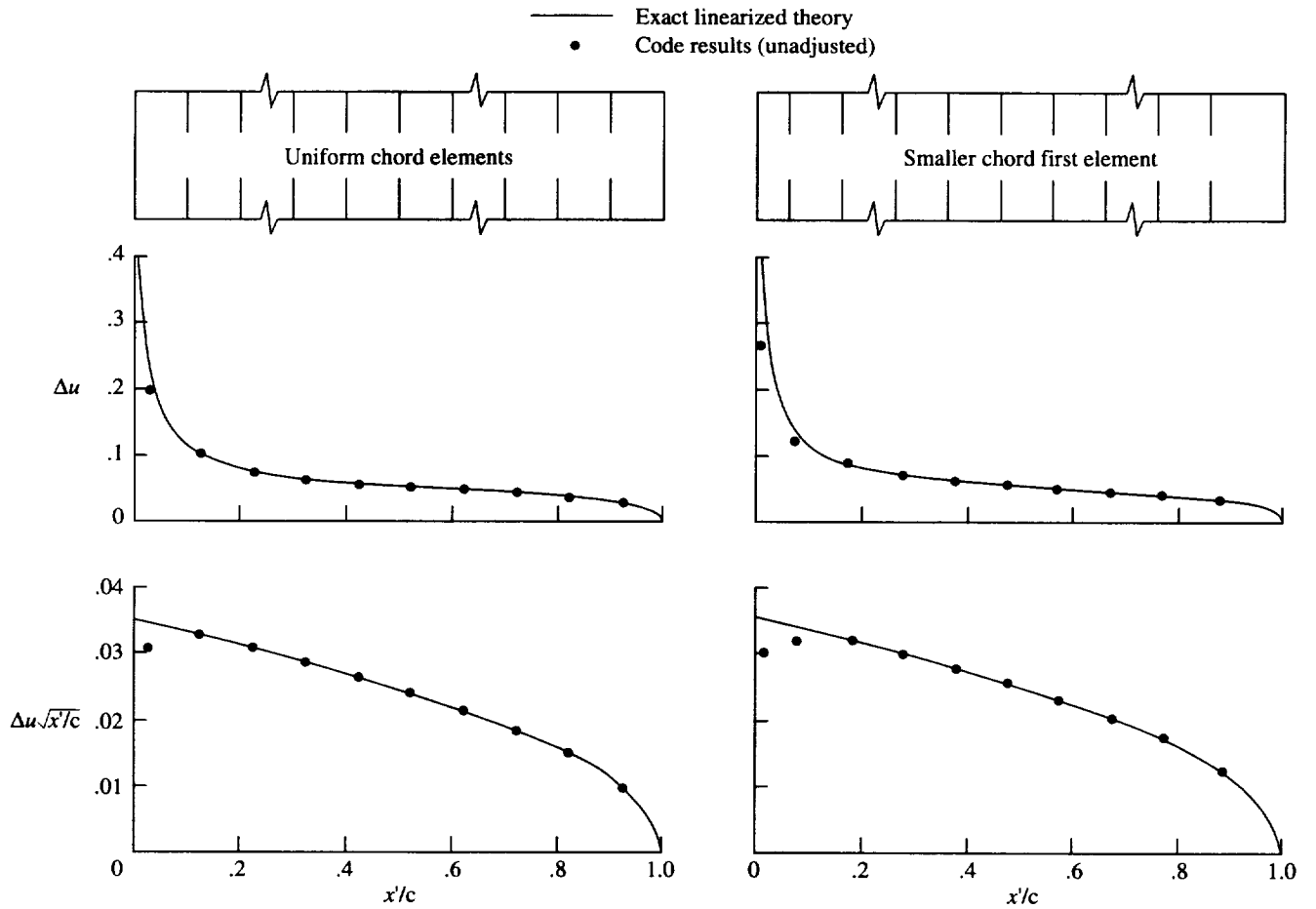


Figure 3. Typical code results for flat two-dimensional wing. $M = 0.01$; $\alpha = 1^\circ$.

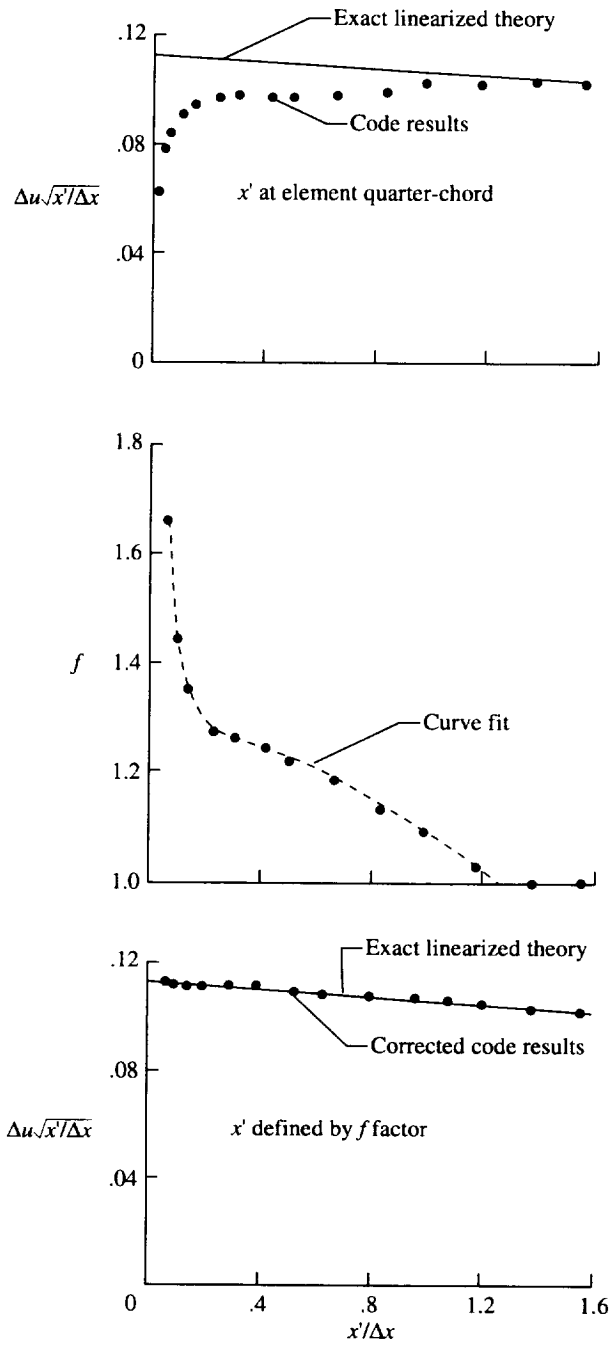


Figure 4. Correction of code perturbation velocity location.

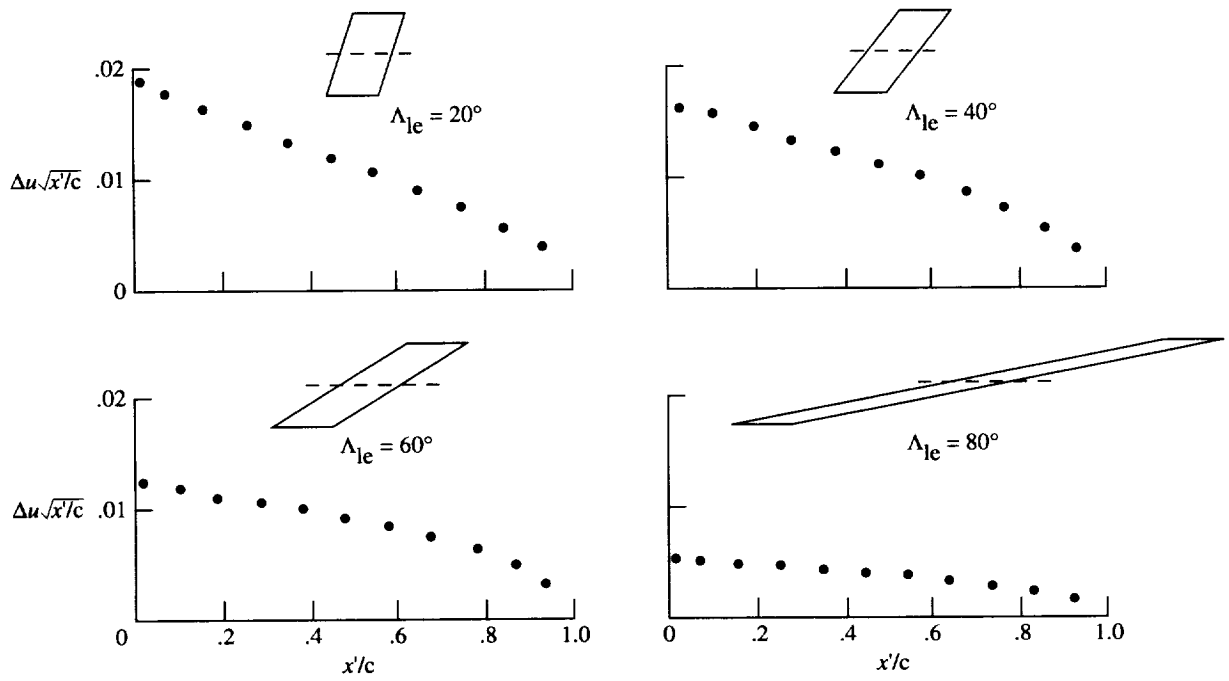
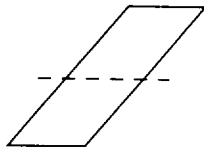


Figure 5. Code velocity distributions for various sweep angles. Flat wing; $M = 0.01$; $\alpha = 1^\circ$.



$\Lambda_{1e} = 40^\circ$

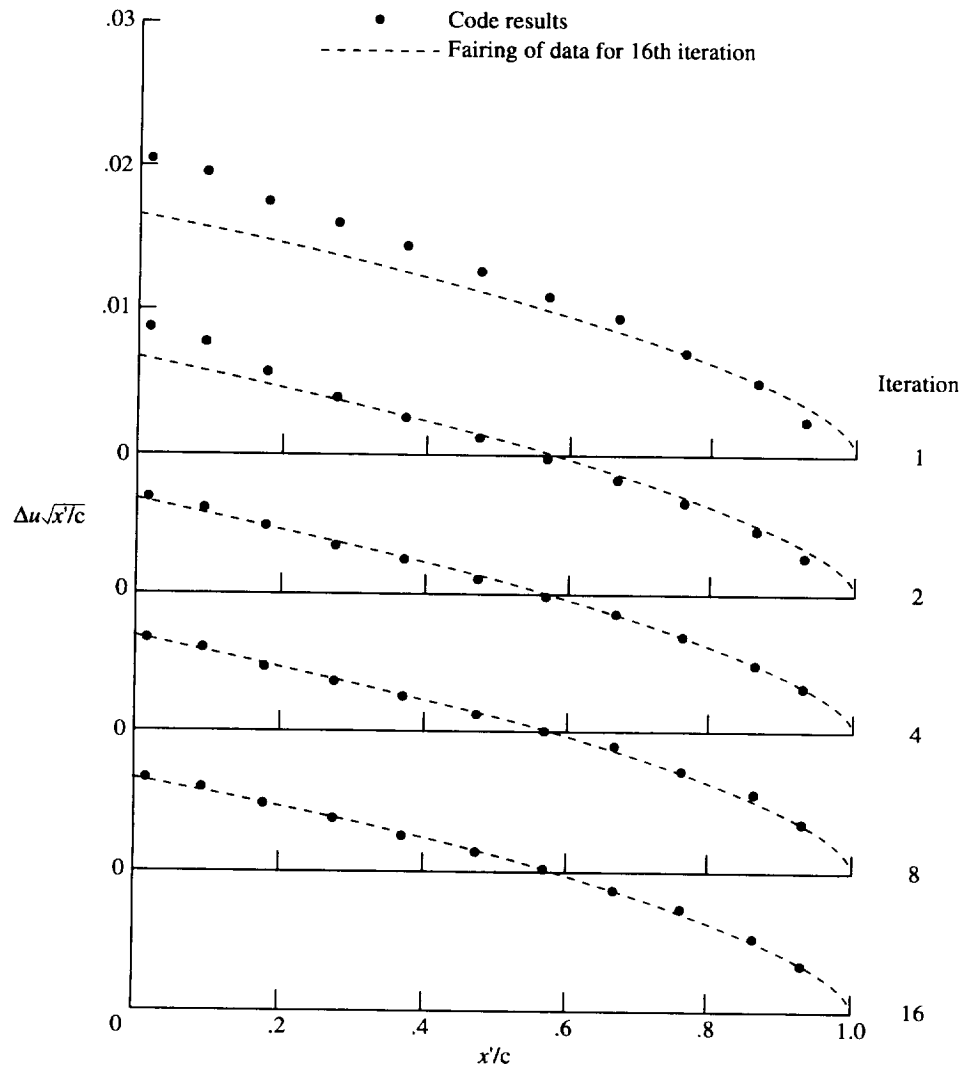


Figure 6. Illustration of solution convergence. $M = 0.01$; $\alpha = 1^\circ$.

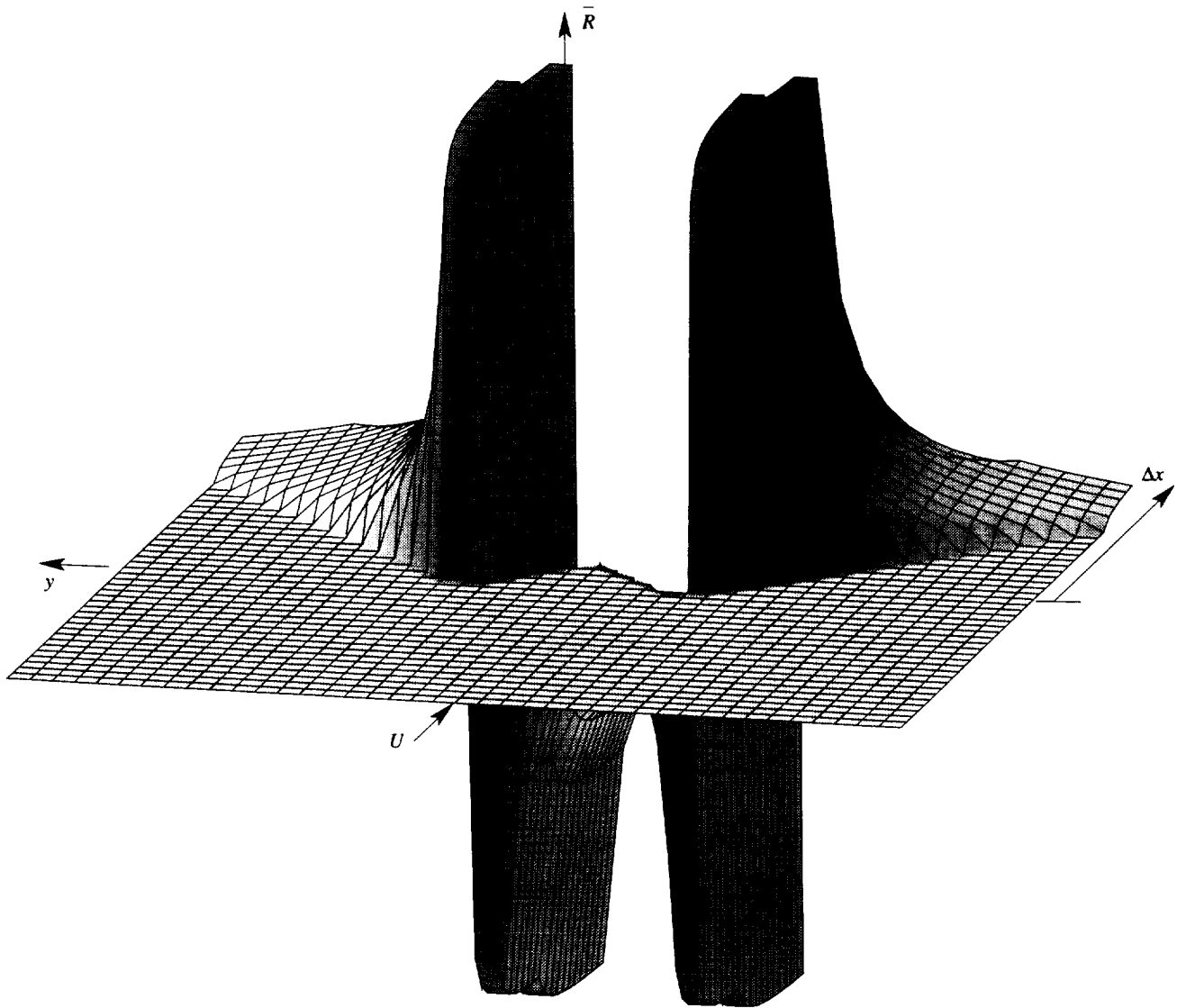
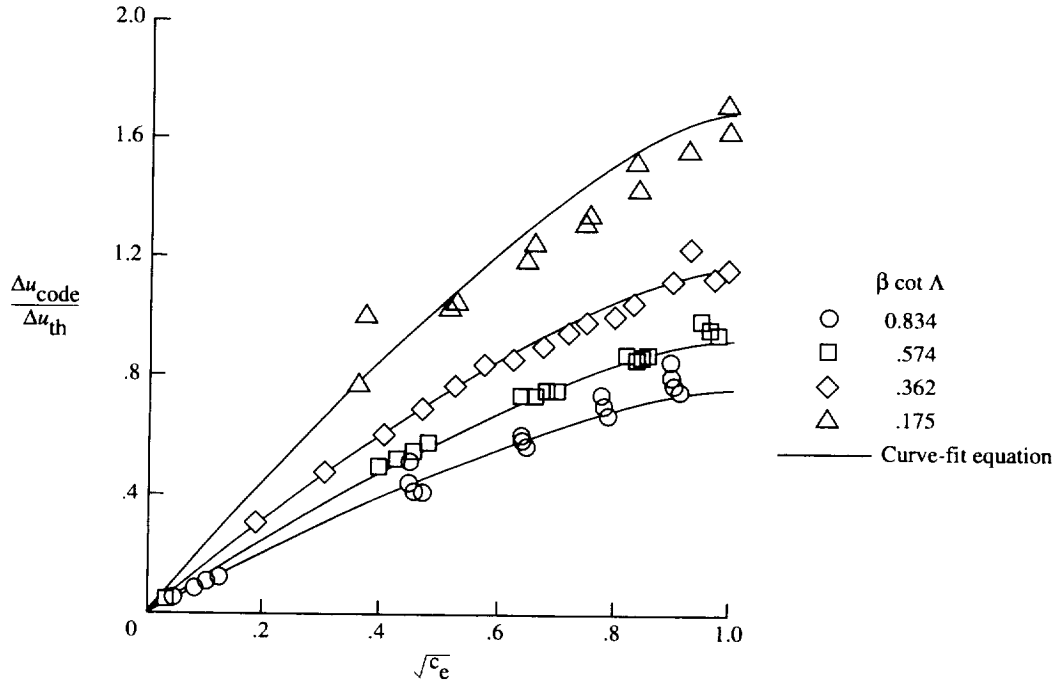
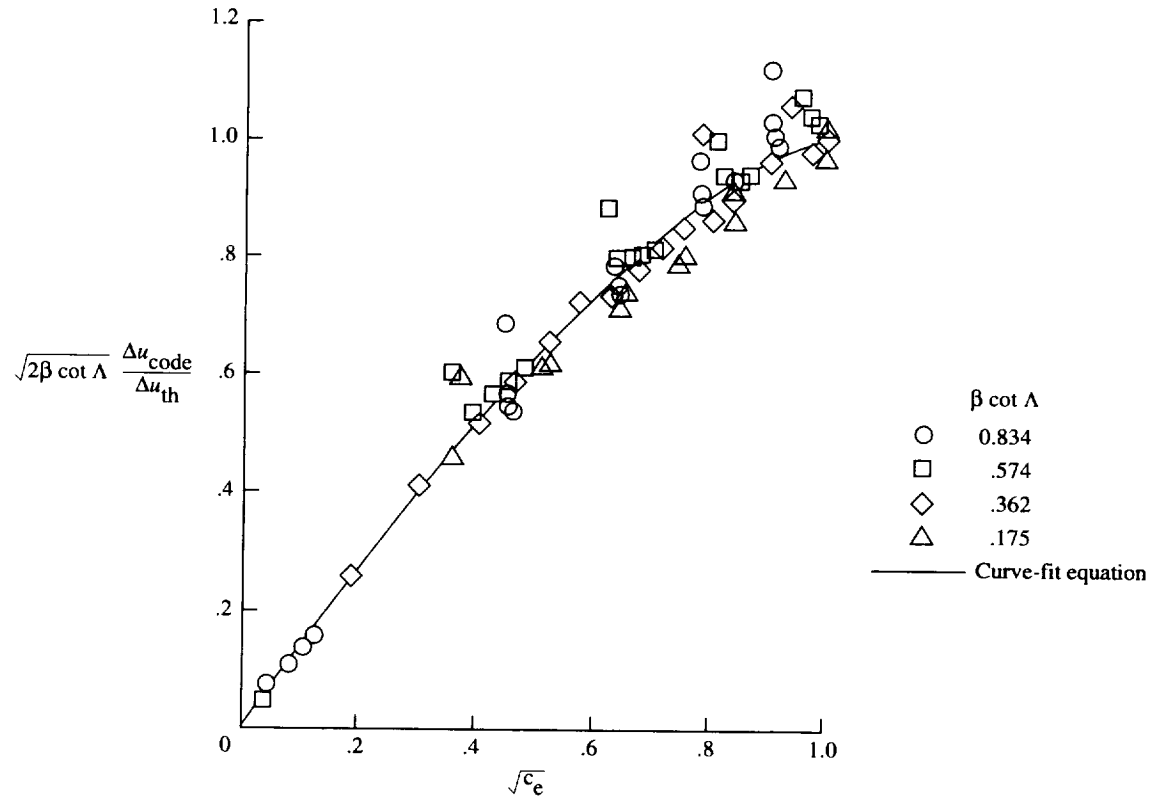


Figure 7. Supersonic influence function.



(a) Velocity ratio.



(b) Velocity ratio parameter.

Figure 8. Supersonic numerical solution for leading-edge elements.

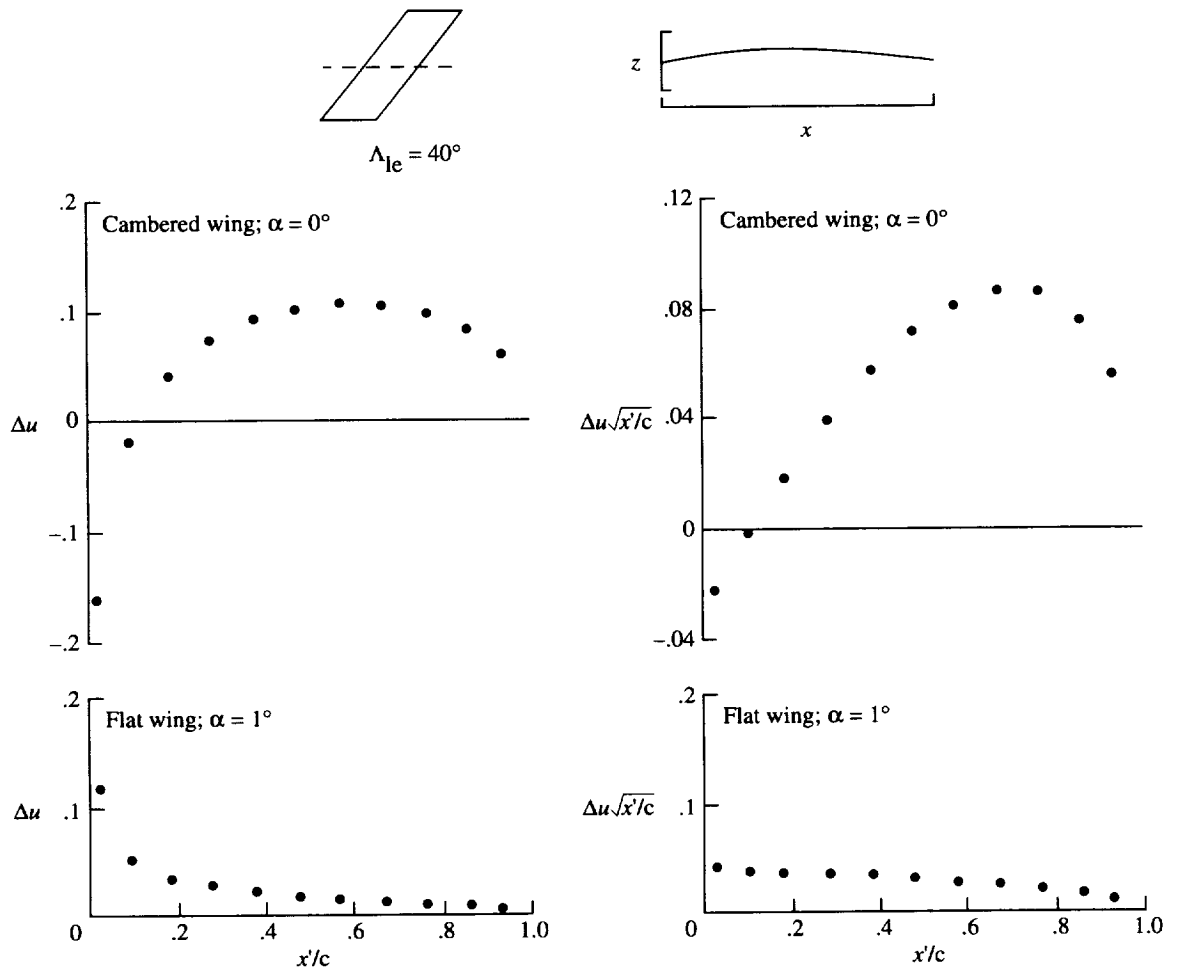


Figure 9. Code velocity distribution for cambered wing and flat wing of same planform. $M = 0.01$.

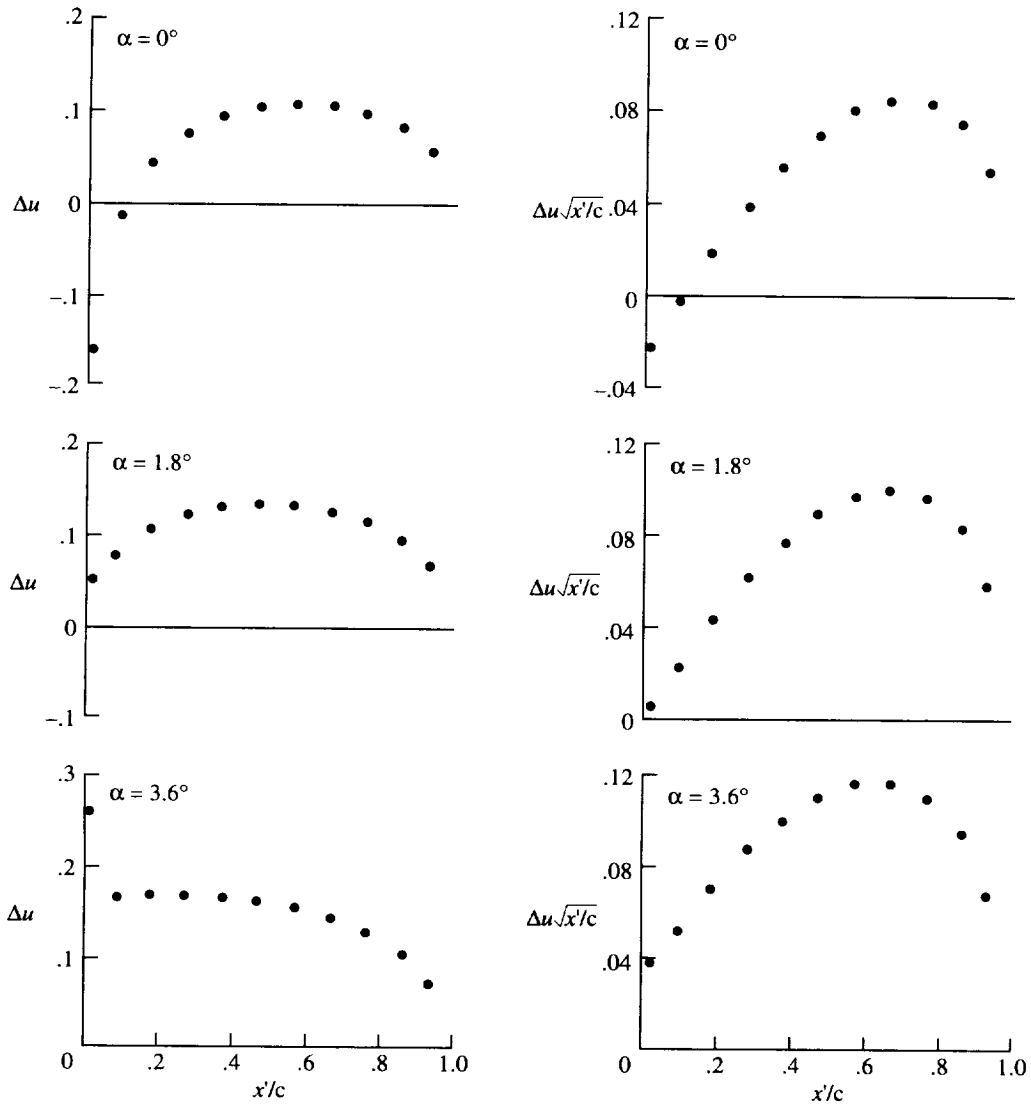


Figure 10. Code velocity distribution for cambered wing at several angles of attack obtained by superposition.

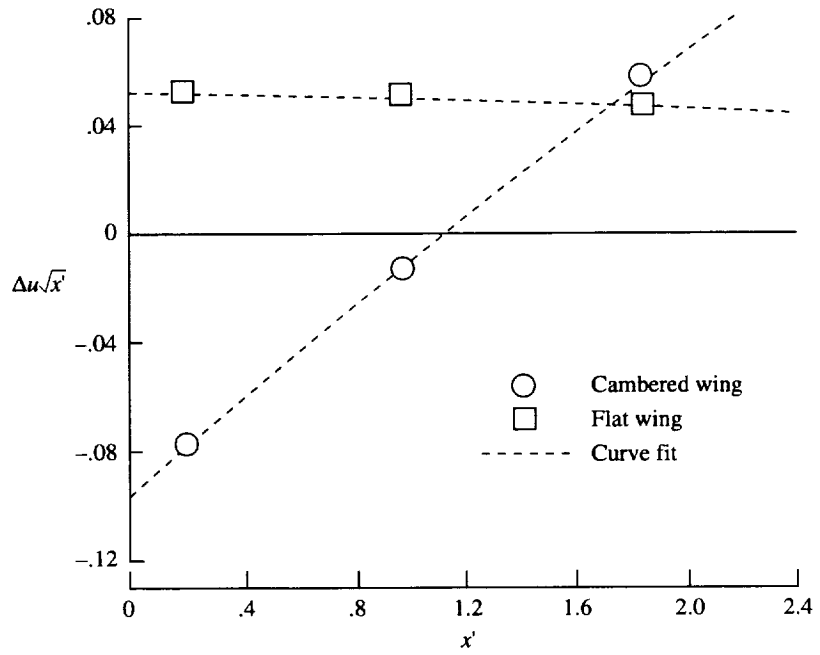


Figure 11. Curve fit used to determine section theoretical thrust coefficients.

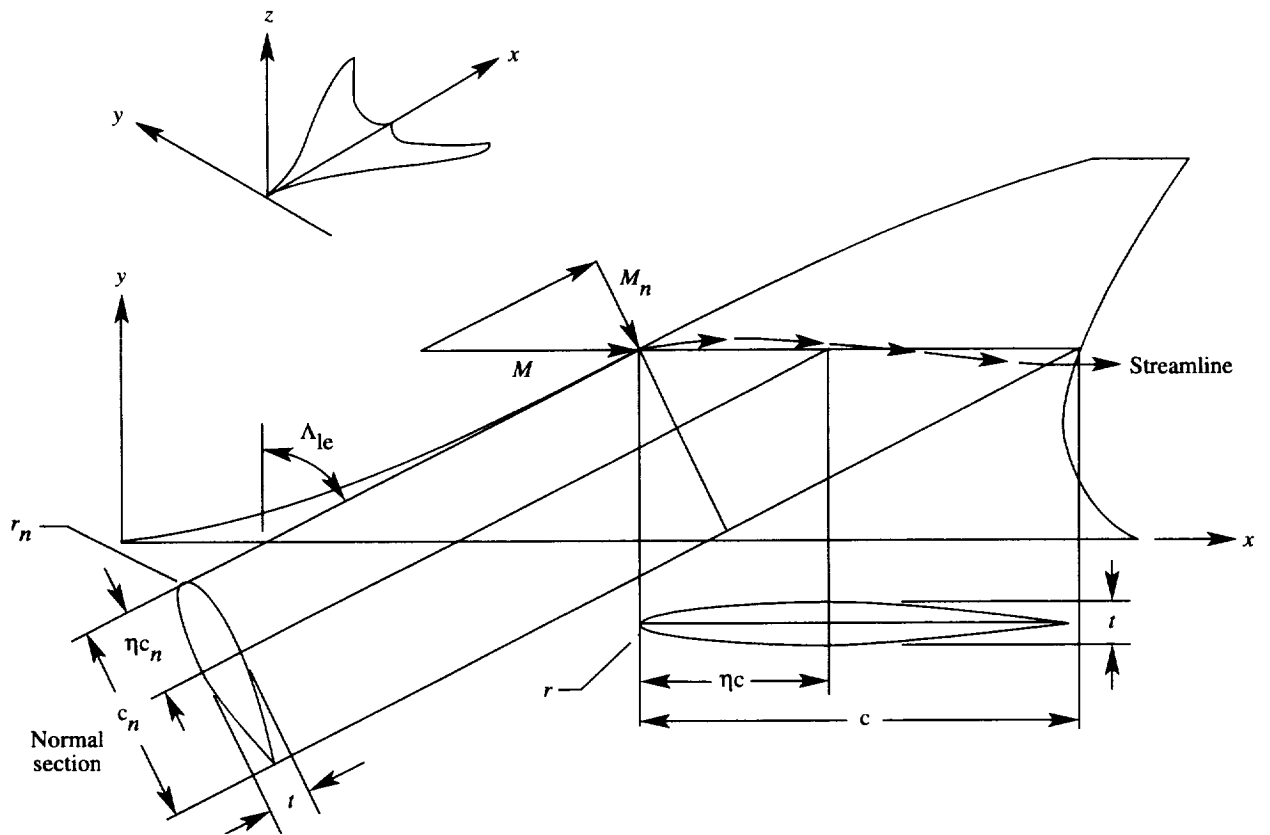


Figure 12. Relationship between streamwise and normal wing sections used for attainable thrust analysis.

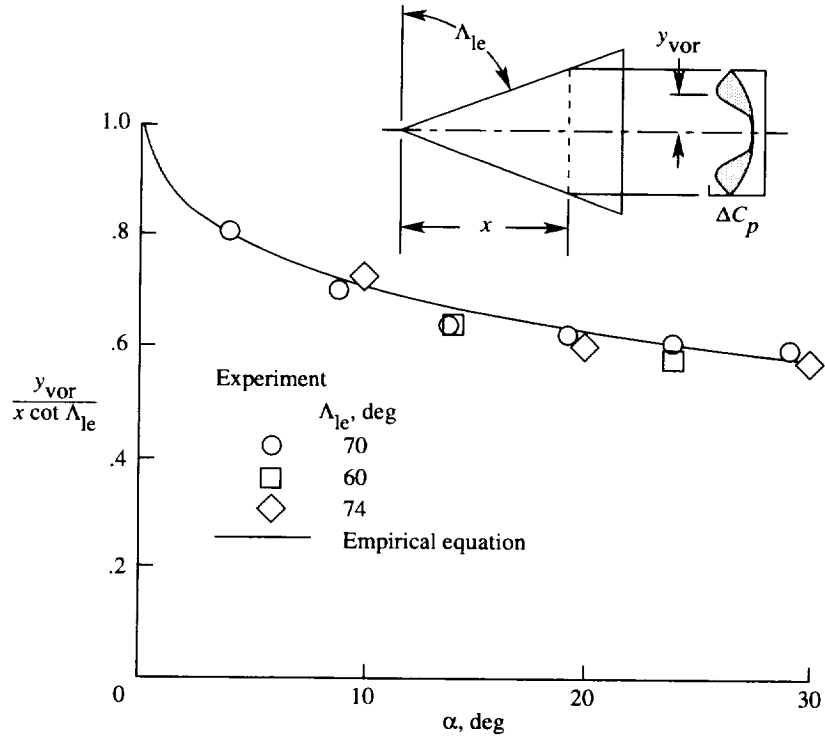


Figure 13. Location of pressure field at center of vortex as given by experimental data.

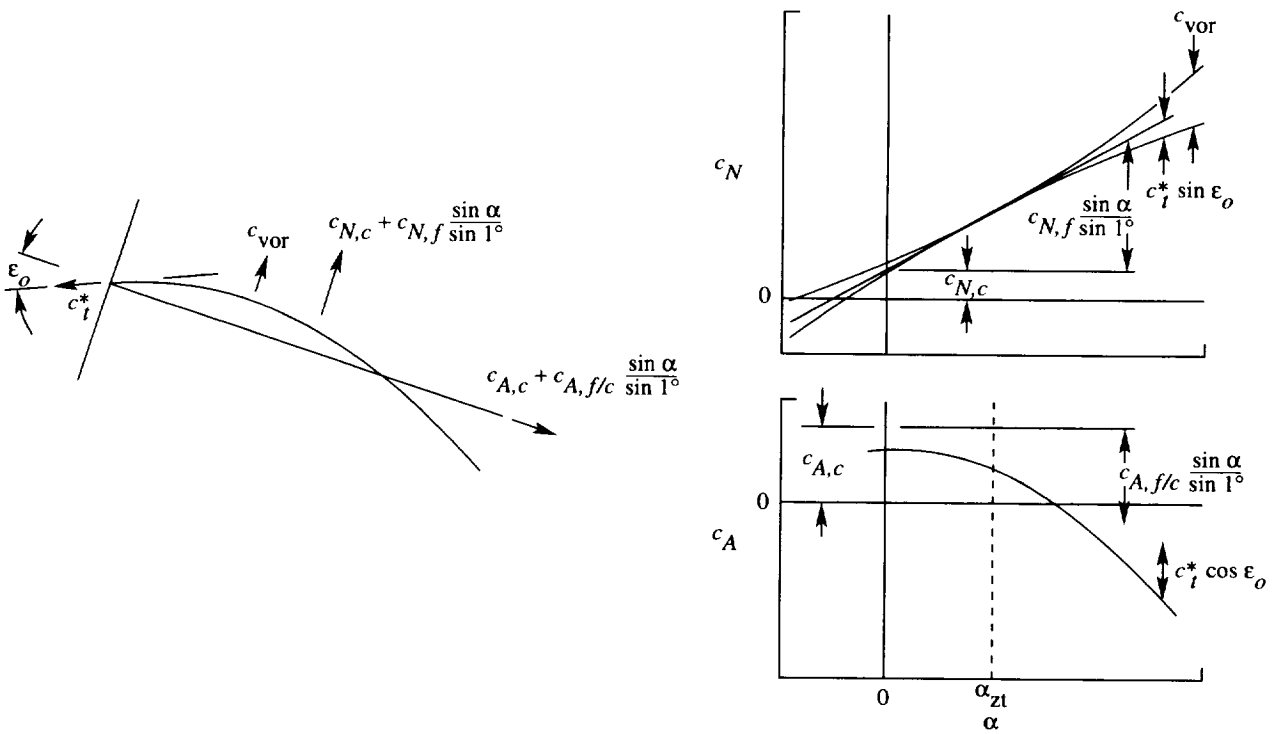


Figure 14. Buildup of section axial- and normal-force coefficients.

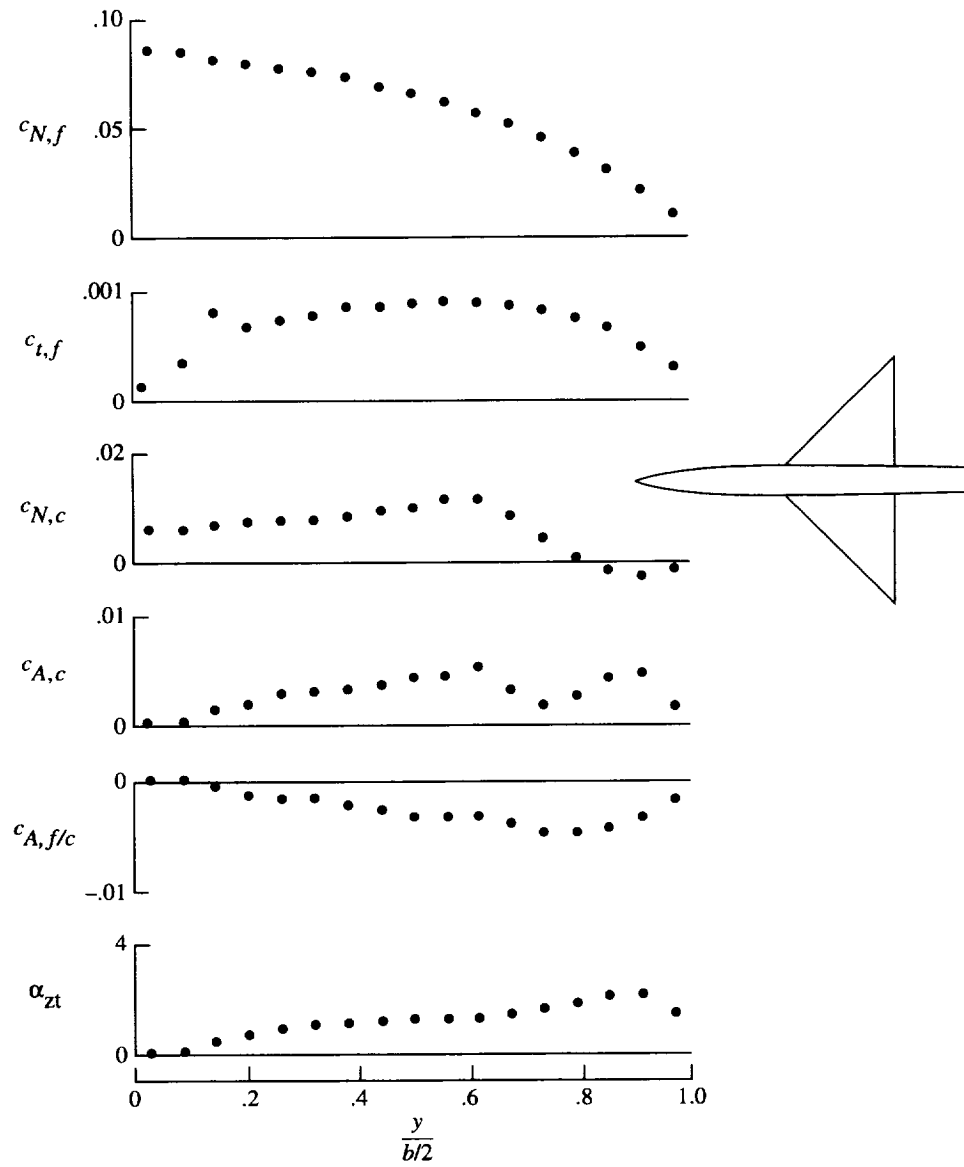


Figure 15. Spanwise variation of wing section coefficients. Aspect ratio 4 wing-body with twist and camber; $M = 0.61$.

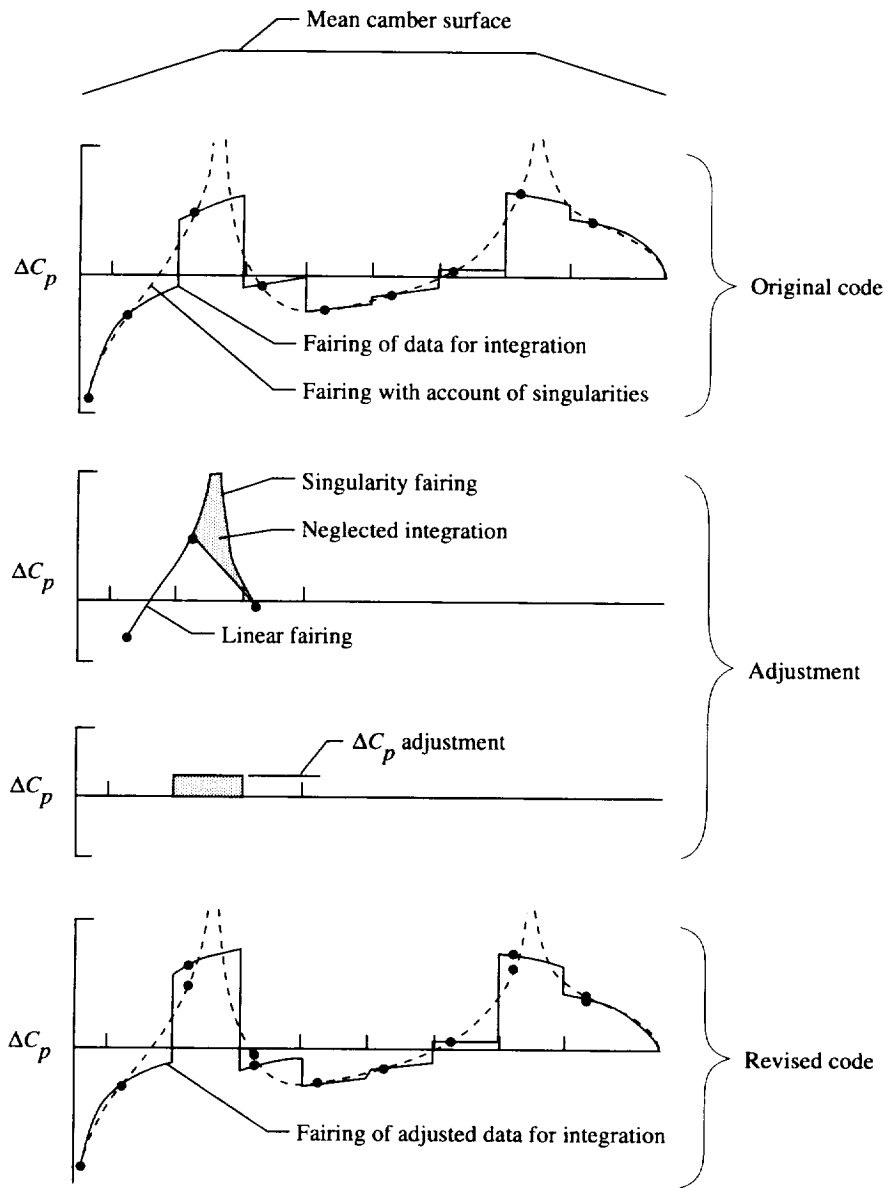


Figure 16. Flap hinge-line singularity adjustment.

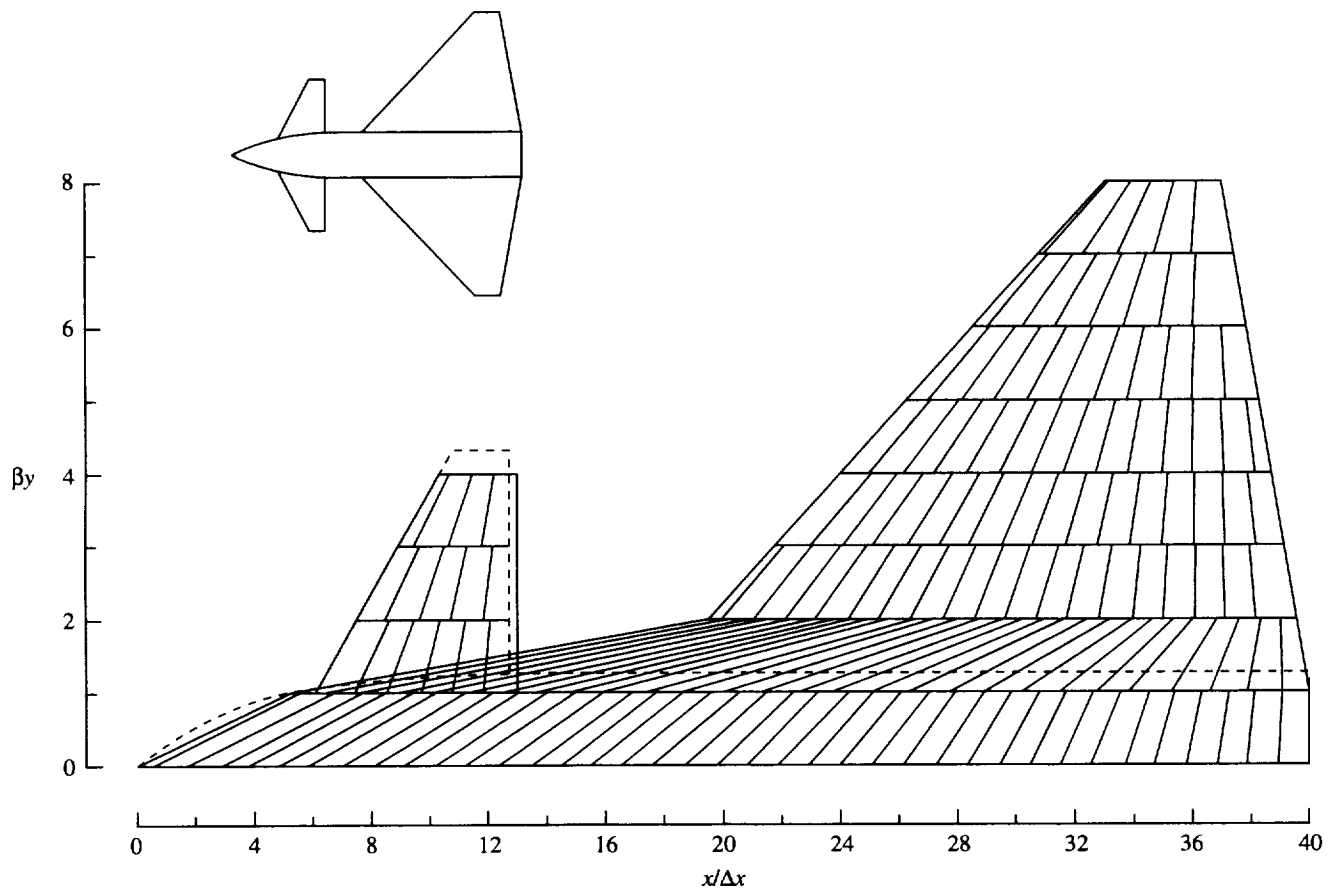


Figure 17. Typical representation of lifting surfaces in AERO2S computer code. Dashed line indicates original planform.

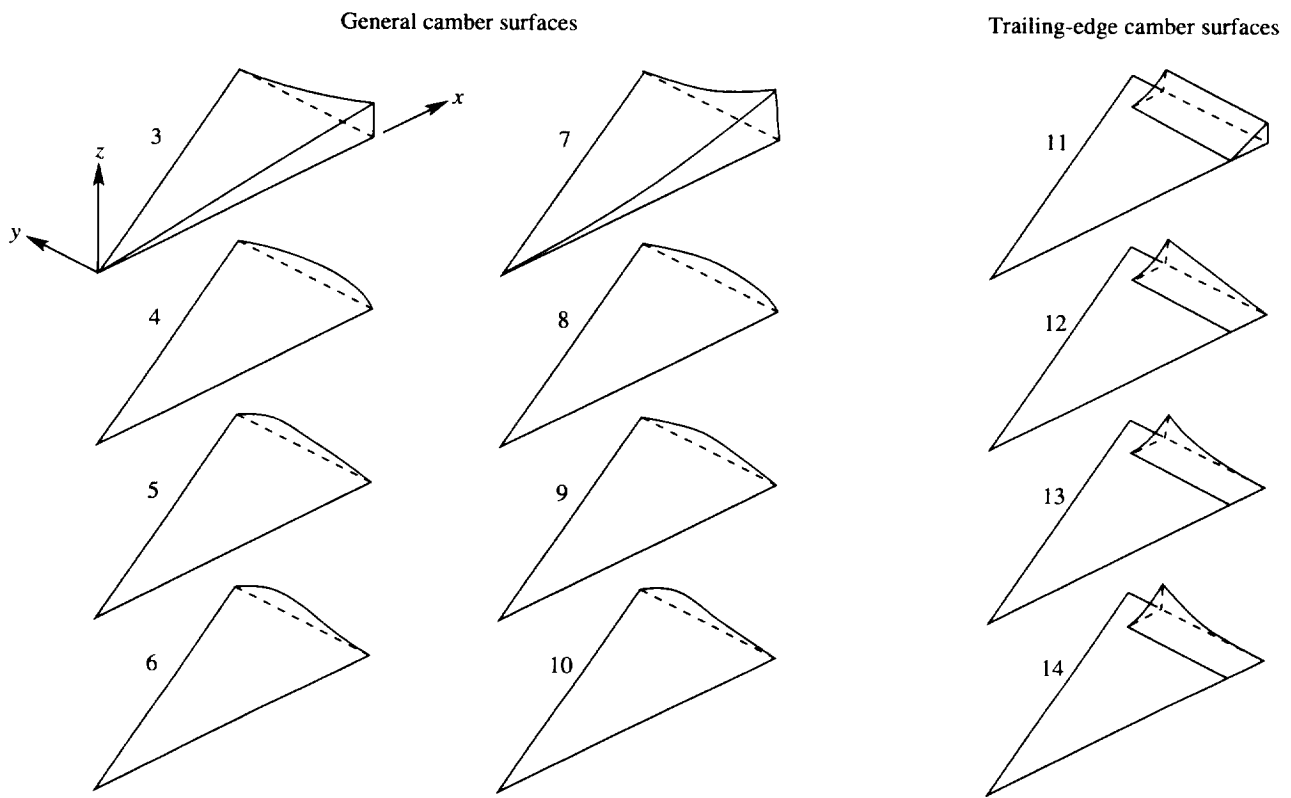


Figure 18. Typical candidate camber surfaces for delta wing example.

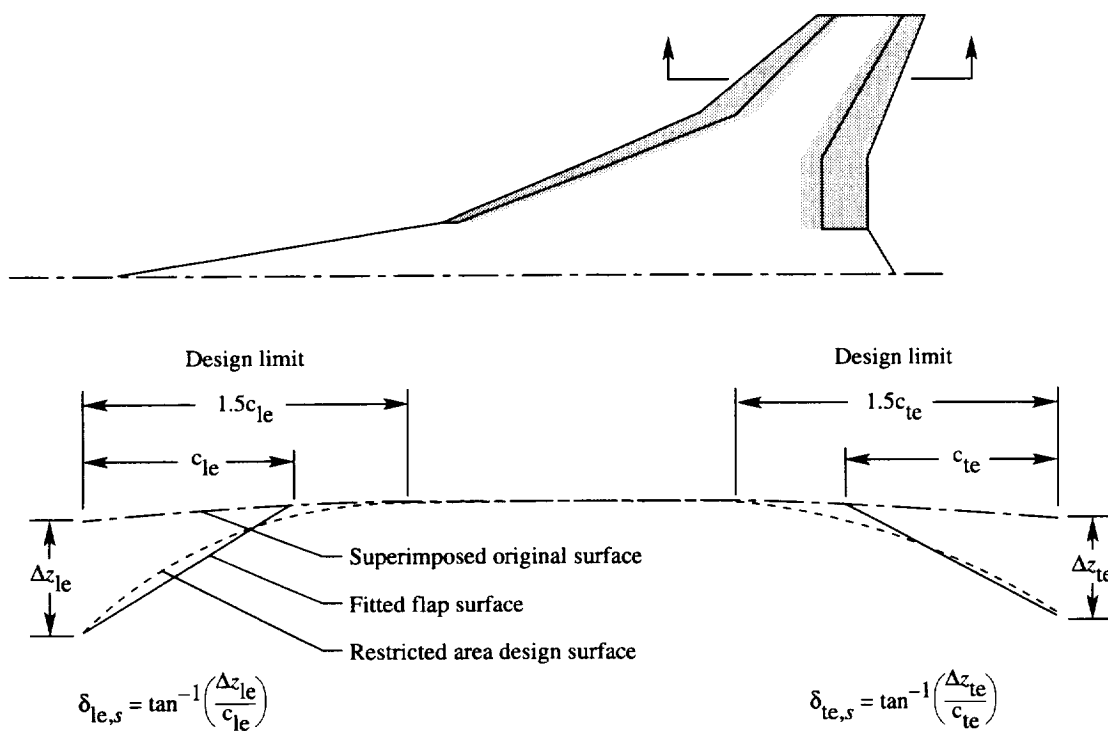


Figure 19. Fitting of flap surfaces to wing design surface. Design areas are shaded.

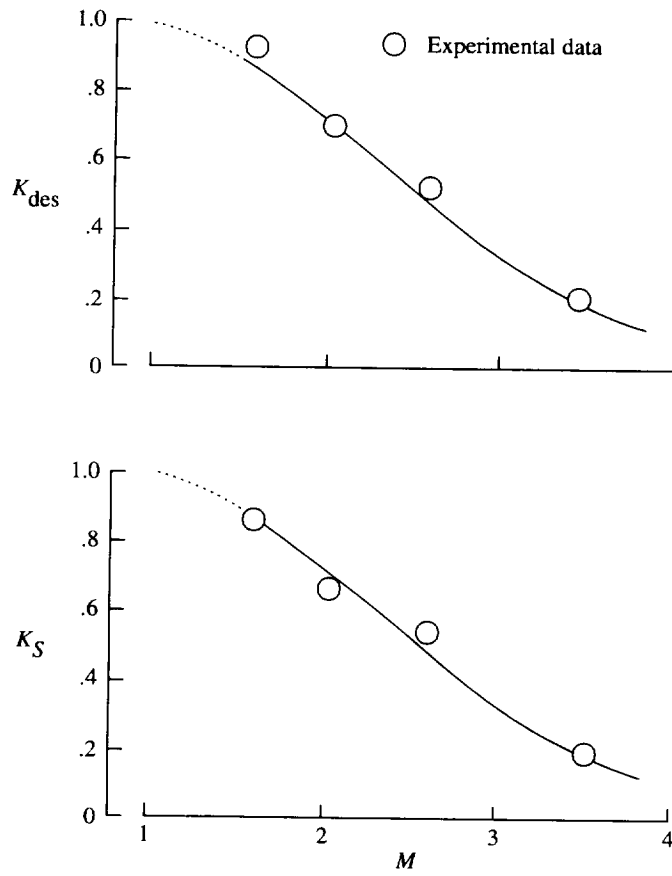


Figure 20. Empirical method factors used to select optimum design lift coefficients and to predict achievable suction parameters.

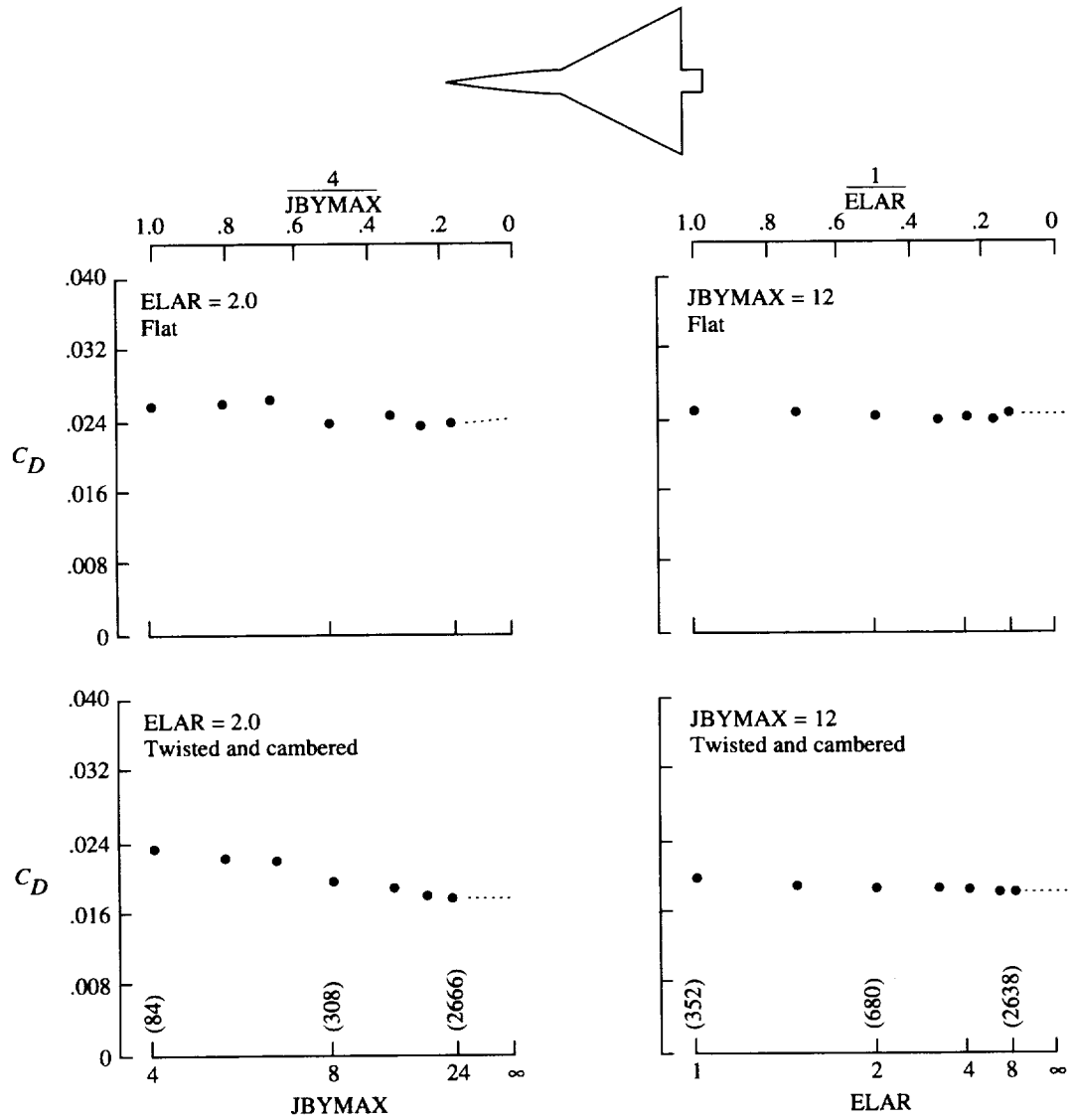


Figure 21. AERO2S code convergence data for aspect ratio 2 wing-body. $M = 0.60$; $R = 3.0 \times 10^6$; $C_L = 0.3$.

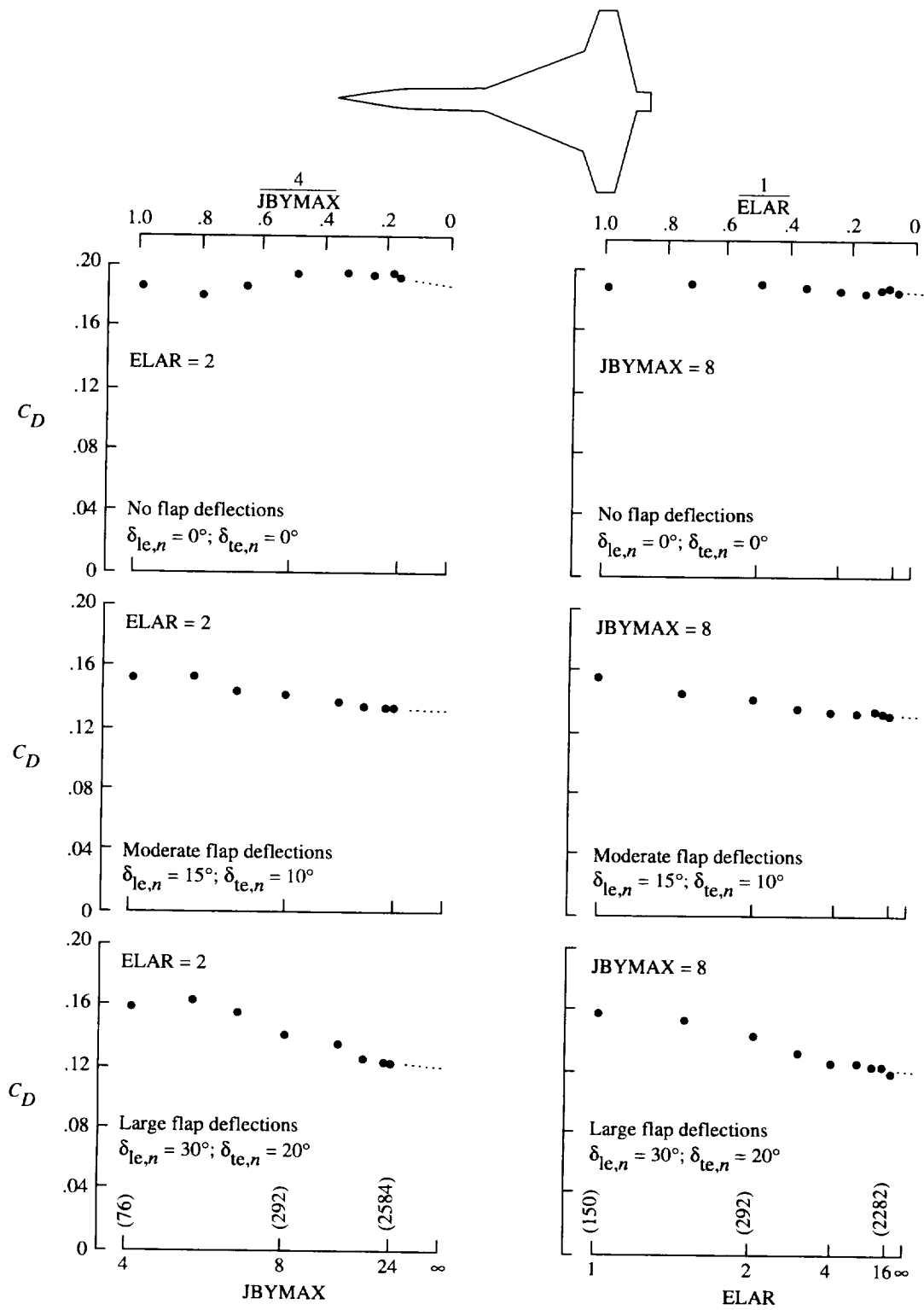


Figure 22. AERO2S code convergence data for cranked-wing fighter. $M = 0.50$; $R = 2.9 \times 10^6$; $C_L = 0.8$.

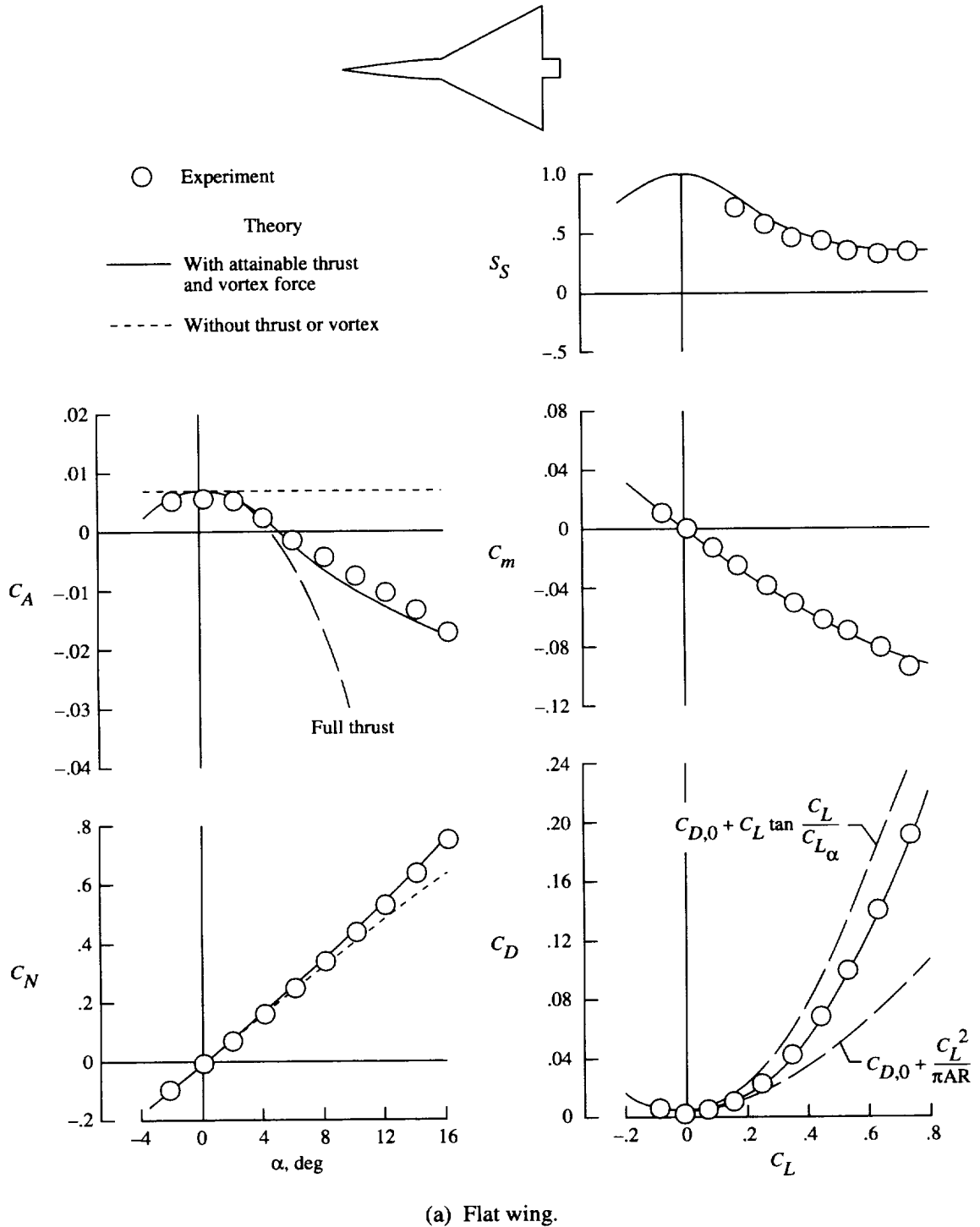
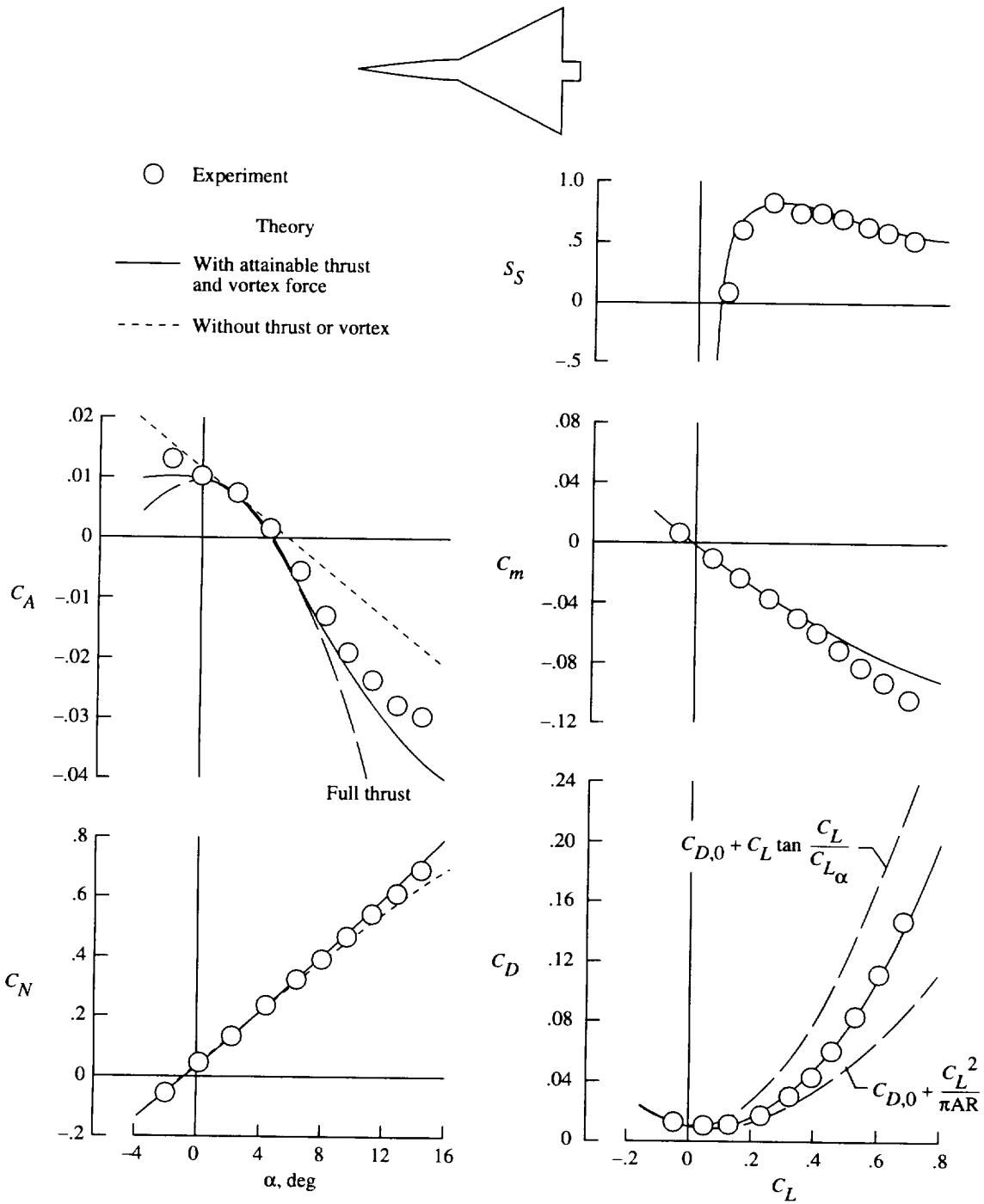


Figure 23. Theoretical and experimental data for aspect ratio 2 wing-body. $M = 0.61$; $R = 3.0 \times 10^6$.



(b) Twisted and cambered wing.

Figure 23. Concluded.

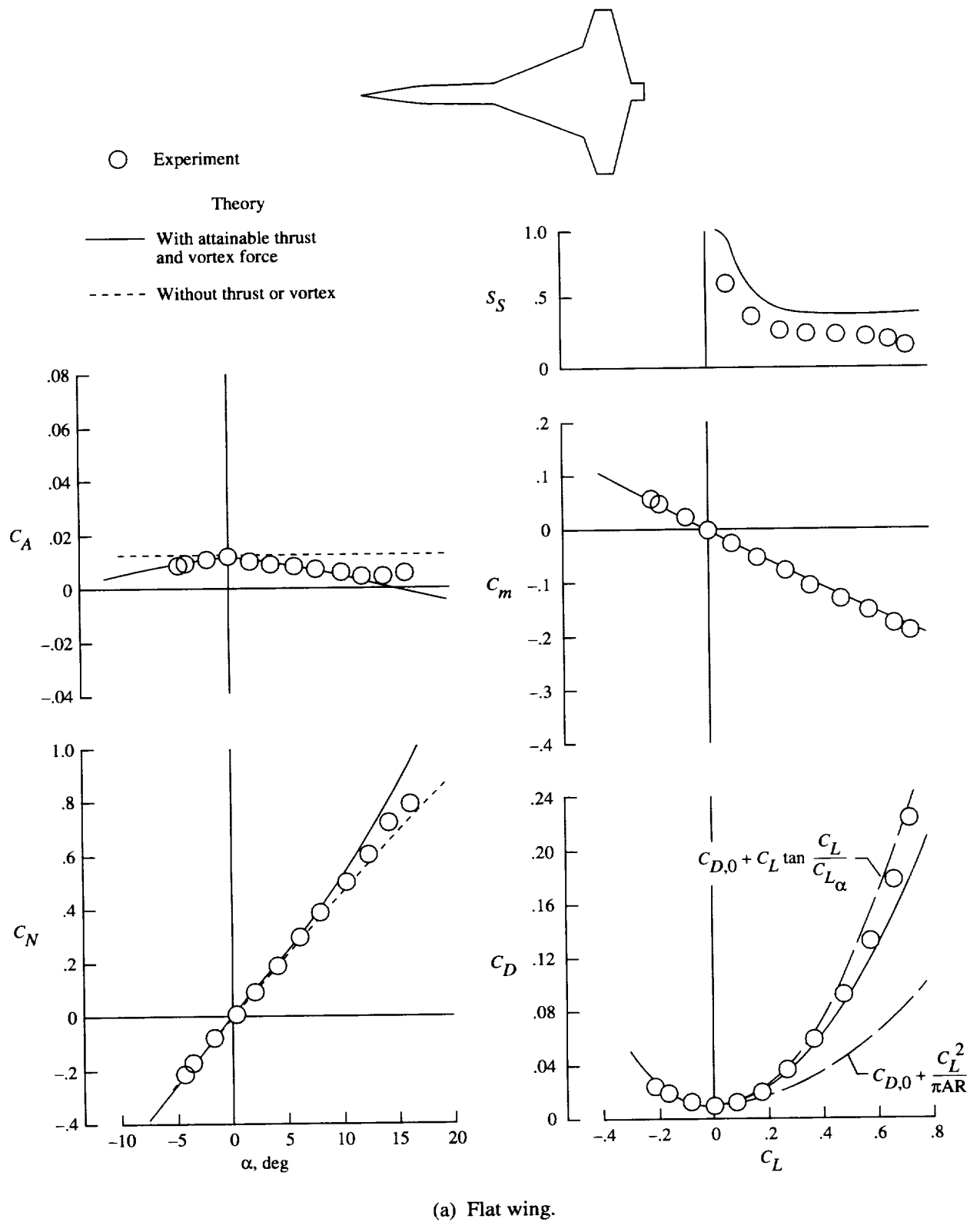
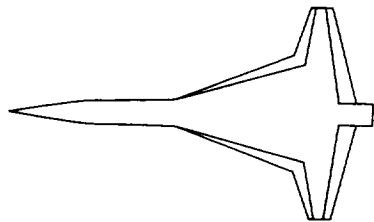


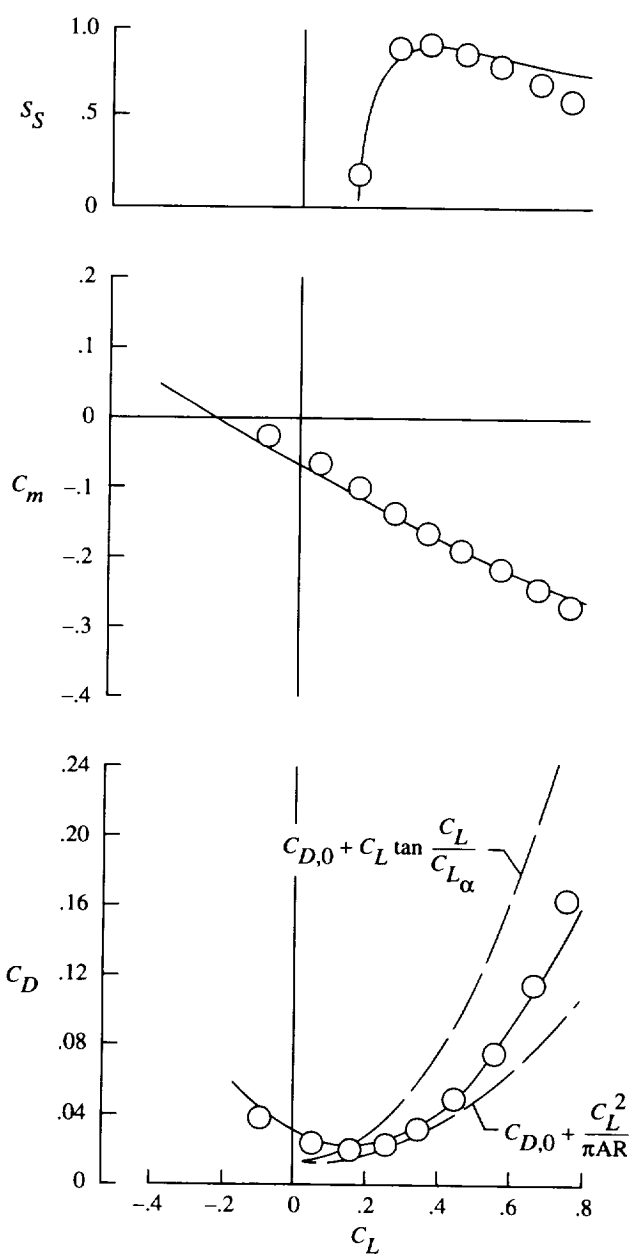
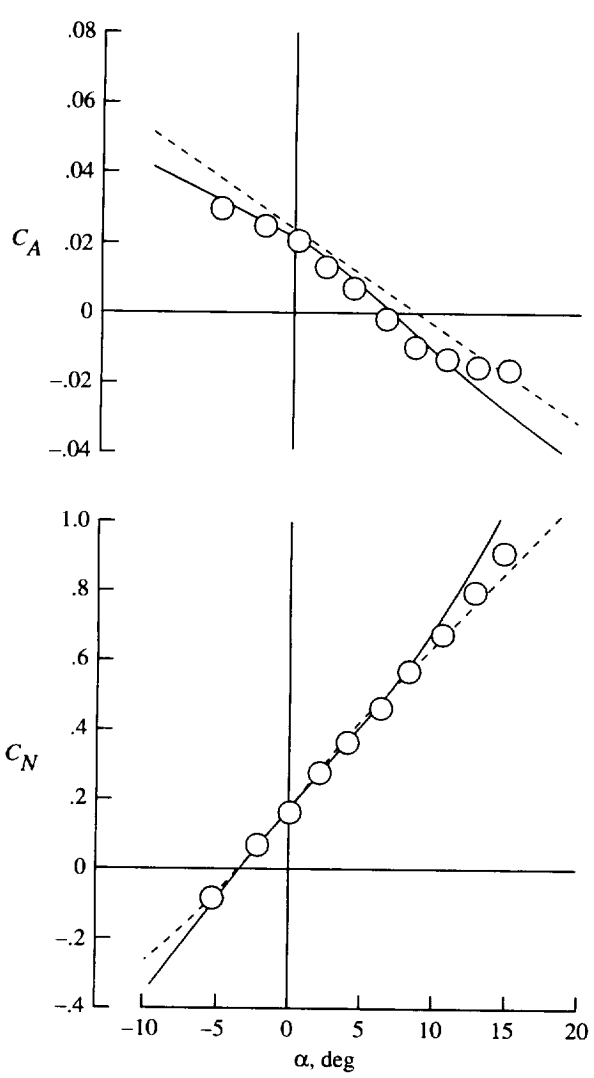
Figure 24. Theoretical and experimental data for cranked-wing fighter. $M = 0.50$; $R = 2.9 \times 10^6$.



○ Experiment

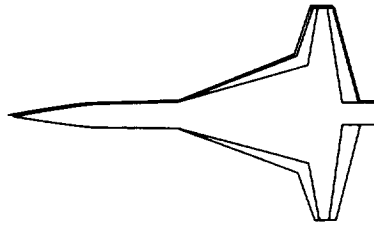
Theory

— With attainable thrust and vortex force
 - - - Without thrust or vortex



(b) Deflected flaps, $\delta_{le,n} = 15^\circ$ and $\delta_{te,n} = 10^\circ$.

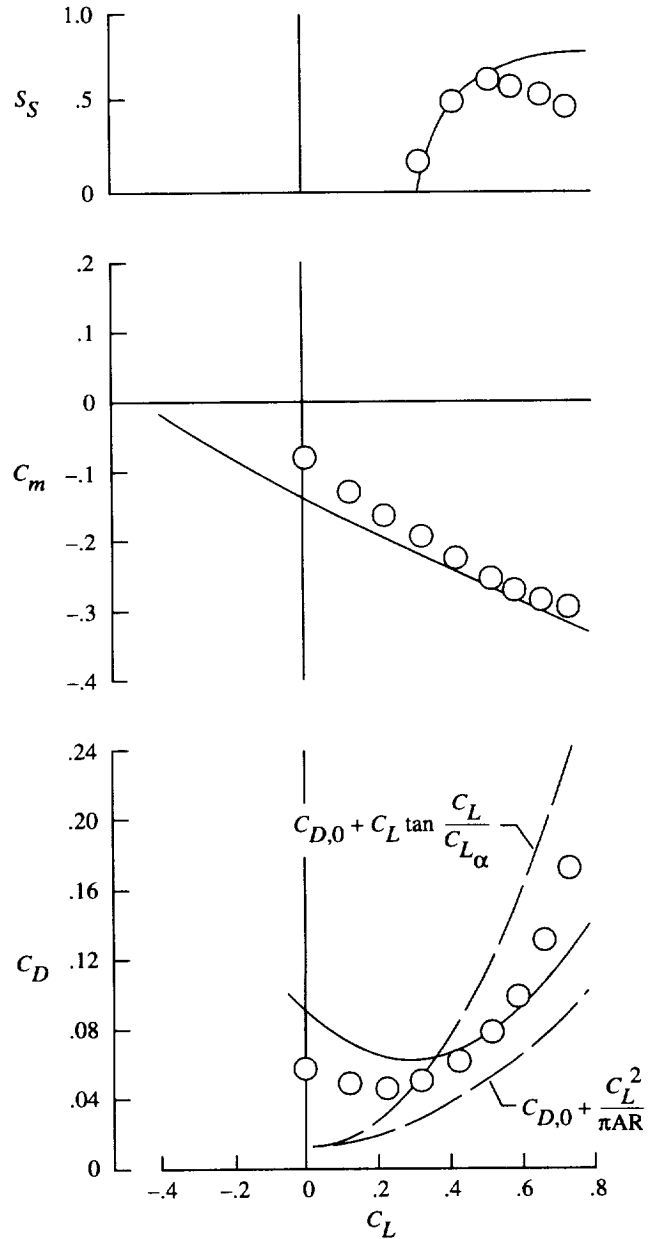
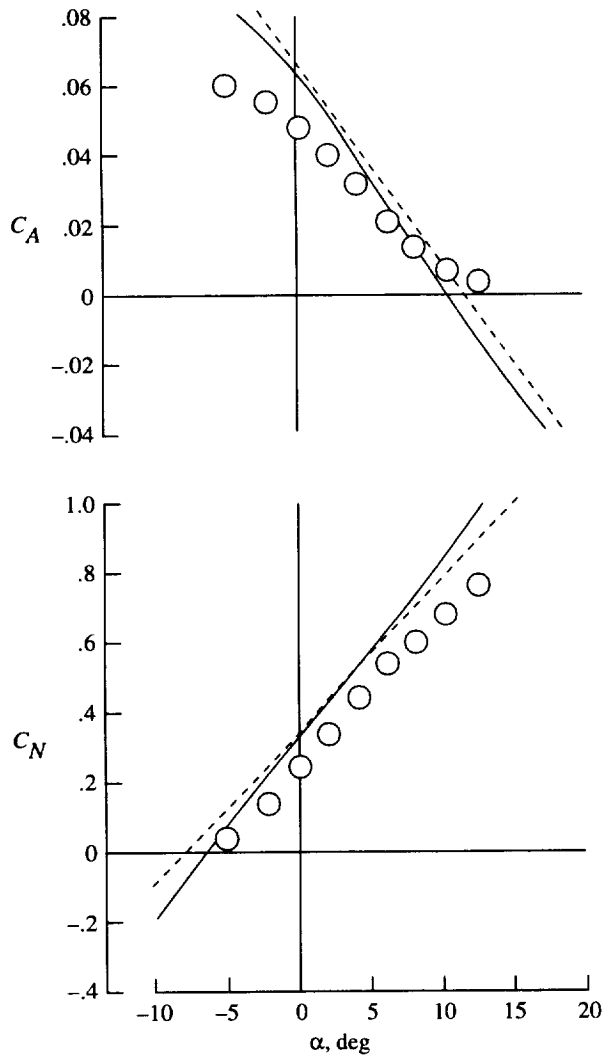
Figure 24. Continued.



○ Experiment

Theory

— With attainable thrust and vortex force
 - - - Without thrust or vortex



(c) Deflected flaps, $\delta_{le,n} = 30^\circ$ and $\delta_{te,n} = 20^\circ$.

Figure 24. Concluded.

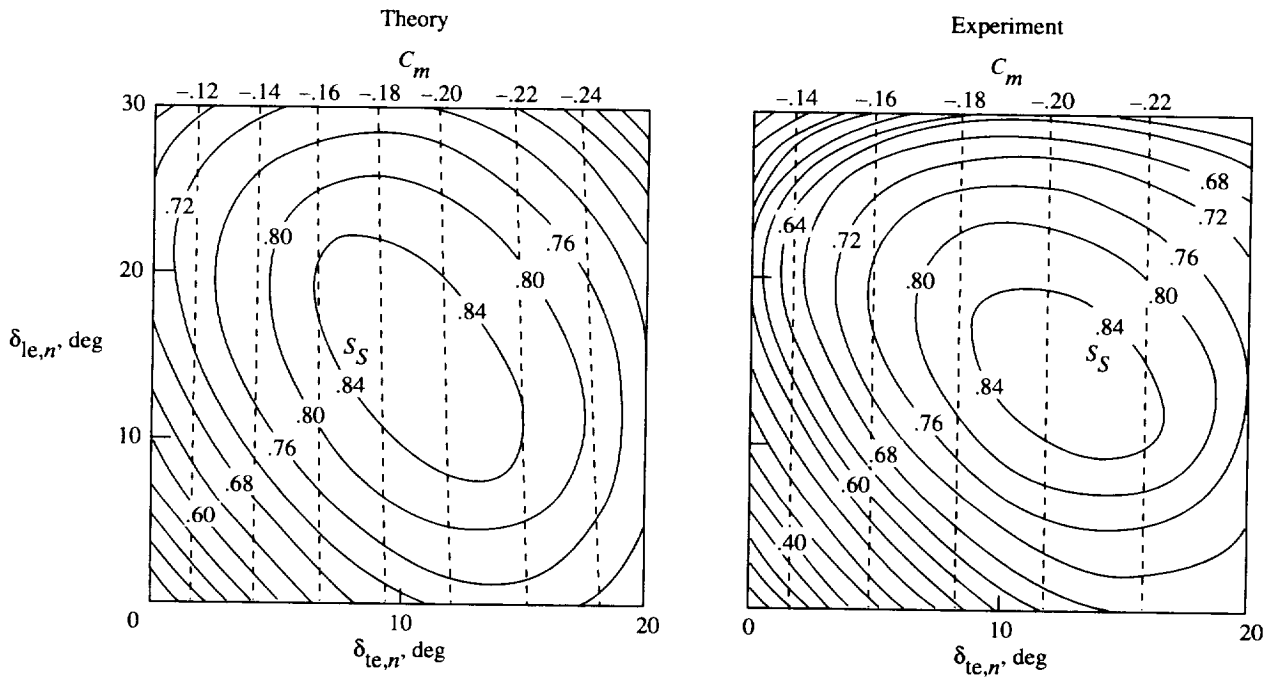
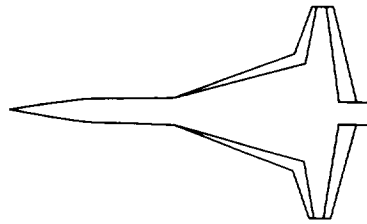
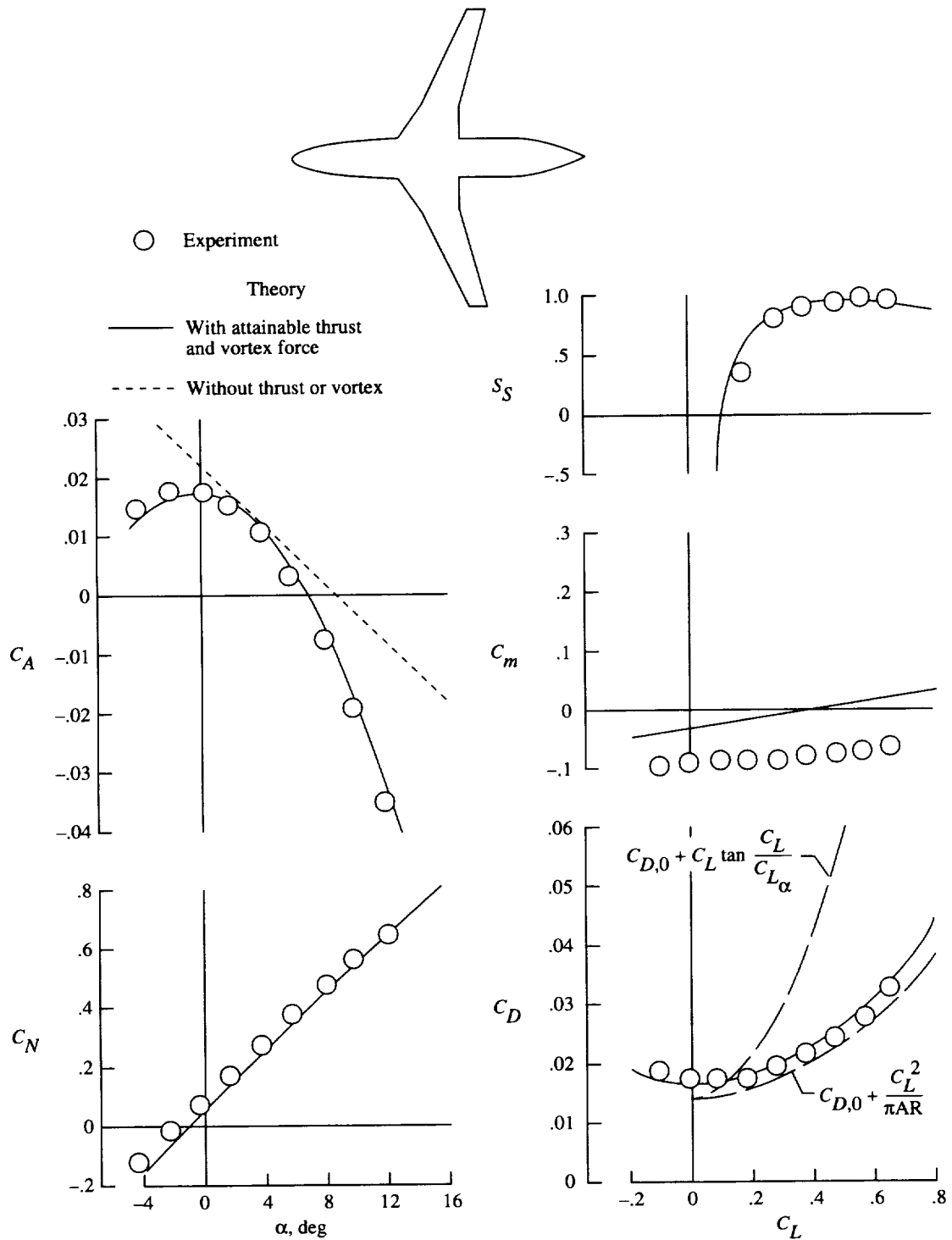
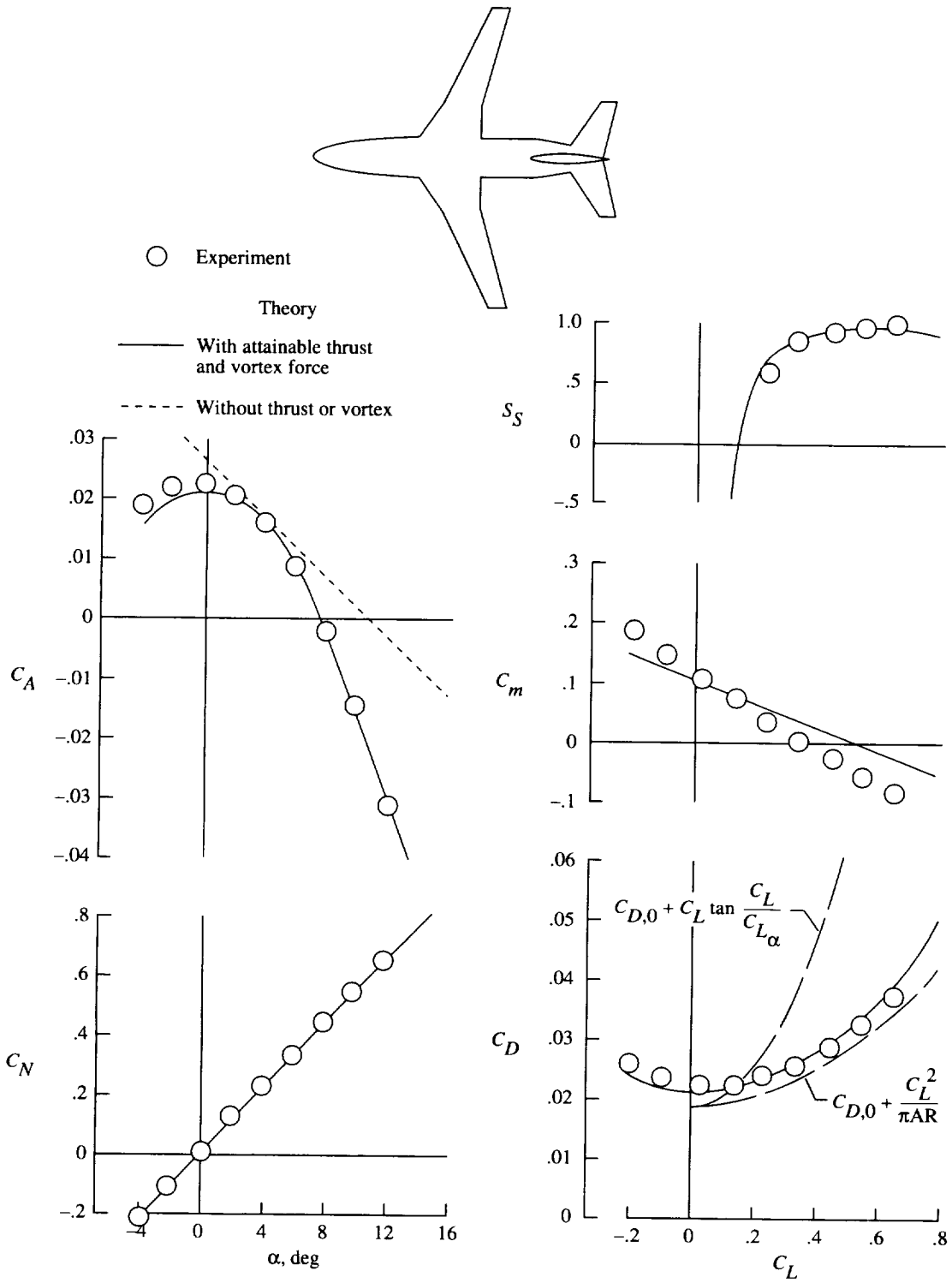


Figure 25. Flap system performance map for cranked-wing fighter. $M = 0.50$; $R = 2.9 \times 10^6$; $C_L = 0.45$.



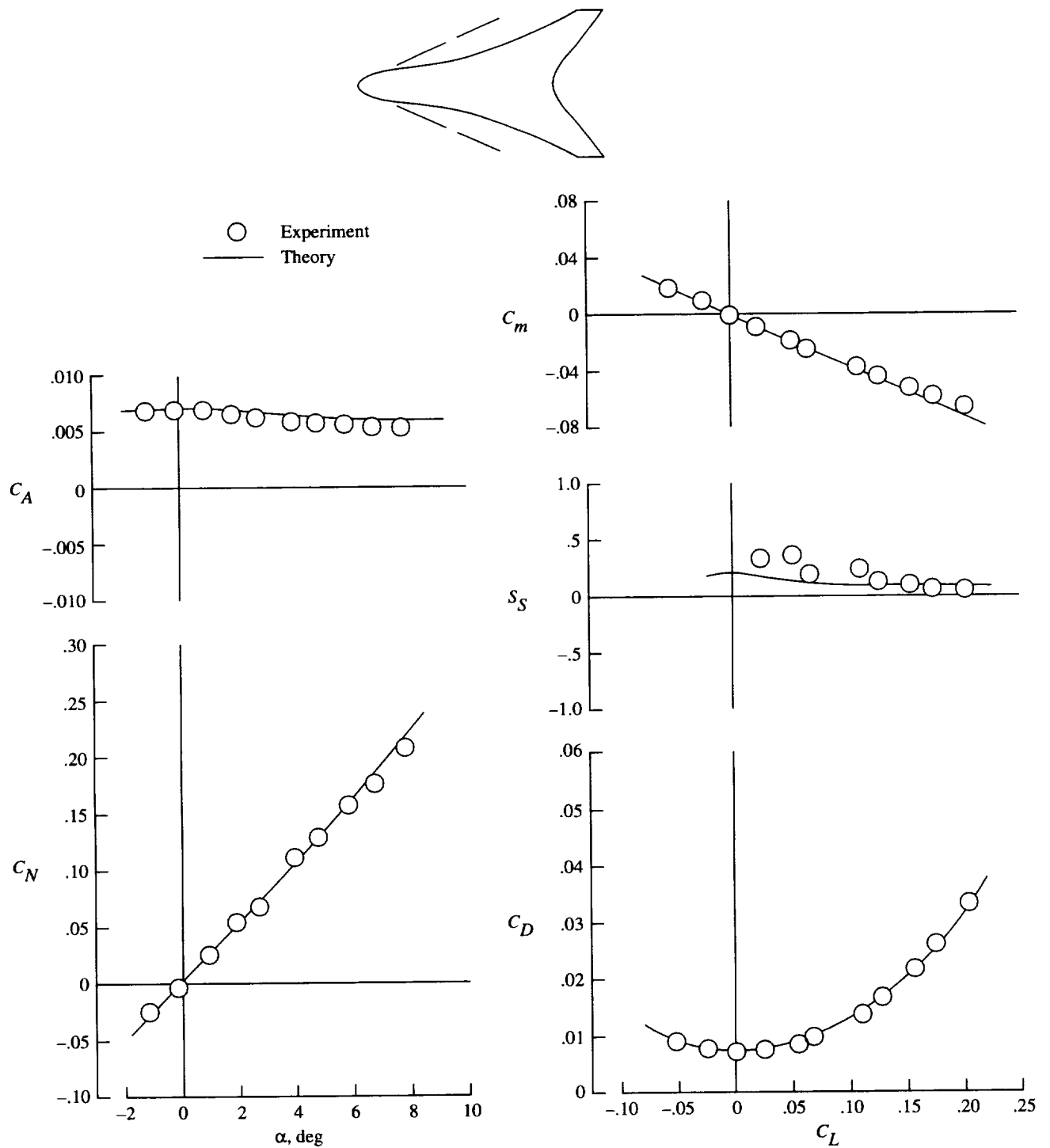
(a) Wing-body.

Figure 26. Theoretical and experimental data for subsonic transport configuration. $M = 0.55$; $R = 2.25 \times 10^6$.



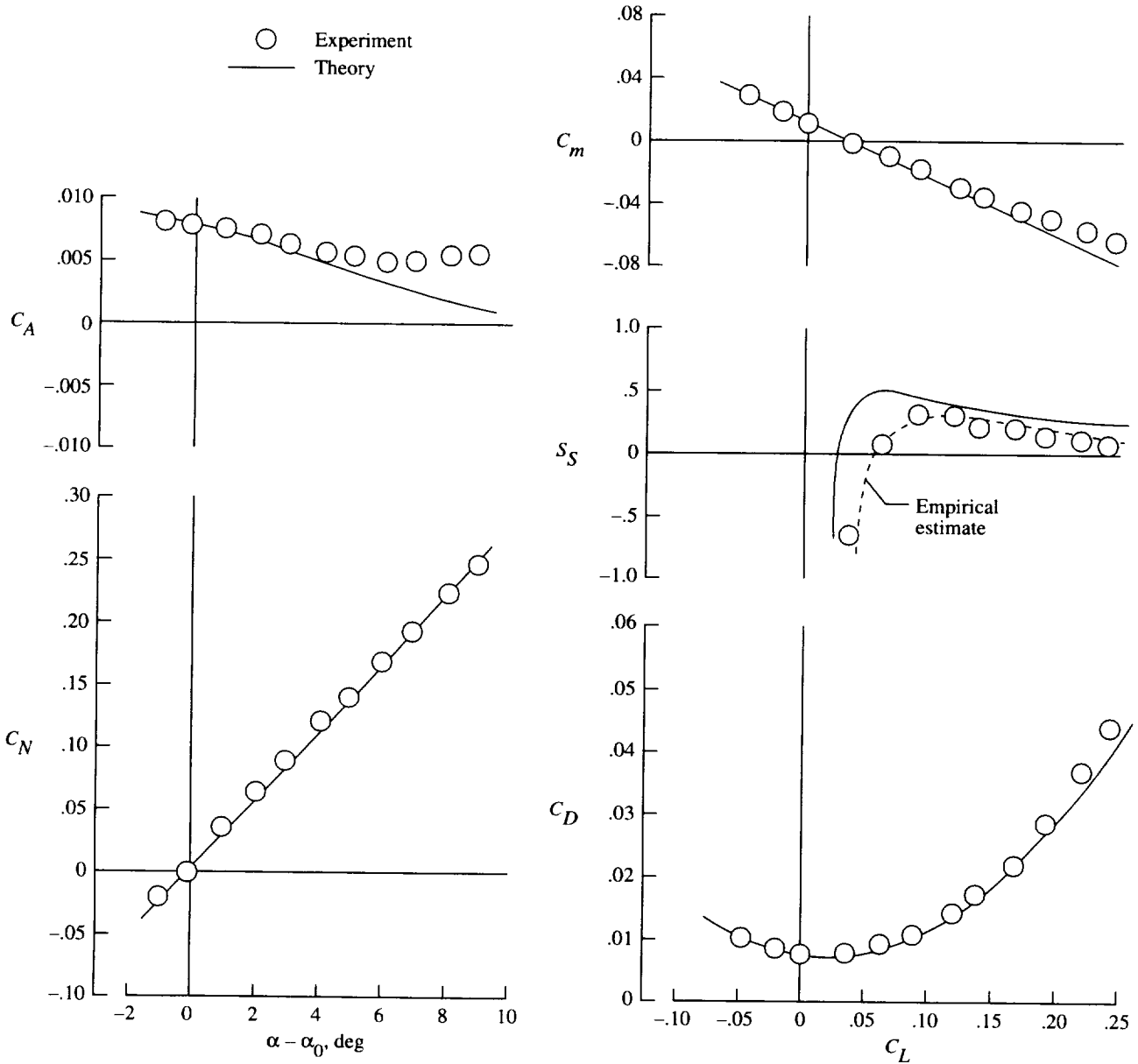
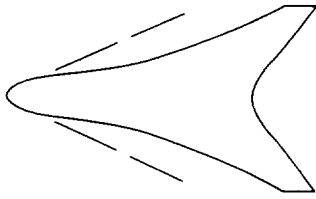
(b) Wing-body with horizontal and vertical tails.

Figure 26. Concluded.



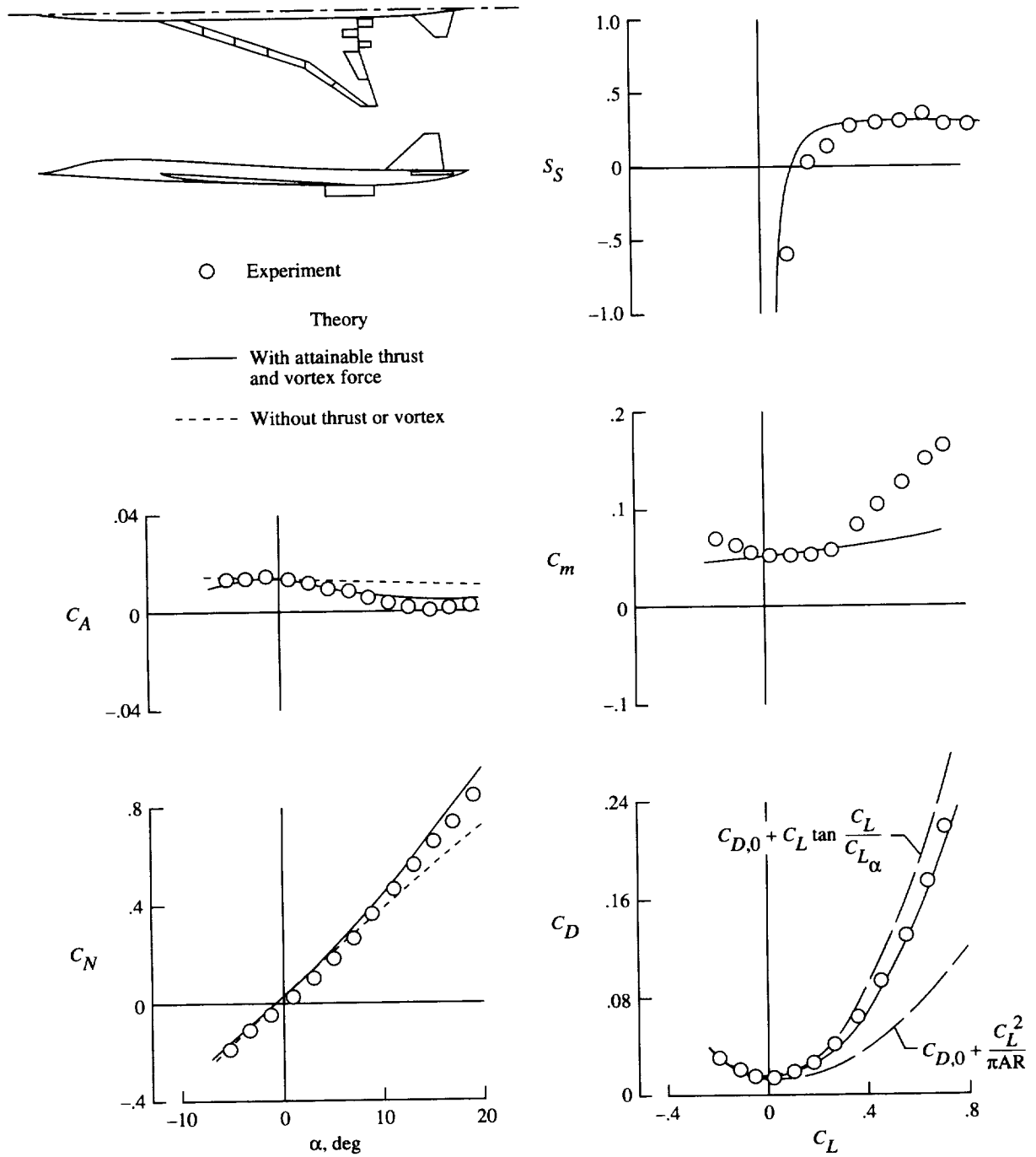
(a) Flat wing.

Figure 27. Theoretical and experimental data for SST wing-body combination. $M = 2.40$; $R = 3.4 \times 10^6$.



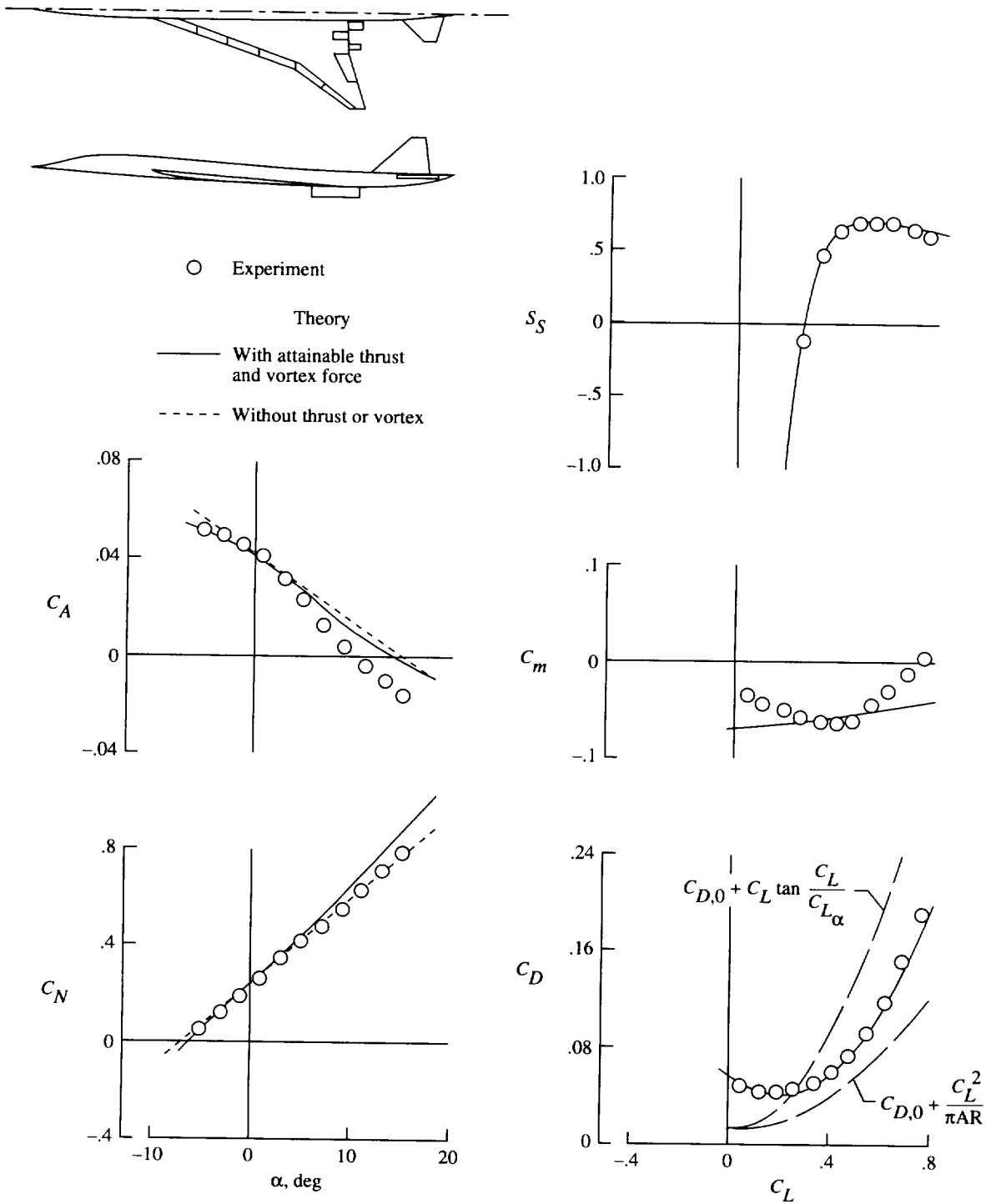
(b) Twisted and cambered wing; $C_{L,des} = 0.08$.

Figure 27. Concluded.



(a) $\delta_{le,n} = 0^\circ$; $\delta_{te,n} = 0^\circ$; $\delta_H = -5^\circ$.

Figure 28. Theoretical and experimental data for arrow wing SST configuration with leading- and trailing-edge flaps and horizontal tail. $M = 0.03$; $R = 4.19 \times 10^6$.



(b) $\delta_{te,n} = 13^\circ/34^\circ/35^\circ/35^\circ/19^\circ/29^\circ$; $\delta_{te,n} = 30^\circ$; $\delta_H = -5^\circ$.

Figure 28. Concluded.

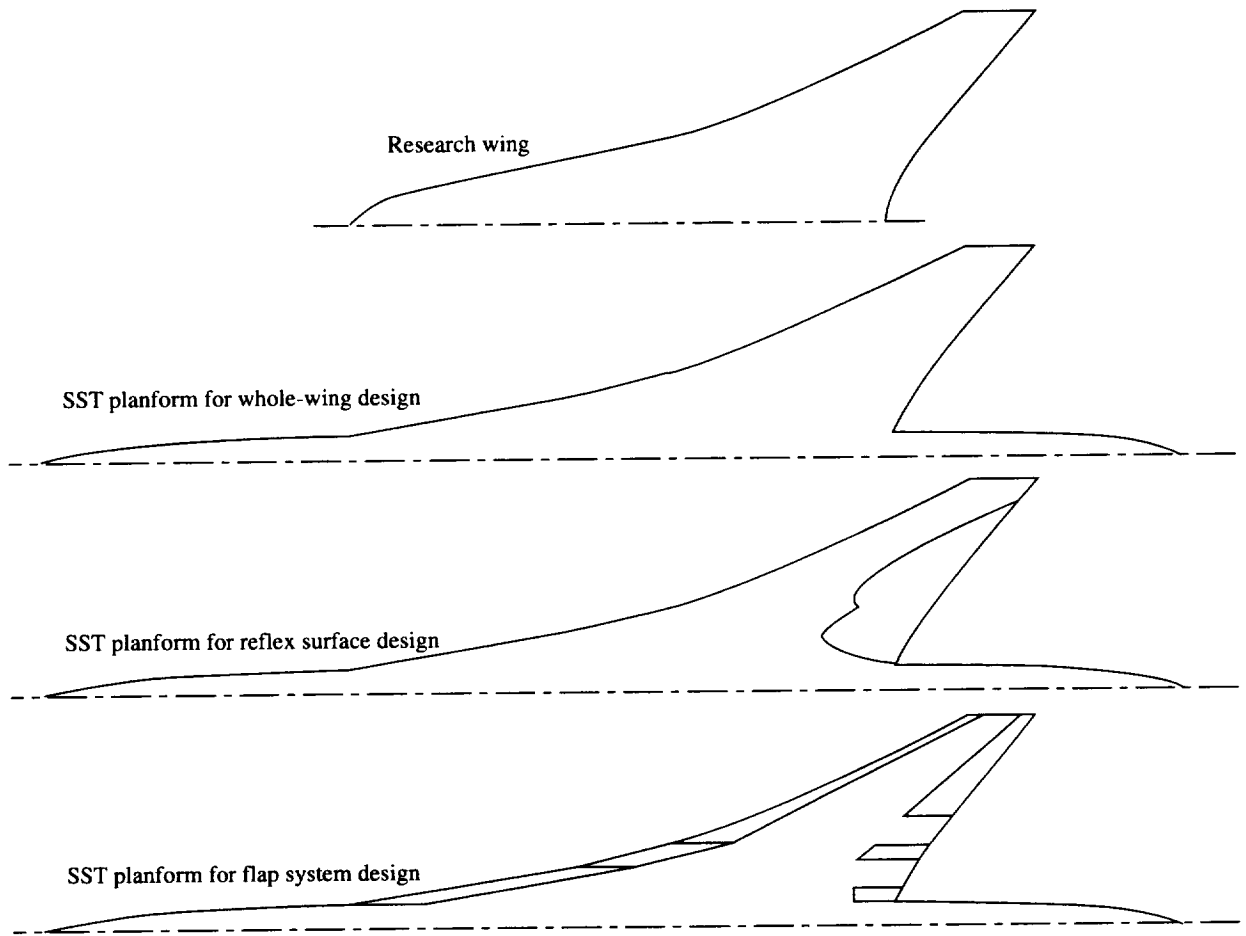


Figure 29. Wing planform used in SST design study.

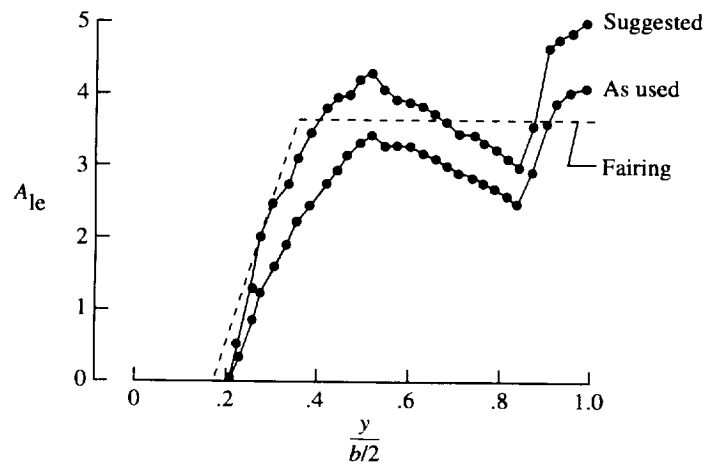
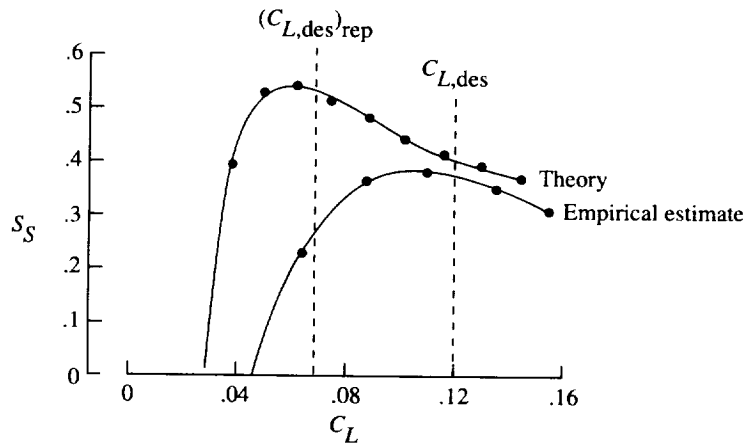
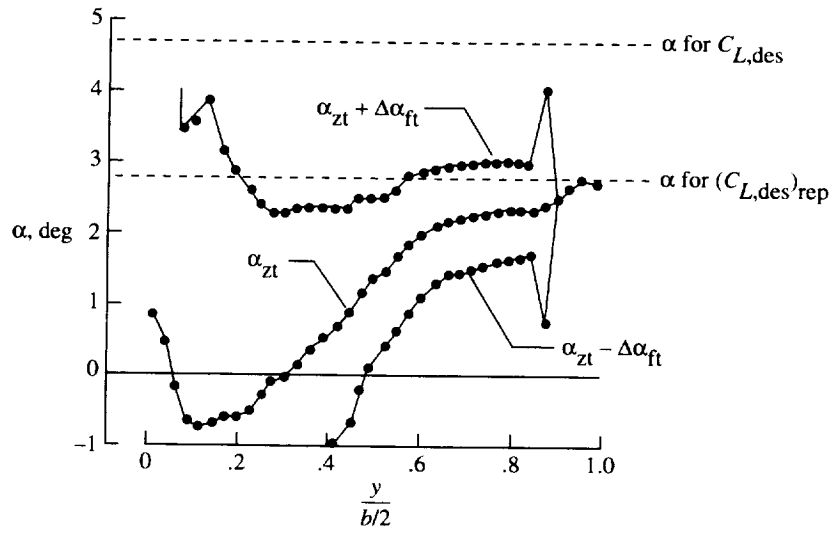
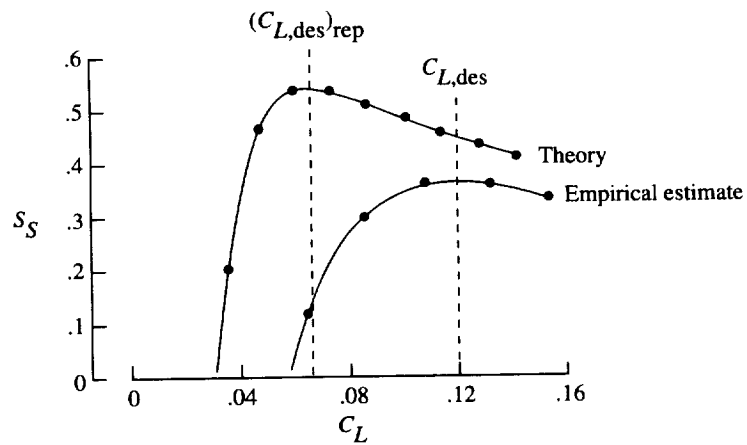
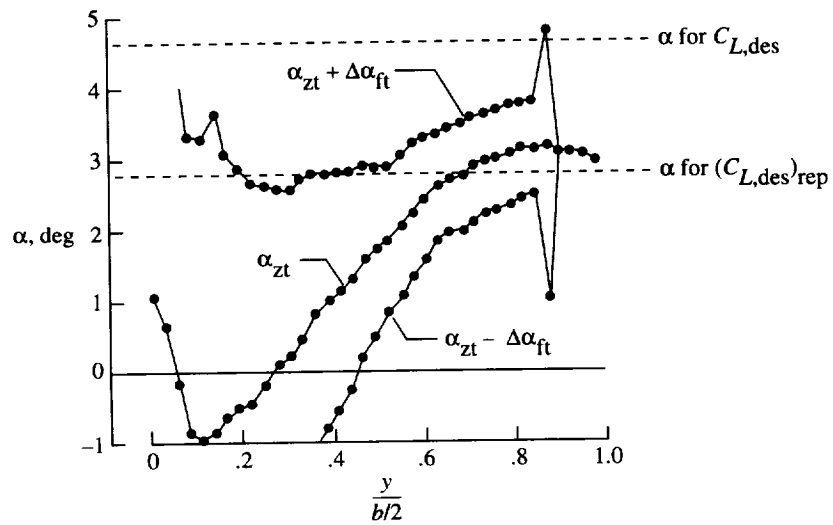
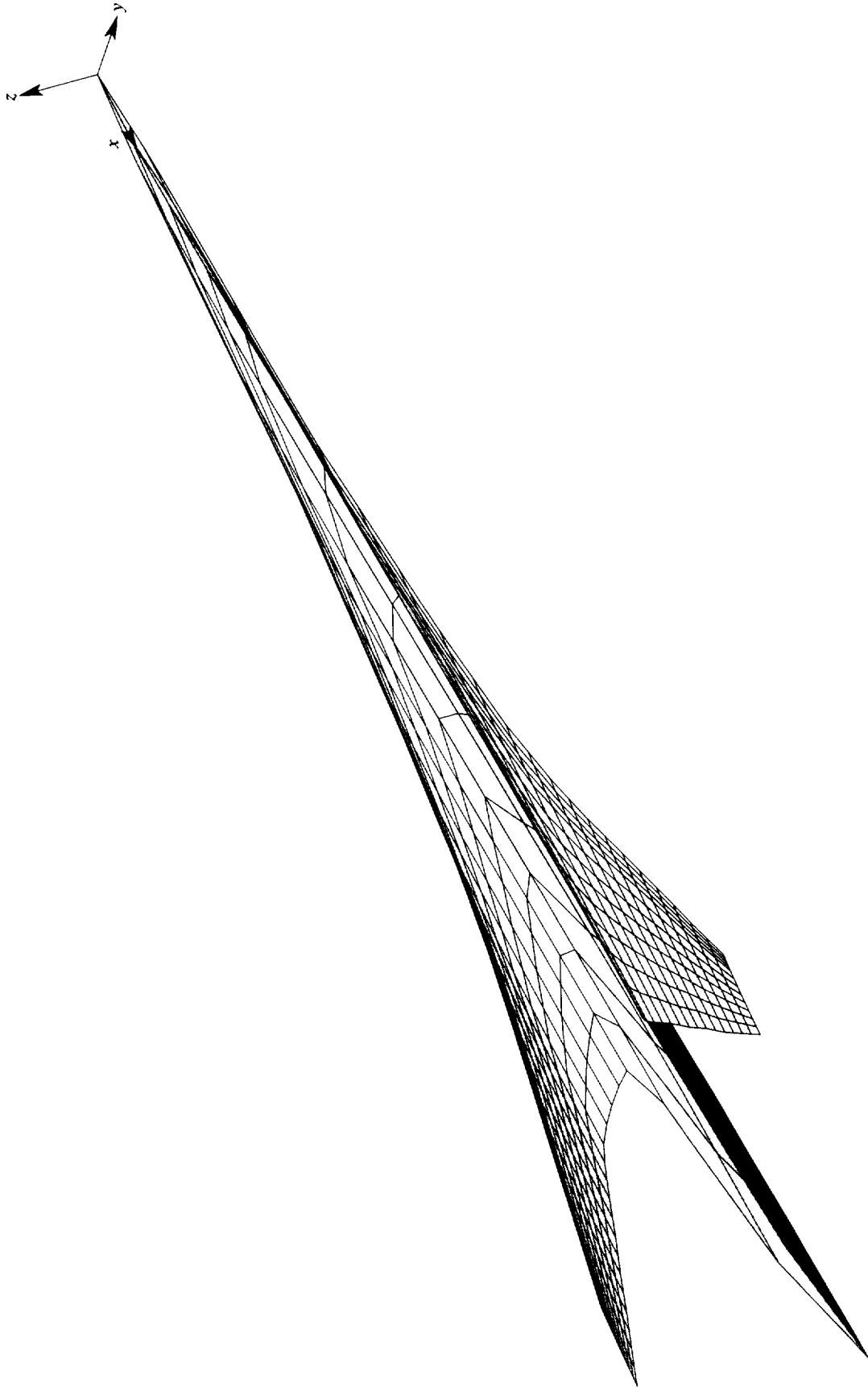


Figure 30. Critical code design parameters from SST whole-wing design. $M = 2.40$; $C_{L,des} = 0.12$.



(a) Critical design parameters.

Figure 31. Code data from SST whole-wing design with imposition of faired leading-edge surface weighting factors.
 $M = 2.40$; $C_{L,des} = 0.12$.



(b) Camber surface.

Figure 31. Concluded.

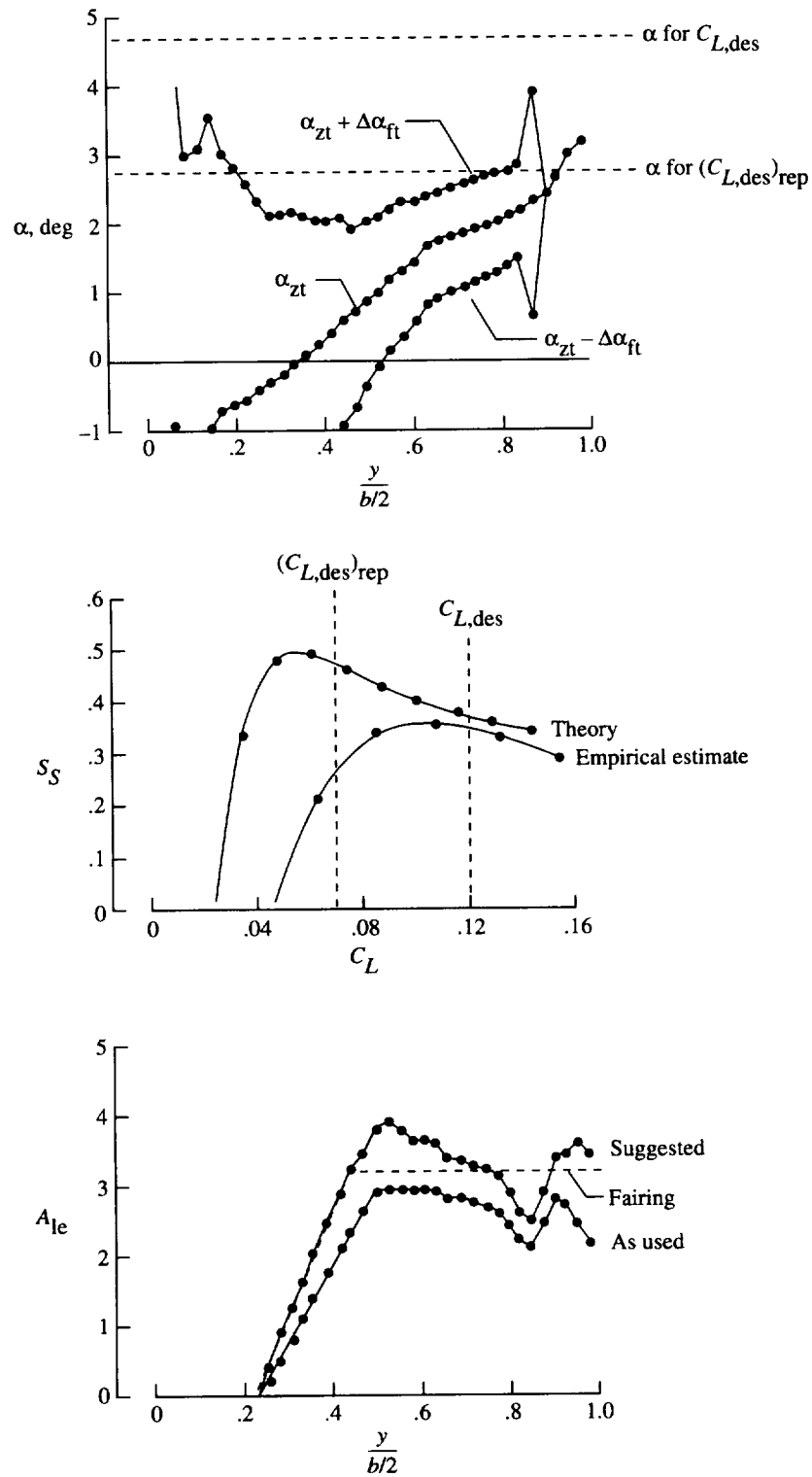


Figure 32. Critical code design parameters from SST reflexed surface wing design. $M = 2.40$; $C_{L,des} = 0.12$.

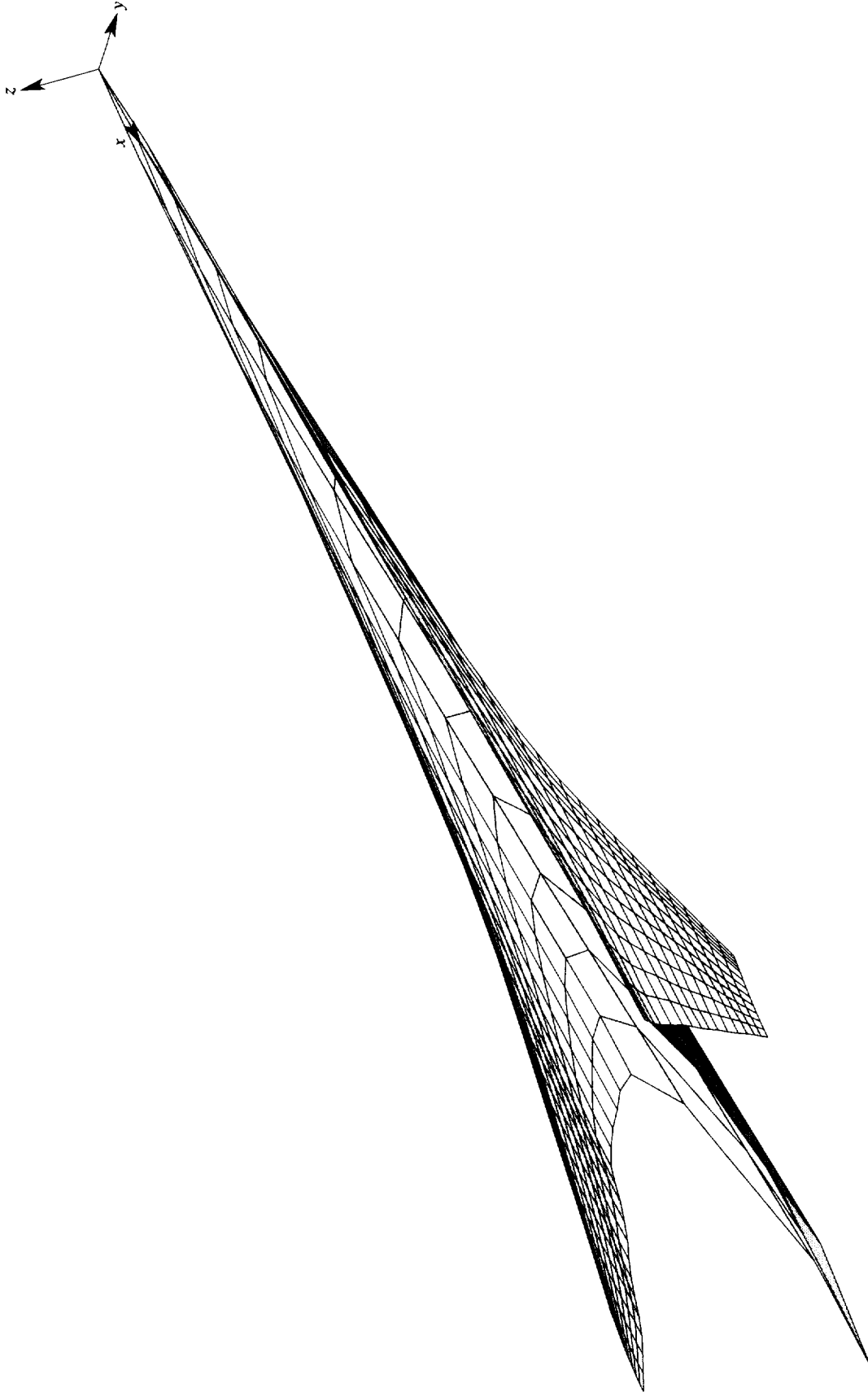


Figure 33. Camber surface from SST reflexed surface wing design with imposed leading-edge surface factors. $M = 2.40$; $C_{L,des} = 0.12$.

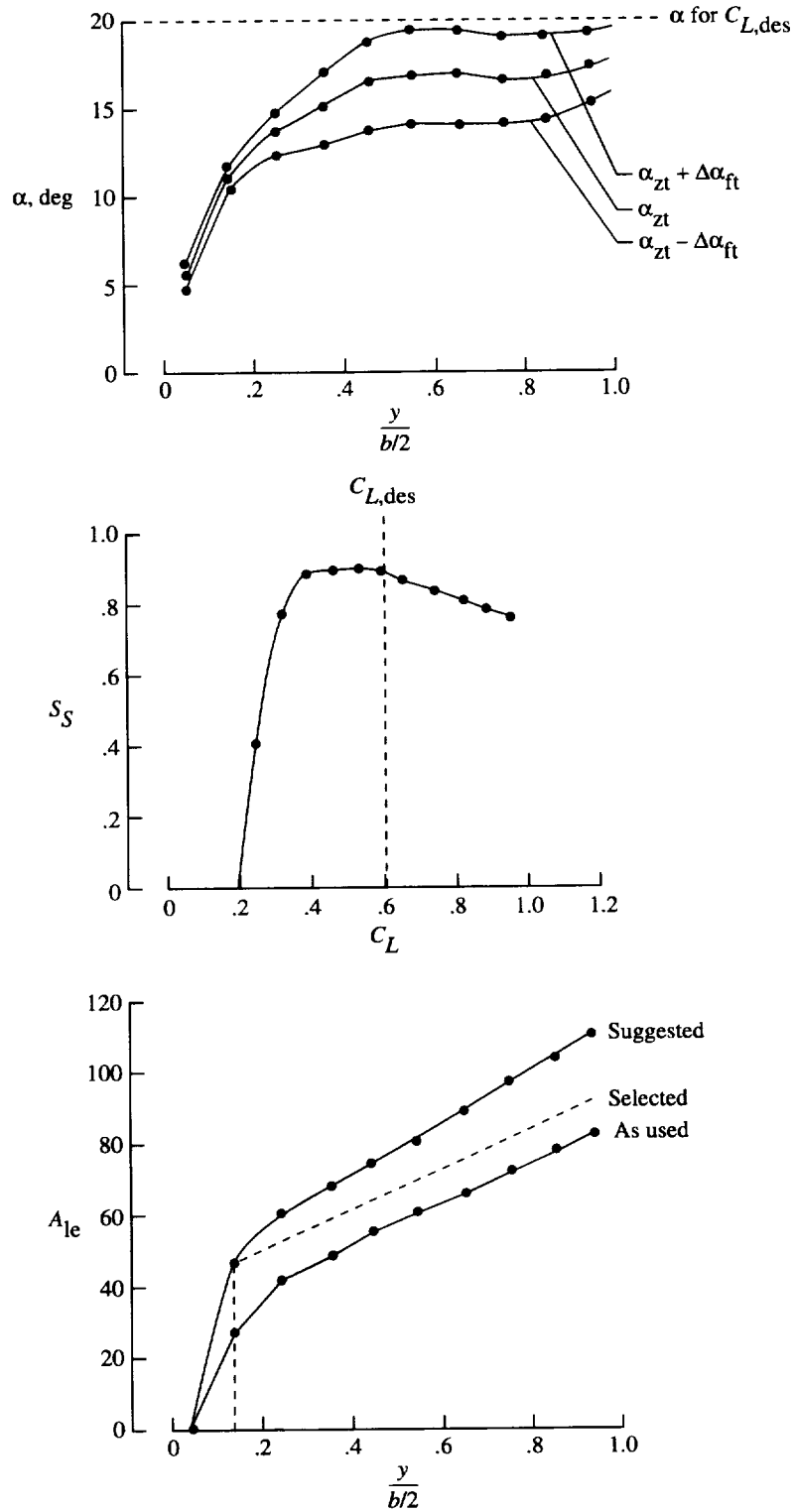
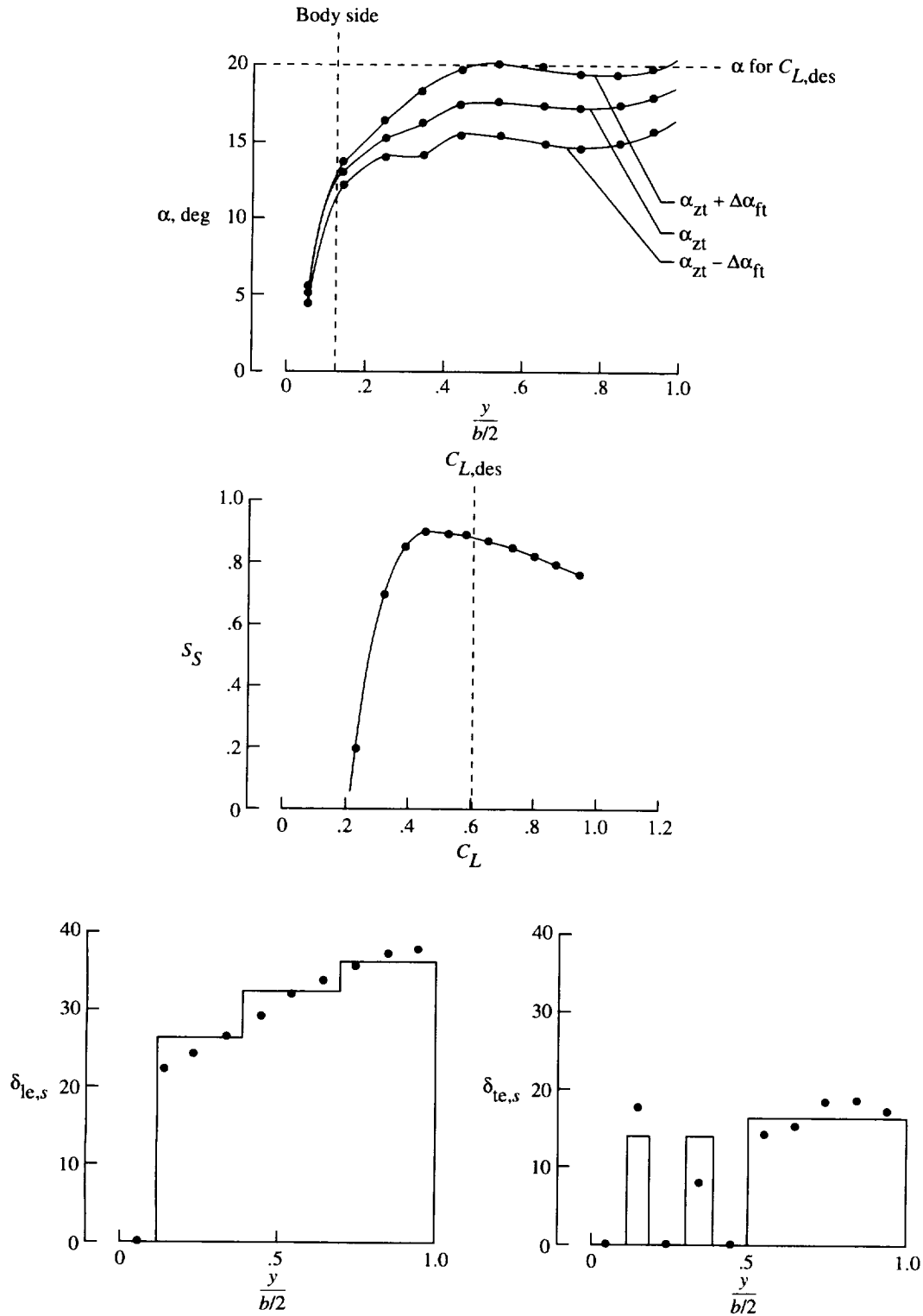
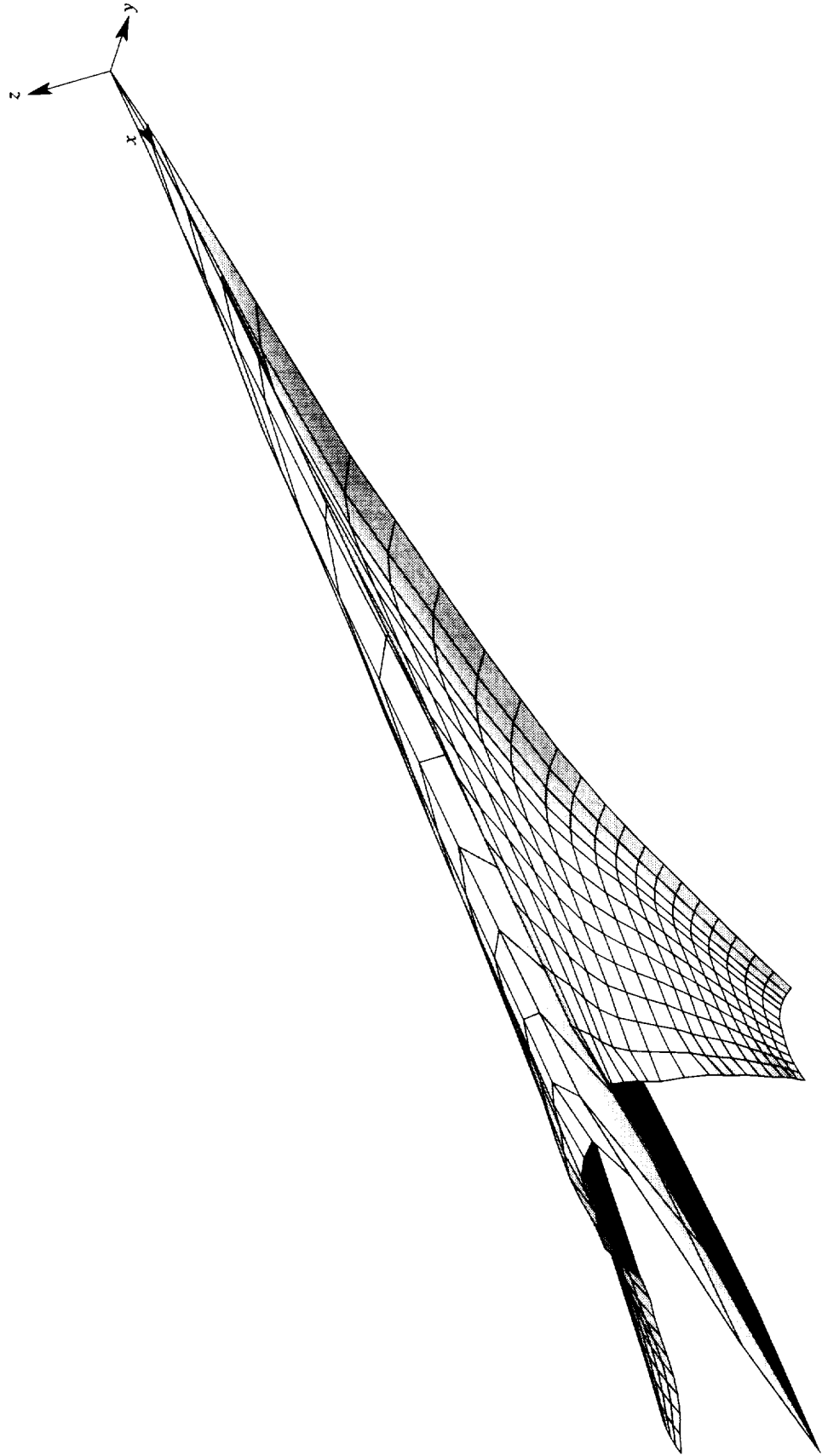


Figure 34. Critical code design parameters from SST mission adaptive surface and flap system design. $M = 0.30$; $C_{L,des} = 0.6$; $C_{m,des} = -0.24$.



(a) Critical design parameters.

Figure 35. Code data from SST mission adaptive surface and flap system design with imposition of faired leading-edge surface factors. $M = 0.30$; $C_{L,des} = 0.6$; $C_{m,des} = -0.24$.



(b) Camber surface.

Figure 35. Concluded.

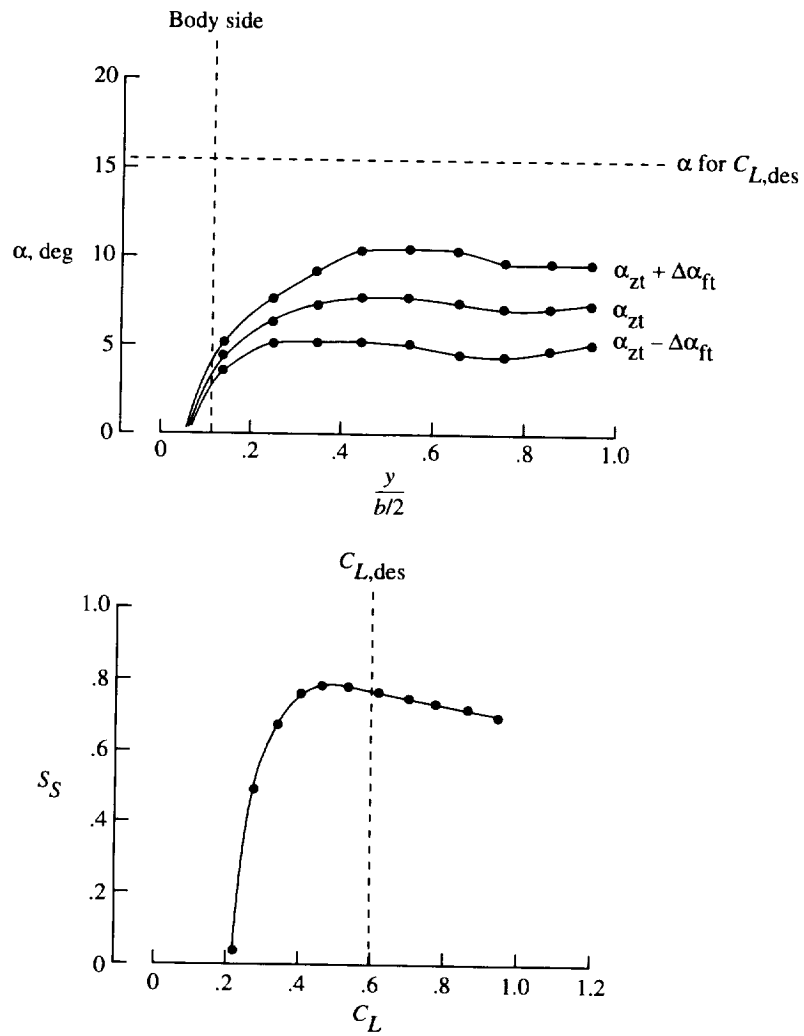
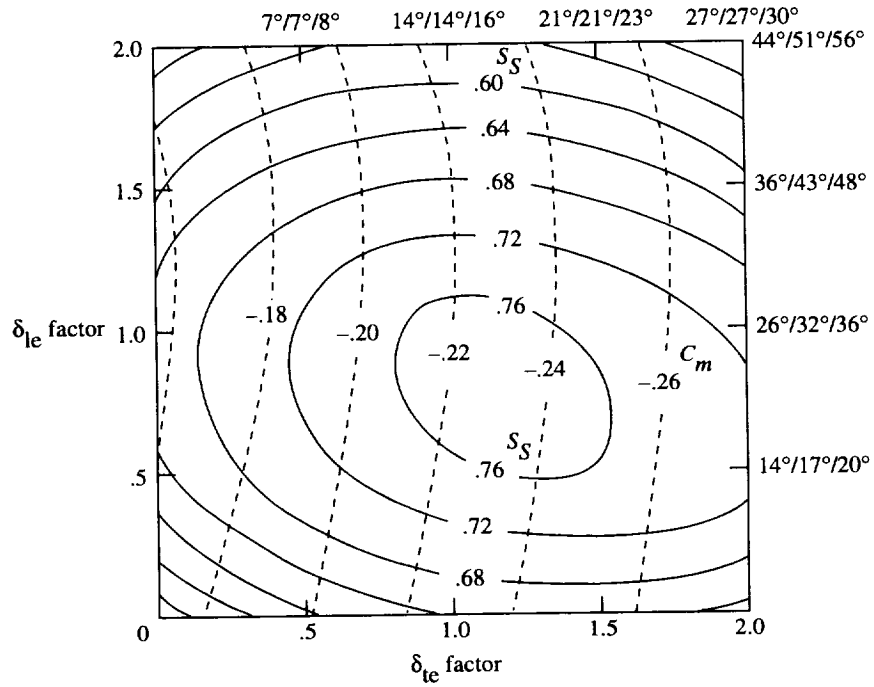
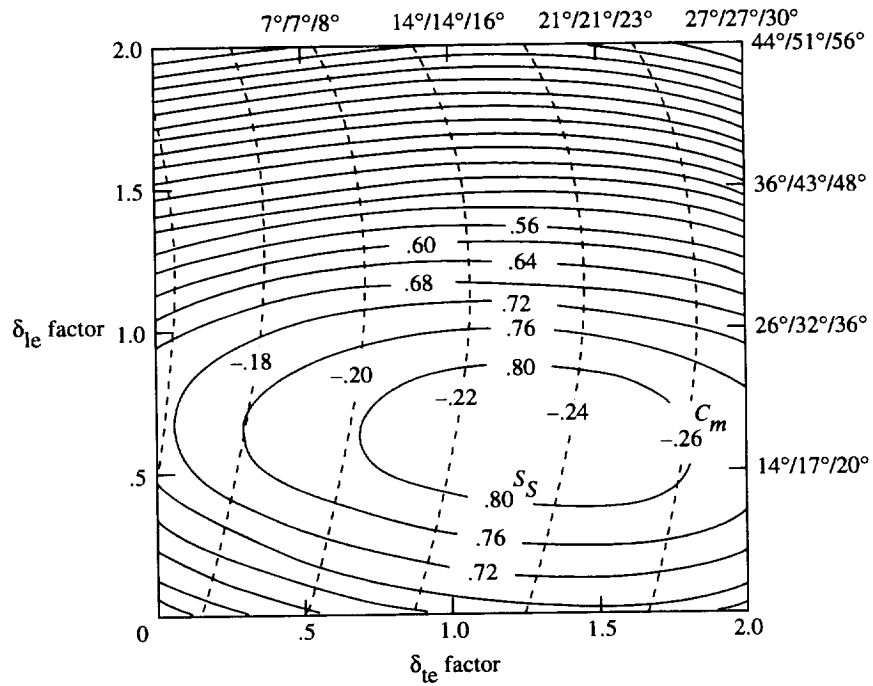


Figure 36. Code data from SST flap system evaluation (AERO2S). $\delta_{le,s} = 26^\circ/32^\circ/36^\circ$; $\delta_{te,s} = 14^\circ/14^\circ/16^\circ$; $M = 0.30$.

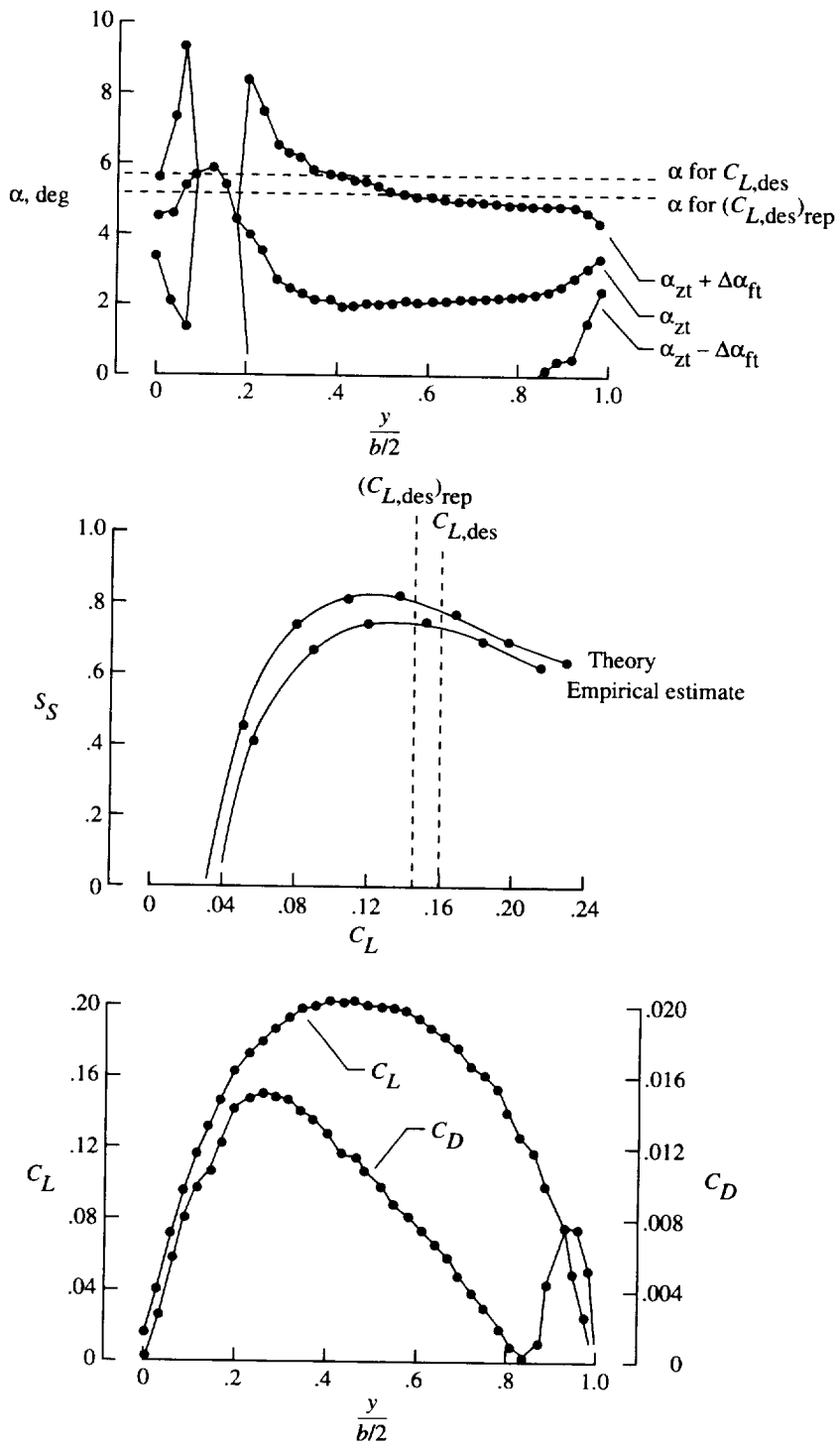


(a) Nine individual runs.



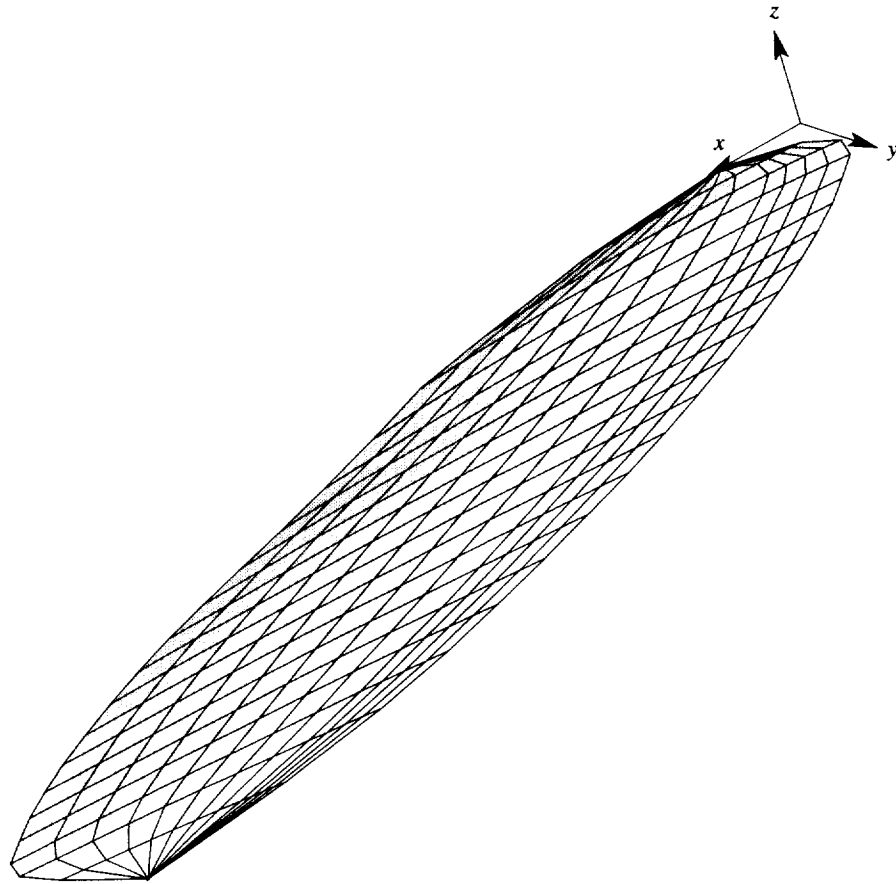
(b) Single run with multiplier factors.

Figure 37. SST flap system performance map derived from AERO2S code results. $M = 0.30$; $R = 2.0 \times 10^6$; $C_L = 0.6$.



(a) Critical design parameters.

Figure 38. Code data from nonsymmetrical elliptical planform wing design. $M = 1.40$; $C_{L,des} = 0.16$.



(b) Camber surface.

Figure 38. Concluded.

REPORT DOCUMENTATION PAGE			Form Approved OMB No. 0704-0188	
Public reporting burden for this collection of information is estimated to average 1 hour per response, including the time for reviewing instructions, searching existing data sources, gathering and maintaining the data needed, and completing and reviewing the collection of information. Send comments regarding this burden estimate or any other aspect of this collection of information, including suggestions for reducing this burden, to Washington Headquarters Services, Directorate for Information Operations and Reports, 1215 Jefferson Davis Highway, Suite 1204, Arlington, VA 22202-4302, and to the Office of Management and Budget, Paperwork Reduction Project (0704-0188), Washington, DC 20503.				
1. AGENCY USE ONLY (Leave blank)	2. REPORT DATE November 1997	3. REPORT TYPE AND DATES COVERED Technical Paper		
4. TITLE AND SUBTITLE Guide to AERO2S and WINGDES Computer Codes for Prediction and Minimization of Drag Due to Lift			5. FUNDING NUMBERS WU 537-09-20-02	
6. AUTHOR(S) Harry W. Carlson, Julio Chu, Lori P. Ozoroski, and L. Arnold McCullers				
7. PERFORMING ORGANIZATION NAME(S) AND ADDRESS(ES) NASA Langley Research Center Hampton, VA 23681-2199			8. PERFORMING ORGANIZATION REPORT NUMBER L-17546	
9. SPONSORING/MONITORING AGENCY NAME(S) AND ADDRESS(ES) National Aeronautics and Space Administration Washington, DC 20546-0001			10. SPONSORING/MONITORING AGENCY REPORT NUMBER NASA TP-3637	
11. SUPPLEMENTARY NOTES Carlson, Lockheed Martin Engineering & Sciences, Hampton, VA; Chu and Ozoroski, Langley Research Center, Hampton, VA; McCullers, ViGYAN, Inc., Hampton, VA.				
12a. DISTRIBUTION/AVAILABILITY STATEMENT Unclassified-Unlimited Subject Category 05 Availability: NASA CASI (301) 621-0390			12b. DISTRIBUTION CODE	
13. ABSTRACT (Maximum 200 words) The computer codes, AERO2S and WINGDES, are now widely used for the analysis and design of airplane lifting surfaces under conditions that tend to induce flow separation. These codes have undergone continued development to provide additional capabilities since the introduction of the original versions over a decade ago. This code development has been reported in a variety of publications (NASA technical papers, NASA contractor reports, and society journals). Some modifications have not been publicized at all. Users of these codes have suggested the desirability of combining in a single document the descriptions of the code development, an outline of the features of each code, and suggestions for effective code usage. This report is intended to supply that need.				
14. SUBJECT TERMS Aerodynamics; Linearized theory; Numerical methods; Attainable thrust			15. NUMBER OF PAGES 144	
			16. PRICE CODE A07	
17. SECURITY CLASSIFICATION OF REPORT Unclassified	18. SECURITY CLASSIFICATION OF THIS PAGE Unclassified	19. SECURITY CLASSIFICATION OF ABSTRACT Unclassified	20. LIMITATION OF ABSTRACT Unlimited	